Green's function methods for charged and neutral excitations

Enzo Monino

Université Fédérale
Toulouse Midi-Pyrénées

THÈSE

En vue de l'obtention du
DOCTORAT DE L'UNIVERSITÉ DE TOULOUSE

Délivré par l'Université Toulouse 3 - Paul Sabatier

Présentée et soutenue par

Enzo MONINO

Le 5 octobre 2023

Méthodes basées sur les fonctions de Green pour les excitations chargées et neutres

Ecole doctorale : **SDM - SCIENCES DE LA MATIERE - Toulouse**

Spécialité : **Physico-Chimie Théorique**

Unité de recherche :
LCPQ - Laboratoire de Chimie et Physique Quantiques

Thèse dirigée par
Pierre-François LOOS

Jury

M. Xavier BLASE, Rapporteur
M. Emmanuel FROMAGER, Rapporteur
Mme Pina ROMANIELLO, Examinatrice
M. Miquel HUIX-ROTLLANT, Examinateur
M. Pierre-François LOOS, Directeur de thèse
Mme Mai DINH PHUONG, Présidente

Green's function methods for charged and neutral excitations

Enzo Monino

Laboratoire de Chimie et Physique Quantiques
Université Toulouse-III Paul-Sabatier

January 3, 2024

À ma famille . . .

Remerciements

Je souhaite en premier lieu remercier mon directeur de thèse, Titou, qui m'a donné la chance de travailler avec lui et qui a fait preuve de beaucoup de patience pendant ces trois années. Il a été un excellent directeur tout du long et n'a cessé d'enrichir ma petite connaissance scientifique. Je le remercie pour son aide scientifique et personnelle ainsi que pour sa disponibilité de tous les jours. Je souhaite également remercier tous les membres des équipes PTEROSOR et TREX qui m'ont aidé et conseillé durant cette thèse. Merci aussi à tous les autres doctorants, post-doctorants et permanents du LCPQ pour leur accueil et leur gentillesse envers moi. Finalement, merci à mon collègue et voisin pendant ces trois années, Abdallah, pour nos nombreuses discussions et pour toute l'aide qu'il m'a apportée.

Contents

List of Abbreviations

AO	**A**tomic **O**rbital
ADC	**A**lgebraic **D**iagrammatic **C**onstruction
BSE	**B**ethe-**S**alpeter **E**quation
CASSCF	**C**omplete-**A**ctive-**S**pace **S**elf-**C**onsistent **F**ield
CASPT2	**C**omplete-**A**ctive-**S**pace second-order **P**erturbation **T**heory
CC	**C**oupled **C**luster
CCSD	**C**oupled **C**luster **S**ingles and **D**oubles
CCSD(T)	**C**oupled **C**luster **S**ingles, **D**oubles and perturbative **T**riples
CCSDT	**C**oupled **C**luster **S**ingles, **D**oubles and **T**riples
CCSDTQ	**C**oupled **C**luster **S**ingles, **D**oubles, **T**riples and **Q**uadruples
CI	**C**onfiguration **I**nteraction
CIS	**C**onfiguration **I**nteraction **S**ingles
CISD	**C**onfiguration **I**nteraction **S**ingles and **D**oubles
DFT	**D**ensity-**F**unctional **T**heory
EA	**E**lectron **A**ffinity
EOM-CC	**E**quation-**O**f-**M**otion **C**oupled **C**luster
EOM-CCSD	**E**quation-**O**f-**M**otion **C**oupled **C**luster **S**ingles and **D**oubles
HF	**H**artree-**F**ock
HOMO	**H**ighest **O**ccupied **M**olecular **O**rbital
IP	**I**onization **P**otential
KS	**K**ohn-**S**ham
LUMO	**L**owest **U**noccupied **M**olecular **O**rbital
MBPT	**M**any-**B**ody **P**erturbation **T**heory
MO	**M**olecular **O**rbital
ph	**p**article-**h**ole
ph	**p**article-**p**article
pp-RPA	**p**article-**p**article **R**andom **P**hase **A**pproximation
ph-RPA	**p**article-**h**ole **R**andom **P**hase **A**pproximation
RHF	**R**estricted **H**artree-**F**ock
RPA	**R**andom **P**hase **A**pproximation
RSPT	**R**ayleigh-**S**chrödinger **P**erturbation **T**heory
SF-ADC	**S**pin-**F**lip **A**lgebraic **D**iagrammatic **C**onstruction
SF-BSE	**S**pin-**F**lip **B**ethe-**S**alpeter **E**quation
SF-CI	**S**pin-**F**lip **C**onfiguration **I**nteraction
SF-EOM-CC	**S**pin-**F**lip **E**quation-**O**f-**M**otion **C**oupled **C**luster
SF-TD-DFT	**S**pin-**F**lip **T**ime-**D**ependent **D**ensity-**F**unctional **T**heory
TDA	**T**amm-**D**ancoff **A**pproximation
TD-DFT	**T**ime-**D**ependent **D**ensity-**F**unctional **T**heory
TD-HF	**T**ime-**D**ependent **H**artree-**F**ock
UHF	**U**nrestricted **H**artree-**F**ock

Introduction

Interaction between light and matter is ubiquitous in nature and numerous examples can be cited. Among them, we can mention photosynthesis [1–3] which is a process used by plants, algae, and some bacteria. It captures sunlight to convert carbon dioxide CO_2 and water H_2O from air and soil to produce dioxygen O_2 and chemical energy in the form of glucose. Another biological example that underlines the interaction between light and molecules is the process of vision that takes place in the retina of the eye [4–8]. Indeed, in the vision process, light is absorbed by a pigment in the eye and leads to an isomerization reaction of the pigment. This reaction is the beginning of the visual process. Many other important applications exist in many different domains like for energetic purposes with the conversion of sunlight to an electric current in photovoltaic cells [9–12] or photocatalysis [13, 14]. Of course many more examples of application can be given but these few examples show that understanding the interaction between light and molecules is fundamental in many relevant areas of physics, chemistry, and biology.

Nowadays, numerical simulation is a very important tool not only in chemistry but in science in general, it allows scientists to model and study complex systems or phenomena that are difficult or impossible to investigate directly. Indeed, using simulations, scientists can explore hostile environments like space or extreme temperature and pressure environments. It enables us to make predictions, test hypotheses, and gain insights into various scientific domains. However, light-molecule interaction is a complex problem that leads to various possible mechanisms like absorption, emission, or scattering. In this thesis, we are only interested in the case of absorption of photons and we will focus on two processes, neutral excitation and ionization. Figure 1 schematically shows the difference between the two cases. The ionization process takes place when the absorbed photon has enough energy to extract an electron from the molecule while a neutral excitation promotes an electron from an occupied electronic state to an excited one. Note that when a molecule is excited from its ground state geometry, the geometry of the excited state can relax. Figure 2 shows some of the different transition energies taking place when looking at neutral excitations. First, an electron absorbs a photon and is promoted from the electronic and vibrational ground state at its equilibrium geometry to one excited state at the same geometry. Then, the molecular structure relaxes (and goes along the horizontal axis) to the equilibrium geometry of the excited state. Next, the electron is deexcited to the electronic ground state at the equilibrium geometry of the excited state. Finally, the geometry of the molecule relaxes to the electronic and vibrational ground state at its equilibrium geometry. Unfortunately, all these processes are extremely challenging to model and in this thesis, we focus only on the so-called vertical excitation energies meaning that we do not take into account any relaxation of the geometries.

Unfortunately, defining an effective method that reliably provides accurate excited-state and ionization energies remains a major challenge in theoretical chemistry. Originally developed, in the context of electricity and magnetism theories, by George Green in its seminal work in 1828 [15], Green's functions are now present in many domains of physics like nuclear physics [16] and condensed matter physics [17–19].

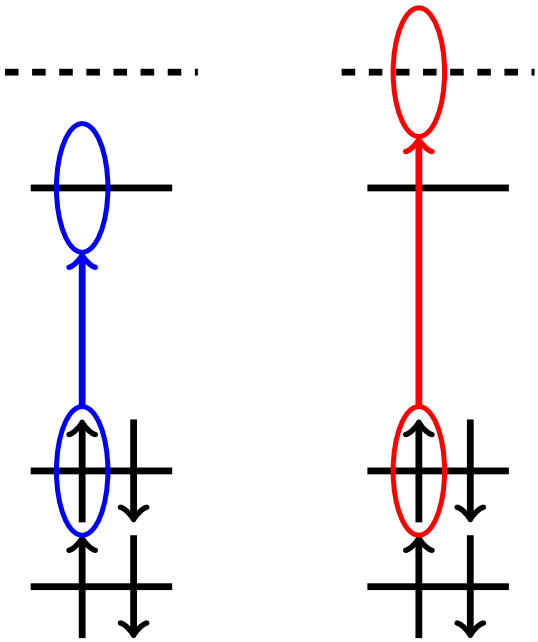

Figure 1: Scheme of a neutral excitation (on the left) that promotes an electron from one electronic state to an excited one and an ionization (on the right) that promotes an electron to the continuum (dashed line).

The use of Green's function methods in quantum chemistry has significantly developed in recent years and has garnered considerable interest due to their ability to target both charged and neutral excitations [20–32]. It is in this context that this work takes place by targeting charged and neutral excitations in molecules using Green's function methods.

This thesis can be considered as a work in four parts and is structured as follows, Chapter 1 is devoted to the establishment of the various methods on which this thesis relies and to setting the notations used throughout this work. After some reminders about the Schrödinger equation and the usual Born-Oppenheimer approximation, we go through the variational principal and the noninteracting electrons case. This set the framework for all the methods that we investigate in this work. First, the Hartree-Fock method is discussed in both restricted and unrestricted formalism. Then, we have a look at the density functional theory (DFT) in the Kohn-Sham formalism. After this, we consider the linear response theory that allows us to obtain an approximation to the time-dependent Schrödinger equation. This leads to the time-dependent Hartree-Fock (TD-HF) and time-dependent DFT (TD-DFT) methods. Afterward, we dive into the many-body perturbation theory by, first investigating the well-known Møller Plesset (MP) perturbation theory and then, by considering Green's function formalism. Within this latter formalism, we examine different approximations, first for the computation of charged excitations using the one-body Green's function and then, for the computation of neutral excitations using the two-body Green's function with the Bethe-Salpeter equation (BSE) formalism.

Chapters 2 and 3 are dedicated to the application of methods for studying neutral (vertical) excitations in atoms and molecules. In chapter 2 we apply the spin-flip formalism to the BSE formalism to access, in particular, double excitations. Dynamical corrections to the static BSE optical excitations are taken into account via perturbative treatment. The performance of this spin-flip BSE formalism is illustrated by computing excited-state energies of the beryllium atom (Be), the hydrogen molecule (H_2)

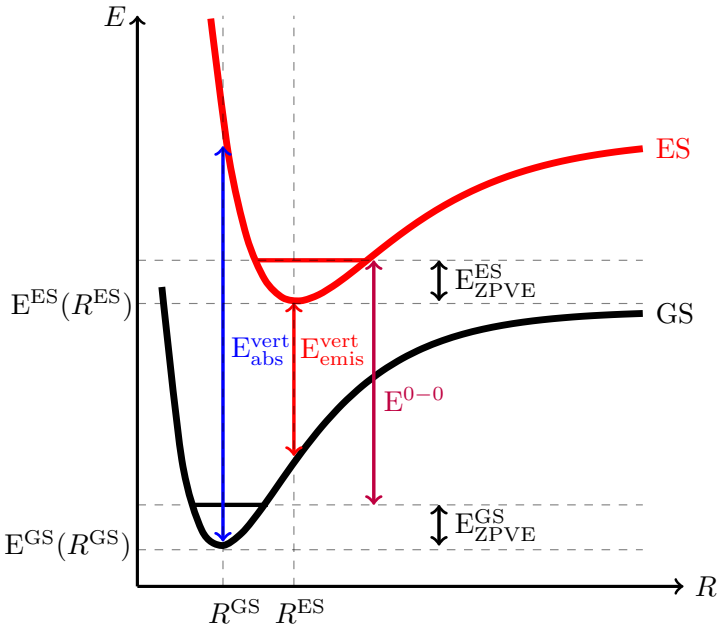

Figure 2: Scheme of neutral vertical transition energy represented by a (blue) vertical arrow. We consider that an electronic excitation is instantaneous at the time scale of the nuclear motion. Thus, this excitation is vertical with respect to the reaction coordinate R that describes the positions of the nuclei. Experimentally, the neutral excitation energy measured is the E^{0-0} energy (purple). To be able to compare computation and measurement we have to obtain the ground state (GS) and excited state (ES) zero-point vibrational energies (ZPVE).

at various bond lengths, and cyclobutadiene in its rectangular and square-planar geometries and compared to other spin-flip methods. In chapter 3, using a large panel of methods, we provide an extensive computational study of the automerization barrier (defined as the difference between the square and rectangular ground-state energies) and the vertical excitation energies at the square and rectangular equilibrium structures of the cyclobutadiene (CBD) molecule. In particular, selected configuration interaction, multi-reference perturbation theory, and coupled-cluster calculations are performed. The spin-flip formalism is also tested within TD-DFT and the algebraic diagrammatic construction schemes. A theoretical best estimate is defined for the automerization barrier and each vertical transition energy.

Chapters 4 and 5 are devoted to the study of some features and connections of different Green's function methods. In chapter 4 we explore the appearance of multiple solutions and unphysical discontinuities in various physical quantities computed within the GW approximation. We then give a simple and efficient regularization procedure inspired by the similarity renormalization group to remove these discontinuities. In chapter 5 we investigate the connections between various Green's function methods and evaluate their performances for charged and neutral excitations. We demonstrate that, within the *GW* approximation, a second-order BSE kernel with dynamical correction is required to predict an inverted gap of a model molecular emitter for thermally activated delayed fluorescence.

Chapter 6 takes the form of documentation for qcmath which is a quantum chemistry software developed during this thesis. This software is designed for electronic structure calculations and it is based on the Wolfram Mathematica language. The purpose of this software is twofold, firstly, to bring together different methods

and features described in this thesis, and secondly, to take advantage of the powerful symbolic nature of Mathematica to help newcomers in quantum chemistry easily develop their ideas.

Chapter 1

Methods

In this chapter, we set the framework for this thesis. We start from the Schrödinger equation and the approximations used in quantum chemistry to solve it. This brings us to one of the core methods of quantum chemistry: the Hartree-Fock (HF) approximation. Then, we discuss another fundamental theory the Density Functional Theory (DFT). We then turn to the excited states part by using linear response theory on these two methods. Finally, we consider the Many-Body Perturbation Theory (MBPT) that leads us to the central concept of this thesis, Green's function methods for charged and neutral excitations.

1.1 Schrodinger equation

The time evolution of a chemical system (i.e. system composed of nuclei and electrons) is described by the time-dependent Schrödinger equation, derived by the physicist Erwin Schrödinger in 1925 and awarded the Nobel Prize in Physics in 1933

$$i\hbar\frac{\partial\Psi(\boldsymbol{x},\boldsymbol{R},t)}{\partial t} = \hat{H}\Psi(\boldsymbol{x},\boldsymbol{R},t), \tag{1.1}$$

where $\Psi(\boldsymbol{x},\boldsymbol{R},t)$ is the molecular wave function that completely determines the state of the system, $\hat{H}$ is the molecular Hamiltonian operator of the system, $\boldsymbol{x} = (\boldsymbol{x}_1,\ldots,\boldsymbol{x}_N) = (\boldsymbol{r},\boldsymbol{s})$ is a composite coordinate vector gathering the spatial coordinates $\boldsymbol{r} = (\boldsymbol{r}_1,\ldots,\boldsymbol{r}_N)$ and spin coordinates $\boldsymbol{s} = (s_1,\ldots,s_N)$ of the N electrons whereas $\boldsymbol{R} = (\boldsymbol{R}_1,\ldots,\boldsymbol{R}_M)$ are the spatial coordinates of the M nuclei.

For a stationary system (i.e. not explicitly time-dependent) and by neglecting relativistic effects, the time-independent Schrödinger equation gives the eigenvalue equation

$$\hat{H}\Psi(\boldsymbol{x},\boldsymbol{R}) = E\,\Psi(\boldsymbol{x},\boldsymbol{R}), \tag{1.2}$$

where $\Psi(\boldsymbol{x},\boldsymbol{R})$ is the stationary molecular wave function and E is the total energy of the system. The non-relativistic molecular Hamiltonian is explicitly given by

$$\begin{aligned}\hat{H} &= \hat{T}_{\mathrm{n}} + \hat{T}_{\mathrm{e}} + \hat{V}_{\mathrm{en}} + \hat{V}_{\mathrm{ee}} + \hat{V}_{\mathrm{nn}} \\ &= -\sum_{A=1}^{M}\frac{\hbar^2}{2M_A}\nabla_A^2 - \sum_{i}^{N}\frac{\hbar^2}{2m_e}\nabla_i^2 - \sum_{i=1}^{N}\sum_{A=1}^{M}\frac{Z_A e^2}{4\pi\epsilon_0|\boldsymbol{R}_A-\boldsymbol{r}_i|} \\ &+ \sum_{i=1}^{N}\sum_{j>i}^{N}\frac{e^2}{4\pi\epsilon_0|\boldsymbol{r}_p-\boldsymbol{r}_j|} + \sum_{A=1}^{M}\sum_{B>A}^{M}\frac{Z_A Z_B e^2}{4\pi\epsilon_0|\boldsymbol{R}_B-\boldsymbol{R}_A|},\end{aligned} \tag{1.3}$$

where ∇_A^2 and ∇_p^2 are the Laplace operators associated with the Ath nucleus and the ith electron, respectively, $\boldsymbol{R}_A$ and Z_A are the nuclear coordinates and charge of nucleus A. The first term $\hat{T}_\mathrm{n}$ is the kinetic energy operator of the nuclei, and then $\hat{T}_\mathrm{e}$ is the kinetic energy operator of the electrons. The next term is $\hat{V}_\mathrm{en}$ which corresponds to the Coulombic attraction between electrons and nuclei. The last two terms correspond to the interelectronic ($\hat{V}_\mathrm{ee}$) and internuclear ($\hat{V}_\mathrm{nn}$) Coulombic repulsions, respectively. From now on atomic units will be used, that consists in using unitless energy $E \leftarrow E/E_h$ and coordinates $r \leftarrow r/a_0$, where $E_h = \hbar^2/(m_e a_0^2)$(= 1 Hartree) corresponds to twice the ionization energy of the hydrogen atom and $a_0 = 4\pi\epsilon_0\hbar^2/(m_e e^2)$ is the Bohr radius. Within the atomic units, the molecular Hamiltonian reads

$$\hat{H} = -\sum_{A=1}^{M}\frac{\nabla_A^2}{2M_A} - \sum_{i=1}^{N}\frac{\nabla_i^2}{2} - \sum_{i=1}^{N}\sum_{A=1}^{M}\frac{Z_A}{r_{iA}} + \sum_{i=1}^{N}\sum_{j>i}^{N}\frac{1}{r_{ij}} + \sum_{A=1}^{M}\sum_{B>A}^{M}\frac{Z_A Z_B}{R_{AB}}, \tag{1.4}$$

where r_{iA} is the distance between the ith electron and the Ath nucleus and r_{ij} is the distance between the ith and the jth electrons. The Schrödinger equation (1.2) cannot be solved except for simple systems, so approximations are needed.

1.2 Born-Oppenheimer approximation

Because nuclei are much heavier than electrons one can assume that they move more slowly. So one can decouple the movement of electrons and nuclei and one can consider that the electrons in a molecule are moving in the field of fixed nuclei. We can see this decoupling as the electrons accommodate instantaneously to any motion of the nuclei, so we can study the electronic part of a system while one keeps the nuclei frozen. This is the so-called Born-Oppenheimer approximation [33], within this approximation the first term in Eq.(1.4), the kinetic energy of the nuclei can be neglected and the last term in Eq.(1.4), the repulsion between nuclei can be considered to be constant and will be omitted. The remaining terms in Eq.(1.4) constitute the electronic Hamiltonian that describes the motion of N electrons in the field of M point charges and it is given by

$$\begin{aligned}\hat{H}_\mathrm{elec} &= \hat{T}_\mathrm{e} + \hat{V}_\mathrm{en} + \hat{V}_\mathrm{ee} \\ &= -\sum_{i=1}^{N}\frac{\nabla_i^2}{2} - \sum_{i=1}^{N}\sum_{A=1}^{M}\frac{Z_A}{r_{iA}} + \sum_{i=1}^{N}\sum_{j>i}^{N}\frac{1}{r_{ij}},\end{aligned} \tag{1.5}$$

With this electronic Hamiltonian in hand, one can write the eigenvalues equation

$$\hat{H}_\mathrm{elec}\Psi_\mathrm{elec}(\boldsymbol{x};\boldsymbol{R}) = E_\mathrm{elec}\Psi_\mathrm{elec}(\boldsymbol{x};\boldsymbol{R}), \tag{1.6}$$

where the solution $\Psi_\mathrm{elec}(\boldsymbol{x};\boldsymbol{R})$ is the electronic wave function that describes the motion of electrons and depends explicitly on the electronic coordinates but depends parametrically on the nuclear coordinates, so does the electronic energy ($E_\mathrm{elec} = E_\mathrm{elec}(\boldsymbol{R})$). It means that for different nuclear geometries, $\Psi_\mathrm{elec}(\boldsymbol{x};\boldsymbol{R})$ is a different function of the electronic coordinates. Then, for fixed nuclei, the total energy includes the constant nuclear repulsion

$$E_\mathrm{tot} = E_\mathrm{elec} + \sum_{A=1}^{M}\sum_{B>A}^{M}\frac{Z_A Z_B}{R_{AB}}. \tag{1.7}$$

Once the electronic problem is solved one can solve the nuclear motion under the same assumptions as for the electronic problem. Indeed, because electrons move much faster than the nuclei, one can average the electronic motion in Eq.(1.4), averaged over the electronic wave function. Then we obtain a nuclear Hamiltonian that describes the motion of the nuclei in the averaged field of the electrons

$$\begin{aligned}\hat{H}_{\text{nuc}} &= -\sum_{A=1}^{M}\frac{\nabla_A^2}{2M_A} + \left\langle -\sum_{i}^{N}\frac{\nabla_i^2}{2} - \sum_{i=1}^{N}\sum_{A=1}^{M}\frac{Z_A}{r_{iA}} + \sum_{i=1}^{N}\sum_{j>i}^{N}\frac{1}{r_{ij}}\right\rangle + \sum_{A=1}^{M}\sum_{B>A}^{M}\frac{Z_A Z_B}{R_{AB}} \\ &= -\sum_{A=1}^{M}\frac{\nabla_A^2}{2M_A} + E_{\text{elec}}(\boldsymbol{R}) + \sum_{A=1}^{M}\sum_{B>A}^{M}\frac{Z_A Z_B}{R_{AB}} \\ &= -\sum_{A=1}^{M}\frac{\nabla_A^2}{2M_A} + E_{\text{tot}}(\boldsymbol{R}),\end{aligned} \tag{1.8}$$

where the total energy $E_{\text{tot}}(\boldsymbol{R})$ gives a potential for nuclear motion so that the nuclei in the Born-Oppenheimer approximation move on a potential energy surface obtained by solving the electronic problem. Then with the nuclear Hamiltonian one can write the nuclear Schrödinger equation

$$\hat{H}_{\text{nuc}}\Psi_{\text{nuc}}(\boldsymbol{R}) = E\Psi_{\text{nuc}}(\boldsymbol{R}), \tag{1.9}$$

where the solution $\Psi_{\text{nuc}}(\boldsymbol{R})$ describes the vibration, rotation, and translation of a molecule. The energy E is the Born-Oppenheimer approximation to the total energy in Eq.(1.2) and it includes electronic and nuclear energies. Thus the approximation to the total wave function in Eq.(1.2) is

$$\Psi(\boldsymbol{x};\boldsymbol{R}) = \Psi_{\text{elec}}(\boldsymbol{x};\boldsymbol{R})\Psi_{\text{nuc}}(\boldsymbol{R}). \tag{1.10}$$

Henceforth, we will only consider the electronic problem and for convenience, in all subsequent developments, we drop the "elec" subscript and will write the electronic wave function $\Psi(\boldsymbol{x};\boldsymbol{R})$. Moreover, we do not write the parameter $\boldsymbol{R}$ in the electronic wave function, meaning that we consider electronic Hamiltonians (Eq.(1.5)) and wave functions at a given nuclear geometry $\boldsymbol{R}$. Thus, we have the many-electron wave function $\Psi(\boldsymbol{x})$, we introduce now the Dirac notation that allows us to write $\Psi(\boldsymbol{x}) = \langle \boldsymbol{x}|\Psi\rangle$ that we can write $|\Psi\rangle$. During all this work we will use the wave function in both notations.

1.3 Variational principle

As previously said in 1.1 the Schrödinger equation cannot be solved exactly and so we need to find approximate solutions. For a given Hamiltonian operator $\hat{H}$, it exists an infinite number of solutions to the Schrödinger equation

$$\hat{H}\,|\Psi_n\rangle = \mathcal{E}_n\,|\Psi_n\rangle\,, \quad n = 0, 1, \ldots, \tag{1.11}$$

with the eigenvalues

$$\mathcal{E}_0 \leq \mathcal{E}_1 \leq \ldots \leq \mathcal{E}_n \leq \ldots. \tag{1.12}$$

Because the Hamiltonian $\hat{H}$ is Hermitian the eigenvalues are real and the corresponding eigenvectors are orthonormal, i.e.

$$\langle \Psi_n|\Psi_m\rangle = \delta_{nm}, \tag{1.13}$$

where

$$\delta_{nm} = \begin{cases} 1, & \text{if } n = m, \\ 0, & \text{otherwise,} \end{cases} \tag{1.14}$$

is the Kronecker delta [34]. Thus, using Eq. (1.11), we have

$$\langle \Psi_m | \hat{H} | \Psi_n \rangle = \mathcal{E}_n \delta_{nm}. \tag{1.15}$$

If we consider that the eigenvectors of the Hamiltonian operator form a complete set then any wave function $|\Phi\rangle$ having the same boundary conditions as the complete set of eigenvectors can be expressed as a linear combination of the eigenvectors

$$\begin{aligned} |\Phi\rangle &= \sum_n c_n |\Psi_n\rangle \\ &= \sum_n |\Psi_n\rangle \langle \Psi_n | \Phi \rangle \end{aligned} \tag{1.16}$$

and

$$\begin{aligned} \langle \Phi| &= \sum_n c_n^* \langle \Psi_n| \\ &= \sum_n \langle \Psi_n | \Phi \rangle \langle \Psi_n| . \end{aligned} \tag{1.17}$$

If we consider a normalized wave function $|\Phi\rangle$, then

$$\begin{aligned} \langle \Phi | \Phi \rangle = 1 &= \sum_{nm} \langle \Phi | \Psi_n \rangle \langle \Psi_n | \Psi_m \rangle \langle \Psi_m | \Phi \rangle \\ &= \sum_{nm} \langle \Phi | \Psi_n \rangle \delta_{nm} \langle \Psi_m | \Phi \rangle \\ &= \sum_n \langle \Phi | \Psi_n \rangle \langle \Psi_n | \Phi \rangle \\ &= \sum_n | \langle \Psi_n | \Phi \rangle |^2. \end{aligned} \tag{1.18}$$

Then the expectation value of the Hamiltonian using the wave function $|\Phi\rangle$ is

$$\langle \Phi | \hat{H} | \Phi \rangle = \sum_{nm} \langle \Phi | \Psi_n \rangle \ \langle \Psi_n | \hat{H} | \Psi_m \rangle \langle \Psi_m | \Phi \rangle . \tag{1.19}$$

Using Eq.(1.15), we end up with

$$\begin{aligned} \langle \Phi | \hat{H} | \Phi \rangle &= \sum_n \mathcal{E}_n | \langle \Psi_n | \Phi \rangle |^2 \\ &= \sum_n \mathcal{E}_n |c_n|^2. \end{aligned} \tag{1.20}$$

Because for all n we have that $\mathcal{E}_n \geq \mathcal{E}_0$, this leads us to the variational principle that states that for any normalized wave function $|\Phi\rangle$ that satisfies the same boundary conditions than the complete set $|\Psi_n\rangle$, the expectation value of the Hamiltonian operator will give an upper bound to the exact ground state energy

$$\langle \Phi | \hat{H} | \Phi \rangle \geq \mathcal{E}_0. \tag{1.21}$$

So the variation method works as follows, we take a normalized trial wave function $|\Phi\rangle$ which depends on parameters (the c_n coefficients) and vary these parameters until the expectation value $\langle \Phi | \hat{H} | \Phi \rangle$ reaches a minimum. Then this minimum is the

variational estimate of the exact ground state energy. If we consider a trial wave function which is a linear combination of a fixed set of N basis orthonormal functions then finding the optimum set of coefficients can be expressed in a matrix form

$$\mathbf{Hc} = \mathbf{c}\boldsymbol{\epsilon} \tag{1.22}$$

where $\mathbf{c}$ is the vector of coefficients, $\mathbf{H}$ is symmetric Hamiltonian matrix of dimension $N \times N$. Thus, this eigenvalue problem can be solved by the diagonalization of the $\mathbf{H}$ matrix, where the lowest eigenvalue gives an upper bound to the exact ground state energy.

1.4 Orbital approximation and Slater determinants

Although the Born-Oppenheimer approximation reduces the number of variables, from $3(N+M)$ to $3N$, solving the electronic Schrödinger equation is still impossible for most chemical systems. Indeed, the interaction between electrons, the term $1/r_{pq}$ in Eq.(1.5), makes it difficult to solve the Schrödinger equation and obtain the electronic wave function. Before getting the many-electron wave function for the fully interacting system one considers first a system of noninteracting electrons with the following electronic Hamiltonian

$$\hat{H} = \sum_{i=1}^{N} \hat{h}(\boldsymbol{r}_i) = \sum_{i=1}^{N} \left[-\frac{\nabla_{r_i}^2}{2} + v(\boldsymbol{r}_i) \right] \tag{1.23}$$

with $\hat{h}(\boldsymbol{r}_i)$ the operator describing the kinetic and potential energies of electron i. Then this operator has a set of eigenfunctions, a set of one-electron functions $(\varphi_i)_{i=1}^{N}$, the so-called spin orbitals

$$\hat{h}(\boldsymbol{r}_i)\varphi_j(\boldsymbol{x}_i) = \epsilon_j \varphi_j(\boldsymbol{x}_i). \tag{1.24}$$

Because $\hat{H}$ is a sum of one-electron Hamiltonians, one eigenfunction is a product of spin-orbital wave functions for each electron

$$\Psi_{\mathrm{HP}}(\boldsymbol{x}_1, \boldsymbol{x}_2, \ldots \boldsymbol{x}_N) = \varphi_1(\boldsymbol{x}_1)\varphi_2(\boldsymbol{x}_2)\ldots\varphi_N(\boldsymbol{x}_N), \tag{1.25}$$

where Ψ_{HP} is the Hartree product [35], each spin-orbital $\varphi_i(\boldsymbol{x})$ is a product of a spin part $\omega(s)$ and a spatial part $\psi_i(\boldsymbol{r})$

$$\varphi_i(\boldsymbol{x}) = \psi_i(\boldsymbol{r})\omega(s), \tag{1.26}$$

with

$$\omega(s) = \begin{cases} \alpha(s), & \text{for spin-up electrons,} \\ \beta(s), & \text{for spin-down electrons.} \end{cases} \tag{1.27}$$

The spin orbitals form an orthonormal set, i.e.

$$\int d\boldsymbol{x}\varphi_i^*(\boldsymbol{x})\varphi_j(\boldsymbol{x}) = \langle \varphi_i | \varphi_j \rangle = \delta_{ij}. \tag{1.28}$$

Because we are only interested in electronic wave function and that electrons are fermions, this wave function needs to obey the antisymmetry principle which is a general statement of the Pauli exclusion principle [36]. This principle states that a many-electron wave function must be antisymmetric to the interchange of coordinates

of any two electrons

$$\Psi(\boldsymbol{x}_1,\ldots,\boldsymbol{x}_i,\ldots,\boldsymbol{x}_j,\ldots,\boldsymbol{x}_N) = -\Psi(\boldsymbol{x}_1,\ldots,\boldsymbol{x}_j,\ldots,\boldsymbol{x}_i,\ldots,\boldsymbol{x}_N). \tag{1.29}$$

However, the Hartree product does not satisfy the antisymmetry principle. Indeed, the Hartree product does not take into account the indistinguishability of electrons because each electron is attached to one particular spin-orbital φ_i. The antisymmetry principle does not distinguish between identical electrons and requires that the electronic wave function must be antisymmetric. By combining the Hartree product with the antisymmetry principle we construct an antisymmetric product of spin orbitals called Slater determinant [37]

$$\Psi(\boldsymbol{x}_1,\ldots,\boldsymbol{x}_N) = \frac{1}{\sqrt{N!}}\begin{vmatrix} \varphi_1(\boldsymbol{x}_1) & \varphi_2(\boldsymbol{x}_1) & \ldots & \varphi_N(\boldsymbol{x}_1) \\ \varphi_1(\boldsymbol{x}_2) & \varphi_2(\boldsymbol{x}_2) & \ldots & \varphi_N(\boldsymbol{x}_2) \\ \vdots & \vdots & \ddots & \vdots \\ \varphi_1(\boldsymbol{x}_N) & \varphi_2(\boldsymbol{x}_N) & \ldots & \varphi_N(\boldsymbol{x}_N) \end{vmatrix} = |\varphi_1(\boldsymbol{x}_1)\ldots\varphi_N(\boldsymbol{x}_N)\rangle\,, \tag{1.30}$$

where $\frac{1}{\sqrt{N!}}$ is a normalization factor. The rows are labeled by electrons and the columns are labeled by spin orbitals. If any two rows or columns in the Slater determinant are swapped, the sign of the determinant will change, and if any two rows or columns are the same the determinant will be zero. Thus, a Slater determinant obeys the antisymmetry principle and the Pauli exclusion principle. Henceforth, we will use the following convention: the indices p, q, r and s are for general orbitals (occupied or vacant), i, j, k, and l denote occupied orbitals and a, b, c and d are for vacant orbitals.

1.5 Hartree-Fock approximation

This part is devoted to one of the core theories in quantum chemistry, the Hartree-Fock (HF) approximation [35, 38]. This method consists of rewriting the Schrödinger equation in N monoeletronic equations and within this approximation, the electronic wave function is written as a Slater determinant of N (occupied) spin orbitals (Eq. (1.30)) , also known as molecular orbitals

$$|\Psi_{\mathrm{HF}}\rangle = |\varphi_1(\boldsymbol{x}_1)\ldots\varphi_N(\boldsymbol{x}_N)\rangle\,. \tag{1.31}$$

The HF energy is defined as

$$E_{\mathrm{HF}} = \langle\Psi_{\mathrm{HF}}|\hat{H}|\Psi_{\mathrm{HF}}\rangle\,, \tag{1.32}$$

and using the electronic Hamiltonian in Eq.(1.5), the previous equation can be worked out to get

$$E_{\mathrm{HF}} = \sum_{i=1}^{N}\langle\varphi_i(\boldsymbol{x}_1)|\hat{H}^{\mathrm{c}}|\varphi_i(\boldsymbol{x}_1)\rangle + \sum_{i=1}^{N}\sum_{j>i}^{N}\left[J_{ij} - K_{ij}\right], \tag{1.33}$$

where the so-called core Hamiltonian (i.e. the one-electron part of the electronic Hamiltonian) is defined as

$$\hat{H}^{\mathrm{c}} = \hat{T}_{\mathrm{e}} + \hat{V}_{\mathrm{en}} = -\sum_{i=1}^{N}\frac{\nabla_i^2}{2} - \sum_{i=1}^{N}\sum_{A=1}^{M}\frac{Z_A}{r_{iA}}, \tag{1.34}$$

whereas J_{ij} and K_{ij} are the bi-eletronic integrals defined as

$$J_{ij} = \langle \varphi_i(\boldsymbol{x}_1)\varphi_j(\boldsymbol{x}_2) | \varphi_i(\boldsymbol{x}_1)\varphi_j(\boldsymbol{x}_2) \rangle = \iint d\boldsymbol{x}_1 d\boldsymbol{x}_2 \varphi_i^*(\boldsymbol{x}_1)\varphi_j^*(\boldsymbol{x}_2) r_{12}^{-1} \varphi_i(\boldsymbol{x}_1)\varphi_j(\boldsymbol{x}_2), \tag{1.35}$$

$$K_{ij} = \langle \varphi_i(\boldsymbol{x}_1)\varphi_j(\boldsymbol{x}_2) | \varphi_j(\boldsymbol{x}_1)\varphi_i(\boldsymbol{x}_2) \rangle = \iint d\boldsymbol{x}_1 d\boldsymbol{x}_2 \varphi_i^*(\boldsymbol{x}_1)\varphi_j^*(\boldsymbol{x}_2) r_{12}^{-1} \varphi_j(\boldsymbol{x}_1)\varphi_i(\boldsymbol{x}_2). \tag{1.36}$$

To get a set of N monoelectronic equations, we introduce the Fock operator and define it as

$$\hat{F}(\boldsymbol{x}_1)\varphi_i(\boldsymbol{x}_1) = \varepsilon_i \varphi_i(\boldsymbol{x}_1), \tag{1.37}$$

with

$$\hat{F}(\boldsymbol{x}_1) = \hat{H}^{\mathrm{c}}(\boldsymbol{x}_1) + \sum_{i=1}^{N} \left[\hat{J}_i(\boldsymbol{x}_1) - \hat{K}_i(\boldsymbol{x}_1) \right], \tag{1.38}$$

where $\hat{J}_i(\boldsymbol{x}_1)$ and $\hat{K}_i(\boldsymbol{x}_1)$ are the Coulomb and exchange operators respectively:

$$\hat{J}_i(\boldsymbol{x}_1)\varphi_j(\boldsymbol{x}_1) = \varphi_j(\boldsymbol{x}_1) \int \varphi_i(\boldsymbol{x}_2) r_{12}^{-1} \varphi_i(\boldsymbol{x}_2) d\boldsymbol{x}_2, \tag{1.39}$$

$$\hat{K}_i(\boldsymbol{x}_1)\varphi_j(\boldsymbol{x}_1) = \varphi_i(\boldsymbol{x}_1) \int \varphi_i(\boldsymbol{x}_2) r_{12}^{-1} \varphi_j(\boldsymbol{x}_2) d\boldsymbol{x}_2. \tag{1.40}$$

One can rewrite Eq. (1.38) as

$$\hat{F}(\boldsymbol{x}_1) = \hat{H}^{\mathrm{c}}(\boldsymbol{x}_1) + \hat{v}_{\mathrm{HF}}(\boldsymbol{x}_1), \tag{1.41}$$

where $\hat{v}_{\mathrm{HF}}(\boldsymbol{x}_1)$ is an effective one-electron potential operator called the Hartree-Fock potential. This one-electron potential is an average potential experienced by electron 1 due to the presence of the $(N-1)$ other electrons. Because of this average potential, the Hartree-Fock approximation is called a **mean-field** approximation. The Coulomb operator represents the average local potential at $\boldsymbol{x}_1$ arising from an electron in orbital φ_i. The exchange does not have a classical interpretation and arises from the antisymmetric nature of the single determinant. Moreover, the exchange operator, unlike the Coulomb operator is said to be a nonlocal operator, meaning that it explicitly depends on the function on which it acts and requires knowledge of the value of this function at any point in space. So far we discussed Hartree-Fock equations for a general set of spin orbitals (φ_i), in the following we will be more specific about the form of these spin orbitals. We will consider two types of spin orbitals, the restricted spin orbitals which are constrained to have the same spatial function for spin-up (α) electrons and spin-down (β) electrons; and unrestricted spin orbitals which have different spatial functions for α and β spins. By considering these two types of spin orbitals it will lead us to two Hartree-Fock formalisms, the restricted Hartree-Fock (RHF) and unrestricted Hartree-Fock (UHF) formalisms.

1.5.1 Restricted Hartree-Fock (RHF) formalism

A restricted set of spin orbitals has the form

$$\varphi_i(\boldsymbol{x}) = \begin{cases} \psi_i(\boldsymbol{r})\alpha(s), & \text{for spin-up electrons,} \\ \psi_i(\boldsymbol{r})\beta(s), & \text{for spin-down electrons,} \end{cases} \tag{1.42}$$

where, for a closed-shell system, each of the occupied spatial orbitals $\{\psi_i | i = 1, \ldots, N/2\}$ or molecular orbitals (MOs) is doubly occupied. After integrating out the spin functions, the Hartree-Fock equation is given by

$$\hat{F}(\boldsymbol{r})\psi_i(\boldsymbol{r}) = \varepsilon_i \psi_i(\boldsymbol{r}), \tag{1.43}$$

and so because of this eigenvalue problem, the set of spatial orbital is orthonormal. In practice, each molecular orbital is expanded as a linear combination of K atomic orbitals (AOs), this is the so-called LCAO approximation. This expansion is done such as

$$\psi_i(\boldsymbol{r}) = \sum_{\mu=1}^{K} c_{\mu i}\chi_\mu(\boldsymbol{r}), \tag{1.44}$$

where the $\chi_\mu(\boldsymbol{r})$ are the AOs. Substituting the expansion in the Hartree-Fock equation, multiplying on the left by $\chi_\mu^*(\boldsymbol{r})$ and integrating, the Hartree-Fock equation (1.43) becomes the Roothaan-Hall equations

$$\sum_{\nu=1}^{K} F_{\mu\nu}c_{\nu i} = \varepsilon_i \sum_{\nu=1}^{K} S_{\mu\nu}c_{\nu i}, \tag{1.45}$$

where we introduced the matrix elements of the $K \times K$ overlap matrix $\boldsymbol{S}$

$$S_{\mu\nu} = \int d\boldsymbol{r}\, \chi_\mu^*(\boldsymbol{r})\chi_\nu(\boldsymbol{r}) = \langle \chi_\mu | \chi_\nu \rangle = \langle \mu | \nu \rangle\,, \tag{1.46}$$

and the matrix elements of the $K \times K$ Fock matrix $\boldsymbol{F}$

$$F_{\mu\nu} = \int d\boldsymbol{r}\, \chi_\mu^*(\boldsymbol{r})\hat{F}(\boldsymbol{r})\chi_\nu(\boldsymbol{r}) = \langle \chi_\mu | \hat{F} | \chi_\nu \rangle = \langle \mu | \hat{F} | \nu \rangle\,. \tag{1.47}$$

In the AO basis, the elements of the Fock matrix can be written as

$$F_{\mu\nu} = H^{\mathrm{c}}_{\mu\nu} + \sum_{\lambda\sigma} P_{\lambda\sigma}\left[\langle \mu\sigma | \nu\lambda \rangle - \frac{1}{2}\langle \mu\sigma | \lambda\nu \rangle\right], \tag{1.48}$$

with

$$H^{\mathrm{c}}_{\mu\nu} = \langle \mu | \hat{H}^{\mathrm{c}} | \nu \rangle\,, \tag{1.49}$$

$$\langle \mu\sigma | \nu\lambda \rangle = \iint \chi_\mu^*(\boldsymbol{r}_1)\chi_\lambda^*(\boldsymbol{r}_2) r_{12}^{-1} \chi_\nu(\boldsymbol{r}_1)\chi_\sigma(\boldsymbol{r}_2) d\boldsymbol{r}_1 d\boldsymbol{r}_2, \tag{1.50}$$

and where the density matrix is defined as

$$P_{\mu\nu} = 2\sum_{p}^{N/2} c_{\mu p} c_{\nu p}^*. \tag{1.51}$$

Thus, the RHF electronic energy is given by

$$E_{\mathrm{RHF}} = \sum_{\mu\nu} P_{\mu\nu} H^{\mathrm{c}}_{\mu\nu} + \frac{1}{2}\sum_{\mu\nu\lambda\sigma}^{N} P_{\mu\nu}P_{\lambda\sigma}G_{\mu\nu\lambda\sigma}, \tag{1.52}$$

which can be written in the matrix form

$$\begin{aligned} E_{\text{RHF}} &= \frac{1}{2}\sum_{\mu\nu} P_{\mu\nu}\left(H^{\text{c}}_{\mu\nu} + F_{\mu\nu}\right) \\ &= \frac{1}{2}\,\text{Tr}\{\boldsymbol{P}(\boldsymbol{H}^{\text{c}} + \boldsymbol{F})\}, \end{aligned} \tag{1.53}$$

where

$$\boldsymbol{F} = \boldsymbol{H}^{\text{c}} + \boldsymbol{G}, \tag{1.54}$$

with

$$G_{\mu\nu} = \sum_{\lambda\sigma} P_{\lambda\sigma} G_{\mu\nu\lambda\sigma}, \qquad G_{\mu\nu\lambda\sigma} = \langle\mu\lambda|\nu\sigma\rangle - \frac{1}{2}\langle\mu\lambda|\sigma\nu\rangle\,. \tag{1.55}$$

The Roothaan-Hall equations (1.45) can be written in matrix form

$$\boldsymbol{FC} = \boldsymbol{SC\varepsilon}, \tag{1.56}$$

where $\boldsymbol{C}$ is the $K \times K$ square matrix of the expansion coefficients $c_{\mu p}$ and $\boldsymbol{\varepsilon}$ is a diagonal matrix of the orbital energies ε_p. Because the AO basis is a non-orthonormal set, this gives rise to the overlap matrix $\boldsymbol{S}$ in Roothaan-Hall equations. This does not allow us to directly diagonalize the Fock matrix $\boldsymbol{F}$ to get the eigenvectors and eigenvalues. So, because of this nonorthogonal basis, we have to reformulate Roothaan-Hall equations into a usual matrix eigenvalue problem by orthogonalizing the AO basis. To do so, we introduce the orthogonalization matrix $\boldsymbol{X}$ such as

$$\boldsymbol{X}^{\dagger}\boldsymbol{S}\boldsymbol{X} = \boldsymbol{I} \tag{1.57}$$

to work on an orthogonal AO basis (where $\boldsymbol{I}$ is the identity matrix). There are mainly two ways to orthogonalize the AO basis set, the symmetric orthogonalization or Löwdin orthogonalization method for which $\boldsymbol{X} = \boldsymbol{S}^{-1/2}$ and the canonical orthogonalization for which $\boldsymbol{X} = \boldsymbol{U}\boldsymbol{s}^{-1/2}$ (where $\boldsymbol{U}$ and $\boldsymbol{s}$ are the eigenvectors and eigenvalues matrices of $\boldsymbol{S}$, respectively). Once we have the matrix $\boldsymbol{X}$ it is possible to transform the functions (χ_μ) to get the orthogonalized basis functions (χ'_μ) and then work with this new set. By doing that it would eliminate the overlap matrix $\boldsymbol{S}$ in Roothaan-Hall equations and then be solved by diagonalization of the Fock matrix. But this procedure is not an efficient one because it would mean that we need either to calculate all the two-electron integrals using the new orbitals or transform all the old integrals $\langle\mu\sigma|\nu\lambda\rangle$ to the new set $\langle\mu'\sigma'|\nu'\lambda'\rangle$. A more efficient way is to consider a new coefficient matrix $\boldsymbol{C}'$ such as

$$\boldsymbol{C}' = \boldsymbol{X}^{-1}\boldsymbol{C}, \tag{1.58}$$

and

$$\boldsymbol{X}^{-1} = \boldsymbol{X}^{\dagger} \tag{1.59}$$

because $\boldsymbol{X}$ is an orthogonal matrix. Thus

$$\boldsymbol{C} = \boldsymbol{X}\boldsymbol{C}'. \tag{1.60}$$

Then, substituting the last equation in Roothaan-Hall equations gives

$$\boldsymbol{FXC}' = \boldsymbol{SXC}'\boldsymbol{\varepsilon}, \tag{1.61}$$

$$\boldsymbol{X}^\dagger\boldsymbol{FXC}' = \boldsymbol{X}^\dagger\boldsymbol{SXC}'\boldsymbol{\varepsilon} \tag{1.62}$$

where we multiplied by $\boldsymbol{X}^\dagger$ on the left, then it yields to

$$\boldsymbol{F}'\boldsymbol{C}' = \boldsymbol{C}'\boldsymbol{\varepsilon}, \tag{1.63}$$

where

$$\boldsymbol{F}' = \boldsymbol{X}^\dagger\boldsymbol{FX}. \tag{1.64}$$

The matrices $\boldsymbol{C}'$ and $\boldsymbol{\varepsilon}$ can be determined by diagonalizing $\boldsymbol{F}'$, and the matrix $\boldsymbol{C}$ is obtained by back-transforming the eigenvectors in the original basis using Eq. (1.60).

1.5.2 Self-consistent field calculation

To obtain the MO coefficients $\boldsymbol{C}$, one has to diagonalize the Fock matrix $\boldsymbol{F}$. However, this matrix does depend on the density matrix $\boldsymbol{P}$ which depends on the MO coefficients itself. So Roothaan-Hall equations are non-linear and they need to be solved iteratively called the self-consistent field (SCF) method. The SCF algorithm is as follows:

1. Specify a molecule with a set of nuclear coordinates $(\boldsymbol{R}_A)$, the atomic numbers (Z_A), the number of electrons N and the AO basis set (χ_μ).
2. Calculate the required integrals $S_{\mu\nu}$, $H^{\mathrm{c}}_{\mu\nu}$ and the two-electrons integrals $\langle\mu\sigma|\nu\lambda\rangle$.
3. Obtain the transformation matrix $\boldsymbol{X}$ by diagonalizing the overlap matrix $\boldsymbol{S}$.
4. Obtain an estimate of the density matrix $\boldsymbol{P}$.
5. Calculate the matrix $\boldsymbol{G}$ using the density matrix $\boldsymbol{P}$ and the two-electron integrals $\langle\mu\sigma|\nu\lambda\rangle$.
6. Build the Fock matrix: $\boldsymbol{F} = \boldsymbol{H}^{\mathrm{c}} + \boldsymbol{G}$.
7. Transform the Fock matrix in the orthogonal basis: $\boldsymbol{F}' = \boldsymbol{X}^\dagger\boldsymbol{FX}$.
8. Diagonalize $\boldsymbol{F}'$ to obtain $\boldsymbol{C}'$ and $\boldsymbol{\varepsilon}$.
9. Back-transform the MOs in the original basis: $\boldsymbol{C} = \boldsymbol{XC}'$.
10. Compute the new density matrix $\boldsymbol{P} = \boldsymbol{CC}^\dagger$ (over the occupied orbitals), and the RHF energy:
$$E_{\mathrm{RHF}} = \frac{1}{2}\,\mathrm{Tr}\{\boldsymbol{P}(\boldsymbol{H}^{\mathrm{c}} + \boldsymbol{F})\}. \tag{1.65}$$
11. Test the convergence of the procedure using the difference $\boldsymbol{FPS} - \boldsymbol{SPF}$ suggested by Pulay [39]. If this difference is lower than a fixed convergence criterion then the test is satisfied. If not, go back to 5.

1.5.3 Unrestricted Hartree-Fock (UHF) formalism

An unrestricted set of spin orbitals has the form

$$\varphi_i(\boldsymbol{x}) = \begin{cases} \psi_i^{\alpha}(\boldsymbol{r})\alpha(s), & \text{for spin-up electrons,} \\ \psi_i^{\beta}(\boldsymbol{r})\beta(s), & \text{for spin-down electrons,} \end{cases} \tag{1.66}$$

where α electrons are described by a set of spatial orbitals $\{\psi_i^{\alpha} | i = 1, \ldots, K\}$ and β electrons are described by a set of spatial orbitals $\{\psi_i^{\beta} | i = 1, \ldots, K\}$. Because we have two sets of spatial orbitals, after integrating out the spin, we have a Hartree-Fock equation for each set

$$\hat{F}^{\alpha}(\boldsymbol{r})\psi_i^{\alpha}(\boldsymbol{r}) = \varepsilon_i^{\alpha}\psi_i^{\alpha}(\boldsymbol{r}), \tag{1.67}$$

$$\hat{F}^{\beta}(\boldsymbol{r})\psi_i^{\beta}(\boldsymbol{r}) = \varepsilon_i^{\beta}\psi_i^{\beta}(\boldsymbol{r}). \tag{1.68}$$

Due to these two separate eigenvalue equations, it ensure that the sets of eigenfunctions $\{\psi_i^{\alpha}\}$ and $\{\psi_i^{\beta}\}$ individually form orthonormal sets. In the same way, we did for restricted orbitals, we expand the unrestricted molecular orbitals in the AO basis

$$\psi_i^{\alpha}(\boldsymbol{r}) = \sum_{\mu=1}^{K} c_{\mu i}^{\alpha}\chi_{\mu}(\boldsymbol{r}), \tag{1.69}$$

$$\psi_i^{\beta}(\boldsymbol{r}) = \sum_{\mu=1}^{K} c_{\mu i}^{\beta}\chi_{\mu}(\boldsymbol{r}). \tag{1.70}$$

Substituting these expansions in the two Hartree-Fock equations, multiplying on the left by $\chi_{\mu}^{*}(\boldsymbol{r})$ and integrating, we get the Pople-Nesbet equations

$$\sum_{\nu=1}^{K} F_{\mu\nu}^{\alpha} c_{\nu i}^{\alpha} = \varepsilon_p^{\alpha} \sum_{\nu=1}^{K} S_{\mu\nu} c_{\nu i}^{\alpha} \tag{1.71}$$

$$\sum_{\nu=1}^{K} F_{\mu\nu}^{\beta} c_{\nu i}^{\beta} = \varepsilon_i^{\beta} \sum_{\nu=1}^{K} S_{\mu\nu} c_{\nu i}^{\beta}, \tag{1.72}$$

where the matrix elements are the same than in Eq. (1.46) and the Fock matrices elements are

$$F_{\mu\nu}^{\alpha} = H_{\mu\nu}^{\mathrm{c}} + \sum_{\lambda\sigma} P_{\lambda\sigma}^{\mathrm{T}} \langle \mu\sigma | \nu\lambda \rangle - P_{\lambda\sigma}^{\alpha} \langle \mu\sigma | \lambda\nu \rangle , \tag{1.73}$$

$$F_{\mu\nu}^{\beta} = H_{\mu\nu}^{\mathrm{c}} + \sum_{\lambda\sigma} P_{\lambda\sigma}^{\mathrm{T}} \langle \mu\sigma | \nu\lambda \rangle - P_{\lambda\sigma}^{\beta} \langle \mu\sigma | \lambda\nu \rangle , \tag{1.74}$$

where the density matrices are defined as

$$P_{\mu\nu}^{\alpha} = \sum_{i}^{N^{\alpha}} c_{\mu i}^{\alpha}(c_{\nu i}^{\alpha}), \tag{1.75}$$

$$P_{\mu\nu}^{\beta} = \sum_{i}^{N^{\beta}} c_{\mu i}^{\beta}(c_{\nu i}^{\beta}), \tag{1.76}$$

with N^{α} and N^{β} are the number of occupied orbitals ψ_i^{α} and ψ_i^{β}, respectively. The density matrix $P_{\lambda\sigma}^{\mathrm{T}}$ is defined as $P_{\lambda\sigma}^{\mathrm{T}} = P_{\mu\nu}^{\alpha} + P_{\mu\nu}^{\beta}$ and the two-electron integrals are

the same that for the (RHF) part. Thus the UHF electronic energy is given by

$$\begin{aligned} E_{\text{UHF}} &= \frac{1}{2}\sum_{\mu\nu}\left[P^{\text{T}}_{\nu\mu}H^{\text{c}}_{\mu\nu} + P^{\alpha}_{\nu\mu}F^{\alpha}_{\mu\nu} + P^{\beta}_{\nu\mu}F^{\beta}_{\mu\nu}\right] \\ &= \frac{1}{2}\,\text{Tr}\Big\{\boldsymbol{P}^{\text{T}}\boldsymbol{H}^{\text{c}} + \boldsymbol{P}^{\alpha}\boldsymbol{F}^{\alpha} + \boldsymbol{P}^{\beta}\boldsymbol{F}^{\beta}\Big\}. \end{aligned} \tag{1.77}$$

Thus, the Pople-Nesbet equations (1.71) and (1.72) can be written in matrix form

$$\boldsymbol{F}^{\alpha}\boldsymbol{C}^{\alpha} = \boldsymbol{S}\boldsymbol{C}^{\alpha}\boldsymbol{\varepsilon}^{\alpha}, \tag{1.78}$$

$$\boldsymbol{F}^{\beta}\boldsymbol{C}^{\beta} = \boldsymbol{S}\boldsymbol{C}^{\beta}\boldsymbol{\varepsilon}^{\beta}. \tag{1.79}$$

In the same we solved the Roothan-Hall equations for the RHF formalism using the SCF procedure we solve the Pople-Nesbet equations. Indeed, we will need to specify the number of electrons α and β and the initial guess for the two density matrices $\boldsymbol{P}^{\alpha}$ and $\boldsymbol{P}^{\beta}$ which will allow us to build the two Fock matrices $\boldsymbol{F}^{\alpha}$ and $\boldsymbol{F}^{\beta}$. Then using the orthogonalization matrix $\boldsymbol{X}$ we transform these two Fock matrices in the orthogonal basis and obtain $\boldsymbol{F}^{\alpha\prime}$ and $\boldsymbol{F}^{\beta\prime}$. By diagonalizing $\boldsymbol{F}^{\alpha\prime}$ and $\boldsymbol{F}^{\beta\prime}$ we get the MO coefficient matrices $\boldsymbol{C}^{\alpha\prime}$ and $\boldsymbol{C}^{\beta\prime}$ and the energies matrices $\boldsymbol{\varepsilon}^{\alpha\prime}$ and $\boldsymbol{\varepsilon}^{\beta\prime}$. Then, after back-transforming the MO coefficient matrices, we can obtain the new density matrices and thus get the UHF energy. Using the same convergence test as for the restricted SCF procedure we have an unrestricted SCF procedure. Unfortunately, the Hartree-Fock approximation is not able to recover the exact ground state energy of a system even in the complete basis set (CBS) limit (meaning using a complete basis set for the linear expansion of the MOs) due to the average treatment of electron-electron interaction. The difference between the exact energy and the energy calculated within the HF approximation, i.e. the error in the HF approximation, is called the correlation energy E_{c}

$$E_{\text{c}} = E - E_{\text{HF}}. \tag{1.80}$$

The goal of the post-HF methods is to recover all or part of the correlation energy. We will describe in the next sections how some of these post-HF methods go beyond the HF approximation.

1.6 Density-functional theory (DFT)

Contrary to the HF approximation, the basic quantity in Density-Functional Theory (DFT) is not the wave function but the electronic density $\rho(\boldsymbol{r})$ defined as

$$\rho(\boldsymbol{r}) = N\int\ldots\int|\Psi(\boldsymbol{x},\boldsymbol{x}_2,\ldots,\boldsymbol{x}_N)|^2 d\boldsymbol{s}\; d\boldsymbol{x}_2\ldots d\boldsymbol{x}_N, \tag{1.81}$$

where Ψ is any antisymmetric wave function and where we integrate over the spin coordinate $\boldsymbol{s}$. The electronic density is normalized to the electron number, i.e. $\int\rho(\boldsymbol{r})d\boldsymbol{r} = N$. The principle of this method is to evaluate the ground state energy of a system of N electrons in a local external potential $v(\boldsymbol{r})$ using a variational formulation involving the electronic density. To do so, DFT is based on two theorems, the Hohenberg-Kohn (HK) theorems [40]. The first theorem proves that the ground state electron density uniquely determines the external potential, while the second HK theorem defines an energy functional for the N electrons system and proves that

the ground state electron density minimizes this energy functional, i.e.

$$E_0 = \min_{\rho(r)} \left\{ F[\rho(\boldsymbol{r})] + \int v(\boldsymbol{r})\rho(\boldsymbol{r})d\boldsymbol{r} \right\}, \tag{1.82}$$

where $F[\rho(\boldsymbol{r})]$ is the universal density functional, meaning independent of the external potential

$$\begin{aligned} F[\rho(\boldsymbol{r})] &= \langle \Psi[\rho(\boldsymbol{r})] | \hat{T} + \hat{V}_{\text{ee}} | \Psi[\rho(\boldsymbol{r})] \rangle \\ &= T[\rho(\boldsymbol{r})] + E_{\text{ee}}[\rho(\boldsymbol{r})], \end{aligned} \tag{1.83}$$

and

$$\int v(\boldsymbol{r})\rho(\boldsymbol{r})d\boldsymbol{r} = \langle \Psi[\rho(\boldsymbol{r})] | \hat{V} | \Psi[\rho(\boldsymbol{r})] \rangle . \tag{1.84}$$

So far, we have not simplified the problem of the polyelectronic Schrödinger equation because according to (1.81) we still have to get the many-electron wave function to get the electronic density. To overcome this difficulty Kohn and Sham [41] found a way to make DFT practical.

1.6.1 Kohn-Sham equations

The basic idea behind the Kohn-Sham (KS) formalism is to assume that the density of interacting electrons with an external potential $v(\boldsymbol{r})$ can be reproduced in a system of non-interacting electrons with an effective local potential $v_{\text{KS}}(\boldsymbol{r})$. In this formalism we can observe similarities with the HF theory, indeed the electrons are treated as independent particles moving in the average field of all others. The difference here is in the effective potential, the exchange and correlation are included using an exchange-correlation functional. We introduce KS orbitals $\phi_i(\boldsymbol{r})$, and the KS energy can be decomposed as

$$\begin{aligned} E_{\text{KS}}[\rho(\boldsymbol{r})] &= \langle \Phi[\rho(\boldsymbol{r})] | \hat{H}_{\text{KS}} | \Phi[\rho(\boldsymbol{r})] \rangle \\ &= \langle \Phi[\rho(\boldsymbol{r})] | \hat{T} + \hat{V}_{\text{KS}} | \Phi[\rho(\boldsymbol{r})] \rangle , \end{aligned} \tag{1.85}$$

where Φ is the total KS wave function and $\hat{V}_{\text{KS}} = \sum_i v_{\text{KS}}(\boldsymbol{r}_i) = \int d\boldsymbol{r}\hat{\rho}(\boldsymbol{r})v_{\text{KS}}(\boldsymbol{r})$. The density functional becomes

$$F_{\text{KS}}[\rho(\boldsymbol{r})] = \langle \Phi[\rho(\boldsymbol{r})] | \hat{T} | \Phi[\rho(\boldsymbol{r})] \rangle = T_{\text{s}}[\rho(\boldsymbol{r})], \tag{1.86}$$

where

$$T_{\text{s}}[\rho(\boldsymbol{r})] = -\frac{1}{2} \sum_{i}^{N/2} \langle \phi_i | \nabla_i^2 | \phi_i \rangle , \tag{1.87}$$

is the non-interacting kinetic energy. Then, we define the exchange-correlation energy E_{xc} as the difference between the universal density functional $F[\rho(\boldsymbol{r})]$ and $T_{\text{KS}}[\rho(\boldsymbol{r})] + E_{\text{H}}$, with E_{H} the classical part of the electron-electron interaction energy called the Hartree energy, i.e.

$$E_{\text{H}}[\rho(\boldsymbol{r})] = \frac{1}{2} \iint \frac{\rho(\boldsymbol{r})\rho(\boldsymbol{r}')}{|\boldsymbol{r} - \boldsymbol{r}'|} d\boldsymbol{r}d\boldsymbol{r}'. \tag{1.88}$$

By doing so, we obtain

$$F[\rho(\boldsymbol{r})] = T_{\text{s}}[\rho(\boldsymbol{r})] + E_{\text{H}}[\rho(\boldsymbol{r})] + E_{\text{xc}}[\rho(\boldsymbol{r})] \tag{1.89}$$

and using Eq. (1.83) we have that the exchange-correlation energy

$$E_{\mathrm{xc}}[\rho(\boldsymbol{r})] = (T[\rho(\boldsymbol{r})] - T_{\mathrm{s}}[\rho(\boldsymbol{r})]) + (E_{\mathrm{ee}}[\rho(\boldsymbol{r})] - E_{\mathrm{H}}[\rho(\boldsymbol{r})]), \tag{1.90}$$

is the sum of two terms: one coming from the difference between the exact kinetic energy $T[\rho(\boldsymbol{r})]$ and the non-interacting kinetic energy $T_{\mathrm{s}}[\rho(\boldsymbol{r})]$, and the other one coming from the difference between the exact interelectronic repulsion $E_{\mathrm{ee}}[\rho(\boldsymbol{r})]$ and the classical Coulomb repulsion $E_{\mathrm{H}}[\rho(\boldsymbol{r})]$. Finally, the KS total energy can be written as

$$\begin{aligned} E_{\mathrm{KS}}[\rho(\boldsymbol{r})] &= F[\rho(\boldsymbol{r})] + \int v(\boldsymbol{r})\rho(\boldsymbol{r})d\boldsymbol{r} \\ &= T_{\mathrm{s}}[\rho(\boldsymbol{r})] + E_{\mathrm{H}}[\rho(\boldsymbol{r})] + E_{\mathrm{xc}}[\rho(\boldsymbol{r})] + E_{\mathrm{ne}}[\rho(\boldsymbol{r})], \end{aligned} \tag{1.91}$$

where

$$E_{\mathrm{ne}}[\rho(\boldsymbol{r})] = -\sum_{A}^{M} \int \frac{Z_A \rho(\boldsymbol{r})}{|\boldsymbol{r}_A - \boldsymbol{r}|} d\boldsymbol{r} = \int v(\boldsymbol{r})\rho(\boldsymbol{r})d\boldsymbol{r} \tag{1.92}$$

is the electron-nucleus attraction energy. As previously said the KS system is non-interacting so the Hamiltonian becomes a sum over single-particle Hamiltonians

$$\hat{H}_{\mathrm{KS}} = \sum_{i}^{N} \hat{h}_{\mathrm{KS}}(\boldsymbol{r}_i) \tag{1.93}$$

with

$$\hat{h}_{\mathrm{KS}}(\boldsymbol{r}) = -\frac{1}{2}\nabla_r^2 + v_{\mathrm{KS}}(\boldsymbol{r}). \tag{1.94}$$

This leads us to a single-particle Schrödinger equation

$$\left[-\frac{1}{2}\nabla_r^2 + v_{\mathrm{KS}}(\boldsymbol{r})\right]\phi_i(\boldsymbol{r}) = \varepsilon_i \phi_i(\boldsymbol{r}), \tag{1.95}$$

where the total wave function is a Slater determinant formed from the occupied KS orbitals ϕ_i. Then the one-electron density is

$$\rho(\boldsymbol{r}) = \sum_{i}^{N/2} |\phi_i(\boldsymbol{r})|^2. \tag{1.96}$$

1.6.2 Kohn-Sham potential

We need to establish the expression for the KS potential v_{KS} and to relate it to the external potential v, to do so we take the functional derivative of Eq. (1.89) with respect to the density $\rho(\boldsymbol{r})$ and we obtain

$$-v(\boldsymbol{r}) = -v_{\mathrm{KS}}(\boldsymbol{r}) + \int \frac{\rho(\boldsymbol{r}')}{|\boldsymbol{r} - \boldsymbol{r}'|} d\boldsymbol{r}' + \frac{\delta E_{\mathrm{xc}}[\rho(\boldsymbol{r})]}{\delta\rho(\boldsymbol{r})}. \tag{1.97}$$

Thus, the KS potential contains the external potential, the Hartree potential and the exchange-correlation potential v_{xc}

$$v_{\mathrm{KS}}(\boldsymbol{r}) = v(\boldsymbol{r}) + v_{\mathrm{H}}(\boldsymbol{r}) + v_{\mathrm{xc}}(\boldsymbol{r}), \tag{1.98}$$

with

$$v_{\mathrm{KS}}(\boldsymbol{r}) = -\frac{\delta T_{\mathrm{s}}[\rho(\boldsymbol{r})]}{\delta\rho(\boldsymbol{r})}, \tag{1.99}$$

$$v(\boldsymbol{r}) = -\sum_{A}^{M}\frac{Z_A}{|\boldsymbol{r}-\boldsymbol{r}_A|}, \tag{1.100}$$

$$v_{\mathrm{H}}(\boldsymbol{r}) = \int\frac{\rho(\boldsymbol{r}')}{|\boldsymbol{r}-\boldsymbol{r}'|}d\boldsymbol{r}', \tag{1.101}$$

$$v_{\mathrm{xc}}(\boldsymbol{r}) = \frac{\delta E_{\mathrm{xc}}[\rho(\boldsymbol{r})]}{\delta\rho(\boldsymbol{r})}. \tag{1.102}$$

Using these results one can write the KS equations as

$$\left[-\frac{1}{2}\nabla_{\boldsymbol{r}}^2 + v(\boldsymbol{r}) + v_{\mathrm{H}}(\boldsymbol{r}) + v_{\mathrm{xc}}(\boldsymbol{r})\right]\phi_i(\boldsymbol{r}) = \varepsilon_i\phi_i(\boldsymbol{r}), \tag{1.103}$$

which can be re-written as

$$\hat{F}_{\mathrm{KS}}(\boldsymbol{r})\phi_i(\boldsymbol{r}) = \varepsilon_i\phi_i(\boldsymbol{r}). \tag{1.104}$$

Because these equations are not linear (v_{KS} depends on the electronic density which depends itself on v_{KS} through the KS orbitals) they have to be solved iteratively, just like the HF equations, by expanding the KS MOs in an AO basis, yielding

$$\boldsymbol{F}_{\mathrm{KS}}\boldsymbol{C} = \boldsymbol{S}\boldsymbol{C}\boldsymbol{\varepsilon}. \tag{1.105}$$

Note that like in the case of the HF approximation we can use restricted and unrestricted spin orbitals which lead us to a set of spatial orbitals for α electrons $\{\phi_i^{\alpha}\}$ and a set of spatial orbitals for β electrons $\{\phi_i^{\beta}\}$. So we would have KS equations for α and β electrons, then we would define the total electronic density as the sum of the α and β electronic densities and solve the two sets of KS equations.

1.6.3 Exchange-correlation functionals

We have seen that the unknown in the KS equations is the exchange-correlation functional, having this functional allows us to obtain the exchange-correlation potential v_{xc} and solve iteratively the KS equations. It is common to split the exchange-correlation energy as a sum of an exchange and correlation components, i.e.

$$E_{\mathrm{xc}}[\rho(\boldsymbol{r})] = E_{\mathrm{x}}[\rho(\boldsymbol{r})] + E_{\mathrm{c}}[\rho(\boldsymbol{r})]. \tag{1.106}$$

There are many approximations of these two functionals which can be classified into various families that depend on their physical input quantities. One can organize these functionals onto the five rungs of Jacob's Ladder of DFT [42].

- The first rung of approximation and the simplest one is the local-density approximation (LDA) and only uses the electronic density ρ. Within this approximation, the exchange-correlation energy density at each position $\boldsymbol{r}$ is assumed to be equal to that of a uniform electron gas with the same density, i.e.

$$E_{\mathrm{xc}}^{\mathrm{LDA}}[\rho(\boldsymbol{r})] = \int\epsilon_{\mathrm{xc}}^{\mathrm{hom}}(\rho(\boldsymbol{r}))d\boldsymbol{r}, \tag{1.107}$$

  where $\epsilon_{\mathrm{xc}}^{\mathrm{hom}}(\rho(\boldsymbol{r}))$ is the exchange-correlation energy per unit volume of a uniform electron gas of density $\rho(\boldsymbol{r})$.

- The second rung in approximating the exchange-correlation functional is the generalized gradient approximation (GGA) and adds the gradient of the electron density $\nabla\rho(\boldsymbol{r})$ as physical input to account the inhomogeneity of the true electron density. The general form of the functional is

$$E_{\mathrm{xc}}^{\mathrm{GGA}}[\rho(\boldsymbol{r})] = \int g_{\mathrm{xc}}(\rho(\boldsymbol{r}), \nabla\rho(\boldsymbol{r}))d\boldsymbol{r}, \tag{1.108}$$

  where the expression of g_{xc} is to be found. As previously said, we split the functional in exchange and correlation contributions and approximation for the two terms is sought separately. Well-known GGA exchange functionals are the B88 and PBE functionals [43, 44]. One of the most famous GGA correlation functional is the LYP functional [45] and by combining it with the B88 exchange functional one has the exchange-correlation functional BLYP [46].

- The third rung is composed of functionals where two additional ingredients are included to go beyond the GGA functionals. These two ingredients are the Laplacian of the electron density $\Delta\rho(\boldsymbol{r}) = \nabla^2\rho(\boldsymbol{r})$ and/or the kinetic energy density

$$\tau = \sum_{i}^{N/2} |\nabla\phi_i|^2. \tag{1.109}$$

  These functionals are called meta-GGA (MGGA) functionals and in practice, the kinetic energy density is the most used input. Among these functionals, one can cite the M06-L [47] and the MS [48, 49] functionals that are widely used.

- The fourth rung functionals are called hybrid density functionals. The idea, introduced by Becke in 1993 [50], behind these functionals is to add a fraction of exact exchange (meaning HF exchange) to any of the functionals of the first three rungs. This leads to hybrid LDA, hybrid GGA, and hybrid meta-GGA, although the latter two types are much more used. Among these functionals we have the global hybrid (GH) functionals such as the well-known B3LYP [50], BH&HLYP [51] or PBE0 [52] and the range-separated hybrid (RSH) functionals where the HF exchange is introduced into the functional via range separation, i.e. the HF exchange is split into a short-range (SR) contribution and a long-range (LR) contribution. Some well-known RSH functionals are the ωB97X-D [53], CAM-B3LYP [54] and LC-ωPBE [55].

- The fifth rung is composed of double hybrids (DH) functionals that use not only occupied orbitals via HF exchange but also virtual orbitals by the mean of methods such as MP2 (second order Møller-Plesset) or random phase approximation (RPA). As in the case of hybrid functionals, we can apply this to the first three rungs and take into account the HF exchange globally or using range separation. Examples of such functionals are the B2PLYP [56] and B2GPPLYP [57].

1.7 Linear-Response Theory

So far we have discussed two methods that approximate the Schrödinger equation by rewriting it as a set of N monoelectronic equations and with the electronic wave function written as a Slater determinant of N spin orbitals. We have seen that within these two approximations, we can obtain an approximate ground state energy of

the system and that in KS-DFT we try to retrieve the HF energetic missing part by using the exchange-correlation energy. Hartree-Fock and DFT are the basis of excited-states methods and we will present two of them, the time-dependent Hartree-Fock (TDHF) and the time-dependent density-functional theory, both in the linear response approach.

1.7.1 Linear-Response Time-Dependent Hartree-Fock (TD-HF)

This section is inspired by the notes of Joshua Goings that can be found on his website[1]. As its name suggests Time-Dependent Hartree-Fock (TDHF) is an approximation to the time-dependent Schrödinger equation using the assumption that the system can at all times be represented by a single Slater determinant composed of time-dependent single-particle wave functions (or time-dependent spin orbitals). Note that we will derive the TDHF equation only for the restricted case but we can do it for the unrestricted one. So we start with the time-dependent Schrödinger equation

$$i\frac{\partial}{\partial t}\Psi(\boldsymbol{x},t) = \hat{H}\Psi(\boldsymbol{x},t), \tag{1.110}$$

where $\hat{H}$ is the time-dependent Hamiltonian [58]

$$\hat{H}(\boldsymbol{r},t) = \hat{H}(\boldsymbol{r}) + \hat{V}(\boldsymbol{r},t), \tag{1.111}$$

with $\hat{H}(\boldsymbol{r})$ defined as in Eq. (1.5) and $\hat{V}(\boldsymbol{r},t)$ is an arbitrary single-particle time-dependent operator

$$\hat{V}(\boldsymbol{r},t) = \sum_{i}^{N}\hat{v}_i(\boldsymbol{r},t), \tag{1.112}$$

By making the same approximation as for the time-independent Hartree-Fock that $\Psi(\boldsymbol{x},t)$ can be written as a single Slater determinant

$$\Psi(\boldsymbol{x},t) = |\varphi_1(\boldsymbol{x},t),\varphi_2(\boldsymbol{x},t),\ldots,\varphi_N(\boldsymbol{x},t)\rangle\,, \tag{1.113}$$

one obtains a time-dependent Hartree-Fock equation

$$\hat{F}(\boldsymbol{r},t)\Psi(\boldsymbol{x},t) = i\frac{\partial}{\partial t}\Psi(\boldsymbol{x},t), \tag{1.114}$$

with $\hat{F}(\boldsymbol{r},t)$ is the time-dependent Fock operator of Eq. (1.38) where we add the time-dependent single-particle potential $\hat{V}(\boldsymbol{r},t)$. The Coulomb and exchange operators acquire a time dependence because of the spin orbitals $\varphi_i(\boldsymbol{x},t)$. One can express the time-dependent Hartree-Fock equation in matrix notation by writing the set of spin orbitals as

$$\varphi_i(\boldsymbol{x},t) = \begin{cases}\psi_i(\boldsymbol{r},t)\alpha(s), & \text{for spin-up electrons,}\\ \psi_i(\boldsymbol{r},t)\beta(s), & \text{for spin-down electrons.}\end{cases} \tag{1.115}$$

Then, after integrating out the spin, we expand these time-dependent spatial orbitals on a basis of K time-independent single-particle wave functions ($\chi_i(\boldsymbol{r})$)

$$\psi_i(\boldsymbol{r},t) = \sum_{\mu}^{K} c_{\mu i}(t)\chi_\mu(\boldsymbol{r}), \tag{1.116}$$

[1] https://joshuagoings.com/notes

and we have

$$\boldsymbol{FC} = i\frac{\partial}{\partial t}\boldsymbol{C} \tag{1.117}$$

Generally, when one talks about the TDHF equations we do not refer to Eq. (1.117) but to the equations obtained in first-order time-dependent perturbation theory, i.e., linear response. To obtain these equations we have to express the TDHF equation in its Dirac form [59], to do this we use the adjoint of Eq. (1.117)

$$\boldsymbol{C}^\dagger\boldsymbol{F} = -i\frac{\partial}{\partial t}\boldsymbol{C}^\dagger \tag{1.118}$$

Using the fact that

$$i\frac{\partial}{\partial t}(\boldsymbol{CC}^\dagger) = i(\frac{\partial}{\partial t}\boldsymbol{C})\boldsymbol{C}^\dagger + i\boldsymbol{C}(\frac{\partial}{\partial t}\boldsymbol{C}^\dagger), \tag{1.119}$$

and substituting Eq. (1.117) and (1.118) in the right-hand-side of the previous equation gives the Dirac form

$$i\frac{\partial}{\partial t}\boldsymbol{P} = \boldsymbol{FP} - \boldsymbol{PF}, \tag{1.120}$$

where $\boldsymbol{P} = \boldsymbol{CC}^\dagger$ is the density matrix. Then, two steps are needed to get the linear response TDHF equations, first, we assume that at $t = 0$ the system is in its electronic ground state, determined by time-independent Hartree-Fock equation (Eq. (1.43)), such that

$$\boldsymbol{F}^{(0)}\boldsymbol{P}^{(0)} - \boldsymbol{P}^{(0)}\boldsymbol{F}^{(0)} = \boldsymbol{0}, \tag{1.121}$$

and

$$\boldsymbol{P}^{(0)}\boldsymbol{P}^{(0)} = \boldsymbol{P}^{(0)}, \tag{1.122}$$

with $\boldsymbol{F}^{(0)}$ and $\boldsymbol{P}^{(0)}$ the unperturbed Fock and density matrices, respectively. The idempotency condition in Eq. (1.122) comes from the fact that at convergence the eigenvectors of the Fock matrix (the $\boldsymbol{C}$) are orthonormal, i.e., $\boldsymbol{CC}^\dagger = \boldsymbol{1}$ and because the density matrix $\boldsymbol{P}$ can be written as $\boldsymbol{P} = \boldsymbol{CC}^\dagger$. The unperturbed Fock matrix elements are given by Eq. (1.47) and at convergence we have

$$F_{pq}^{(0)} = \delta_{pq}\varepsilon_p. \tag{1.123}$$

The density matrix elements are given by

$$P_{ij}^{(0)} = \delta_{ij} \tag{1.124}$$

and

$$P_{ia}^{(0)} = P_{ai}^{(0)} = P_{ab}^{(0)} = 0. \tag{1.125}$$

We recall the convention of this work with indices i, j, k and l that correspond to occupied orbitals, a, b, c and d are for vacant orbitals and p, q, r and s denote general orbitals. Then a time-dependent perturbation is applied to the system and we analyze the first-order (linear) response to this perturbation. The density matrix is assumed to be decomposed as

$$\boldsymbol{P} = \boldsymbol{P}^{(0)} + \boldsymbol{P}^{(1)}, \tag{1.126}$$

and similarly for the Fock matrix

$$\boldsymbol{F} = \boldsymbol{F}^{(0)} + \boldsymbol{F}^{(1)}, \tag{1.127}$$

where the superscript (1) holds for the first-order time-dependent change. Inserting Eq. (1.126) and (1.127) in the TDHF equation (1.117) and taking all the first-order terms gives

$$i\frac{\partial}{\partial t}\boldsymbol{P}^{(1)} = \boldsymbol{F}^{(0)}\boldsymbol{P}^{(1)} - \boldsymbol{P}^{(1)}\boldsymbol{F}^{(0)} + \boldsymbol{F}^{(1)}\boldsymbol{P}^{(0)} - \boldsymbol{P}^{(0)}\boldsymbol{F}^{(1)}, \tag{1.128}$$

or in terms of matrix elements

$$i\frac{\partial}{\partial t}P^{(1)}_{pr} = \sum_q \left[F^{(0)}_{pq}P^{(1)}_{qr} - P^{(1)}_{pq}F^{(0)}_{qr} + F^{(1)}_{pq}P^{(0)}_{qr} - P^{(0)}_{pq}F^{(1)}_{qr}\right]. \tag{1.129}$$

One can describe the time-dependent perturbation by a single Fourier component

$$g_{pq} = \frac{1}{2}\left[f_{pq}e^{-i\omega t} + f^*_{qp}e^{i\omega t}\right], \tag{1.130}$$

where f_{pq} is the one-electron operator which describes the applied perturbation. This perturbation acts on the electron density which results in changes in the Fock matrix that are given to first-order as

$$\Delta F^{(0)}_{pq} = \sum_{st}\frac{\partial F^{(0)}_{pq}}{\partial P_{st}}P^{(1)}_{st}, \tag{1.131}$$

such that the first-order change in the Fock matrix is

$$F^{(1)}_{pq} = g_{pq} + \Delta F^{(0)}_{pq}. \tag{1.132}$$

Similarly, the first-order density matrix response is written as

$$P^{(1)}_{pq} = \frac{1}{2}\left[d_{pq}e^{-i\omega t} + d^*_{pq}e^{i\omega t}\right], \tag{1.133}$$

where d_{pq} are the perturbation densities. Inserting Eq. (1.132) and (1.133) in Eq. (1.129) and collecting the terms containing $e^{-i\omega t}$ gives

$$\omega d_{pr} = \sum_q F^{(0)}_{pq}d_{qr} - d_{pq}F^{(0)}_{qr} + \left(f_{pq} + \sum_{st}\frac{\partial F^{(0)}_{pq}}{\partial P_{st}}d_{st}\right)P^{(0)}_{qr} - P^{(0)}_{pq}\left(f_{qr} + \sum_{st}\frac{\partial F^{(0)}_{qr}}{\partial P_{st}}d_{st}\right). \tag{1.134}$$

The remaining terms containing $e^{i\omega t}$ lead to the complex conjugate of the above equation. The idempotency condition of Eq. (1.122) for the first-order change of the density matrix gives

$$\sum_q \left\{P^{(0)}_{pq}P^{(1)}_{qr} + P^{(1)}_{pq}P^{(0)}_{qr}\right\} = P^{(1)}_{pr}, \tag{1.135}$$

which restricts the form of the matrix d_{pq} in Eq. (1.134) such that occupied-occupied d_{ii} and virtual-virtual d_{aa} blocks are zero, then only the occupied-virtual d_{ia} and virtual-occupied d_{ai} are non zero and are taken into account. As an example to show it we consider the element d_{ii} which is proportional to $P^{(1)}_{ii}$ written as

$$P^{(1)}_{ii} = \sum_q \left\{P^{(0)}_{iq}P^{(1)}_{qi} + P^{(1)}_{iq}P^{(0)}_{qi}\right\}, \tag{1.136}$$

which gives

$$P^{(1)}_{ii} = P^{(0)}_{ii}P^{(1)}_{ii} + P^{(1)}_{ii}P^{(0)}_{ii}. \tag{1.137}$$

Then using Eq. (1.124) we have that

$$P_{ii}^{(1)} = P_{ii}^{(1)} + P_{ii}^{(1)}, \tag{1.138}$$

which is only true for $P_{ii}^{(1)} = 0$. Following the same arguments we get that only the occupied-virtual d_{ia} and virtual-occupied d_{ai} blocks are non-zero. Using these non-zero blocks and considering the diagonal nature of the unperturbed Fock and density matrices we obtain the two equations

$$F_{aa}^{(0)} x_{ai} - x_{ai} F_{ii}^{(0)} + \left(f_{ai} + \sum_{bj} \left[\frac{\partial F_{ai}^{(0)}}{\partial P_{bj}} x_{bj} + \frac{\partial F_{ai}^{(0)}}{\partial P_{jb}} y_{bj} \right] \right) P_{ii}^{(0)} = \omega x_{ai}, \tag{1.139}$$

and

$$F_{ii}^{(0)} y_{ai} - y_{ai} F_{aa}^{(0)} - P_{ii}^{(0)} \left(f_{ia} + \sum_{bj} \left[\frac{\partial F_{ia}^{(0)}}{\partial P_{bj}} x_{bj} + \frac{\partial F_{ia}^{(0)}}{\partial P_{jb}} y_{bj} \right] \right) = \omega y_{ai}, \tag{1.140}$$

where, as a convention, we set $x_{ai} = d_{ai}$ and $y_{ai} = d_{ia}$. Now, if we look at the derivatives inside the previous equation we have

$$\begin{aligned} \sum_{rs} \frac{\partial F_{pq}^{(0)}}{\partial P_{rs}} &= \sum_{rs} \frac{\partial}{\partial P_{rs}} \left(H_{pq}^{c} + P_{rs} \left[\langle ps|qr\rangle - \langle ps|rq\rangle \right] \right) \\ &= \langle ps|qr\rangle - \langle ps|rq\rangle = \langle ps||qr\rangle . \end{aligned} \tag{1.141}$$

Finally, by taking the zero-frequency limit, i.e., $f_{ai} = f_{ia} \to 0$, meaning that the system is perturbed by an infinitesimal perturbation and using Eq. (1.123) and (1.124), i.e., the fact that $F_{pp}^{(0)} = \varepsilon_p$ and $P_{ii}^{(0)} = 1$ one obtains the linear response TDHF equation which is a non-Hermitian eigenvalue equation, also called the random phase approximation (RPA) [60]

$$\begin{pmatrix} \mathbf{A}^{\mathrm{ph}} & \mathbf{B}^{\mathrm{ph}} \\ -\mathbf{B}^{\mathrm{ph}} & -\mathbf{A}^{\mathrm{ph}} \end{pmatrix} \cdot \begin{pmatrix} \boldsymbol{X}^{\mathrm{ph}} & \mathbf{Y}^{\mathrm{ph}} \\ \mathbf{Y}^{\mathrm{ph}} & \boldsymbol{X}^{\mathrm{ph}} \end{pmatrix} = \begin{pmatrix} \boldsymbol{X}^{\mathrm{ph}} & \mathbf{Y}^{\mathrm{ph}} \\ \mathbf{Y}^{\mathrm{ph}} & \boldsymbol{X}^{\mathrm{ph}} \end{pmatrix} \cdot \begin{pmatrix} \boldsymbol{\Omega}^{\mathrm{ph}} & \mathbf{0} \\ \mathbf{0} & -\boldsymbol{\Omega}^{\mathrm{ph}} \end{pmatrix} \tag{1.142}$$

where Ω_m is the diagonal matrix of the excitation energies, $\boldsymbol{X}_m$ and $\boldsymbol{Y}_m$ matrices are the transition coefficients, and the matrix elements are defined as where Ω_m is the diagonal matrix of the excitation energies, $\boldsymbol{X}^{\mathrm{ph}}$ and $\mathbf{Y}^{\mathrm{ph}}$ matrices are the transition coefficients, and the matrix elements are defined as

$$A_{ia,jb}^{\mathrm{ph}} = (\epsilon_a^{\mathrm{HF}} - \epsilon_i^{\mathrm{HF}})\delta_{ij}\delta_{ab} + \langle ib||aj\rangle \tag{1.143}$$

$$B_{ia,jb}^{\mathrm{ph}} = \langle ij||ab\rangle \tag{1.144}$$

The leading term on the diagonal of the $\boldsymbol{A}$ matrix is the energy difference between the orbitals i and a which are the orbitals from which and to which the electronic transition occurs. The other terms included in the $\boldsymbol{A}$ and $\boldsymbol{B}$ matrices are the anti-symmetrized two-electron integrals from the linear response of the Coulomb and exchange operators to the first-order changes in the single-particle orbitals. The excitation energies and transition coefficients are obtained by diagonalization of Eq. (1.142), the obtained eigenvalues are the excitation energies and the eigenvectors are the transition coefficients. Throughout this thesis we will distinguish two types of traditional RPA, the first one is the direct RPA, also called dRPA, where one only

takes the direct term in the antisymmetrized two-electron integrals of Eq. (1.143) and (1.144). The second one is the exchange RPA, also called RPAx, where we take the antisymmetrized two-electron integrals, so this is the TDHF described above. The RPA theory can also be used for ground state correlation by considering two harmonic excitation energy problems [61], the RPA one and the Tamm–Dancoff approximation (TDA) which sets $\boldsymbol{B} = 0$ in Eq. (1.142) and thus solves

$$\boldsymbol{A}\boldsymbol{Z} = \nu\boldsymbol{Z}. \tag{1.145}$$

TDA includes only excitation operators but RPA also includes de-excitation operators, which can be thought of as correlating the ground state [62]. The ground state correlation energy in RPA is given by the difference between the zero point energies of these two harmonic oscillator excitation problems with correlated (RPA) and uncorrelated (TDA) ground states. So we have

$$E_c^{\text{RPA}} = \frac{1}{2}\left(\sum_m \Omega_m^{\text{ph}} - \text{Tr}(\boldsymbol{A})\right) \tag{1.146}$$

where we only take the positive excitation energies Ω_m.

1.7.2 Particle-Particle RPA (pp-RPA)

The traditional RPA (dRPA and RPAx) previously described can be interpreted as an attempt to treat particle-hole fermionic excitations as bosons [63], so it is also called particle-hole RPA or ph-RPA. By considering non-number conserving excitations and de-excitations [63] and using the equation of motion approach [61] leads to the particle-particle RPA (pp-RPA) eigenvalue problem [64]

$$\begin{pmatrix} \mathbf{C}^{\text{pp}} & \mathbf{B}^{\text{pp/hh}} \\ -\left(\mathbf{B}^{\text{pp/hh}}\right)^\dagger & -\boldsymbol{D}^{\text{hh}} \end{pmatrix} \cdot \begin{pmatrix} \boldsymbol{X}^{\text{pp}} & \mathbf{Y}^{\text{hh}} \\ \mathbf{Y}^{\text{pp}} & \boldsymbol{X}^{\text{hh}} \end{pmatrix} = \begin{pmatrix} \boldsymbol{\Omega}^{\text{pp}} & \mathbf{0} \\ \mathbf{0} & \boldsymbol{\Omega}^{\text{hh}} \end{pmatrix} \cdot \begin{pmatrix} \boldsymbol{X}^{\text{pp}} & \mathbf{Y}^{\text{hh}} \\ \mathbf{Y}^{\text{pp}} & \boldsymbol{X}^{\text{hh}} \end{pmatrix} \tag{1.147}$$

where $\boldsymbol{\Omega}^{\text{pp/hh}}$ are the diagonal matrices of the double addition/removal excitation energies, labeled by n, and the matrix elements are defined as

$$C_{ab,cd}^{\text{pp}} = (\epsilon_a + \epsilon_b)\delta_{ac}\delta_{bd} + \langle ab||cd\rangle \tag{1.148a}$$

$$B_{ab,ij}^{\text{pp/hh}} = \langle ab||ij\rangle \tag{1.148b}$$

$$D_{ij,kl}^{\text{hh}} = -(\epsilon_i + \epsilon_j)\delta_{ik}\delta_{jl} + \langle ij||kl\rangle \tag{1.148c}$$

The $\boldsymbol{X}^{\text{pp/hh}}$ and $\mathbf{Y}^{\text{pp/hh}}$ are the double addition/removal transition coefficients matrices. In the same way we did for the ph-RPA, we can obtain the correlation energy at the pp-RPA level using [64]

$$E_c^{\text{pp-RPA}} = \frac{1}{2}\left(\sum_n \Omega_n^{\text{pp}} - \sum_n \Omega_n^{\text{hh}} - \text{Tr}\boldsymbol{C}^{\text{pp}} - \text{Tr}\boldsymbol{D}^{\text{hh}}\right) \tag{1.149}$$

1.7.3 Linear-Response Time-Dependent Density Functional Theory (TD-DFT)

This section is highly inspired by Ref. [58] and by a lecture given by Pina Romaniello during doctoral lectures. Time-dependent DFT (TDDFT) is the time-dependent version of DFT, it is based on two foundations which are the Runge-Gross theorem [65] and the action integral that allow us to obtain the time-dependent Kohn-Sham equations. The Runge-Gross theorem can be seen as the time-dependent analog of the first Hohenberg-Kohn theorem and it gives the one-to-one mapping between time-dependent potentials and time-dependent functionals. Then, using the action integral one can establish a variational principle for time-dependent densities.

1.7.3.1 Runge-Gross theorem

The Runge-Gross theorem states that the exact time-dependent electron density given by

$$\rho(\boldsymbol{r},t) = \int |\Psi(\boldsymbol{r}_1,\boldsymbol{r}_2,\boldsymbol{r}_3,\ldots,\boldsymbol{r}_N,t)|^2 \, d\boldsymbol{r}_2 \, d\boldsymbol{r}_3 \, \ldots \, d\boldsymbol{r}_N \tag{1.150}$$

determines the time-dependent external potential, $\hat{V}(\boldsymbol{r},t)$ given by Eq. (1.112), up to a purely time-dependent function. Here, we do not give the proof of this theorem but we simply explain it. We refer to the interested readers to Ref. [58] for the derivation of the proof. To prove this theorem we need to demonstrate that two densities that evolve from the same initial state under the influence of two different potentials are always different if the two potentials differ by more than a purely time-dependent function. Then, by assuming that the two potentials can be Taylor expanded, two additional steps are needed. First, it can be shown that two different current densities corresponding to two distinctive potentials are always different. Then, we can derive that different current densities need distinctive electron densities [58]. This shows the one-to-one mapping between the time-dependent density and the external potential, and thus the potential and the wave function are functional of the density [58].

1.7.3.2 Action integral

The Runge-Gross theorem is not a practical tool to extract the time-dependent density. To do so, similarly to the time-independent case, we need a variational principle that is provided by the least action principle. If the time-dependent wave function $\Psi(\boldsymbol{r},t)$ is a solution of the time-dependent Schrödinger equation

$$i\frac{\partial}{\partial t}\Psi(\boldsymbol{r},t) = \hat{H}(\boldsymbol{r},t)\Psi(\boldsymbol{r},t) \tag{1.151}$$

where $\hat{H}$ is defined by Eq. (1.111). Then, the wave function corresponds to a stationary point of the quantum mechanical action integral

$$A[\rho(\boldsymbol{r},t)] = \int_{t_0}^{t_1} dt \, \langle \Psi[\rho(\boldsymbol{r},t)] | i\frac{\partial}{\partial t} - \hat{H}(\boldsymbol{r},t) | \Psi[\rho(\boldsymbol{r},t)] \rangle \tag{1.152}$$

and the exact electron density $\rho(\boldsymbol{r},t)$ is obtained from

$$\frac{\delta A[\rho(\boldsymbol{r},t)]}{\delta \rho(\boldsymbol{r},t)} = 0 \tag{1.153}$$

The action integral can be split into two parts, a universal one that only depends on the number of electrons in the system and a part that depends on the applied potential $v(\boldsymbol{r},t)$

$$A[\rho(\boldsymbol{r},t)] = B[\rho(\boldsymbol{r},t)] - \int_{t_0}^{t_1} dt \int d\boldsymbol{r}\rho(\boldsymbol{r},t)v(\boldsymbol{r},t) \tag{1.154}$$

where $B[\rho(\boldsymbol{r},t)]$ is given by

$$B[\rho(\boldsymbol{r},t)] = \int_{t_0}^{t_1} dt \left\langle \Psi[\rho(\boldsymbol{r},t)] | i\frac{\partial}{\partial t} - \hat{T}_{\mathrm{e}}(\boldsymbol{r}) - \hat{V}_{\mathrm{ee}}(\boldsymbol{r}) | \Psi[\rho(\boldsymbol{r},t)] \right\rangle . \tag{1.155}$$

1.7.3.3 Time-dependent Kohn-Sham equations

Finally, similarly to the time-independent case, we assume that a time-dependent non-interacting reference system exists with an effective external one-particle potential $v_{\mathrm{KS}}(\boldsymbol{r},t)$ of which the electron density $\rho_{\mathrm{KS}}(\boldsymbol{r},t)$ is equal to the exact electron density $\rho(\boldsymbol{r},t)$ of the real interacting system. This non-interacting system is described by a single Slater determinant formed by the occupied time-dependent Kohn-Sham (single-particle) orbitals $\phi_i(\boldsymbol{r},t)$. Then, the electron density is given by

$$\rho(\boldsymbol{r},t) = \rho_{\mathrm{KS}}(\boldsymbol{r},t) = \sum_i^N |\phi_i(\boldsymbol{r},t)|^2. \tag{1.156}$$

The orbitals are given as the solutions of the time-dependent one-particle Schrödinger equation

$$i\frac{\partial}{\partial t}\phi_i(\boldsymbol{r},t) = \left[-\frac{1}{2}\nabla_i^2 + v_{\mathrm{KS}}(\boldsymbol{r},t)\right]\phi_i(\boldsymbol{r},t), \tag{1.157}$$

We can note that the non-interacting electron density is also determined by Eq. (1.153) and that in the case of the non-interacting system, we have that $\hat{V}_{\mathrm{ee}} = 0$. Thus, the action integral is given by

$$A_{\mathrm{S}}[\rho(\boldsymbol{r},t)] = B_{\mathrm{S}}[\rho(\boldsymbol{r},t)] - \int_{t_0}^{t_1} dt \int d\boldsymbol{r}\rho(\boldsymbol{r},t)v_{\mathrm{KS}}(\boldsymbol{r},t) \tag{1.158}$$

with

$$B_{\mathrm{S}}[\rho(\boldsymbol{r},t)] = \int_{t_0}^{t_1} dt \left\langle \Psi[\rho(\boldsymbol{r},t)] | i\frac{\partial}{\partial t} - \hat{T}_{\mathrm{e}}(\boldsymbol{r}) | \Psi[\rho(\boldsymbol{r},t)] \right\rangle . \tag{1.159}$$

Using Eq. (1.153) we get

$$\frac{\delta A_{\mathrm{S}}[\rho(\boldsymbol{r},t)]}{\delta\rho(\boldsymbol{r},t)} = 0 = \frac{\delta B_{\mathrm{S}}[\rho(\boldsymbol{r},t)]}{\delta\rho(\boldsymbol{r},t)} - v_{\mathrm{KS}}(\boldsymbol{r},t) \tag{1.160}$$

where the time-dependent potential is unique thanks to the Runge-Gross theorem. Now, if we look at the action integral of the interacting system, we have that

$$\begin{aligned} A[\rho(\boldsymbol{r},t)] = B_{\mathrm{S}}[\rho(\boldsymbol{r},t)] - \int_{t_0}^{t_1} dt \int d\boldsymbol{r}\rho(\boldsymbol{r},t)v_{\mathrm{KS}}(\boldsymbol{r},t) - \frac{1}{2}\int_{t_0}^{t_1} dt \int d\boldsymbol{r} \int d\boldsymbol{r}' \frac{\rho(\boldsymbol{r},t)\rho(\boldsymbol{r}',t)}{|\boldsymbol{r}-\boldsymbol{r}'|} \\ - A_{\mathrm{xc}}[\rho(\boldsymbol{r},t)] \end{aligned} \tag{1.161}$$

with $A_{\mathrm{xc}}[\rho(\boldsymbol{r},t)]$, the exchange-correlation part of the action integral, defined by

$$A_{\mathrm{xc}}[\rho(\boldsymbol{r},t)] = B_{\mathrm{S}}[\rho(\boldsymbol{r},t)] - \frac{1}{2}\int_{t_0}^{t_1} dt \int d\boldsymbol{r} \int d\boldsymbol{r}' \frac{\rho(\boldsymbol{r},t)\rho(\boldsymbol{r}',t)}{|\boldsymbol{r}-\boldsymbol{r}'|} - B[\rho(\boldsymbol{r},t)]. \tag{1.162}$$

Then, by plugging Eq. (1.161) into Eq. (1.153), we have

$$\frac{\delta B_{\mathrm{S}}[\rho(\boldsymbol{r},t)]}{\delta\rho(\boldsymbol{r},t)} = v(\boldsymbol{r},t) + \int d\boldsymbol{r}' \frac{\rho(\boldsymbol{r}',t)}{|\boldsymbol{r}-\boldsymbol{r}'|} + \frac{\delta A_{\mathrm{xc}}[\rho(\boldsymbol{r},t)]}{\delta\rho(\boldsymbol{r},t)} \tag{1.163}$$

Thus, using Eq. (1.154) we get this expression for the time-dependent Kohn-Sham potential

$$v_{\mathrm{KS}}(\boldsymbol{r},t) = v(\boldsymbol{r},t) + \int d\boldsymbol{r}' \frac{\rho(\boldsymbol{r}',t)}{|\boldsymbol{r}-\boldsymbol{r}'|} + \frac{\delta A_{\mathrm{xc}}[\rho(\boldsymbol{r},t)]}{\delta\rho(\boldsymbol{r},t)}. \tag{1.164}$$

By inserting this expression into Eq. (1.151) we obtain the time-dependent Kohn-Sham equations

$$i\frac{\partial}{\partial t}\phi_i(\boldsymbol{r},t) = \hat{F}\phi_i(\boldsymbol{r},t), \tag{1.165}$$

where the $\phi_i(\boldsymbol{r},t)$ orbitals are the time-dependent Kohn-Sham (single-particle) orbitals and $\hat{F}$ is the time-dependent Kohn-Sham operator

$$\hat{F} = -\frac{1}{2}\nabla_r^2 + v_{\mathrm{KS}}(\boldsymbol{r},t), \tag{1.166}$$

with $v_{\mathrm{KS}}(\boldsymbol{r},t)$ the time-dependent Kohn-Sham potential

$$v_{\mathrm{KS}}(\boldsymbol{r},t) = v(\boldsymbol{r},t) + v_{\mathrm{H}}(\boldsymbol{r},t) + v_{\mathrm{xc}}(\boldsymbol{r},t), \tag{1.167}$$

where $v(\boldsymbol{r},t)$ is the time-dependent external potential, $v_{\mathrm{H}}(\boldsymbol{r},t)$ is the time-dependent Hartree potential and $v_{\mathrm{xc}}(\boldsymbol{r},t)$ is the time-dependent exchange-correlation potential with

$$v_{\mathrm{H}}(\boldsymbol{r},t) = \int \frac{\rho(\boldsymbol{r}',t)}{|\boldsymbol{r}-\boldsymbol{r}'|} d\boldsymbol{r}', \tag{1.168}$$

$$v_{\mathrm{xc}}(\boldsymbol{r},t) = \frac{\delta A_{xc}[\rho(\boldsymbol{r},t)]}{\delta\rho(\boldsymbol{r},t)}. \tag{1.169}$$

Note that different expressions can be used for the time-dependent external potential [66].$A_{xc}[\rho(\boldsymbol{r},t)]$ is the exchange-correlation action functional of the time-dependent density. As for the time-independent case, the time-dependent Kohn-Sham equations are single-particle equations in which each electron is treated individually in the field of all others. Also, like in the time-independent case, all the exchange and correlation effects are collected in the $v_{\mathrm{xc}}(\boldsymbol{r},t)$ potential. The exact time-dependent exchange-correlation action functional (also called the xc kernel) is not known, and we need to make an approximation. The approximation that we usually make is the so-called adiabatic local density approximation (ALDA) in which the originally non-local (in time) time-dependent xc kernel is replaced with a time-independent local one, based on the assumption that the density varies only slowly with time. This approximation allows the use of a standard local ground-state xc potential (from the time-independent DFT) in the TDDFT framework that we discussed in Section 1.6.3. Then, by doing the same procedure as for the linear-response TDHF (RPAx) we obtain

the linear-response TDDFT equation [67–69]

$$\begin{pmatrix} \boldsymbol{A} & \boldsymbol{B} \\ -\boldsymbol{B} & -\boldsymbol{A} \end{pmatrix} \begin{pmatrix} \boldsymbol{X}_m \\ \boldsymbol{Y}_m \end{pmatrix} = \Omega \begin{pmatrix} \boldsymbol{X}_m \\ \boldsymbol{Y}_m \end{pmatrix}, \tag{1.170}$$

where the matrix elements are defined as [58]

$$A_{ia,jb} = \delta_{ij}\delta_{ab}\left(\varepsilon_a - \varepsilon_i\right) + \langle ij|ab\rangle + \langle ij|f_{xc}|ab\rangle\,, \tag{1.171}$$

$$B_{ia,jb} = \langle ib|aj\rangle + \langle ib|f_{xc}|aj\rangle\,, \tag{1.172}$$

with f_{xc} the response of the exchange-correlation potential and it corresponds to the second functional derivative of the exchange-correlation energy, also called the xc kernel, and given by

$$\langle ij|f_{xc}|ab\rangle = \iint \phi_i^*(\boldsymbol{r})\phi_j^*(\boldsymbol{r}')\frac{\delta^2 E_{\text{xc}}}{\delta\rho(\boldsymbol{r})\delta\rho(\boldsymbol{r}')}\phi_a(\boldsymbol{r})\phi_b(\boldsymbol{r}'). \tag{1.173}$$

Again, by solving Eq. (1.170) we get the excitation energies and the transition coefficients.

1.8 Many Body Perturbation Theory (MBPT)

The first part of this section is highly inspired by Ref [70]. The whole idea behind the perturbation theory (PT) is the splitting of the Hamiltonian into two pieces: a zeroth-order Hamiltonian (or unperturbed) $\hat{H}^{(0)}$ with known eigenvalues and eigenvectors, and a perturbation $\hat{\mathcal{V}}$. First, we look at the general Rayleigh and Schrödinger PT (RSPT) to establish the framework. Then we investigate a particular case of RSPT known as the Møller-Plesset PT (MPPT) [71] where the zeroth-order Hamiltonian is the Hartree-Fock one. Finally, we look at another important tool of MBPT based on Green's functions. We discuss the one-particle Green's function and how to find it thanks to the Dyson equation by introducing an effective potential called the self-energy. Then, we look at some approximations for the self-energy like the GW, T-matrix, and Second Born approximations. Next, we go through the Bethe-Salpeter equation (BSE) that allows us to have access to neutral excitations and that relies on the two-particle Green's function.

1.8.1 Rayleigh-Schrödinger Perturbation Theory (RSPT)

In RSPT, we want to solve the following eigenvalue equation

$$\hat{H}\,|\Psi_n\rangle = (\hat{H}^{(0)} + \hat{\mathcal{V}})\,|\Psi_n\rangle = E_n\,|\Psi_n\rangle \tag{1.174}$$

where we choose the zeroth-order Hamiltonian $\hat{H}^{(0)}$ such that we know its eigenvalues $E_n^{(0)}$ and eigenstates $|\Psi_n^{(0)}\rangle$, meaning that they satisfy the eigenvalue equation

$$\hat{H}^{(0)}\,|\Psi_n^{(0)}\rangle = E_n^{(0)}\,|\Psi_n^{(0)}\rangle \tag{1.175}$$

with the orthonormality condition $\langle\Psi_n^{(0)}|\Psi_m^{(0)}\rangle = \delta_{nm}$. By introducing a coupling constant λ in the partitioned Hamiltonian as

$$\hat{H}^{(0)} + \lambda\hat{\mathcal{V}} \tag{1.176}$$

and by considering a small perturbation $\hat{\mathcal{V}}$, meaning that the perturbed eigenvalues and eigenstates are close to the unperturbed ones, we can do a Taylor expansion in λ as

$$E_n = E_n^{(0)} + \lambda E_n^{(1)} + \lambda^2 E_n^{(2)} + \dots \tag{1.177}$$

$$|\Psi_n\rangle = |\Psi_n^{(0)}\rangle + \lambda |\Psi_n^{(1)}\rangle + \lambda^2 |\Psi_n^{(2)}\rangle + \dots \tag{1.178}$$

We then do the convenient choice of the intermediate normalization $\langle \Psi_n^{(0)} | \Psi_n \rangle = 1$. Thus, multiplying Eq. (1.178) by $\langle \Psi_n^{(0)}|$ we get

$$\langle \Psi_n^{(0)} | \Psi_n \rangle = \langle \Psi_n^{(0)} | \Psi_n^{(0)} \rangle + \lambda \langle \Psi_n^{(0)} | \Psi_n^{(1)} \rangle + \lambda^2 \langle \Psi_n^{(0)} | \Psi_n^{(2)} \rangle + \dots = 1 \tag{1.179}$$

This implies that $\langle \Psi_n^{(0)} | \Psi_n^{(p)} \rangle = 0 \; \forall p \geq 1$, so each order correction to the wave function is orthogonal to the zeroth-order one. Using the expansions of the eigenvalues and eigenstates in Eq. (1.174) we get

$$\begin{aligned} &\left(\hat{H}^{(0)} + \hat{\mathcal{V}}\right)(|\Psi_n^{(0)}\rangle + \lambda |\Psi_n^{(1)}\rangle + \lambda^2 |\Psi_n^{(2)}\rangle + \dots) \\ &= (E_n^{(0)} + \lambda E_n^{(1)} + \lambda^2 E_n^{(2)} + \dots)(|\Psi_n^{(0)}\rangle + \lambda |\Psi_n^{(1)}\rangle + \lambda^2 |\Psi_n^{(2)}\rangle + \dots) \end{aligned} \tag{1.180}$$

Then, by sorting in the order of λ, at zeroth order we get back the unperturbed system

$$\hat{H}^{(0)} |\Psi_n^{(0)}\rangle = E_n^{(0)} |\Psi_n^{(0)}\rangle \tag{1.181}$$

At first order, we have

$$\hat{H}^{(0)} |\Psi_n^{(1)}\rangle + \hat{\mathcal{V}} |\Psi_n^{(0)}\rangle = E_n^{(0)} |\Psi_n^{(1)}\rangle + E_n^{(1)} |\Psi_n^{(0)}\rangle \tag{1.182}$$

For the second order, we have

$$\hat{H}^{(0)} |\Psi_n^{(2)}\rangle + \hat{\mathcal{V}} |\Psi_n^{(1)}\rangle = E_n^{(0)} |\Psi_n^{(2)}\rangle + E_n^{(1)} |\Psi_n^{(1)}\rangle + E_n^{(2)} |\Psi_n^{(0)}\rangle \tag{1.183}$$

Multiplying the last three equations by $\langle \Psi_n^{(0)}|$ we get the following expressions

$$E_n^{(0)} = \left\langle \Psi_n^{(0)} \middle| \hat{H}^{(0)} \middle| \Psi_n^{(0)} \right\rangle \tag{1.184}$$

$$E_n^{(1)} = \left\langle \Psi_n^{(0)} \middle| \hat{\mathcal{V}} \middle| \Psi_n^{(0)} \right\rangle \tag{1.185}$$

$$E_n^{(2)} = \langle \Psi_n^{(0)} | \hat{\mathcal{V}} |\Psi_n^{(1)}\rangle \tag{1.186}$$

where, first, we used the orthonormalization of the zeroth order wave function, then we used the orthogonality $\langle \Psi_n^{(0)} | \Psi_n^{(1)} \rangle = 0$ and finally the fact that $\langle \Psi_n^{(0)}| \hat{H}^{(0)} = E_n^{(0)} \langle \Psi_n^{(0)}|$. Writing

$$\hat{H}^{(0)} |\Psi_n^{(1)}\rangle + \hat{\mathcal{V}} |\Psi_n^{(0)}\rangle = E_n^{(0)} |\Psi_n^{(1)}\rangle + E_n^{(1)} |\Psi_n^{(0)}\rangle \tag{1.187}$$

as

$$\left(\hat{H}^{(0)} - E_n^{(0)}\right) |\Psi_n^{(1)}\rangle = (E_n^{(1)} - \hat{\mathcal{V}}) |\Psi_n^{(0)}\rangle \tag{1.188}$$

then, expanding the first order corrected wave function $|\Psi_n^{(1)}\rangle$ in terms of the (supposed) complete set of eigenvectors of the unperturbed Hamiltonian $\hat{H}^{(0)}$

$$|\Psi_n^{(1)}\rangle = \sum_{m\neq n} C_{mn} |\Psi_m^{(0)}\rangle \tag{1.189}$$

where the restriction on the sum indices comes from the orthonormality of the eigenvectors which also leads to

$$C_{mn} = \langle \Psi_m^{(0)} | \Psi_n^{(1)} \rangle \tag{1.190}$$

We can then write

$$|\Psi_n^{(1)}\rangle = \sum_{m\neq n} |\Psi_m^{(0)}\rangle \langle \Psi_m^{(0)} | \Psi_n^{(1)} \rangle \tag{1.191}$$

Multiplying Eq. (1.188) by $\langle \Psi_l^{(0)}|$ with $l \neq n$ and using the expression of $|\Psi_n^{(1)}\rangle$, we obtain

$$\left(E_l^{(0)} - E_n^{(0)}\right) \langle \Psi_l^{(0)} | \Psi_n^{(1)} \rangle = E_n^{(1)} \langle \Psi_l^{(0)} | \Psi_n^{(0)} \rangle - \langle \Psi_l^{(0)}| \hat{\mathcal{V}} |\Psi_n^{(0)}\rangle \tag{1.192}$$

and using the orthogonality of unperturbed eigenvectors we get

$$\langle \Psi_l^{(0)}| \hat{\mathcal{V}} |\Psi_n^{(0)}\rangle = \left(E_n^{(0)} - E_l^{(0)}\right) \langle \Psi_l^{(0)} | \Psi_n^{(1)} \rangle \tag{1.193}$$

Using the expansion of $|\Psi_n^{(1)}\rangle$ in the expression of the second order energy leads to

$$E_n^{(2)} = \langle \Psi_n^{(0)}| \hat{\mathcal{V}} |\Psi_n^{(1)}\rangle = \sum_{m\neq n} \langle \Psi_n^{(0)}| \hat{\mathcal{V}} |\Psi_m^{(0)}\rangle \langle \Psi_m^{(0)} | \Psi_n^{(1)} \rangle \tag{1.194}$$

Thus, using Eq. (1.193) yields to

$$E_n^{(2)} = \sum_{m\neq n} \frac{\langle \Psi_n^{(0)}| \hat{\mathcal{V}} |\Psi_m^{(0)}\rangle \langle \Psi_m^{(0)}| \hat{\mathcal{V}} |\Psi_n^{(0)}\rangle}{E_n^{(0)} - E_m^{(0)}} = -\sum_{m\neq n} \frac{|\langle \Psi_n^{(0)}| \hat{\mathcal{V}} |\Psi_m^{(0)}\rangle|^2}{E_m^{(0)} - E_n^{(0)}} \tag{1.195}$$

Now that we have established the framework of RSPT we take a look at the particular case where the unperturbed Hamiltonian $\hat{H}^{(0)}$ is the HF one $\hat{H}^{\mathrm{HF}}$ known as MPPT. In the following, we consider only ground state energy corrections and so $n = 0$. In MPPT the partitioning of the Hamiltonian is

$$\hat{H} = \hat{H}^{\mathrm{HF}} + \hat{\mathcal{V}} \tag{1.196}$$

where $\boldsymbol{H}^{\mathrm{HF}}$ is the Hartree-Fock Hamiltonian

$$\hat{H}^{\mathrm{HF}} = \sum_i^N \hat{f}(\boldsymbol{x}_i) = \sum_i^N \left[\hat{H}^{\mathrm{c}}(\boldsymbol{x}_i) + \hat{v}_{\mathrm{HF}}(\boldsymbol{x}_i)\right] \tag{1.197}$$

and the perturbation $\hat{\mathcal{V}}$ is

$$\hat{\mathcal{V}} = \hat{H} - \hat{H}^{\mathrm{HF}} \tag{1.198}$$

$$= \sum_{i}^{N} \hat{H}^{\mathrm{c}}(\boldsymbol{x}_i) + \sum_{i}^{N}\sum_{j>i}^{N} \frac{1}{r_{ij}} - \sum_{i}^{N} \hat{F}(\boldsymbol{x}_i) \tag{1.199}$$

$$= \sum_{i}^{N}\sum_{j>i}^{N} \frac{1}{r_{ij}} - \sum_{i}^{N} \hat{v}_{\mathrm{HF}}(\boldsymbol{x}_i) \tag{1.200}$$

The HF wave function $|\Psi_{\mathrm{HF}}\rangle$ is an eigenvector of $\hat{H}^{\mathrm{HF}}$, i.e.,

$$\hat{H}^{\mathrm{HF}} |\Psi_{\mathrm{HF}}\rangle = E_0^{(0)} |\Psi_{\mathrm{HF}}\rangle \tag{1.201}$$

where the eigenvalue is given by the sum of occupied orbital energies

$$E_0^{(0)} = \sum_{i}^{\mathrm{occ}} \varepsilon_i^{\mathrm{HF}} \tag{1.202}$$

which is the zeroth-order perturbation energy. Then, as we have seen, the first-order perturbation energy is defined as

$$E_0^{(1)} = \langle \Psi_{\mathrm{HF}} | \hat{\mathcal{V}} | \Psi_{\mathrm{HF}} \rangle \tag{1.203}$$

$$= \langle \Psi_{\mathrm{HF}} | \sum_{i}^{N}\sum_{j>i}^{N} \frac{1}{r_{ij}} | \Psi_{\mathrm{HF}} \rangle - \langle \Psi_{\mathrm{HF}} | \sum_{i}^{N} \hat{v}_{\mathrm{HF}}(\boldsymbol{x}_i) | \Psi_{\mathrm{HF}} \rangle \tag{1.204}$$

$$= \frac{1}{2} \sum_{ij}^{\mathrm{occ}} \langle ij||ij \rangle - \sum_{i}^{\mathrm{occ}} \langle i | \hat{v}_{\mathrm{HF}} | i \rangle \tag{1.205}$$

$$= -\frac{1}{2} \sum_{ij}^{\mathrm{occ}} \langle ij||ij \rangle \tag{1.206}$$

The sum of the zeroth and first-order energies gives us back the HF one

$$E_{\mathrm{HF}} = E_0^{(0)} + E_0^{(1)} = \sum_{i}^{\mathrm{occ}} \varepsilon_i^{\mathrm{HF}} - \frac{1}{2} \sum_{ij}^{\mathrm{occ}} \langle ij||ij \rangle \tag{1.207}$$

This shows us that to go beyond the HF energy we need to go at least to the second order of perturbation. We have seen that the second-order energy is given by

$$E_0^{(2)} = -\sum_{n \neq 0} \frac{|\, \langle \Psi_0^{(0)} |\, \hat{\mathcal{V}}\, | \Psi_n^{(0)} \rangle\, |^2}{E_n^{(0)} - E_0^{(0)}} \tag{1.208}$$

where $|\Psi_n^{(0)}\rangle$ could be a single, double, triple, ... excited determinants but, due to Slater-Condon's rules, for a two-body operator like the perturbation $\hat{\mathcal{V}}$, the triple and higher excitations with respect to $|\Psi_0^{(0)}\rangle$ give matrix elements $\left\langle \Psi_0^{(0)} \middle| \hat{\mathcal{V}} \middle| \Psi_n^{(0)} \right\rangle$ that vanish. Moreover, the single excited determinant also provides a vanishing matrix

element due to Brillouin's theorem

$$\langle \Psi_0^{(0)} | \hat{\mathcal{V}} | \Psi_i^a \rangle = \sum_j^{\text{occ}} \langle ij||aj\rangle - \langle i|\hat{v}_{\text{HF}}|a\rangle \tag{1.209}$$

$$= \sum_j^{\text{occ}} \langle ij||aj\rangle - \langle i|\hat{v}_{\text{HF}}|a\rangle \tag{1.210}$$

$$= \sum_j^{\text{occ}} \langle ij||aj\rangle - \sum_j^{\text{occ}} \langle ij||aj\rangle \tag{1.211}$$

$$= 0 \tag{1.212}$$

Thus, the only possibility that remains is a doubly excited determinant that gives us

$$\langle \Psi_0^{(0)} | \hat{\mathcal{V}} | \Psi_{ij}^{ab} \rangle = \langle ij||ab\rangle \tag{1.213}$$

The only missing part is

$$E_n^{(0)} = E_{ij}^{ab,(0)} = E_0^{(0)} + \varepsilon_a^{\text{HF}} + \varepsilon_b^{\text{HF}} - \varepsilon_i^{\text{HF}} - \varepsilon_j^{\text{HF}} \tag{1.214}$$

and using the antisymmetry property of the integrals, which leads to the so-called MP2 correlation energy

$$E_c^{\text{MP2}} = E_0^{(2)} = \frac{1}{4} \sum_{ij}^{\text{occ}} \sum_{ab}^{\text{vir}} \frac{|\langle ij||ab\rangle|^2}{\varepsilon_i^{\text{HF}} + \varepsilon_j^{\text{HF}} - \varepsilon_a^{\text{HF}} - \varepsilon_b^{\text{HF}}} \tag{1.215}$$

1.8.2 One-particle Green's function

Now, we turn to another important tool of many-body theory where the fundamental quantity is the Green's function. This part is highly inspired by a lecture given by Pina Romaniello during doctoral lectures. The concepts of one-particle and two-particle Green's functions are introduced and we look at some existing approximations. We consider $|\Psi_0^N\rangle$ the normalized ground state wave function of a N electrons system described by the second quantized Hamiltonian

$$\hat{H} = \int d\boldsymbol{x}_1 \hat{\Psi}^\dagger(\boldsymbol{x}_1) h(\boldsymbol{r}_1) \hat{\Psi}(\boldsymbol{x}_1) + \frac{1}{2} \iint d\boldsymbol{x}_1 d\boldsymbol{x}_2 \hat{\Psi}^\dagger(\boldsymbol{x}_1) \hat{\Psi}^\dagger(\boldsymbol{x}_2) v(\boldsymbol{r}_1, \boldsymbol{r}_2) \hat{\Psi}(\boldsymbol{x}_1) \hat{\Psi}(\boldsymbol{x}_2), \tag{1.216}$$

where

$$h(\boldsymbol{r}_1) = \frac{1}{2}\nabla^2 + v(\boldsymbol{r}_1) \tag{1.217}$$

is the one-electron Hamiltonian and

$$v(\boldsymbol{r}_1, \boldsymbol{r}_2) = \frac{1}{|\boldsymbol{r}_1 - \boldsymbol{r}_2|} \tag{1.218}$$

is the Coulomb interaction. Then, $\hat{\Psi}^\dagger(\boldsymbol{x})$ and $\hat{\Psi}(\boldsymbol{x})$ are the creation and annihilation, respectively, field operators with the space-spin coordinate $\boldsymbol{x} = (\boldsymbol{r}, s)$. The time-ordered one-particle Green's function at zero temperature is defined as

$$\begin{aligned} iG(1,2) &= \left\langle \Psi_0^N \middle| T\left[\hat{\Psi}_H(1)\hat{\Psi}_H^\dagger(2)\right] \middle| \Psi_0^N \right\rangle \\ &= \theta(t_1 - t_2)\left\langle \Psi_0^N \middle| \hat{\Psi}_H(1)\hat{\Psi}_H^\dagger(2) \middle| \Psi_0^N \right\rangle - \theta(t_2 - t_1)\left\langle \Psi_0^N \middle| \hat{\Psi}_H^\dagger(2)\hat{\Psi}_H(1) \middle| \Psi_0^N \right\rangle, \end{aligned} \tag{1.219}$$

where the indices 1 and 2 stand for space-spin-time coordinates $1 = (\boldsymbol{r}_1, s_1, t_1) = (\boldsymbol{x}_1, t_1)$ and $2 = (\boldsymbol{r}_2, s_2, t_2) = (\boldsymbol{x}_2, t_2)$, T is the Wick time-ordering operator which orders the operators with larger times on the left. In practice, this is done using the Heaviside step function θ

$$\theta(t_1 - t_2) = \begin{cases} 0, & t_1 < t_2, \\ 1, & t_1 \geq t_2. \end{cases} \tag{1.220}$$

The time-dependency is introduced by the annihilation and creation field operators in the Heisenberg representation

$$\hat{\Psi}_H(1) = e^{i\hat{H}t_1}\hat{\Psi}(\boldsymbol{x}_1)e^{-i\hat{H}t_1}, \tag{1.221}$$

$$\hat{\Psi}_H^\dagger(2) = e^{i\hat{H}t_2}\hat{\Psi}^\dagger(\boldsymbol{x}_2)e^{-i\hat{H}t_2}. \tag{1.222}$$

Now, we try to explain the physical meaning of Eq. (1.219).

- If $t_1 > t_2$, then only the first term is non-zero, and an electron is added at coordinates $(\boldsymbol{x}_2, t_2)$ to the ground state of the system by the action of $\hat{\Psi}^\dagger(\boldsymbol{x}_2)$. This extra electron interacts with its environment and creates a depletion in the charge density around it to form a quasi-electron propagated through the system from t_2 to t_1 under the influence of the Hamiltonian $\hat{H}$. Then, an electron is removed at coordinates $(\boldsymbol{x}_1, t_1)$ and the one-particle Green's function $G(1,2)$ is the probability amplitude to find an electron in $(\boldsymbol{x}_1, t_1)$ that was previously introduced in $(\boldsymbol{x}_2, t_2)$. So, for $t_1 > t_2$ the one-particle Green's function describes a particle propagation.

- If $t_2 > t_1$, then it is the second term that is non zero and thus the one-particle Green's function $G(1,2)$ is the probability amplitude to find a hole in $(\boldsymbol{x}_2, t_2)$ when an electron was removed at $(\boldsymbol{x}_1, t_1)$. So, for $t_2 > t_1$ the one-particle Green's function describes a hole propagation.

In the absence of time-dependent external potential, the one-particle Green's function depends only on the time difference $\tau = t_1 - t_2$. By introducing the closure relation

$$\sum_k \sum_M \left|\Psi_k^M\right\rangle \left\langle \Psi_k^M\right| = \hat{1}, \tag{1.223}$$

where $\left|\Psi_k^M\right\rangle$ is the k-th state of the M-electron system and apply it in Eq. (1.219) for the $(N-1)$ and $(N+1)$-electron states, we obtain

$$\begin{aligned} iG(\boldsymbol{x}_1,\boldsymbol{x}_2;\tau) = \theta(\tau)\sum_m \left\langle \Psi_0^N \middle| \hat{\Psi}(\boldsymbol{x}_1) \middle| \Psi_m^{N+1} \right\rangle \left\langle \Psi_m^{N+1} \middle| \hat{\Psi}^\dagger(\boldsymbol{x}_2) \middle| \Psi_0^N \right\rangle e^{i(E_0^N - E_m^{N+1})\tau} \\ - \theta(-\tau)\sum_n \left\langle \Psi_0^N \middle| \hat{\Psi}^\dagger(\boldsymbol{x}_2) \middle| \Psi_n^{N-1} \right\rangle \left\langle \Psi_n^{N-1} \middle| \hat{\Psi}(\boldsymbol{x}_1) \middle| \Psi_0^N \right\rangle e^{-i(E_0^N - E_n^{N-1})\tau}, \end{aligned} \tag{1.224}$$

with Ψ_0^N the ground state of the N-electron system and E_0^N its corresponding energy, Ψ_m^{N+1} the m-th state of the $(N+1)$-electron system and E_m^{N+1} its energy and Ψ_n^{N-1} the n-th state of the $(N-1)$-electron system and E_n^{N-1} its energy. One can then write the previous equation as

$$\begin{aligned} iG(\boldsymbol{x}_1,\boldsymbol{x}_2;\tau) = \theta(\tau)\sum_m f_m(\boldsymbol{x}_1) f_m^*(\boldsymbol{x}_2) e^{i(E_0^N - E_m^{N+1})\tau} \\ - \theta(-\tau)\sum_n g_n(\boldsymbol{x}_1) g_n^*(\boldsymbol{x}_2) e^{-i(E_0^N - E_n^{N-1})\tau}, \end{aligned} \tag{1.225}$$

where the terms

$$f_m(\boldsymbol{x}) = \left\langle \Psi_0^N \middle| \hat{\Psi}(\boldsymbol{x}) \middle| \Psi_m^{N+1} \right\rangle, \tag{1.226}$$

and

$$g_n(\boldsymbol{x}) = \left\langle \Psi_n^{N-1} \middle| \hat{\Psi}^\dagger(\boldsymbol{x}) \middle| \Psi_0^N \right\rangle, \tag{1.227}$$

are the so-called Lehmann amplitudes. Then, using the relation

$$\int_{-\infty}^{+\infty} dt \left[\theta(\pm t) e^{-i\alpha t}\right] e^{i\omega t} = \lim_{\eta\to 0^+} \frac{\pm i}{\omega - \alpha \pm i\eta}, \tag{1.228}$$

with 0^+ and η two positive infinitesimals, one can obtain the Fourier transform of the one-particle Green's function

$$G(\boldsymbol{x}_1,\boldsymbol{x}_2;\omega) = \int_{-\infty}^{+\infty} d\tau G(\boldsymbol{x}_1,\boldsymbol{x}_2;\tau) e^{i\omega\tau}, \tag{1.229}$$

to arrive at the Lehmann representation in frequency space of the one-particle Green's function

$$G(\boldsymbol{x}_1,\boldsymbol{x}_2;\omega) = \lim_{\eta\to 0^+} \left[\sum_m \frac{f_m(\boldsymbol{x}_1) f_m^*(\boldsymbol{x}_2)}{\omega - (E_m^{N+1} - E_0^N) + i\eta} + \sum_n \frac{g_n(\boldsymbol{x}_1) g_n^*(\boldsymbol{x}_2)}{\omega - (E_0^N - E_n^{N-1}) - i\eta} \right]. \tag{1.230}$$

The poles of the one-particle Green's function are at the electron addition $(E_m^{N+1} - E_0^N)$ and removal $(E_0^N - E_n^{N-1})$ energies of the N-electron system. The smallest electron removal energy gives the ionization potential IP$= -(E_0^N - E_0^{N-1})$ and the smallest electron addition energy gives the electron affinity EA$= E_0^N - E_0^{N+1}$. For practical reasons, one can write the one-particle Green's function in a basis set, if we consider a complete set (ϕ_i) of orthonormal orbitals then the one-particle Green's function can be written as

$$G(\boldsymbol{x}_1,\boldsymbol{x}_2;\omega) = \sum_m \frac{\phi_m(\boldsymbol{x}_1)\phi_m^*(\boldsymbol{x}_2)}{\omega - \varepsilon_m + i\eta} + \sum_n \frac{\phi_n(\boldsymbol{x}_1)\phi_n^*(\boldsymbol{x}_2)}{\omega - \varepsilon_n - i\eta}, \tag{1.231}$$

so one can see that the one-particle Green's function can be evaluated at different levels of theory depending on the choice of orbitals and energies ϕ_k and ε_k. So far we can't have the one-particle Green's function because the Lehmann amplitudes in Eq. (1.226) and (1.227) need the ground state wave function of the N-electron system. Another way to obtain it is by its propagation in time and one can show that the one-particle Green's function verifies

$$\left[\frac{\partial}{\partial t_1} - h(\boldsymbol{r}_1)\right] G(1,2) - \int d3\Sigma(1,3)G(3,2) = \delta(1,2), \tag{1.232}$$

with δ Dirac's delta function and Σ the so-called Hartree-exchange-correlation (Hxc) self-energy operator that contains the two-electron effects. The equation of motion in Eq. (1.232) can be reformulated and give the Dyson equation for the one-particle Green's function

$$G(1,2) = G_0(1,2) - i\int d3d4\; G_0(1,4)v(4,3^+)G^{(2)}(4,3;2,3^+) \tag{1.233}$$

where G_0 is the non interacting one-particle Green's function and $G^{(2)}$ is the two-particle Green's function. One can make a parallel between the Kohn-Sham theory where the two-electron interactions (which are unknown) are in the Kohn-Sham potential and the exchange-correlation self-energy. The difference is that the self-energy is nonlocal. It can be shown that the Hartree-exchange-correlation self-energy is of the form

$$\begin{aligned}\Sigma(1,2) = {} & v_H(1)\delta(1,2) + iv(1^+,2)G(1,2) \\ & + i\int d3d4d5d6\; v(1^+,3)G(1,4)\Xi(4,6;2,5)L(5,3;6,3^+),\end{aligned} \tag{1.234}$$

where v_H is the Hartree potential, Ξ is the effective interaction

$$\Xi(4,6;2,5) = \frac{\delta\Sigma(4,2)}{\delta G(5,6)}, \tag{1.235}$$

and L is the generalized response function

$$L(5,3;6,3) = \frac{\delta G(5,6)}{\delta\varphi(3)}\Big|_{\varphi=0}, \tag{1.236}$$

where φ is a fictitious external potential. The physical meaning of the self-energy is that the particle can scatter against the density of the system (Hartree term), it can exchange with another particle of the system and it can perturb the system, i.e., it can have an effective interaction with the system (Ξ) then the system responds (L) and the particle feels this response through the Coulomb interaction. Making approximations to Ξ and L gives rise to various approximations to the self-energy Σ and so different Green's function theories.

1.8.2.1 GW approximation

In 1965, Hedin derived a set of coupled equations [17] that yields, in principle, the exact self-energy and leads to another expression for the self-energy

$$\begin{aligned}\Sigma(1,2) &= v_H(1)\delta(1,2) + \mathbf{\Sigma}^{\text{xc}}(1,2) \\ &= v_H(1)\delta(1,2) + i\int d3d4G(1,4)W(3,1^+)\Gamma(4,2;3),\end{aligned} \tag{1.237}$$

where we introduced the exchange-correlation (xc) self-energy that is defined as $\mathbf{\Sigma}^{\text{xc}} = \Sigma - v_H$, with W as the dynamically screened Coulomb interaction and Γ as the so-called "vertex" function. The dynamically screened Coulomb interaction is written

$$W(1,2) = \int d3\varepsilon^{-1}(1,3)v(3,2), \tag{1.238}$$

with ε the dielectric function

$$\varepsilon(1,2) = \delta(1,2) - \int d3\chi_0(1,3)v(3,2), \tag{1.239}$$

and where χ_0 is the noninteracting polarizability

$$\chi_0 = -iG(1,2^+)G(2,1^+). \tag{1.240}$$

The neglect of the vertex in Eq. (1.237), i.e., $\Gamma(4,2;3) = \delta(1,2)\delta(2,3)$, leads to the GW approximation and gives the xc self-energy

$$\mathbf{\Sigma}^{\text{xc}}(1,2) = iG(1,2)W(2,1^+). \tag{1.241}$$

In the GW formalism, the dynamical screening is computed at the direct random-phase approximation (dRPA) level and its spectral representation is given by

$$W_{pq,rs}(\omega) = \langle pr|qs\rangle + \sum_m \sum_i M^{\text{ph}}_{pq,m} M^{\text{ph}}_{rs,m} \left[\frac{1}{\omega - \Omega^{\text{ph}}_m + i\eta} - \frac{1}{\omega + \Omega^{\text{ph}}_m - i\eta}\right], \tag{1.242}$$

with Ω^{ph}_m the excitation energies (eigenvalues) of Eq. (1.142), η a positive infinitesimal and $M^{\text{ph}}_{pq,m}$ the screened two-electron integrals (or spectral weights) of expression

$$M^{\text{ph}}_{pq,m} = \sum_{ia} \langle pi|qa\rangle \left(\boldsymbol{X}^{\text{ph}} + \mathbf{Y}^{\text{ph}}\right)_{ia,m} \tag{1.243}$$

where $\boldsymbol{X}^{\text{ph}}$ and $\mathbf{Y}^{\text{ph}}$ are the transition coefficients (eigenvectors) of Eq. (1.142). The exchange-correlation (xc) self-energy can be split in an exchange (x) and a correlation (c) contributions, then its spectral representation reads, respectively,

$$\Sigma^{\text{x}}_{pq} = -\sum_i \langle pi|iq\rangle \tag{1.244}$$

$$\Sigma^{\text{c}}_{pq}(\omega) = \Sigma^{GW}_{pq}(\omega) = \sum_{im} \frac{M^{\text{ph}}_{pi,m} M^{\text{ph}}_{qi,m}}{\omega - \epsilon_i + \Omega^{\text{ph}}_m} + \sum_{am} \frac{M^{\text{ph}}_{pa,m} M^{\text{ph}}_{qa,m}}{\omega - \epsilon_a - \Omega^{\text{ph}}_m} \tag{1.245}$$

Within the *GW* approximation the correlation energy of the system can be obtained in two ways, the first one is by using the RPA correlation energy of Eq. (1.146) and

the second one is by using the Galitskii-Migdal functional [72]

$$E_c^{\mathrm{GM}} = -\frac{i}{2}\sum_{pq}^{\infty}\int \frac{d\omega}{2\pi}\Sigma^{\mathrm{c}}_{pq}(\omega)G_{pq}(\omega)e^{i\omega\eta} \tag{1.246}$$

and applying it to the GW approximation leads to

$$E_c^{\mathrm{GM}} = \sum_{iam}\frac{M^{\mathrm{ph}}_{ai,m}M^{\mathrm{ph}}_{ai,m}}{\epsilon_a - \epsilon_i + \Omega^{\mathrm{ph}}_m} \tag{1.247}$$

1.8.2.2 T-matrix approximation

When the screening is not important, i.e., at low density, one can use the rough approximation $L(5,3;6,3) \approx G(5,3)G(3,6)$ in Eq. (1.236) where we neglect the interaction and concentrate on a better approximation for $\Xi(4,6;2,5)$ in Eq. (1.235). One uses the self-energy ansatz

$$\Sigma(1,2) = \int d3d5\; G(5,3)T(1,3;2,5), \tag{1.248}$$

and one can do the approximation

$$\frac{\delta\Sigma(4,2)}{\delta G(5,6)} \approx T(4,6;2,5) \tag{1.249}$$

in Eq. (1.234). Then, one can find Dyson equations for $T = T_1 + T_2$

$$T_1(1,3;2,5) = iv(1,3)\delta(3,5^+)\delta(1,2) + i\int d4d6\; v(1^+,3)G(1,4)G(3,6)T_1(4,6;2,5) \tag{1.250}$$

and

$$T_2(1,3;2,5) = iv(1,3)\delta(2,3)\delta(1,5) + i\int d4d6\; v(1^+,3)G(1,4)G(3,6)T_2(4,6;2,5). \tag{1.251}$$

So, we end up with the self-energy expression

$$\Sigma(1,2) = \int d3d5\; G(5,3)\left[T_1(1,3;2,5) + T_2(1,3;2,5)\right]. \tag{1.252}$$

Using Fourier transform and projection into the MO space [73] it yields the correlation part of the T-matrix self-energy

$$\Sigma^{GT}_{pq}(\omega) = \sum_{in}\frac{M^{\mathrm{pp}}_{pi,n}M^{\mathrm{pp}}_{qi,n}}{\omega + \epsilon_i - \Omega^{\mathrm{pp}}_n} + \sum_{an}\frac{M^{\mathrm{hh}}_{pa,n}M^{\mathrm{hh}}_{qa,n}}{\omega + \epsilon_a - \Omega^{\mathrm{hh}}_n} \tag{1.253}$$

where the pp and hh versions of the screened two-electron integrals read

$$M^{\mathrm{pp}}_{pq,n} = \sum_{c<d}\langle pq||cd\rangle\, X^{\mathrm{pp}}_{cd,n} + \sum_{k<l}\langle pq||kl\rangle\, Y^{\mathrm{pp}}_{kl,n} \tag{1.254a}$$

$$M^{\mathrm{hh}}_{pq,n} = \sum_{c<d}\langle pq||cd\rangle\, X^{\mathrm{hh}}_{cd,n} + \sum_{k<l}\langle pq||kl\rangle\, Y^{\mathrm{hh}}_{kl,n} \tag{1.254b}$$

The components $X^{\mathrm{pp/hh}}_{cd,n}$ and $Y^{\mathrm{pp/hh}}_{kl,n}$ are the double addition/removal eigenvector components of the pp-RPA eigenvalue problem in Eq. (1.147). Similarly to the GW

case, within the T-matrix approximation, the correlation energy of the system can be obtained by using the pp-RPA correlation energy of Eq. (1.149) or the Galitskii-Migdal functional that gives

$$E_c^{\mathrm{GM}} = \sum_{ijn} \frac{M_{ij,n}^{\mathrm{pp}} M_{ij,n}^{\mathrm{pp}}}{\epsilon_i + \epsilon_j - \Omega_n^{\mathrm{pp}}} - \sum_{abn} \frac{M_{ab,n}^{\mathrm{hh}} M_{ab,n}^{\mathrm{hh}}}{\epsilon_a + \epsilon_b - \Omega_n^{\mathrm{hh}}} \tag{1.255}$$

1.8.2.3 Second-Born approximation

By doing an expansion to second-order in v in the T-matrix, one obtains the second Born approximation ($2B$)

$$\Sigma^{2B}(1,2) = \Sigma^{HF}(1,2) + \Sigma^{(2)}(1,2) \tag{1.256}$$

where Σ^{HF} is the Hartree-Fock self-energy given by

$$\Sigma^{HF}(1,2) = v_H(1)\delta(1,2) + iv(1,2)G(1,2^+) \tag{1.257}$$

and $\Sigma^{(2)}$ is the sum of the two terms

$$\Sigma^{(2a)}(1,2) = -i^2 G(1,2) \int d3d4\; v(1,3)G(3,4)G(4,3)v(4,2), \tag{1.258}$$

$$\Sigma^{(2b)}(1,2) = i^2 \int d3d4\; G(1,3)v(1,4)G(3,4)G(4,2)v(3,2). \tag{1.259}$$

These terms are called second-order direct and exchange terms and $\Sigma^{(2)}$ is the second-order self-energy that is also written as Σ^{GF2} where GF2 stands for second-order Green's function. Using algebraic derivation for the second-order self-energy [74] leads to the expression

$$\Sigma_{pq}^{\mathrm{GF2}}(\omega) = \frac{1}{2}\sum_{ija} \frac{\langle pa||ij\rangle\ \langle qa||ij\rangle}{\omega + \epsilon_a - \epsilon_i - \epsilon_j} + \frac{1}{2}\sum_{iab} \frac{\langle pi||ab\rangle\ \langle qi||ab\rangle}{\omega + \epsilon_i - \epsilon_a - \epsilon_b} \tag{1.260}$$

Finally, within the second-Born approximation, the correlation energy of the system is obtained at the MP2 level defined as [70]

$$E_c^{\mathrm{MP2}} = \frac{1}{4}\sum_{ijab} \frac{|\ \langle ij||ab\rangle\ |^2}{\epsilon_i + \epsilon_j - \epsilon_a - \epsilon_b} \tag{1.261}$$

1.8.2.4 Level of self-consistency

In many-body perturbation Green's function theory one of the target quantities are the quasiparticle energies $\varepsilon_p^{\mathrm{QP}}$, i.e., the poles of the one-particle Green's function in Eq. (1.219), which correspond to the proper addition/removal energies. Because the exchange-correlation part of the self-energy in Eq. (1.234) depends on the one-particle Green's function we are in the presence of a self-consistent process by nature and this gives rise to different schemes where we can use all the different self-energies presented. In its simplest version called G_0, one performs only a single iteration, and the quasiparticles $\varepsilon_p^{\mathrm{QP}}$ are obtained by solving the frequency-dependent quasiparticle equation

$$\omega = \varepsilon_p^{\mathrm{KS}} + \Sigma_{pp}^{\mathrm{xc}}(\omega) - V_p^{\mathrm{xc}} \tag{1.262}$$

procedure G_0@KS
Perform KS calculation to get $\boldsymbol{\varepsilon}^{\mathrm{KS}}$, $\boldsymbol{c}^{KS}$ and $\boldsymbol{V}^{\mathrm{xc}}$
AO to MO transformation for two electrons integrals: $\langle \mu\nu|\lambda\sigma\rangle \xrightarrow{\boldsymbol{c}^{KS}} \langle pq|rs\rangle$

if *GW* **then**
Construct RPA matrices $\boldsymbol{A}^{\mathrm{RPA}}$ and $\boldsymbol{B}^{\mathrm{RPA}}$ from $\boldsymbol{\varepsilon}^{\mathrm{KS}}$ and $\langle pq|rs\rangle$
Compute RPA eigenvalues $\boldsymbol{\Omega}^{\mathrm{RPA}}$ and eigenvectors $\boldsymbol{X}^{\mathrm{RPA}} + \boldsymbol{Y}^{\mathrm{RPA}}$
Construct screened two-electron integrals M^m_{pq}

else if *GT* **then**
Construct pp-RPA matrices $\boldsymbol{A}^{\text{pp-RPA}}$ and $\boldsymbol{B}^{\text{pp-RPA}}$ from $\boldsymbol{\varepsilon}^{\mathrm{KS}}$ and $\langle pq||rs\rangle$
Compute pp-RPA eigenvalues $\boldsymbol{\Omega}^{\text{pp-RPA}}$ and eigenvectors $\boldsymbol{X}^{\text{pp-RPA}}$, $\boldsymbol{Y}^{\text{pp-RPA}}$
Construct the integrals $\langle pq|\chi_n^{N\pm2}\rangle$
end if

for $p = 1, \ldots, N$ **do**
Compute diagonal of the self-energy $\Sigma^{\mathrm{xc}}_{pp}(\omega)$ at $\omega = \varepsilon^{\mathrm{KS}}_p$
Compute renormalization factors Z_p
Evaluate $\varepsilon^{\mathrm{QP}}_p = \varepsilon^{\mathrm{KS}}_p + Z_p \left[\Sigma^{\mathrm{xc}}_{pp}(\varepsilon^{\mathrm{KS}}_p) - V^{\mathrm{xc}}_p\right]$
end for
end procedure

Figure 1.1: Pseudo-algortihm for the G_0 procedure.The case *GF*2 is not written because we only need the two-electron integrals for the computation of the self-energy.

where all the needed quantities for the computation of the exchange-correlation self-energy are constructed at the Kohn-Sham level and

$$V^{\mathrm{xc}}_p = \int \phi_p(\boldsymbol{x}) v_{\mathrm{xc}}(\boldsymbol{r}) \phi_p(\boldsymbol{x}) d\boldsymbol{x} \tag{1.263}$$

with v_{xc} the local Kohn-Sham exchange-correlation potential. Because Eq. (1.262) is nonlinear, it will generate the quasiparticle solution and a finite number of satellite resonances. Because one is usually interested in the quasiparticle solution, Eq. (1.262) is often linearized around $\omega = \varepsilon^{\mathrm{KS}}_p$, which yields to

$$\varepsilon^{\mathrm{QP}}_p = \varepsilon^{\mathrm{KS}}_p + Z_p \left[\Sigma^{\mathrm{xc}}_{pp}(\varepsilon^{\mathrm{KS}}_p) - V^{\mathrm{xc}}_p\right] \tag{1.264}$$

where

$$Z_p = \left[1 - \frac{\partial \Sigma^{\mathrm{xc}}_{pp}(\omega)}{\partial \omega}\Big|_{\omega=\varepsilon^{\mathrm{KS}}_p}\right]^{-1} \tag{1.265}$$

is a renormalization factor, with $0 \leq Z_p \leq 1$, which represents the spectral weight of the quasiparticle solution. As previously said, Eq. (1.262) has satellite resonances, which will have smaller spectral weights. Fig. 1.1 summarize the G_0 procedure.

Another scheme is the "eigenvalue" self-consistent or evG where several iterations

procedure EVG@KS
Perform KS calculation to get $\boldsymbol{\varepsilon}^{\mathrm{KS}}$, $\boldsymbol{c}^{KS}$ and $\boldsymbol{V}^{\mathrm{xc}}$
AO to MO transformation for two electrons integrals: $\langle \mu\nu|\lambda\sigma\rangle \xrightarrow{\boldsymbol{c}^{KS}} \langle pq|rs\rangle$
Set $\boldsymbol{\varepsilon}^{G_{-1}} = \boldsymbol{\varepsilon}^{\mathrm{KS}}$ and $n = 0$
while max $|\Delta| > \tau$ **do**
if *GW* **then**
Construct RPA matrices $\boldsymbol{A}^{\mathrm{RPA}}$ and $\boldsymbol{B}^{\mathrm{RPA}}$ from $\boldsymbol{\varepsilon}^{G_{n-1}}$ and $\langle pq|rs\rangle$
Compute RPA eigenvalues $\boldsymbol{\Omega}^{\mathrm{RPA}}$ and eigenvectors $\boldsymbol{X}^{\mathrm{RPA}} + \boldsymbol{Y}^{\mathrm{RPA}}$
Construct screened two-electron integrals M^{m}_{pq}

else if *GT* **then**
Construct pp-RPA matrices $\boldsymbol{A}^{\text{pp-RPA}}$ and $\boldsymbol{B}^{\text{pp-RPA}}$ from $\boldsymbol{\varepsilon}^{G_{n-1}}$ and $\langle pq||rs\rangle$
Compute pp-RPA eigenvalues $\boldsymbol{\Omega}^{\text{pp-RPA}}$ and eigenvectors $\boldsymbol{X}^{\text{pp-RPA}}$, $\boldsymbol{Y}^{\text{pp-RPA}}$
Construct the integrals $\left\langle pq\middle|\chi^{N\pm2}_{n}\right\rangle$
end if

for $p = 1, \ldots, N$ **do**
Compute diagonal of the self-energy $\Sigma^{\mathrm{xc}}_{pp}(\omega)$ at $\omega = \boldsymbol{\varepsilon}^{G_{n-1}}_{p}$
Evaluate $\boldsymbol{\varepsilon}^{G_n}_{p} = \varepsilon^{\mathrm{KS}}_{p} + \left[\Sigma^{\mathrm{xc}}_{pp}(\boldsymbol{\varepsilon}^{G_{n-1}}_{p}) - V^{\mathrm{xc}}_{p}\right]$
end for
$\Delta = \boldsymbol{\varepsilon}^{G_n} - \boldsymbol{\varepsilon}^{G_{n-1}}$
$n \leftarrow n + 1$
end while
end procedure

Figure 1.2: Pseudo-algortihm for the evG procedure. The case *GF*2 is not written because we only need the two-electron integrals for the computation of the self-energy.

are performed in which only the one-electron energies entering the definition of the Green's function in Eq.(1.219) are updated by the quasiparticle energies obtained at the previous iteration. Note that the corresponding orbitals remain evaluated at the KS level, Fig. 1.2 summarizes the evG procedure. Finally, the last presented scheme is the quasiparticle self-consistent (qsG) scheme, where both the one-electron energies and the orbitals are updated until convergence is reached. This is done by the diagonalization of an effective Fock matrix, that includes explicitly a frequency-independent Hermitian self-energy defined as

$$\tilde{\Sigma}^{\mathrm{xc}}_{pq} = \frac{1}{2}\left[\Sigma^{\mathrm{xc}}_{pq}(\varepsilon_p) + \Sigma^{\mathrm{xc}}_{qp}(\varepsilon_p)\right], \tag{1.266}$$

this procedure is outlined in Fig. 1.3

1.8.3 Two-particle Green's function and Bethe-Salpeter equation

The Bethe-Salpeter Equation (BSE) has a very similar structure to the TD-DFT and deals with neutral excitations as measured by optical (i.e. absorption) spectroscopy.

procedure QSG@KS
Perform KS calculation to get $\boldsymbol{\varepsilon}^{\text{KS}}$, $\boldsymbol{c}^{KS}$ and $\boldsymbol{V}^{\text{xc}}$
Set $\boldsymbol{\varepsilon}^{G_{-1}} = \boldsymbol{\varepsilon}^{\text{KS}}$, $\boldsymbol{c}^{G_{-1}} = \boldsymbol{c}^{KS}$ and $n = 0$

while max $|\Delta| > \tau$ **do**
AO to MO transformation for two electrons integrals: $\langle \mu\nu|\lambda\sigma\rangle \xrightarrow{\boldsymbol{c}^{G_{n-1}}} \langle pq|rs\rangle$
if GW **then**
Construct RPA matrices $\boldsymbol{A}^{\text{RPA}}$ and $\boldsymbol{B}^{\text{RPA}}$ from $\boldsymbol{\varepsilon}^{G_{n-1}}$ and $\langle pq|rs\rangle$
Compute RPA eigenvalues $\boldsymbol{\Omega}^{\text{RPA}}$ and eigenvectors $\boldsymbol{X}^{\text{RPA}} + \boldsymbol{Y}^{\text{RPA}}$
Construct screened two-electron integrals M^{m}_{pq}

else if GT **then**
Construct pp-RPA matrices $\boldsymbol{A}^{\text{pp-RPA}}$ and $\boldsymbol{B}^{\text{pp-RPA}}$ from $\boldsymbol{\varepsilon}^{G_{n-1}}$ and $\langle pq||rs\rangle$
Compute pp-RPA eigenvalues $\boldsymbol{\Omega}^{\text{pp-RPA}}$ and eigenvectors $\boldsymbol{X}^{\text{pp-RPA}}$, $\boldsymbol{Y}^{\text{pp-RPA}}$
Construct the integrals $\langle pq|\chi_n^{N\pm 2}\rangle$
end if
Evaluate $\boldsymbol{\Sigma}^{\text{xc}}(\boldsymbol{\varepsilon}^{G_{n-1}})$ and form $\tilde{\boldsymbol{\Sigma}}^{\text{xc}} \leftarrow \frac{1}{2}\left[\boldsymbol{\Sigma}^{\text{xc}}(\boldsymbol{\varepsilon}^{G_{n-1}})^{\dagger} + \boldsymbol{\Sigma}^{\text{xc}}(\boldsymbol{\varepsilon}^{G_{n-1}})\right]$
Form $\boldsymbol{F}$ from $\boldsymbol{c}^{G_{n-1}}$ and then $\tilde{\boldsymbol{F}} = \boldsymbol{F} + \tilde{\boldsymbol{\Sigma}}^{\text{xc}}$
Diagonalize $\tilde{\boldsymbol{F}}$ to get $\boldsymbol{\varepsilon}^{G_n}$ and $\boldsymbol{c}^{G_n}$
$\Delta = \boldsymbol{\varepsilon}^{G_n} - \boldsymbol{\varepsilon}^{G_{n-1}}$
$n \leftarrow n + 1$
end while
end procedure

Figure 1.3: Pseudo-algortihm for the qsG procedure. The case $GF2$ is not written because we only need the two-electron integrals for the computation of the self-energy.

Unlike TD-DFT, where the central quantity is the electron density $\rho(\boldsymbol{r}, t)$, the BSE central quantity is the Green's function G and the exchange-correlation potential $v_{\text{xc}}(\boldsymbol{r}, t)$ is replaced by the generalized exchange-correlation self-energy $\boldsymbol{\Sigma}^{\text{xc}}$ [26]. One can obtain a Dyson equation that links the generalized four-point susceptibility L and Ξ the BSE kernel as [26]

$$L(1,2;3,4) = L_0(1,2;3,4) + \int d5d6d7d8\; L_0(1,2;3,4)\Xi(5,6;7,8)L(7,8;3,4) \quad (1.267)$$

with L_0 the noninteracting particle four-point susceptibility and defined as

$$L_0(1,2;3,4) = G(1,4)G(2,3). \quad (1.268)$$

The BSE kernel derives from the exchange-correlation self-energy

$$\Xi(5,6;7,8) = v(5,7)\delta(5,6)\delta(7,8) + \frac{\delta\boldsymbol{\Sigma}^{\text{xc}}(5,6)}{\delta G(7,8)} \quad (1.269)$$

We can see that the expression of the BSE kernel depends on the choice of the self-energy approximation and this is one of the subjects of Chapter 5 but in the general setting, we have to solve a non-linear eigenvalue problem of the form

$$\begin{pmatrix} \mathbf{A}^{\text{BSE}}(\Omega_\nu^{\text{BSE}}) & \mathbf{B}^{\text{BSE}}(\Omega_\nu^{\text{BSE}}) \\ -\mathbf{B}^{\text{BSE}}(-\Omega_\nu^{\text{BSE}}) & -\mathbf{A}^{\text{BSE}}(-\Omega_\nu^{\text{BSE}}) \end{pmatrix} \cdot \begin{pmatrix} \boldsymbol{X}_\nu^{\text{BSE}} \\ \mathbf{Y}_\nu^{\text{BSE}} \end{pmatrix} = \Omega_\nu^{\text{BSE}} \begin{pmatrix} \boldsymbol{X}_\nu^{\text{BSE}} \\ \mathbf{Y}_\nu^{\text{BSE}} \end{pmatrix} \quad (1.270)$$

where the index v runs over single, double, and potentially higher excitations. Of course, the expressions of matrices $\mathbf{A}^{\text{BSE}}$ and $\mathbf{B}^{\text{BSE}}$ depend on the type of quasiparticles and the kernel that one considers but they have the following generic expressions

$$A_{ia,jb}^{\text{BSE}}(\omega) = A_{ia,jb} + \Xi_{ia,jb}(\omega) \quad (1.271a)$$

$$B_{ia,jb}^{\text{BSE}}(\omega) = B_{ia,jb} + \Xi_{ia,bj}(\omega) \quad (1.271b)$$

with the following static parts

$$A_{ia,jb} = (\epsilon_a - \epsilon_i)\delta_{ij}\delta_{ab} + \langle ib||aj\rangle \quad (1.272a)$$

$$B_{ia,jb} = \langle ij||ab\rangle \quad (1.272b)$$

where the ϵ_p's are quasiparticle energies and $\Xi_{pq,rs}(\omega)$ is an element of the dynamical correlation kernel computed at a given level of theory. So, a BSE calculation adds excitonic effects (i.e., the electron-hole binding energy) to the underlying fundamental gap calculation (obtained from the charged excitation energies). This underlying calculation provides quasiparticle energies and a kernel that are used to build the BSE Hamiltonian from which one can extract the vertical excitations of the system.

1.8.4 Algebraic Diagrammatic Construction

In this part one presents another way to obtain charged and neutral excitations from the Green's function formalism, called the Algebraic Diagrammatic Construction (ADC) scheme. The ADC scheme was introduced by Schirmer in 1982 for the computation of neutral excitations in finite systems by using it for the polarization propagator [75]. Then, Schirmer extended this scheme for the computation of charged excitations by applying it to the one-body Green's function or more precisely to the self-energy [76]. It is worth mentioning that the two-particle propagator was also

used within the ADC scheme leading to the calculation of the two-electron removal energies [77]. The ADC method can be seen as a scheme that can be applied to different propagators to obtain different types of excitation energies. First, one takes a look at the ADC scheme for charged excitations and then one reviews it for neutral excitations. Note that this section is highly inspired by Refs. [75, 76, 78, 79] and one refers to these to interested readers.

1.8.4.1 Charged excitations

For the computation of charged excitations using the ADC scheme, two approaches exist. First, the original formulation called the Dyson-ADC scheme [76] where the computation of electron affinity and ionization potential is coupled by applying the ADC scheme to both components of the self-energy. Then, there is the non-Dyson ADC scheme [80] where these computations are non-coupled by only employing the scheme on each component of the the one-body Green's function, separately. One with the Dyson-ADC scheme, we begin with the Dyson equation [81]

$$\boldsymbol{G}(\omega) = \boldsymbol{G}_0(\omega) + \boldsymbol{G}_0(\omega) \cdot \boldsymbol{\Sigma}(\omega) \cdot \boldsymbol{G}(\omega) \tag{1.273}$$

where $\boldsymbol{G}(\omega)$ is the one-body Green's function (1-GF), $\boldsymbol{G}_0(\omega)$ is the non-interacting 1-GF and $\boldsymbol{\Sigma}(\omega)$ is the self-energy. One has that

$$\boldsymbol{G}(\omega) - \boldsymbol{G}_0(\omega) = \boldsymbol{G}_0(\omega) \cdot \boldsymbol{\Sigma}(\omega) \cdot \boldsymbol{G}(\omega) \tag{1.274}$$

that one can also write

$$\boldsymbol{\Sigma}(\omega) = \boldsymbol{G}_0(\omega)^{-1} \cdot (\boldsymbol{G}(\omega) - \boldsymbol{G}_0(\omega)) \cdot \boldsymbol{G}(\omega)^{-1} \tag{1.275}$$

Thus, one obtains

$$\boldsymbol{\Sigma}(\omega) = \boldsymbol{G}_0(\omega)^{-1} - \boldsymbol{G}(\omega)^{-1} \tag{1.276}$$

or, equivalently

$$\boldsymbol{G}(\omega) = (\boldsymbol{G}_0(\omega)^{-1} - \boldsymbol{\Sigma}(\omega))^{-1} \tag{1.277}$$

From there one needs to express the 1-GF of Eq. (1.230) in a complete set of orthonormal one-particle orbitals. To do so one has to explicit the field operators in this basis as

$$\hat{\Psi}(\boldsymbol{x}) = \sum_p \phi_p(\boldsymbol{x}) \hat{a}_p, \tag{1.278}$$

$$\hat{\Psi}^\dagger(\boldsymbol{x}) = \sum_p \phi_p^*(\boldsymbol{x}) \hat{a}_p^\dagger. \tag{1.279}$$

where $\hat{c}_p$ and $\hat{c}_p^\dagger$ are the creation and annihilation operators, respectively. Then, the 1-GF can be written as

$$G(\boldsymbol{x}_1, \boldsymbol{x}_2; \omega) = \sum_{pq} G_{pq}(\omega) \phi_p(\boldsymbol{x}_1) \phi_q^*(\boldsymbol{x}_2) \tag{1.280}$$

with

$$\begin{aligned} G_{pq}(\omega) &= \int d\boldsymbol{x}_1 d\boldsymbol{x}_2 \, \phi_p^*(\boldsymbol{x}_1) G(\boldsymbol{x}_1, \boldsymbol{x}_2; \omega) \phi_q(\boldsymbol{x}_2) \\ &= \sum_m \frac{\langle \Psi_0 | \hat{a}_p | \Psi_m^{N+1} \rangle \langle \Psi_m^{N+1} | \hat{a}_q^\dagger | \Psi_0 \rangle}{\omega - (E_m^{N+1} - E_0^N) + i\eta} + \sum_n \frac{\langle \Psi_0 | \hat{a}_q^\dagger | \Psi_n^{N-1} \rangle \langle \Psi_n^{N-1} | \hat{a}_p | \Psi_0 \rangle}{\omega - (E_0^N - E_n^{N-1}) - i\eta} \\ &\equiv G_{pq}^+(\omega) + G_{pq}^-(\omega) \end{aligned} \tag{1.281}$$

where $G_{pq}^+(\omega)$ and $G_{pq}^-(\omega)$ describe electron attachment and detachment processes, respectively. Because the infinitesimal number η is not important for further derivations one drops it. The $|\Psi_m^{N+1}\rangle$ and $|\Psi_n^{N-1}\rangle$ are the exact eigenstates of the $(N+1)-$ and $(N-1)-$electron system with energies E_m^{N+1} and E_n^{N-1}, respectively. Each component of the 1-GF can be expressed in a matrix formulation as

$$\boldsymbol{G}^\pm(\omega) = \boldsymbol{Q}^\pm \cdot \left(\omega \mathbf{1} - \boldsymbol{E}^\pm\right)^{-1} \cdot \boldsymbol{Q}^{\pm\dagger} \tag{1.282}$$

where $\boldsymbol{E}^\pm$ are the diagonal matrices of exact vertical attachment $E_m^+ = \left(E_m^{N+1} - E_0^N\right)$ and ionization $E_n^- = \left(E_0^N - E_n^{N-1}\right)$ energies. The $\boldsymbol{Q}^\pm$ matrices are the so-called spectroscopic amplitudes with elements $Q_{pm}^+ = \langle \Psi_0 | \hat{a}_p | \Psi_m^{N+1} \rangle$ and $Q_{qn}^- = \langle \Psi_0 | \hat{a}_q^\dagger | \Psi_n^{N-1} \rangle$. Since the 1-GF is expressed in the eigenstates of the system, Eq. (1.282) is called its diagonal representation. The self-energy can be written as [76]

$$\boldsymbol{\Sigma}(\omega) = \boldsymbol{\Sigma}_\mathrm{s}(\infty) + \boldsymbol{\Sigma}_\mathrm{d}(\omega) \tag{1.283}$$

where $\boldsymbol{\Sigma}_\mathrm{s}(\infty)$ is the static (ω-independent) part and $\boldsymbol{\Sigma}_\mathrm{d}(\omega)$ is the dynamical (ω-dependent) part. In the same way we did for the 1-GF, the dynamical part of the self-energy can be written as [78]

$$\boldsymbol{\Sigma}_\mathrm{d}(\omega) = \boldsymbol{\Sigma}_\mathrm{d}^+(\omega) + \boldsymbol{\Sigma}_\mathrm{d}^-(\omega) \tag{1.284}$$

where $\boldsymbol{\Sigma}_\mathrm{d}^+(\omega)$ gives the $(N+1)-$particle energy, also called electron affinity and the $\boldsymbol{\Sigma}_\mathrm{d}^-(\omega)$ part gives the $(N-1)-$particle energy or ionization potential. Again, as we did in Eq. (1.282), we can write the self-energy in a compact diagonal representation as [78]

$$\boldsymbol{\Sigma}_\mathrm{d}^\pm(\omega) = \boldsymbol{m}^{\pm\dagger} \cdot (\omega \mathbf{1} - \boldsymbol{\Omega}^\pm)^{-1} \cdot \boldsymbol{m}^\pm \tag{1.285}$$

where $\boldsymbol{\Omega}^\pm$ are the diagonal matrices of the pole positions and $\boldsymbol{m}^\pm$ are the corresponding matrices of amplitudes. Note that the poles and amplitudes of the self-energy cannot be directly linked to physical quantities[78]. Thus, using the fact that $\boldsymbol{G}_0(\omega)^{-1} = \omega \mathbf{1} - \boldsymbol{\epsilon}$ with $\boldsymbol{\epsilon}$ the diagonal matrix of one-particle orbital energies (here we take Hartee-Fock orbitals as it is done in the original derivation in [76]) and Eq. (1.277), we can write the 1-GF a

$$\boldsymbol{G}(\omega) = \left(\omega \mathbf{1} - \boldsymbol{\epsilon} - \boldsymbol{\Sigma}(\infty) - \boldsymbol{m}^{-\dagger} \cdot (\omega - \boldsymbol{\Omega}^-)^{-1} \cdot \boldsymbol{m}^- - \boldsymbol{m}^{+\dagger} \cdot (\omega - \boldsymbol{\Omega}^+)^{-1} \cdot \boldsymbol{m}^+\right)^{-1} \tag{1.286}$$

This Dyson equation involving a matrix inversion problem is equivalent, when using partitioning techniques, to the eigenvalue problem [76, 78]

$$\boldsymbol{A}\boldsymbol{Q} = \boldsymbol{Q}\boldsymbol{E}, \quad \boldsymbol{Q}\boldsymbol{Q}^\dagger = \mathbf{1} \tag{1.287}$$

with $\boldsymbol{E}$ and $\boldsymbol{Q}$ the diagonal matrix of eigenvalues, *i.e.* the charged excitation energies of the system, and the matrix of eigenvectors, respectively, of matrix $\boldsymbol{A}$ where

$$\boldsymbol{A} = \begin{pmatrix} \boldsymbol{\epsilon} + \boldsymbol{\Sigma}(\infty) & \boldsymbol{m}^{-\dagger} & \boldsymbol{m}^{+\dagger} \\ \boldsymbol{m}^{-} & \boldsymbol{\Omega}^{-} & \boldsymbol{0} \\ \boldsymbol{m}^{+} & \boldsymbol{0} & \boldsymbol{\Omega}^{+} \end{pmatrix} \tag{1.288}$$

One can easily see how to go from the matrix $\boldsymbol{A}$ to the expression of the 1-GF in Eq. (1.286) by doing a matrix-vector multiplication and solving the resulting system of equations (see Appendix A). Note that by expressing $\boldsymbol{\Sigma}_{\mathrm{s}}(\infty)$ in terms of the 1-GF and by using Eq. (1.277) we can self-consistently compute it if an approximation for $\boldsymbol{\Sigma}_{\mathrm{d}}(\omega)$ is given [76]. However, this eigenvalue problem is not very practical because one does not know the expressions of the different blocks in the matrix $\boldsymbol{A}$. This is where the ADC scheme comes into play and it applies to each component of Eq. (1.285) independently. In the following, one drops the subscript s and d in the expression of the self-energy. When one talks about $\boldsymbol{\Sigma}(\omega)$ one refers to the dynamic part and to the static part when one uses $\boldsymbol{\Sigma}(\infty)$. The next step is to postulate that it exists a non-diagonal representation of the self-energy for each of its component

$$\Sigma^{\pm}_{pq}(\omega) = \boldsymbol{V}^{\pm\dagger}_{p} \cdot (\omega \boldsymbol{1} - \boldsymbol{C}^{\pm})^{-1} \cdot \boldsymbol{V}^{\pm}_{q} \tag{1.289}$$

where $\boldsymbol{C}$ is a hermitian matrix referred to as the ADC secular matrix and $\boldsymbol{V}_p$ is a constant vector of effective coupling matrix elements. This gives us the following eigenvalue problem

$$\boldsymbol{B}\boldsymbol{Q} = \boldsymbol{Q}\boldsymbol{E}, \quad \boldsymbol{Q}\boldsymbol{Q}^{\dagger} = \boldsymbol{1} \tag{1.290}$$

where

$$\boldsymbol{B} = \begin{pmatrix} \boldsymbol{\epsilon} + \boldsymbol{\Sigma}(\infty) & \boldsymbol{V}^{-\dagger} & \boldsymbol{V}^{+\dagger} \\ \boldsymbol{V}^{-} & \boldsymbol{C}^{-} & \boldsymbol{0} \\ \boldsymbol{V}^{+} & \boldsymbol{0} & \boldsymbol{C}^{+} \end{pmatrix} \tag{1.291}$$

Then, we suppose that we have the perturbation expansion for the $\boldsymbol{C}$ and $\boldsymbol{V}$ matrices

$$\boldsymbol{C}^{\pm} = \boldsymbol{C}^{(0)\pm} + \boldsymbol{C}^{(1)\pm} + \boldsymbol{C}^{(2)\pm} + \cdots \tag{1.292}$$

$$\boldsymbol{V}^{\pm}_{p} = \boldsymbol{V}^{(1)\pm}_{p} + \boldsymbol{V}^{(2)\pm}_{p} + \cdots \tag{1.293}$$

Note that $\boldsymbol{C}^{(0)\pm}$ is also referred as $\boldsymbol{K}$ in the literature and it is the diagonal matrix of the Hartree-Fock energies of the possible $(N \pm 1)$ electrons configurations ($1p/1h$, $2p$-$1h$, $2h$-$1p$, $3p$-$2h$, ...). The perturbation expansion of $\boldsymbol{V}_p$ starts at first-order because the expansion of the self-energy $\boldsymbol{\Sigma}$ begins at second-order [78]. Then, one uses the perturbation expansions in Eq. (1.292) and Eq. (1.293) in the expression of the self-energy in Eq. (1.289) and one sorts by order [78]. The ADC scheme can be seen as the following procedure, we first compare the formal perturbation expansion of the ADC form to the original diagrammatic perturbation expansion for the (dynamical) self-energy part $\Sigma^{\pm}_{pq}(\omega)$ through a given order n of perturbation theory. This gives the ADC(n) approximation scheme and it allows us to determine the different terms in the expansion of $\boldsymbol{C}$ and $\boldsymbol{V}_p$. At second-order, the ADC form or ADC(2) has the following expression for the self-energy

$$\Sigma^{\pm}_{pq}(\omega) = \boldsymbol{V}^{(1)\pm\dagger}_{p} \cdot (\omega \boldsymbol{1} - \boldsymbol{C}^{(0)\pm})^{-1} \cdot \boldsymbol{V}^{(1)\pm}_{q} \tag{1.294}$$

Note that at the second-order, there is no contribution from the static self-energy and so the upper left block of the matrix $\boldsymbol{B}$ is only the $\boldsymbol{\epsilon}$ matrix [78]. At third-order, the

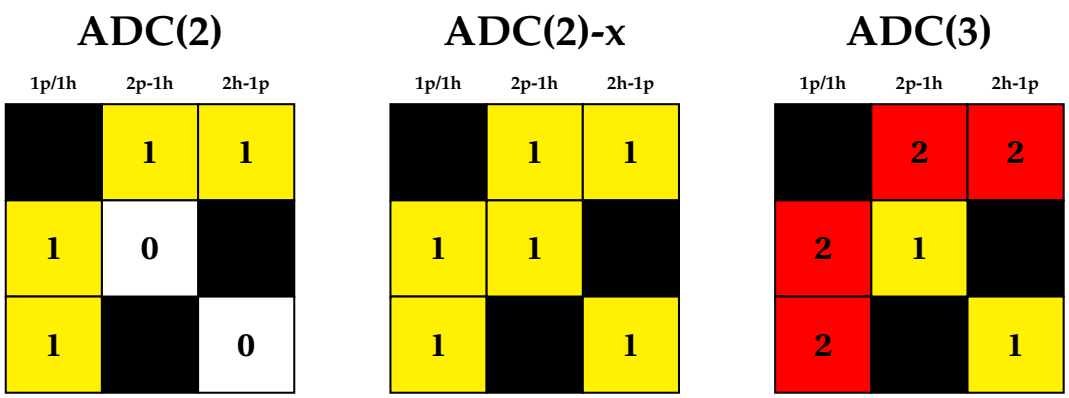

Figure 1.4: Perturbative structure of the matrix $\boldsymbol{B}$ within the Dyson ADC scheme. The black blocks represent the $\boldsymbol{\epsilon}(+\boldsymbol{\Sigma}(\omega))$ and $\mathbf{0}$ blocks. The colour of the blocks represents the order of perturbation theory (white: zeroth-order, yellow: first-order, red: second-order).

ADC(3) scheme gives the subsequent expression

$$\begin{aligned}\Sigma^{\pm}_{pq}(\omega) = \boldsymbol{V}_p^{(1)\pm\dagger} \cdot (\omega\mathbf{1} - \boldsymbol{C}^{(0)\pm})^{-1} \cdot \boldsymbol{V}_q^{(1)\pm} \\ + \boldsymbol{V}_p^{(2)\pm\dagger} \cdot (\omega\mathbf{1} - \boldsymbol{C}^{(0)\pm})^{-1} \cdot \boldsymbol{V}_q^{(1)\pm} + \boldsymbol{V}_p^{(1)\pm\dagger} \cdot (\omega\mathbf{1} - \boldsymbol{C}^{(0)\pm})^{-1} \cdot \boldsymbol{V}_q^{(2)\pm} \\ + \boldsymbol{V}_p^{(1)\pm\dagger} \cdot (\omega\mathbf{1} - \boldsymbol{C}^{(0)\pm})^{-1} \cdot \boldsymbol{C}^{(1)\pm} \cdot (\omega\mathbf{1} - \boldsymbol{C}^{(0)\pm})^{-1} \cdot \boldsymbol{V}_q^{(1)\pm}\end{aligned} \tag{1.295}$$

The ADC(2)-x approximation is an extension of ADC(2) where the diagonal blocks $\boldsymbol{C}^{\pm}$ are evaluated up to first-order where the first-order terms come from the ADC(3) approximation [82, 83]. Note that this approximation does not have a rigorous theoretical justification in perturbation theory and is an *ad hoc* extension of ADC(2). By looking at the expressions of the self-energy approximations, one can get the structure of the matrix $\boldsymbol{B}$ for these three approximations and it is represented in Figure 1.4. Note that for second and third-order, the configuration space comprises $2p$-$1h$ and $2h$-$1p$ configurations but from fourth-order, the space extends to the $3p$-$2h$ and $3h$-$2p$ configurations [76, 78]. Expressions of the blocks $\boldsymbol{C}^{\pm}$ and $\boldsymbol{V}_p^{\pm}$ up to fourth-order are given in Ref. [78]. Now, one takes a brief look at the non-Dyson ADC scheme or direct ADC scheme [80] and this part is highly inspired by Ref. [83]. In this non-Dyson scheme, the charged excitation energies are computed by directly approximating the spectral form of each component of the 1-GF by writing them in a non-diagonal representation [83]

$$\boldsymbol{G}^{\pm}(\omega) = \boldsymbol{T}^{\pm} \cdot \left(\omega\boldsymbol{S}^{\pm} - \boldsymbol{D}^{\pm}\right)^{-1} \cdot \boldsymbol{T}^{\pm} \tag{1.296}$$

where the matrices $\boldsymbol{D}^{\pm}$ and $\boldsymbol{T}^{\pm}$ contain information about vertical charged excitation energies and transition probabilities, respectively, but are expressed in a different (noneigenstate) basis of $(N+1)$- and $(N-1)$-electron configurations $\left|\Psi_{+\mu}\right\rangle$ and $\left|\Psi_{-\mu}\right\rangle$. The $\boldsymbol{S}^{\pm}$ matrices describe the overlap of $(N+1)$- and $(N-1)$-electron basis states within each set and we choose $\left|\Psi_{+\mu}\right\rangle$ and $\left|\Psi_{-\mu}\right\rangle$ such that $\boldsymbol{G}^{+}(\omega)$ and $\boldsymbol{G}^{-}(\omega)$do not couple. Then, the $\boldsymbol{D}^{\pm}$, $\boldsymbol{T}^{\pm}$, and $\boldsymbol{S}^{\pm}$ matrices are evaluated up to the order n in perturbation theory which corresponds to the nth-order non-Dyson ADC approximation ADC(n). Thus, the charged excitation energies are computed as

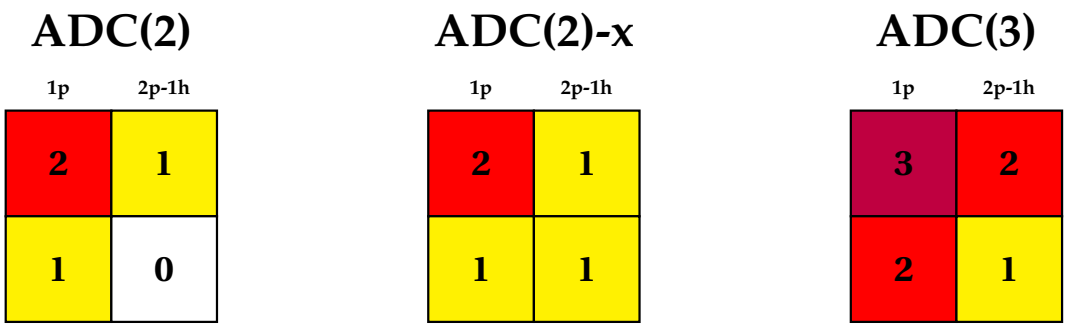

Figure 1.5: Perturbative structure of the matrix $\boldsymbol{D}^{+}$ within the non-Dyson ADC scheme for $\boldsymbol{G}^{+}(\omega)$. Note that in the case of $\boldsymbol{G}^{-}(\omega)$ one has the following space: $1h$ and $2h$-$1p$. The colour of the blocks represents the order of perturbation theory (white: zeroth-order, yellow: first-order, red: second-order, purple: third-order).

eigenvalues of the matrices $\tilde{\boldsymbol{\Omega}}^{\pm}$ given by

$$\boldsymbol{D}^{\pm} \cdot \boldsymbol{Y}^{\pm} = \boldsymbol{S}^{\pm} \cdot \boldsymbol{Y}^{\pm} \cdot \tilde{\boldsymbol{\Omega}}^{\pm} \tag{1.297}$$

Finally, one obtains an approximation for the 1-GF like one had for the self-energy in the Dyson-ADC scheme, and one gets the matrix structure displayed in Figure 1.5. Expressions for the different approximations and for both schemes (Dyson and non-Dyson) are given in the references mentioned in the text.

1.8.4.2 Neutral excitations

The way to compute neutral excitations within the ADC scheme is similar to the one for the computation of charged excitations. The main difference is that we need to start from the polarization propagator [75]. We start by expressing it in the eigenstates of the system [79]

$$\begin{aligned} \Pi_{pq,rs}(\omega) = &\sum_{n\neq 0} \frac{\langle \Psi_0 | \hat{a}_q^{\dagger} \hat{a}_p | \Psi_n \rangle \ \langle \Psi_n | \hat{a}_r^{\dagger} \hat{a}_s | \Psi_0 \rangle}{\omega + E_0^N - E_n^N + i\eta} \\ &+ \sum_{n\neq 0} \frac{\langle \Psi_0 | \hat{a}_r^{\dagger} \hat{a}_s | \Psi_n \rangle \ \langle \Psi_n | \hat{a}_q^{\dagger} \hat{a}_p | \Psi_0 \rangle}{\omega - \left(E_n^N - E_0^N\right) - i\eta} \end{aligned} \tag{1.298}$$

where $|\Psi_0\rangle$ is the ground-state and $|\Psi_n\rangle$ is the n-th excited-state of the N-electron system with their corresponding energies E_0^N and E_n^N. Note that, the polarization propagator can also be written as the sum of two terms $\boldsymbol{\Pi}(\omega) = \boldsymbol{\Pi}^{+}(\omega) + \boldsymbol{\Pi}^{-}(\omega)$. Simply by looking at the expression of the polarization propagator, we can see that the same physical information is given by each of these parts and so it is necessary to only look at one of them. Thus, by choosing $\boldsymbol{\Pi}^{+}(\omega)$, the neutral excitation energies $\Delta E = E_n^N - E_0^N$ are given by its poles. In what follows, we drop the superscript $+$ for more clarity. Moreover, as it is not important for further development, we also drop the infinitesimal number η. As we have done for the case of charged excitations, we can write the propagator in a compact matrix diagonal representation as [79]

$$\boldsymbol{\Pi}(\omega) = \boldsymbol{x}^{\dagger} \cdot (\omega \mathbf{1} - \boldsymbol{\Omega})^{-1} \cdot \boldsymbol{x} \tag{1.299}$$

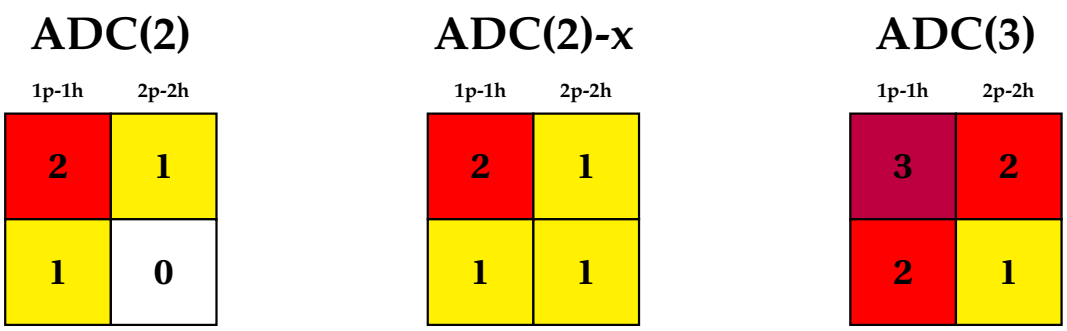

Figure 1.6: Perturbative structure of the matrix $\boldsymbol{M}$. The colour of the blocks represents the order of perturbation theory (white: zeroth-order, yellow: first-order, red: second-order, purple: third-order).

where $\boldsymbol{\Omega}$ is the diagonal matrix of vertical excitation energies and $\boldsymbol{x}$ is the matrix of transition amplitudes. Then, we postulate its non-diagonal representation [75, 79]

$$\boldsymbol{\Pi}(\omega) = \boldsymbol{f}^{\dagger} \cdot (\omega \mathbf{1} - \boldsymbol{M})^{-1} \cdot \boldsymbol{f} \tag{1.300}$$

where $\boldsymbol{M}$ is the non-diagonal matrix representation of an effective Hamiltonian and $\boldsymbol{f}$ is the matrix of the effective transition moments [75, 79]. Again, we can do a perturbation expansion for the different terms as

$$\boldsymbol{M} = \boldsymbol{M}^{(0)} + \boldsymbol{M}^{(1)} + \boldsymbol{M}^{(2)} + \cdots \tag{1.301}$$

$$\boldsymbol{f} = \boldsymbol{f}^{(0)} + \boldsymbol{f}^{(1)} + \boldsymbol{f}^{(2)} + \cdots \tag{1.302}$$

and the matrix inversion of Eq. (1.300) is equivalent to the diagonalization of the matrix $\boldsymbol{M}$ at a desired order of perturbation theory [79]. This gives us the following eigenvalue problem

$$\boldsymbol{M} \cdot \boldsymbol{Y} = \boldsymbol{Y} \cdot \boldsymbol{\Omega}, \quad \boldsymbol{Y}\boldsymbol{Y}^{\dagger} = \mathbf{1} \tag{1.303}$$

where $\boldsymbol{\Omega}$ is the diagonal matrix of vertical excitation energies with the corresponding matrix of eigenvectors $\boldsymbol{Y}$. As we did in the case of charged excitations, we can arrange the different blocks of the matrix $\boldsymbol{M}$ and it gives the matrix structure displayed in Figure 1.6. One can note that at the ADC(2) level, the $1p$-$1h$ block contains terms up to second-order whereas the $2p$-$2h$ block has only zeroth-order terms. It means that single excitations are described using second-order terms while double excitations are only described by energy differences within the ADC(2) approximation. At third-order, the $2p$-$2h$ block contains couplings between the excited configurations [84]. Again, these couplings are included in ADC(2)-x as an *ad hoc* extension of ADC(2) with, as one will see in the next chapters, very mitigated results. Again, expressions for the different approximations are given in the references mentioned in the text. Note that links between ADC and other approximations in the Green's function formalism for charged and neutral excitations will be discussed in Chapter 5.

Chapter 2

Spin-conserved and spin-flip optical excitations from the Bethe-Salpeter equation formalism

This chapter is the subject of the following publication: E. Monino and P. F. Loos. *J. Chem. Theory Comput. (Open Access)* **17**, 2852 (2021).

Like adiabatic time-dependent density-functional theory (TD-DFT), the Bethe-Salpeter equation (BSE) formalism of many-body perturbation theory, in its static approximation, is "blind" to double (and higher) excitations, which are ubiquitous, for example, in conjugated molecules like polyenes. Here, we apply the spin-flip *ansatz* (which considers the lowest triplet state as the reference configuration instead of the singlet ground state) to the BSE formalism in order to access, in particular, double excitations. The present scheme is based on a spin-unrestricted version of the *GW* approximation employed to compute the charged excitations and screened Coulomb potential required for the BSE calculations. Dynamical corrections to the static BSE optical excitations are taken into account via an unrestricted generalization of our recently developed (renormalized) perturbative treatment. The performance of the present spin-flip BSE formalism is illustrated by computing excited-state energies of the beryllium atom, the hydrogen molecule at various bond lengths, and cyclobutadiene in its rectangular and square-planar geometries. Note that in this chapter we use chemist's notation for the two-electron integrals.

Due to the ubiquitous influence of processes involving electronic excited states in physics, chemistry, and biology, their faithful description from first principles has been one of the grand challenges faced by theoretical chemists since the dawn of computational chemistry. Accurately predicting ground- and excited-state energies (hence excitation energies) is particularly valuable in this context, and it has concentrated most of the efforts within the community. An armada of theoretical and computational methods have been developed to this end, each of them being plagued by its own flaws [25, 58, 85–94]. The fact that none of these methods is successful in every chemical scenario has encouraged chemists to carry on the development of new excited-state methodologies, their main goal being to get the most accurate excitation energies (and properties) at the lowest possible computational cost in the most general context [93].

Originally developed in the framework of nuclear physics [95], and popularized in condensed-matter physics [18, 96, 97], one of the new emerging method in the computational chemistry landscape is the Bethe-Salpeter equation (BSE) formalism [19, 25, 26, 95, 98–101] from many-body perturbation theory [102, 103] which, based on an underlying *GW* calculation to compute accurate charged excitations (*i.e.*, ionization potentials and electron affinities) and the dynamically-screened Coulomb potential [17, 104], is able to provide accurate optical (*i.e.*, neutral) excitations for molecular systems at a rather modest computational cost [25–27, 105–121]. Most of BSE implementations rely on the so-called static approximation [26, 117, 119, 122], which approximates the dynamical (*i.e.*, frequency-dependent) BSE kernel by its static limit. Like adiabatic time-dependent density-functional theory (TD-DFT) [65, 67–69], the static BSE formalism is plagued by the lack of double (and higher) excitations, which are, for example, ubiquitous in conjugated molecules like polyenes [123–130] or the ground state of open-shell molecules [131–133]. Indeed, both adiabatic TD-DFT [134–138] and static BSE [29, 139–142] can only access (singlet and triplet) single excitations with respect to the reference determinant usually taken as the closed-shell singlet ground state. Double excitations are even challenging for state-of-the-art methods [93, 130, 143–145], like the approximate third-order coupled-cluster (CC3) method [146, 147] or equation-of-motion coupled-cluster with singles, doubles and triples (EOM-CCSDT) [148–151].

One way to access double excitations is via the spin-flip formalism established by Krylov in 2001 [152–154], with earlier attempts by Bethe [155], as well as Shibuya and McKoy [156]. The idea behind the spin-flip *ansatz* is rather simple: instead of considering the singlet ground state as reference, the reference configuration is taken as the lowest triplet state. In such a way, one can access the singlet ground state and the singlet doubly-excited state via a spin-flip deexcitation and excitation (respectively), the difference of these two excitation energies providing an estimate of the double excitation. We refer the interested reader to Refs. [87, 94, 157] for detailed reviews on spin-flip methods. Note that a similar idea has been exploited by the group of Yang to access double excitations in the context of the particle-particle random-phase approximation [64, 158–162].

One obvious issue of spin-flip methods is that not all double excitations are accessible in such a way. Moreover, spin-flip methods are usually hampered by spin contamination [94] (*i.e.*, artificial mixing with configurations of different spin multiplicities) due to spin incompleteness of the configuration interaction expansion as well as the possible spin contamination of the reference configuration [163]. This issue can be alleviated by increasing the excitation order at a significant cost or by selectively complementing the spin-incomplete configuration set with the missing configurations [164–171].

Nowadays, spin-flip techniques are widely available for many types of methods such as equation-of-motion coupled cluster (EOM-CC) [152, 172–175], configuration interaction (CI) [153, 154, 165, 176, 177], TD-DFT [168, 170, 178–180], the algebraic-diagrammatic construction (ADC) scheme [181, 182], and others [183–186] with successful applications in bond breaking processes [187], radical chemistry [188–195], and photochemistry in general [182, 196–198] to mention a few.

Here we apply the spin-flip technique to the BSE formalism in order to access, in particular, double excitations [142], but not only. The present BSE calculations are based on the spin-unrestricted version of both *GW* (Sec. 2.1) and BSE (Sec. 2.2). To the best of our knowledge, the present study is the first to apply the spin-flip formalism to the BSE method. Moreover, we also go beyond the static approximation by taking into account dynamical effects (Sec. 2.2.2) via an unrestricted generalization

of our recently developed (renormalized) perturbative correction which builds on the seminal work of Strinati [18, 19, 199], Romaniello and collaborators [140, 141], and Rohlfing and coworkers [200–204]. We also discuss the computation of oscillator strengths (Sec. 2.2.3) and the expectation value of the spin operator $\langle \hat{S}^2 \rangle$ as a diagnostic of the spin contamination for both ground and excited states (Sec. 2.2.4). Computational details are reported in Sec. 2.3 and our results for the beryllium atom Be (Subsec. 2.4.1), the hydrogen molecule H_2 (Subsec. 2.4.2), and cyclobutadiene C_4H_4 (Subsec. 2.4.3) are discussed in Sec. 2.4. Finally, we draw our conclusions in Sec. 2.5. Unless otherwise stated, atomic units are used.

2.1 Unrestricted *GW* formalism

Let us consider an electronic system consisting of $n = n_\uparrow + n_\downarrow$ electrons (where $n_\uparrow$ and $n_\downarrow$ are the number of spin-up and spin-down electrons, respectively) and N one-electron basis functions. The number of spin-up and spin-down occupied orbitals are $O_\uparrow = n_\uparrow$ and $O_\downarrow = n_\downarrow$, respectively, and, assuming the absence of linear dependencies in the one-electron basis set, there is $V_\uparrow = N - O_\uparrow$ and $V_\downarrow = N - O_\downarrow$ spin-up and spin-down virtual (*i.e.*, unoccupied) orbitals. The number of spin-conserved (sc) single excitations is then $S^{\text{sc}} = S^{\text{sc}}_{\uparrow\uparrow} + S^{\text{sc}}_{\downarrow\downarrow} = O_\uparrow V_\uparrow + O_\downarrow V_\downarrow$, while the number of spin-flip (sf) excitations is $S^{\text{sf}} = S^{\text{sf}}_{\uparrow\downarrow} + S^{\text{sf}}_{\downarrow\uparrow} = O_\uparrow V_\downarrow + O_\downarrow V_\uparrow$. Let us denote as $\psi_{p_\sigma}(\boldsymbol{r})$ the pth spatial orbital associated with the spin-σ electrons (where $\sigma = \uparrow$ or $\downarrow$) and ε_{p_σ} its one-electron energy. It is important to understand that, in a spin-conserved excitation the hole orbital ψ_{i_σ} and particle orbital ψ_{a_σ} have the same spin σ. In a spin-flip excitation, the hole and particle states, ψ_{i_σ} and $\psi_{a_{\bar{\sigma}}}$, have opposite spins, σ and $\bar{\sigma}$. We assume real quantities throughout this manuscript, i and j are occupied orbitals, a and b are unoccupied orbitals, p, q, r, and s indicate arbitrary orbitals, and m labels single excitations. Moreover, we consider systems with collinear spins and a spin-independent Hamiltonian without contributions such as spin-orbit interaction.

2.1.1 The dynamical screening

The pillar of Green's function many-body perturbation theory is the (time-ordered) one-body Green's function, which has poles at the charged excitations (i.e., ionization potentials and electron affinities) of the system [139]. The spin-σ component of the one-body Green's function reads [122, 139]

$$G^\sigma(\boldsymbol{r}_1, \boldsymbol{r}_2; \omega) = \sum_i \frac{\psi_{i_\sigma}(\boldsymbol{r}_1)\psi_{i_\sigma}(\boldsymbol{r}_2)}{\omega - \varepsilon_{i_\sigma} - i\eta} + \sum_a \frac{\psi_{a_\sigma}(\boldsymbol{r}_1)\psi_{a_\sigma}(\boldsymbol{r}_2)}{\omega - \varepsilon_{a_\sigma} + i\eta} \tag{2.1}$$

where η is a positive infinitesimal. As readily seen in Eq. (2.1), the Green's function can be evaluated at different levels of theory depending on the choice of orbitals and energies, ψ_{p_σ} and ε_{p_σ}. For example, G^σ_{KS} is the independent-particle Green's function built with Kohn-Sham (KS) orbitals $\psi^{\text{KS}}_{p_\sigma}(\boldsymbol{r})$ and one-electron energies $\varepsilon^{\text{KS}}_{p_\sigma}$ [40, 41, 205]. Within self-consistent schemes, these quantities can be replaced by quasiparticle energies and orbitals evaluated within the *GW* approximation (see below) [17, 104].

Based on the spin-up and spin-down components of G defined in Eq. (2.1), one can easily compute the non-interacting polarizability (which is a sum over spins)

$$\chi_0(\boldsymbol{r}_1, \boldsymbol{r}_2; \omega) = -\frac{i}{2\pi} \sum_\sigma \int G^\sigma(\boldsymbol{r}_1, \boldsymbol{r}_2; \omega + \omega') G^\sigma(\boldsymbol{r}_1, \boldsymbol{r}_2; \omega') d\omega' \tag{2.2}$$

and subsequently the dielectric function

$$\epsilon(\boldsymbol{r}_1, \boldsymbol{r}_2; \omega) = \delta(\boldsymbol{r}_1 - \boldsymbol{r}_2) - \int \frac{\chi_0(\boldsymbol{r}_1, \boldsymbol{r}_3; \omega)}{|\boldsymbol{r}_2 - \boldsymbol{r}_3|} d\boldsymbol{r}_3 \tag{2.3}$$

where $\delta(\boldsymbol{r})$ is the Dirac delta function. Based on this latter ingredient, one can access the dynamically-screened Coulomb potential

$$W(\boldsymbol{r}_1, \boldsymbol{r}_2; \omega) = \int \frac{\epsilon^{-1}(\boldsymbol{r}_1, \boldsymbol{r}_3; \omega)}{|\boldsymbol{r}_2 - \boldsymbol{r}_3|} d\boldsymbol{r}_3 \tag{2.4}$$

which is naturally spin independent as the bare Coulomb interaction $|\boldsymbol{r}_1 - \boldsymbol{r}_2|^{-1}$ does not depend on spin coordinates.

Within the GW formalism [17, 102, 104], the dynamical screening is computed at the random-phase approximation (RPA) level by considering only the manifold of the spin-conserved neutral excitations. In the orbital basis, the spectral representation of W is

$$W_{p_\sigma q_\sigma, r_{\sigma'} s_{\sigma'}}(\omega) = (p_\sigma q_\sigma | r_{\sigma'} s_{\sigma'}) + \sum_m (p_\sigma q_\sigma | m)(r_{\sigma'} s_{\sigma'} | m) \times \left[\frac{1}{\omega - \Omega_m^{\mathrm{sc,RPA}} + i\eta} - \frac{1}{\omega + \Omega_m^{\mathrm{sc,RPA}} - i\eta} \right] \tag{2.5}$$

where the bare two-electron integrals are [206]

$$(p_\sigma q_\tau | r_{\sigma'} s_{\tau'}) = \int \frac{\psi_{p_\sigma}(\boldsymbol{r}_1) \psi_{q_\tau}(\boldsymbol{r}_1) \psi_{r_{\sigma'}}(\boldsymbol{r}_2) \psi_{s_{\tau'}}(\boldsymbol{r}_2)}{|\boldsymbol{r}_1 - \boldsymbol{r}_2|} d\boldsymbol{r}_1 d\boldsymbol{r}_2 \tag{2.6}$$

and the screened two-electron integrals (or spectral weights) are explicitly given by

$$(p_\sigma q_\sigma | m) = \sum_{ia\sigma'} (p_\sigma q_\sigma | i_{\sigma'} a_{\sigma'}) (\mathbf{X}_m^{\mathrm{sc,RPA}} + \mathbf{Y}_m^{\mathrm{sc,RPA}})_{i_{\sigma'} a_{\sigma'}} \tag{2.7}$$

In Eqs. (2.5) and (2.7), the spin-conserved RPA neutral excitations $\Omega_m^{\mathrm{sc,RPA}}$ and their corresponding eigenvectors, $\mathbf{X}_m^{\mathrm{sc,RPA}}$ and $\mathbf{Y}_m^{\mathrm{sc,RPA}}$, are obtained by solving a linear response system of the form

$$\begin{pmatrix} \mathbf{A} & \mathbf{B} \\ -\mathbf{B} & -\mathbf{A} \end{pmatrix} \cdot \begin{pmatrix} \mathbf{X}_m \\ \mathbf{Y}_m \end{pmatrix} = \Omega_m \begin{pmatrix} \mathbf{X}_m \\ \mathbf{Y}_m \end{pmatrix} \tag{2.8}$$

where the expressions of the matrix elements of $\mathbf{A}$ and $\mathbf{B}$ are specific of the method and of the spin manifold. The spin structure of these matrices, though, is general

$$\mathbf{A}^{\mathrm{sc}} = \begin{pmatrix} \mathbf{A}^{\uparrow\uparrow,\uparrow\uparrow} & \mathbf{A}^{\uparrow\uparrow,\downarrow\downarrow} \\ \mathbf{A}^{\downarrow\downarrow,\uparrow\uparrow} & \mathbf{A}^{\downarrow\downarrow,\downarrow\downarrow} \end{pmatrix} \qquad \mathbf{B}^{\mathrm{sc}} = \begin{pmatrix} \mathbf{B}^{\uparrow\uparrow,\uparrow\uparrow} & \mathbf{B}^{\uparrow\uparrow,\downarrow\downarrow} \\ \mathbf{B}^{\downarrow\downarrow,\uparrow\uparrow} & \mathbf{B}^{\downarrow\downarrow,\downarrow\downarrow} \end{pmatrix} \tag{2.9a}$$

$$\mathbf{A}^{\mathrm{sf}} = \begin{pmatrix} \mathbf{A}^{\uparrow\downarrow,\uparrow\downarrow} & \mathbf{0} \\ \mathbf{0} & \mathbf{A}^{\downarrow\uparrow,\downarrow\uparrow} \end{pmatrix} \qquad \mathbf{B}^{\mathrm{sf}} = \begin{pmatrix} \mathbf{0} & \mathbf{B}^{\uparrow\downarrow,\downarrow\uparrow} \\ \mathbf{B}^{\downarrow\uparrow,\uparrow\downarrow} & \mathbf{0} \end{pmatrix} \tag{2.9b}$$

In the absence of instabilities, the linear eigenvalue problem (2.8) has particle-hole symmetry which means that the eigenvalues are obtained by pairs $\pm\Omega_m$. In such a case, $(\mathbf{A} - \mathbf{B})^{1/2}$ is positive definite, and Eq. (2.8) can be recast as a Hermitian

problem of half its original dimension

$$(\mathbf{A}-\mathbf{B})^{1/2}\cdot(\mathbf{A}+\mathbf{B})\cdot(\mathbf{A}-\mathbf{B})^{1/2}\cdot\mathbf{Z}=\boldsymbol{\Omega}^2\cdot\mathbf{Z} \tag{2.10}$$

where the excitation amplitudes are

$$\mathbf{X}+\mathbf{Y}=\boldsymbol{\Omega}^{-1/2}\cdot(\mathbf{A}-\mathbf{B})^{1/2}\cdot\mathbf{Z} \tag{2.11}$$

Within the Tamm-Dancoff approximation (TDA), the coupling terms between the resonant and anti-resonant parts, $\mathbf{A}$ and $-\mathbf{A}$, are neglected, which consists in setting $\mathbf{B}=\mathbf{0}$. In such a case, Eq. (2.8) reduces to a straightforward Hermitian problem of the form:

$$\mathbf{A}\cdot\mathbf{X}_m=\Omega_m\mathbf{X}_m \tag{2.12}$$

Note that, for spin-flip excitations, it is quite common to enforce the TDA especially when one considers a triplet reference as the first "excited-state" is usually the ground state of the closed-shell system (hence, corresponding to a negative excitation energy).

At the RPA level, the matrix elements of $\mathbf{A}$ and $\mathbf{B}$ are

$$A^{\mathrm{RPA}}_{i_\sigma a_\tau, j_{\sigma'} b_{\tau'}}=\delta_{ij}\delta_{ab}\delta_{\sigma\sigma'}\delta_{\tau\tau'}(\varepsilon_{a_\tau}-\varepsilon_{i_\sigma})+(i_\sigma a_\tau|b_{\sigma'}j_{\tau'}) \tag{2.13a}$$

$$B^{\mathrm{RPA}}_{i_\sigma a_\tau, j_{\sigma'} b_{\tau'}}=(i_\sigma a_\tau|j_{\sigma'}b_{\tau'}) \tag{2.13b}$$

from which we obtain the following expressions

$$A^{\mathrm{sc,RPA}}_{i_\sigma a_\sigma, j_{\sigma'} b_{\sigma'}}=\delta_{ij}\delta_{ab}\delta_{\sigma\sigma'}(\varepsilon_{a_\sigma}-\varepsilon_{i_\sigma})+(i_\sigma a_\sigma|b_{\sigma'}j_{\sigma'}) \tag{2.14a}$$

$$B^{\mathrm{sc,RPA}}_{i_\sigma a_\sigma, j_{\sigma'} b_{\sigma'}}=(i_\sigma a_\sigma|j_{\sigma'}b_{\sigma'}) \tag{2.14b}$$

for the spin-conserved excitations and

$$A^{\mathrm{sf,RPA}}_{i_\sigma a_{\bar\sigma}, j_{\bar\sigma} b_{\bar\sigma}}=\delta_{ij}\delta_{ab}(\varepsilon_{a_{\bar\sigma}}-\varepsilon_{i_\sigma}) \tag{2.15a}$$

$$B^{\mathrm{sf,RPA}}_{i_\sigma a_{\bar\sigma}, j_{\bar\sigma} b_\sigma}=0 \tag{2.15b}$$

for the spin-flip excitations.

2.1.2 The *GW* self-energy

Within the acclaimed *GW* approximation [17, 104], the exchange-correlation (xc) part of the self-energy

$$\begin{aligned}\Sigma^{\mathrm{xc},\sigma}(\boldsymbol{r}_1,\boldsymbol{r}_2;\omega)&=\Sigma^{\mathrm{x},\sigma}(\boldsymbol{r}_1,\boldsymbol{r}_2)+\Sigma^{\mathrm{c},\sigma}(\boldsymbol{r}_1,\boldsymbol{r}_2;\omega)\\&=\frac{i}{2\pi}\int G^\sigma(\boldsymbol{r}_1,\boldsymbol{r}_2;\omega+\omega')W(\boldsymbol{r}_1,\boldsymbol{r}_2;\omega')e^{i\eta\omega'}d\omega'\end{aligned} \tag{2.16}$$

is, like the one-body Green's function, spin-diagonal, and its spectral representation reads

$$\Sigma^{\mathrm{x}}_{p_\sigma q_\sigma} = -\sum_i (p_\sigma i_\sigma | i_\sigma q_\sigma) \tag{2.17a}$$

$$\begin{aligned}\Sigma^{\mathrm{c}}_{p_\sigma q_\sigma}(\omega) = &\sum_{im} \frac{(p_\sigma i_\sigma|m)(q_\sigma i_\sigma|m)}{\omega - \varepsilon_{i_\sigma} + \Omega^{\mathrm{sc,RPA}}_m - i\eta} \\ &+ \sum_{am} \frac{(p_\sigma a_\sigma|m)(q_\sigma a_\sigma|m)}{\omega - \varepsilon_{a_\sigma} - \Omega^{\mathrm{sc,RPA}}_m + i\eta}\end{aligned} \tag{2.17b}$$

where the self-energy has been split in its exchange (x) and correlation (c) contributions. The Dyson equation linking the Green's function and the self-energy holds separately for each spin component

$$\begin{aligned}[G^\sigma(\boldsymbol{r}_1, \boldsymbol{r}_2; \omega)]^{-1} = &[G^\sigma_{\mathrm{KS}}(\boldsymbol{r}_1, \boldsymbol{r}_2; \omega)]^{-1} \\ &+ \Sigma^{\mathrm{xc},\sigma}(\boldsymbol{r}_1, \boldsymbol{r}_2; \omega) - v^{\mathrm{xc}}(\boldsymbol{r}_1)\delta(\boldsymbol{r}_1 - \boldsymbol{r}_2)\end{aligned} \tag{2.18}$$

where $v^{\mathrm{xc}}(\boldsymbol{r})$ is the KS (local) exchange-correlation potential. The target quantities here are the quasiparticle energies $\varepsilon^{GW}_{p_\sigma}$, *i.e.*, the poles of G [see Eq. (2.1)], which correspond to well-defined addition/removal energies (unlike the KS orbital energies). Because the exchange-correlation part of the self-energy is, itself, constructed with the Green's function [see Eq. (2.16)], the present process is, by nature, self-consistent. The same comment applies to the dynamically-screened Coulomb potential W entering the definition of Σ^{xc} [see Eq. (2.16)] which is also constructed from G [see Eqs. (2.2), (2.3), and (2.4)].

2.1.3 Level of self-consistency

This is where GW schemes differ. In its simplest perturbative (*i.e.*, one-shot) version, known as G_0W_0 [207–215], a single iteration is performed, and the quasiparticle energies $\varepsilon^{GW}_{p_\sigma}$ are obtained by solving the frequency-dependent quasiparticle equation

$$\omega = \varepsilon^{\mathrm{KS}}_{p_\sigma} + \Sigma^{\mathrm{xc}}_{p_\sigma}(\omega) - V^{\mathrm{xc}}_{p_\sigma} \tag{2.19}$$

where $\Sigma^{\mathrm{xc}}_{p_\sigma}(\omega) \equiv \Sigma^{\mathrm{xc}}_{p_\sigma p_\sigma}(\omega)$ and its offspring quantities have been constructed at the KS level, and

$$V^{\mathrm{xc}}_{p_\sigma} = \int \psi_{p_\sigma}(\boldsymbol{r}) v^{\mathrm{xc}}(\boldsymbol{r}) \psi_{p_\sigma}(\boldsymbol{r}) d\boldsymbol{r} \tag{2.20}$$

Because, from a practical point of view, one is usually interested by the so-called quasiparticle solution (or peak), the quasiparticle equation (2.19) is often linearized around $\omega = \varepsilon^{\mathrm{KS}}_{p_\sigma}$, yielding

$$\varepsilon^{GW}_{p_\sigma} = \varepsilon^{\mathrm{KS}}_{p_\sigma} + Z_{p_\sigma}[\Sigma^{\mathrm{xc}}_{p_\sigma}(\varepsilon^{\mathrm{KS}}_{p_\sigma}) - V^{\mathrm{xc}}_{p_\sigma}] \tag{2.21}$$

where

$$Z_{p_\sigma} = \left[1 - \left.\frac{\partial \Sigma^{\mathrm{xc}}_{p_\sigma}(\omega)}{\partial \omega}\right|_{\omega = \varepsilon^{\mathrm{KS}}_{p_\sigma}}\right]^{-1} \tag{2.22}$$

is a renormalization factor (with $0 \leq Z_{p_\sigma} \leq 1$) which also represents the spectral weight of the quasiparticle solution. In addition to the principal quasiparticle peak

which, in a well-behaved case, contains most of the spectral weight, the frequency-dependent quasiparticle equation (2.19) generates a finite number of satellite resonances with smaller weights [216].

Within the "eigenvalue" self-consistent GW scheme (known as evGW) [118, 209, 215, 217–219], several iterations are performed during which only the one-electron energies entering the definition of the Green's function [see Eq. (2.1)] are updated by the quasiparticle energies obtained at the previous iteration (the corresponding orbitals remain evaluated at the KS level).

Finally, within the quasiparticle self-consistent GW (qsGW) scheme [220–224], both the one-electron energies and the orbitals are updated until convergence is reached. These are obtained via the diagonalization of an effective Fock matrix which includes explicitly a frequency-independent and Hermitian self-energy defined as

$$\tilde{\Sigma}^{\mathrm{xc}}_{p_\sigma q_\sigma} = \frac{1}{2}\left[\Sigma^{\mathrm{xc}}_{p_\sigma q_\sigma}(\varepsilon_{p_\sigma}) + \Sigma^{\mathrm{xc}}_{q_\sigma p_\sigma}(\varepsilon_{p_\sigma})\right] \tag{2.23}$$

2.2 Unrestricted Bethe-Salpeter equation formalism

Like its TD-DFT cousin [58, 65, 67, 68], the BSE formalism [19, 95, 98–101] deals with the calculation of (neutral) optical excitations as measured by absorption spectroscopy [105–118] . Using the BSE formalism, one can access the spin-conserved and spin-flip excitations. In a nutshell, BSE builds on top of a GW calculation by adding up excitonic effects (*i.e.*, the electron-hole binding energy) to the GW fundamental gap which is itself a corrected version of the KS gap. The purpose of the underlying GW calculation is to provide quasiparticle energies and a dynamically-screened Coulomb potential that are used to build the BSE Hamiltonian from which the vertical excitations of the system are extracted.

2.2.1 Static approximation

Within the so-called static approximation of BSE, the Dyson equation that links the generalized four-point susceptibility $L^{\sigma\sigma'}(\boldsymbol{r}_1, \boldsymbol{r}_2; \boldsymbol{r}'_1, \boldsymbol{r}'_2; \omega)$ and the BSE kernel $\Xi^{\sigma\sigma'}(\boldsymbol{r}_3, \boldsymbol{r}_5; \boldsymbol{r}_4, \boldsymbol{r}_6)$ is [122, 139]

$$\begin{aligned} L^{\sigma\sigma'}(\boldsymbol{r}_1, \boldsymbol{r}_2; \boldsymbol{r}'_1, \boldsymbol{r}'_2; \omega) = {} & L_0^{\sigma\sigma'}(\boldsymbol{r}_1, \boldsymbol{r}_2; \boldsymbol{r}'_1, \boldsymbol{r}'_2; \omega) \\ & + \int L_0^{\sigma\sigma'}(\boldsymbol{r}_1, \boldsymbol{r}_4; \boldsymbol{r}'_1, \boldsymbol{r}_3; \omega)\Xi^{\sigma\sigma'}(\boldsymbol{r}_3, \boldsymbol{r}_5; \boldsymbol{r}_4, \boldsymbol{r}_6) \\ & \times L^{\sigma\sigma'}(\boldsymbol{r}_6, \boldsymbol{r}_2; \boldsymbol{r}_5, \boldsymbol{r}'_2; \omega) d\boldsymbol{r}_3 d\boldsymbol{r}_4 d\boldsymbol{r}_5 d\boldsymbol{r}_6 \end{aligned} \tag{2.24}$$

where

$$L_0^{\sigma\sigma'}(\boldsymbol{r}_1, \boldsymbol{r}_2; \boldsymbol{r}'_1, \boldsymbol{r}'_2; \omega) = \frac{1}{2\pi}\int G^{\sigma}(\boldsymbol{r}_1, \boldsymbol{r}'_2; \omega + \omega')G^{\sigma'}(\boldsymbol{r}'_1, \boldsymbol{r}_2; \omega')d\omega' \tag{2.25}$$

is the non-interacting analog of the two-particle correlation function L.

Within the GW approximation, the static BSE kernel is

$$i\Xi^{\sigma\sigma'}(\boldsymbol{r}_3, \boldsymbol{r}_5; \boldsymbol{r}_4, \boldsymbol{r}_6) = \frac{\delta(\boldsymbol{r}_3 - \boldsymbol{r}_4)\delta(\boldsymbol{r}_5 - \boldsymbol{r}_6)}{|\boldsymbol{r}_3 - \boldsymbol{r}_6|} - \delta_{\sigma\sigma'}W(\boldsymbol{r}_3, \boldsymbol{r}_4; \omega = 0)\delta(\boldsymbol{r}_3 - \boldsymbol{r}_6)\delta(\boldsymbol{r}_4 - \boldsymbol{r}_6) \tag{2.26}$$

where, as usual, we have not considered the higher-order terms in W by neglecting the derivative $\delta W/\delta G$ [18, 19, 199, 225].

As readily seen in Eq. (2.26), the static approximation consists in neglecting the frequency dependence of the dynamically-screened Coulomb potential. In this case, the spin-conserved and spin-flip BSE optical excitations are obtained by solving the usual Casida-like linear response (eigen)problem:

$$\begin{pmatrix} \mathbf{A}^{\mathrm{BSE}} & \mathbf{B}^{\mathrm{BSE}} \\ -\mathbf{B}^{\mathrm{BSE}} & -\mathbf{A}^{\mathrm{BSE}} \end{pmatrix} \cdot \begin{pmatrix} \mathbf{X}_m^{\mathrm{BSE}} \\ \mathbf{Y}_m^{\mathrm{BSE}} \end{pmatrix} = \Omega_m^{\mathrm{BSE}} \begin{pmatrix} \mathbf{X}_m^{\mathrm{BSE}} \\ \mathbf{Y}_m^{\mathrm{BSE}} \end{pmatrix} \tag{2.27}$$

Defining the elements of the static screening as $W^{\mathrm{stat}}_{p_\sigma q_\sigma, r_{\sigma'} s_{\sigma'}} = W_{p_\sigma q_\sigma, r_{\sigma'} s_{\sigma'}}(\omega = 0)$, the general expressions of the BSE matrix elements are

$$A^{\mathrm{BSE}}_{i_\sigma a_\tau, j_{\sigma'} b_{\tau'}} = A^{\mathrm{RPA}}_{i_\sigma a_\tau, j_{\sigma'} b_{\tau'}} - \delta_{\sigma\sigma'} W^{\mathrm{stat}}_{i_\sigma j_{\sigma'}, b_{\tau'} a_\tau} \tag{2.28a}$$

$$B^{\mathrm{BSE}}_{i_\sigma a_\tau, j_{\sigma'} b_{\tau'}} = B^{\mathrm{RPA}}_{i_\sigma a_\tau, j_{\sigma'} b_{\tau'}} - \delta_{\sigma\sigma'} W^{\mathrm{stat}}_{i_\sigma b_{\tau'}, j_{\sigma'} a_\tau} \tag{2.28b}$$

from which we obtain the following expressions for the spin-conserved and spin-flip BSE excitations:

$$A^{\mathrm{sc,BSE}}_{i_\sigma a_\sigma, j_{\sigma'} b_{\sigma'}} = A^{\mathrm{sc,RPA}}_{i_\sigma a_\sigma, j_{\sigma'} b_{\sigma'}} - \delta_{\sigma\sigma'} W^{\mathrm{stat}}_{i_\sigma j_{\sigma'}, b_{\sigma'} a_\sigma} \tag{2.29a}$$

$$B^{\mathrm{sc,BSE}}_{i_\sigma a_\sigma, j_{\sigma'} b_{\sigma'}} = B^{\mathrm{sc,RPA}}_{i_\sigma a_\sigma, j_{\sigma'} b_{\sigma'}} - \delta_{\sigma\sigma'} W^{\mathrm{stat}}_{i_\sigma b_{\sigma'}, j_{\sigma'} a_\sigma} \tag{2.29b}$$

$$A^{\mathrm{sf,BSE}}_{i_\sigma a_{\bar{\sigma}}, j_\sigma b_{\bar{\sigma}}} = A^{\mathrm{sf,RPA}}_{i_\sigma a_{\bar{\sigma}}, j_\sigma b_{\bar{\sigma}}} - W^{\mathrm{stat}}_{i_\sigma j_\sigma, b_{\bar{\sigma}} a_{\bar{\sigma}}} \tag{2.29c}$$

$$B^{\mathrm{sf,BSE}}_{i_\sigma a_{\bar{\sigma}}, j_{\bar{\sigma}} b_\sigma} = -W^{\mathrm{stat}}_{i_\sigma b_\sigma, j_{\bar{\sigma}} a_{\bar{\sigma}}} \tag{2.29d}$$

At this stage, it is of particular interest to discuss the form of the spin-flip matrix elements defined in Eqs. (2.29c) and (2.29d). As readily seen from Eq. (2.15a), at the RPA level, the spin-flip excitations are given by the difference of one-electron energies, hence missing out on key exchange and correlation effects. This is also the case at the TD-DFT level when one relies on (semi-)local functionals. This explains why most of spin-flip TD-DFT calculations are performed with global hybrid functionals containing a substantial amount of Hartree-Fock exchange as only the exact exchange integral of the form $(i_\sigma j_\sigma | b_{\bar{\sigma}} a_{\bar{\sigma}})$ survive spin-symmetry requirements. At the BSE level, these matrix elements are, of course, also present thanks to the contribution of $W^{\mathrm{stat}}_{i_\sigma j_\sigma, b_{\bar{\sigma}} a_{\bar{\sigma}}}$ as evidenced in Eq. (2.5) but it also includes correlation effects.

2.2.2 Dynamical correction

In order to go beyond the ubiquitous static approximation of BSE [19, 132, 140, 141, 200–202, 204, 226–231] (which is somehow similar to the adiabatic approximation of TD-DFT [123, 124, 131, 132, 136, 137, 232]), we have recently implemented, following Strinati's seminal work [18, 19, 199] (see also the work of Romaniello *et al.* [140] and Sangalli *et al.* [141]), a renormalized first-order perturbative correction in order to take into consideration the dynamical nature of the screened Coulomb potential W [29, 142]. This dynamical correction to the static BSE kernel (dubbed as dBSE in the following) does permit to recover additional relaxation effects coming from higher excitations.

Our implementation follows closely the work of Rohlfing and co-workers [200–203] in which they computed the dynamical correction in the TDA and plasmon-pole approximation. However, our scheme goes beyond the plasmon-pole approximation as the spectral representation of the dynamically-screened Coulomb potential is

computed exactly at the RPA level consistently with the underlying GW calculation:

$$\widetilde{W}_{p_\sigma q_\sigma, r_{\sigma'} s_{\sigma'}}(\omega) = (p_\sigma q_\sigma | r_{\sigma'} s_{\sigma'}) + \sum_m (p_\sigma q_\sigma | m)(r_{\sigma'} s_{\sigma'} | m) \times \left[\frac{1}{\omega - (\varepsilon^{GW}_{s_{\sigma'}} - \varepsilon^{GW}_{q_\sigma}) - \Omega^{\text{sc,RPA}}_m + i\eta} + \frac{1}{\omega - (\varepsilon^{GW}_{r_{\sigma'}} - \varepsilon^{GW}_{p_\sigma}) - \Omega^{\text{sc,RPA}}_m + i\eta} \right] \tag{2.30}$$

The dBSE non-linear response problem is

$$\begin{pmatrix} \mathbf{A}^{\text{dBSE}}(\Omega^{\text{dBSE}}_m) & \mathbf{B}^{\text{dBSE}}(\Omega^{\text{dBSE}}_m) \\ -\mathbf{B}^{\text{dBSE}}(-\Omega^{\text{dBSE}}_m) & -\mathbf{A}^{\text{dBSE}}(-\Omega^{\text{dBSE}}_m) \end{pmatrix} \cdot \begin{pmatrix} \mathbf{X}^{\text{dBSE}}_m \\ \mathbf{Y}^{\text{dBSE}}_m \end{pmatrix} = \Omega^{\text{dBSE}}_m \begin{pmatrix} \mathbf{X}^{\text{dBSE}}_m \\ \mathbf{Y}^{\text{dBSE}}_m \end{pmatrix} \tag{2.31}$$

where the dynamical matrices are generally defined as

$$A^{\text{dBSE}}_{i_\sigma a_\tau, j_{\sigma'} b_{\tau'}}(\omega) = A^{\text{RPA}}_{i_\sigma a_\tau, j_{\sigma'} b_{\tau'}} - \delta_{\sigma\sigma'} \widetilde{W}_{i_\sigma j_{\sigma'}, b_{\tau'} a_\tau}(\omega) \tag{2.32a}$$

$$B^{\text{dBSE}}_{i_\sigma a_\tau, j_{\sigma'} b_{\tau'}}(\omega) = B^{\text{RPA}}_{i_\sigma a_\tau, j_{\sigma'} b_{\tau'}} - \delta_{\sigma\sigma'} \widetilde{W}_{i_\sigma b_{\tau'}, j_{\sigma'} a_\tau}(\omega) \tag{2.32b}$$

from which one can easily obtained the matrix elements for the spin-conserved and spin-flip manifolds similarly to Eqs. (2.29a), (2.29b), (2.29c), and (2.29d). Following Rayleigh-Schrödinger perturbation theory, we then decompose the non-linear eigenproblem (2.31) as a zeroth-order static (*i.e.*, linear) reference and a first-order dynamic (*i.e.*, non-linear) perturbation such that

$$\begin{pmatrix} \mathbf{A}^{\text{dBSE}}(\omega) & \mathbf{B}^{\text{dBSE}}(\omega) \\ -\mathbf{B}^{\text{dBSE}}(-\omega) & -\mathbf{A}^{\text{dBSE}}(-\omega) \end{pmatrix} = \begin{pmatrix} \mathbf{A}^{(0)} & \mathbf{B}^{(0)} \\ -\mathbf{B}^{(0)} & -\mathbf{A}^{(0)} \end{pmatrix} + \begin{pmatrix} \mathbf{A}^{(1)}(\omega) & \mathbf{B}^{(1)}(\omega) \\ -\mathbf{B}^{(1)}(-\omega) & -\mathbf{A}^{(1)}(-\omega) \end{pmatrix} \tag{2.33}$$

with

$$A^{(0)}_{i_\sigma a_\tau, j_{\sigma'} b_{\tau'}} = A^{\text{BSE}}_{i_\sigma a_\tau, j_{\sigma'} b_{\tau'}} \tag{2.34a}$$

$$B^{(0)}_{i_\sigma a_\tau, j_{\sigma'} b_{\tau'}} = B^{\text{BSE}}_{i_\sigma a_\tau, j_{\sigma'} b_{\tau'}} \tag{2.34b}$$

and

$$A^{(1)}_{i_\sigma a_\tau, j_{\sigma'} b_{\tau'}}(\omega) = -\delta_{\sigma\sigma'} \widetilde{W}_{i_\sigma j_{\sigma'}, b_{\tau'} a_\tau}(\omega) + \delta_{\sigma\sigma'} W^{\text{stat}}_{i_\sigma j_{\sigma'}, b_{\tau'} a_\tau} \tag{2.35a}$$

$$B^{(1)}_{i_\sigma a_\tau, j_{\sigma'} b_{\tau'}}(\omega) = -\delta_{\sigma\sigma'} \widetilde{W}_{i_\sigma b_{\tau'}, j_{\sigma'} a_\tau}(\omega) + \delta_{\sigma\sigma'} W^{\text{stat}}_{i_\sigma b_{\tau'}, j_{\sigma'} a_\tau} \tag{2.35b}$$

The dBSE excitation energies are then obtained via

$$\Omega^{\text{dBSE}}_m = \Omega^{\text{BSE}}_m + \zeta_m \Omega^{(1)}_m \tag{2.36}$$

where $\Omega^{\text{BSE}}_m \equiv \Omega^{(0)}_m$ are the static (zeroth-order) BSE excitation energies obtained by solving Eq. (2.27), and

$$\Omega^{(1)}_m = (\mathbf{X}^{\text{BSE}}_m)^\intercal \cdot \mathbf{A}^{(1)}(\Omega^{\text{BSE}}_m) \cdot \mathbf{X}^{\text{BSE}}_m \tag{2.37}$$

are first-order corrections (with $\mathbf{X}_m^{\mathrm{BSE}} \equiv \mathbf{X}_m^{(0)}$) obtained within the dynamical TDA (dTDA) with the renormalization factor

$$\zeta_m = \left[1 - (\mathbf{X}_m^{\mathrm{BSE}})^\intercal \cdot \left. \frac{\partial \mathbf{A}^{(1)}(\omega)}{\partial \omega} \right|_{\omega=\Omega_m^{\mathrm{BSE}}} \cdot \mathbf{X}_m^{\mathrm{BSE}} \right]^{-1} \tag{2.38}$$

which, unlike the *GW* case [see Eq. (2.22)], is not restricted to be between 0 and 1. In most cases, the value of ζ_m is close to unity which indicates that the perturbative expansion behaves nicely.

2.2.3 Oscillator strengths

Oscillator strengths, *i.e.*, transition dipole moments from the ground to the corresponding excited state, are key quantities that are linked to experimental intensities and are usually used to probe the quality of excited-state calculations [84, 233–235].

For the spin-conserved transitions, the x component of the transition dipole moment is

$$\mu_{x,m}^{\mathrm{sc}} = \sum_{ia\sigma} (i_\sigma|x|a_\sigma)(\mathbf{X}_m^{\mathrm{sc}} + \mathbf{Y}_m^{\mathrm{sc}})_{i_\sigma a_\sigma} \tag{2.39}$$

where

$$(p_\sigma|x|q_{\sigma'}) = \int \psi_{p_\sigma}(\boldsymbol{r})\, x\, \psi_{q_{\sigma'}}(\boldsymbol{r}) d\boldsymbol{r} \tag{2.40}$$

are one-electron integrals in the orbital basis. The total oscillator strength in the so-called length gauge [235] is given by

$$f_m^{\mathrm{sc}} = \frac{2}{3}\Omega_m^{\mathrm{sc}} \left[\left(\mu_{x,m}^{\mathrm{sc}}\right)^2 + \left(\mu_{y,m}^{\mathrm{sc}}\right)^2 + \left(\mu_{z,m}^{\mathrm{sc}}\right)^2 \right] \tag{2.41}$$

For spin-flip transitions, we have $f_m^{\mathrm{sf}} = 0$ as the transition matrix elements $(i_\sigma|x|a_{\bar{\sigma}})$ vanish via integration over the spin coordinate.

2.2.4 Spin contamination

One of the key issues of linear response formalism based on unrestricted references is spin contamination or the artificial mixing with configurations of different spin multiplicities. As nicely explained in Ref. [94], there are two sources of spin contamination: i) spin contamination of the reference configuration for which, for example, $\langle \hat{S}^2 \rangle > 2$ for high-spin triplets, and ii) spin contamination of the excited states due to spin incompleteness of the CI expansion. The latter issue is an important source of spin contamination in the present context as BSE is limited to single excitations with respect to the reference configuration. Specific schemes have been developed to palliate these shortcomings and we refer the interested reader to Ref. [94] for a detailed discussion on this matter.

In order to monitor closely how contaminated are these states, we compute

$$\langle \hat{S}^2 \rangle_m = \langle \hat{S}^2 \rangle_0 + \Delta \langle \hat{S}^2 \rangle_m \tag{2.42}$$

where

$$\langle \hat{S}^2 \rangle_0 = \frac{n_\uparrow - n_\downarrow}{2} \left(\frac{n_\uparrow - n_\downarrow}{2} + 1 \right) + n_\downarrow - \sum_p (p_\uparrow|p_\downarrow)^2 \tag{2.43}$$

is the expectation value of $\hat{S}^2$ for the reference configuration, the first term corresponding to the exact value of $\langle \hat{S}^2 \rangle$, and

$$(p_\sigma | q_{\sigma'}) = \int \psi_{p_\sigma}(\boldsymbol{r}) \psi_{q_{\sigma'}}(\boldsymbol{r}) d\boldsymbol{r} \tag{2.44}$$

are overlap integrals between spin-up and spin-down orbitals.

For a given single excitation m, the explicit expressions of $\Delta \langle \hat{S}^2 \rangle_m^{\text{sc}}$ and $\Delta \langle \hat{S}^2 \rangle_m^{\text{sf}}$ can be found in the Appendix of Ref. [168] for spin-conserved and spin-flip excitations, and are functions of the vectors $\mathbf{X}_m$ and $\mathbf{Y}_m$ as well as the orbital overlaps defined in Eq. (2.44).

2.3 Computational details

All the systems under investigation here have a closed-shell singlet ground state and we consider the lowest triplet state as reference for the spin-flip calculations adopting the unrestricted formalism throughout this work. The G_0W_0 calculations performed to obtain the screened Coulomb potential and the quasiparticle energies required to compute the BSE neutral excitations are performed using an unrestricted Hartree-Fock (UHF) starting point, and the G_0W_0 quasiparticle energies are obtained by linearizing the frequency-dependent quasiparticle equation [see Eq. (2.21)]. Note that the entire set of orbitals and energies is corrected. Further details about our implementation of G_0W_0 can be found in Refs. [27, 29, 216, 236, 237].

Here, we do not investigate how the starting orbitals affect the BSE@G_0W_0 excitation energies. This is left for future work. However, it is worth mentioning that, for the present (small) molecular systems, Hartree-Fock is usually a good starting point [27–29], although improvements could certainly be obtained with starting orbitals and energies computed with, for example, optimally-tuned range-separated hybrid (RSH) functionals [238–241]. Besides, G_0W_0@UHF and evGW@UHF yield similar quasiparticle energies, while G_0W_0 allows us to avoid rather laborious iterations as well as the significant additional computational effort of evGW [27, 29, 237]. In the following, all linear response calculations are performed within the TDA to ensure consistency between the spin-conserved and spin-flip results. Finally, the infinitesimal η is set to 100 meV for all calculations.

All the static and dynamic BSE calculations (labeled in the following as SF-BSE and SF-dBSE respectively) are performed with the software `QuAcK` [242], developed in our group and freely available on `github`. The standard and extended spin-flip ADC(2) calculations [SF-ADC(2)-s and SF-ADC(2)-x, respectively] as well as the SF-ADC(3) [181] are performed with Q-CHEM 5.2.1 [243]. Spin-flip TD-DFT calculations [178] (also performed with Q-CHEM 5.2.1) considering the BLYP [43, 45], B3LYP [43, 45, 50], and BH&HLYP [45, 51] functionals with contains 0%, 20%, and 50% of exact exchange are labeled as SF-TD-BLYP, SF-TD-B3LYP, and SF-TD-BH&HLYP, respectively. Additionally, we have performed spin-flip TD-DFT calculations considering the following the RSH functionals: CAM-B3LYP [54], LC-ωPBE08 [55], and ωB97X-D [53, 244]. In the present context, the main difference between these RSHs is their amount of exact exchange at long range: 75% for CAM-B3LYP and 100% for both LC-ωPBE08 and ωB97X-D. EOM-CCSD excitation energies [245–247] are computed with Gaussian 09 [248]. As a consistency check, we systematically perform SF-CIS calculations [152] with both `QuAcK` and Q-CHEM, and make sure that they yield identical excitation energies. Throughout this work, all spin-flip and spin-conserved calculations are performed with a UHF reference.

2.4 Results

2.4.1 Beryllium atom

As a first example, we consider the simple case of the beryllium atom in a small basis (6-31G) which was considered by Krylov in two of her very first papers on spin-flip methods [152, 153]. It was also considered in later studies thanks to its pedagogical value [94, 164]. Beryllium has a ^1S ground state with $1s^2 2s^2$ configuration. The excitation energies corresponding to the first singlet and triplet single excitations $2s \rightarrow 2p$ with P spatial symmetries as well as the first singlet and triplet double excitations $2s^2 \rightarrow 2p^2$ with D and P spatial symmetries (respectively) are reported in Table 2.1 and depicted in Fig. 2.1.

On the left side of Fig. 2.1, we report SF-TD-DFT excitation energies (red lines) obtained with the BLYP, B3LYP, and BH&HLYP functionals, which correspond to an increase of exact exchange from 0% to 50%. As mentioned in Ref. [94], the $^3P(1s^2 2s^1 2p^1)$ and the $^1P(1s^2 2s^1 2p^1)$ states are degenerate at the SF-TD-BLYP level. Indeed, due to the lack of coupling terms in the spin-flip block of the SD-TD-DFT equations (see Subsec. 2.2.1), their excitation energies are given by the energy difference between the $2s$ and $2p$ orbitals and both states are strongly spin contaminated. Including exact exchange, like in SF-TD-B3LYP and SF-TD-BH&HLYP, lifts this degeneracy and improves the description of both states. However, the SF-TD-BH&HLYP excitation energy of the $^1P(1s^2 2s^1 2p^1)$ state is still off by 1.6 eV as compared to the FCI reference. For the other states, the agreement between SF-TD-BH&HLYP and FCI is significantly improved. Spin-flip TD-DFT calculations performed with CAM-B3LYP and ωB97X-D are only slightly more accurate than their global hybrid counterparts, while SF-TD-LC-ωPBE08 yields more significant improvements although it does not reach the accuracy of SF-(d)BSE.

The center part of Fig. 2.1 shows the SF-(d)BSE results (blue lines) alongside the SF-CIS excitation energies (purple lines). All of these are computed with 100% of exact exchange with the additional inclusion of correlation in the case of SF-BSE and SF-dBSE thanks to the introduction of static and dynamical screening, respectively. Overall, the SF-CIS and SF-BSE excitation energies are closer to FCI than the SF-TD-DFT ones, except for the lowest triplet state where the SF-TD-BH&HLYP excitation energy is more accurate probably due to error compensation. At the exception of the ^1D state, SF-BSE improves over SF-CIS with a rather small contribution from the additional dynamical effects included in the SF-dBSE scheme. Note that the exact exchange seems to spin purified the $^3P(1s^2 2s^1 2p^1)$ state while the singlet states at the SF-BSE level are slightly more spin contaminated than their SF-CIS counterparts.

Table 2.1 and Fig. 2.1 also gathers results obtained at the partially self-consistent SF-(d)BSE@evGW and fully self-consistent SF-(d)BSE@qsGW levels. The SF-(d)BSE excitation energies are quite stable with respect to the underlying GW scheme which nicely illustrates that UHF eigenstates are actually an excellent starting point in this particular case.

The right side of Fig. 2.1 illustrates the performance of the SF-ADC methods. Interestingly, SF-BSE and SF-ADC(2)-s have rather similar accuracies, except again for the ^1D state where SF-ADC(2)-s has clearly the edge over SF-BSE. Finally, both SF-ADC(2)-x and SF-ADC(3) yield excitation energies very close to FCI for this simple system with significant improvements for the lowest ^3P state and the ^1D doubly-excited state. Although the (d)BSE and ADC(2)-s have obvious theoretical similarities, we would like to mention that they are not strictly identical as ADC(2) includes key

second-order exchange contributions that are not included at the GW level even in the case of more elaborate schemes like evGW and qsGW.

Table 2.1: Excitation energies (in eV) with respect to the $^1S(1s^2 2s^2)$ singlet ground state of Be obtained at various methods with the 6-31G basis set. All the spin-flip calculations have been performed with an unrestricted reference. The $\langle \hat{S}^2 \rangle$ value associated with each state is reported in parenthesis (when available).

	Excitation energies (eV)				
Method	$^1S(1s^2 2s^2)$	$^3P(1s^2 2s^1 2p^1)$	$^1P(1s^2 2s^1 2p^1)$	$^3P(1s^2 2p^2)$	$^1D(1s^2 2p^2)$
SF-TD-BLYP[1]	(0.002)	3.210(1.000)	3.210(1.000)	6.691(1.000)	7.598(0.013)
SF-TD-B3LYP[1]	(0.001)	3.332(1.839)	4.275(0.164)	6.864(1.000)	7.762(0.006)
SF-TD-BH&HLYP[1]	(0.000)	2.874(1.981)	4.922(0.023)	7.112(1.000)	8.188(0.002)
SF-TD-CAM-B3LYP	(0.001)	3.186(1.960)	4.554(0.043)	7.020(1.000)	7.933(0.008)
SF-TD-ωB97X-D	(0.006)	3.337(1.867)	4.717(0.147)	7.076(1.000)	8.247(0.040)
SF-TD-LC-ωPBE08	(0.014)	3.434(1.720)	5.904(0.287)	7.088(1.000)	9.471(0.073)
SF-CIS[2]	(0.002)	2.111(2.000)	6.036(0.014)	7.480(1.000)	8.945(0.006)
SF-BSE@G_0W_0	(0.004)	2.399(1.999)	6.191(0.023)	7.792(1.000)	9.373(0.013)
SF-BSE@evGW	(0.004)	2.407(1.999)	6.199(0.023)	7.788(1.000)	9.388(0.013)
SF-BSE@qsGW	(0.057)	2.376(1.963)	6.241(0.048)	7.668(1.000)	9.417(0.004)
SF-dBSE@G_0W_0		2.363	6.263	7.824	9.424
SF-dBSE@evGW		2.369	6.273	7.820	9.441
SF-dBSE@qsGW		2.335	6.317	7.689	9.470
SF-ADC(2)-s		2.433	6.255	7.745	9.047
SF-ADC(2)-x		2.866	6.581	7.664	8.612
SF-ADC(3)		2.863	6.579	7.658	8.618
FCI[2]	**(0.000)**	**2.862(2.000)**	**6.577(0.000)**	**7.669(2.000)**	**8.624(0.000)**

[1] Excitation energies taken from Ref. [94].
[2] Excitation energies taken from Ref. [152].

2.4.2 Hydrogen molecule

Our second example deals with the dissociation of the H_2 molecule, which is a prototypical system for testing new electronic structure methods and, specifically, their accuracy in the presence of strong correlation (see, for example, Refs. [249–252], and references therein). The $X\,^1\Sigma_g^+$ ground state of H_2 has an electronic configuration $(1\sigma_g)^2$ configuration. The variation of the excitation energies associated with the three lowest singlet excited states with respect to the elongation of the H−H bond are of particular interest here. The lowest singly excited state $B\,^1\Sigma_u^+$ has a $(1\sigma_g)(1\sigma_u)$ configuration, while the singly excited state $E\,^1\Sigma_g^+$ and the doubly excited state $F\,^1\Sigma_g^+$ have $(1\sigma_g)(2\sigma_g)$ and $(1\sigma_u)^2$ configurations, respectively. Because these latter two excited states interact strongly and form an avoided crossing around $R(\mathrm{H}-\mathrm{H}) = 1.4$ Å, they are usually labeled as the $EF\,^1\Sigma_g^+$ state. Note that this avoided crossing is not visible with non-spin-flip methods restricted to single excitations (such as CIS, TD-DFT, and BSE) as these are "blind" to double excitations. Three methods, in their standard and spin-flip versions, are studied here (CIS, TD-BH&HLYP and BSE) and are compared to the reference EOM-CCSD excitation energies (that is equivalent to FCI in the case of H_2). All these calculations are performed with the cc-pVQZ basis.

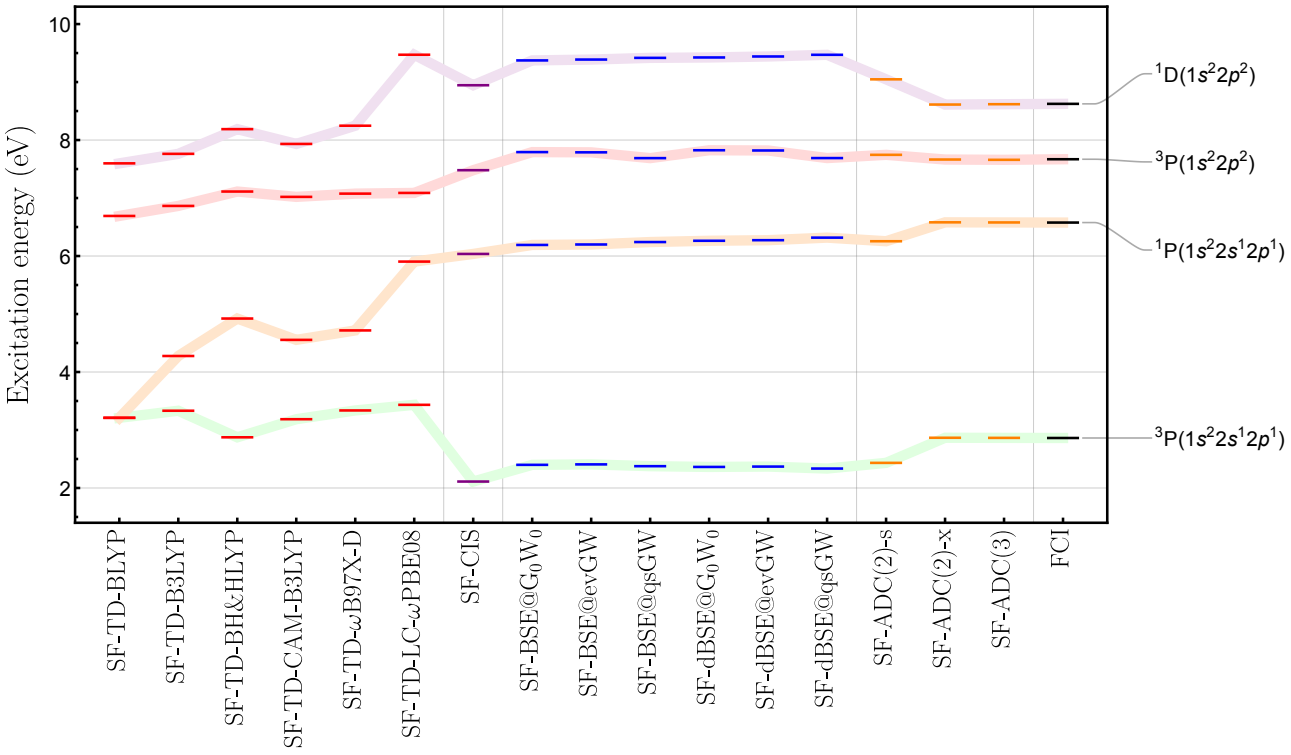

Figure 2.1: Excitation energies (in eV) with respect to the $^1S(1s^2 2s^2)$ singlet ground state of Be obtained with the 6-31G basis at various levels of theory: SF-TD-DFT (red), SF-CIS (purple), SF-BSE (blue), SF-ADC (orange), and FCI (black). All the spin-flip calculations have been performed with an unrestricted reference.

The top panel of Fig. 2.2 shows the CIS (dotted lines) and SF-CIS (dashed lines) excitation energies as functions of $R(\mathrm{H}-\mathrm{H})$. The EOM-CCSD reference energies are represented by solid lines. We observe that both CIS and SF-CIS poorly describe the $\mathrm{B}\,^1\Sigma_u^+$ state in the dissociation limit with an error greater than 1 eV, while CIS, unlike SF-CIS, is much more accurate around the equilibrium geometry. Similar observations can be made for the $\mathrm{E}\,^1\Sigma_g^+$ state with a good description at the CIS level for all bond lengths. SF-CIS does not model accurately the $\mathrm{E}\,^1\Sigma_g^+$ state before the avoided crossing, but the agreement between SF-CIS and EOM-CCSD is much satisfactory for bond length greater than 1.6 Å. Oppositely, SF-CIS describes better the $\mathrm{F}\,^1\Sigma_g^+$ state before the avoided crossing than after, while this state is completely absent at the CIS level. Indeed, as mentioned earlier, CIS is unable to locate any avoided crossing as it cannot access double excitations. At the SF-CIS level, the avoided crossing between the E and F states is qualitatively reproduced and placed at a slightly larger bond length [$R(\mathrm{H}-\mathrm{H}) \approx 1.5$ Å] than at the EOM-CCSD level.

In the central panel of Fig. 2.2, we report the (SF-)TD-BH&HLYP results. SF-TD-BH&HLYP shows, at best, qualitative agreement with EOM-CCSD, while the TD-BH&HLYP excitation energies of the B and E states are only trustworthy around equilibrium but inaccurate at dissociation. Note that H_2 is a rather challenging system for (SF)-TD-DFT from a general point of view [251, 253–255]. Similar graphs for (SF-)TD-BLYP and (SF-)TD-B3LYP are reported in Appendix B from which one can draw similar conclusions. Notably, one can see that the $\mathrm{E}\,^1\Sigma_g^+$ and $\mathrm{F}\,^1\Sigma_g^+$ states crossed without interacting at the SF-TD-BLYP level due to the lack of Hartree-Fock exchange. In Appendix B, we also report the potential energy curves of H_2 obtained with three RSHs (CAM-B3LYP, ωB97X-D, and LC-ωPBE08), which only brought a modest

improvement and rather sharp avoided crossings as compared to EOM-CCSD.

In the bottom panel of Fig. 2.2, (SF-)BSE excitation energies for the same three singlet states are represented. SF-BSE provides surprisingly accurate excitation energies for the B $^1\Sigma_u^+$ state with errors between 0.05 and 0.3 eV, outperforming in the process the standard BSE formalism. However SF-BSE does not describe well the E $^1\Sigma_g^+$ state with error ranging from half an eV to 1.6 eV. Similar performances are observed at the BSE level around equilibrium with a clear improvement in the dissociation limit. Remarkably, SF-BSE shows a good agreement with EOM-CCSD for the F $^1\Sigma_g^+$ doubly-excited state, resulting in an avoided crossing around $R(\mathrm{H}-\mathrm{H}) = 1.6$ Å. A similar graph comparing (SF-)dBSE and EOM-CCSD excitation energies can be found in Appendix B where it is shown that dynamical effects do not affect the present conclusions. One would also notice a little "kink" in the potential energy curves of the B $^1\Sigma_u^+$ and E $^1\Sigma_g^+$ states around $R(\mathrm{H}-\mathrm{H}) = 1.2$ Å computed at the (d)BSE@G_0W_0 level. This unfortunate feature is due to the appearance of the symmetry-broken UHF solution and the lack of self-consistent in G_0W_0. Indeed, $R = 1.2$ Å corresponds to the location of the well-known Coulson-Fischer point [256]. Note that, as mentioned earlier, all the calculations are performed with a UHF reference even the ones based on a closed-shell singlet reference. If one relies solely on the restricted HF solution, this kink disappears and one obtains smooth potential energy curves (see Appendix B).

The right side of Fig. 2.2 shows the amount of spin contamination as a function of the bond length for SF-CIS (top), SF-TD-BH&HLYP (center), and SF-BSE (bottom). Overall, one can see that $\langle \hat{S}^2 \rangle$ behaves similarly for SF-CIS and SF-BSE with a small spin contamination of the B $^1\Sigma_u^+$ at short bond length. In contrast, the B state is much more spin contaminated at the SF-TD-BH&HLYP level. For all spin-flip methods, the E state is strongly spin contaminated as expected, while the $\langle \hat{S}^2 \rangle$ values associated with the F state only deviate significantly from zero for short bond length and around the avoided crossing where it strongly couples with the spin contaminated E state.

2.4.3 Cyclobutadiene

Cyclobutadiene (CBD) is an interesting example as the electronic character of its ground state can be tuned via geometrical deformation [94, 172, 173, 181, 257–261]. In the D_{2h} rectangular geometry of the A_g singlet ground state, the highest occupied molecular orbital (HOMO) and lowest unoccupied molecular orbital (LUMO) are non-degenerate, and the singlet ground state can be safely labeled as single-reference with well-defined doubly-occupied orbitals. However, in the D_{4h} square-planar geometry of the A_{2g} triplet state, the HOMO and LUMO are strictly degenerate, and the electronic ground state, which is still of singlet nature with B_{1g} spatial symmetry (hence violating Hund's rule), is strongly multi-reference with singly occupied orbitals (*i.e.*, singlet open-shell state). In this case, single-reference methods notoriously fail. Nonetheless, the lowest triplet state of symmetry $^3A_{2g}$ remains of single-reference character and is then a perfect starting point for spin-flip calculations. The D_{2h} and D_{4h} optimized geometries of the ^1A_g and $^3A_{2g}$ states of CBD have been extracted from Ref. [173] and have been obtained at the CCSD(T)/cc-pVTZ level. For comparison purposes, EOM-SF-CCSD and SF-ADC excitation energies have been extracted from Ref. [173] and Ref. [181], respectively. All of them have been obtained with a UHF reference like the SF-BSE calculations performed here.

Tables 2.2 and 2.3 report excitation energies (with respect to the singlet ground state) obtained at the D_{2h} and D_{4h} geometries, respectively, for several methods using the spin-flip *ansatz*. All these results are represented in Fig. 2.3. For each geometry,

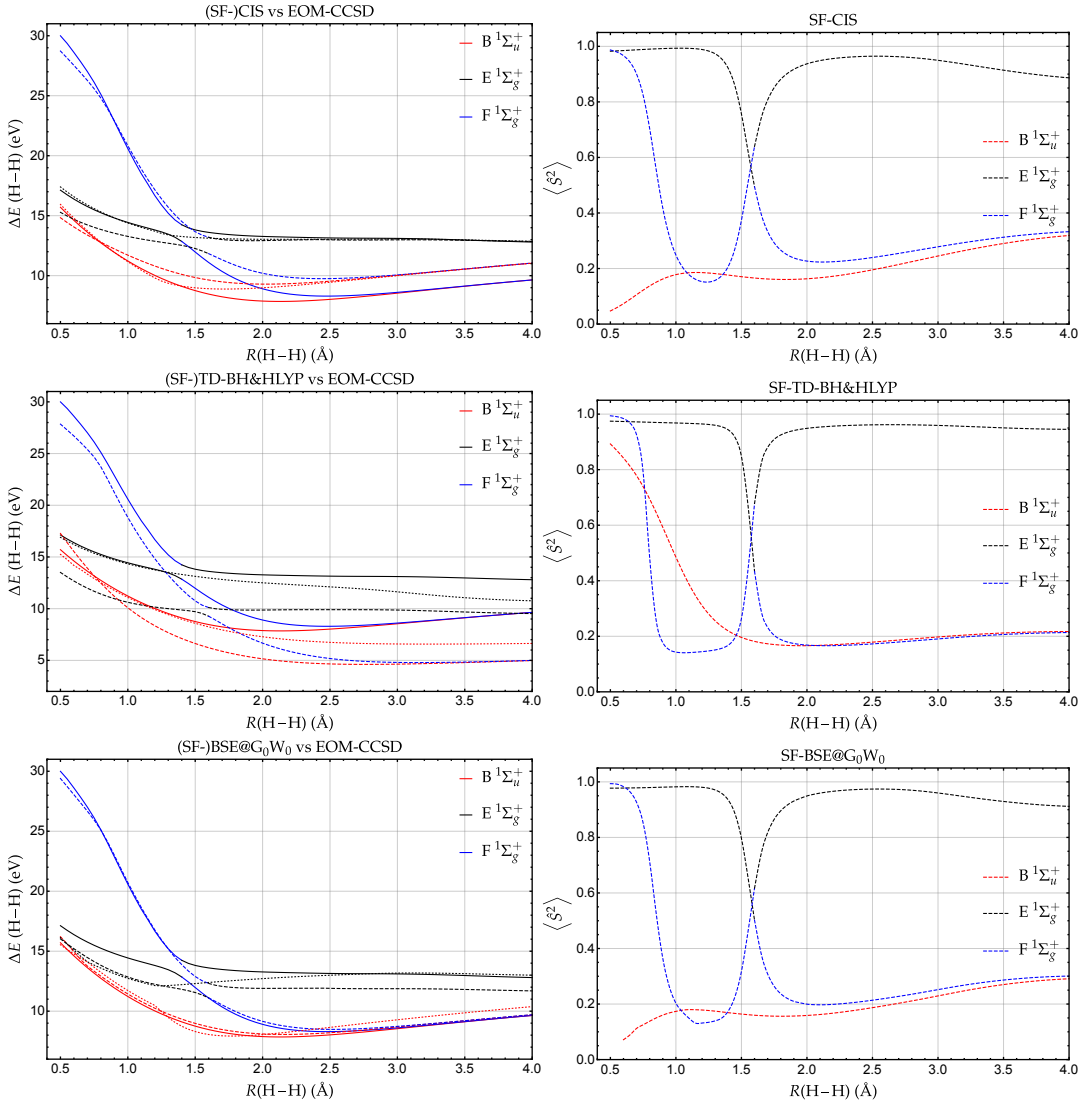

Figure 2.2: Excitation energies with respect to the $X\,^1\Sigma_g^+$ ground state (left) and expectation value of the spin operator $\langle \hat{S}^2 \rangle$ (right) of the $B\,^1\Sigma_u^+$ (red), $E\,^1\Sigma_g^+$ (black), and $F\,^1\Sigma_g^+$ (blue) states of H_2 obtained with the cc-pVQZ basis at the (SF-)CIS (top), (SF-)TD-BH&HLYP (middle), and (SF-)BSE (bottom) levels of theory. The reference EOM-CCSD excitation energies are represented as solid lines, while the results obtained with and without spin-flip are represented as dashed and dotted lines, respectively. All the spin-conserved and spin-flip calculations have been performed with an unrestricted reference. The raw data are reported in Appendix B.

three excited states are under investigation: i) the $1\,^3B_{1g}$, $1\,^1B_{1g}$, and $2\,^1A_g$ states of the D_{2h} geometry; ii) the $1\,^3A_{2g}$, $2\,^1A_{1g}$, and $1\,^1B_{2g}$ states of the D_{4h} geometry. It is important to mention that the $2\,^1A_{1g}$ state of the rectangular geometry has a significant double excitation character [130], and is then hardly described by second-order methods [such as CIS(D) [262, 263], ADC(2) [79, 264], CC2 [265], or EOM-CCSD [245–247]] and remains a real challenge for third-order methods [as, for example, ADC(3) [79, 84, 266], CC3 [146], or EOM-CCSDT [148–151]].

Comparing the present SF-BSE@G_0W_0 results for the rectangular geometry (see Table 2.2) to the most accurate ADC level, *i.e.*, SF-ADC(3), we have a difference in excitation energy of 0.017 eV for the $1\,^3B_{1g}$ state. This difference grows to 0.572 eV for the $1\,^1B_{1g}$ state and then shrinks to 0.212 eV for the $2\,^1A_g$ state. Overall, adding dynamical corrections via the SF-dBSE@G_0W_0 scheme does not improve the accuracy of the excitation energies [as compared to SF-ADC(3)] with errors of 0.052, 0.393, and 0.293 eV for the $1\,^3B_{1g}$, $1\,^1B_{1g}$, and $2\,^1A_g$ states, respectively.

Now, looking at Table 2.3 which gathers the results for the square-planar geometry, we see that, at the SF-BSE@G_0W_0 level, the first two states are wrongly ordered with the triplet $1\,^3B_{1g}$ state lower than the singlet $1\,^1A_g$ state. (The same observation can be made at the SF-TD-B3LYP level.) This is certainly due to the poor Hartree-Fock reference which lacks opposite-spin correlation and this issue could be potentially alleviated by using a better starting point for the GW calculation, as discussed in Sec. 2.3. Nonetheless, it is pleasing to see that adding the dynamical correction in SF-dBSE@G_0W_0 not only improves the agreement with SF-ADC(3) but also retrieves the right state ordering. Then, CBD stands as an excellent example for which dynamical corrections are necessary to get the right chemistry at the SF-BSE level. Another interesting feature is the wrong ordering of the $2\,^1A_{1g}$ and $1\,^1B_{2g}$ states at the SF-B3LYP, SF-BH&HLYP, and SF-CIS levels which give the former higher in energy than the latter. This issue does not appear at the SF-BSE, SF-ADC, and SF-EOM-SF-CCSD levels. Here again, one does not observe a clear improvement by considering RSHs instead of global hybrids (BH&HLYP seems to perform particularly well in the case of CBD), although it is worth mentioning that RSH-based SF-TD-DFT calculations yield accurate excitation for the double excitation $1\,^1A_g \rightarrow 2\,^1A_g$ in the D_{2h} geometry.

2.5 Conclusion

In this work, we have presented the extension of the BSE approach of many-body perturbation theory to the spin-flip formalism in order to access double excitations in realistic molecular systems. The present spin-flip calculations rely on a spin-unrestricted version of the GW approximation and the BSE formalism with, on top of this, a dynamical correction to the static BSE optical excitations via an unrestricted generalization of our recently developed renormalized perturbative treatment. Taking the beryllium atom, the dissociation of the hydrogen molecule, and cyclobutadiene in two different geometries as examples, we have shown that the spin-flip BSE formalism can accurately model double excitations and seems to surpass systematically its spin-flip TD-DFT parent. Further improvements could be obtained thanks to a better choice of the starting orbitals and their energies and we hope to investigate this in a forthcoming paper. Techniques to alleviate the spin contamination in spin-flip BSE will also be explored in the near future. We hope to these new encouraging results will stimulate new developments around the BSE formalism to further establish it as a valuable *ab inito* alternative to TD-DFT for the study of molecular excited states.

Table 2.2: Vertical excitation energies (with respect to the singlet $X\,^1A_g$ ground state) of the $1\,^3B_{1g}$, $1\,^1B_{1g}$, and $2\,^1A_g$ states of CBD at the D_{2h} rectangular equilibrium geometry of the $X\,^1A_g$ ground state. All the spin-flip calculations have been performed with an unrestricted reference and the cc-pVTZ basis set.

Method	Excitation energies (eV)		
	$1\,^3B_{1g}$	$1\,^1B_{1g}$	$2\,^1A_g$
SF-TD-B3LYP[1]	1.750	2.260	4.094
SF-TD-BH&HLYP[1]	1.583	2.813	4.528
SF-TD-CAM-B3LYP	1.790	2.379	4.238
SF-TD-ωB97X-D	1.771	2.366	4.212
SF-TD-LC-ωPBE08	1.941	2.464	4.428
SF-CIS[2]	1.521	3.836	5.499
EOM-SF-CCSD[3]	1.654	3.416	4.360
EOM-SF-CCSD(fT)[3]	1.516	3.260	4.205
EOM-SF-CCSD(dT)[3]	1.475	3.215	4.176
SF-ADC(2)-s[4]	1.573	3.208	4.247
SF-ADC(2)-x[4]	1.576	3.141	3.796
SF-ADC(3)[2]	1.456	3.285	4.334
SF-BSE@G_0W_0[1]	1.438	2.704	4.540
SF-dBSE@G_0W_0[11]	1.403	2.883	4.621

[1] This work.
[2] Values from Ref. [94].
[3] Values from Ref. [173].
[4] Values from Ref. [181].

Table 2.3: Vertical excitation energies (with respect to the singlet $X\,^1B_{1g}$ ground state) of the $1\,^3A_{2g}$, $2\,^1A_{1g}$, and $1\,^1B_{2g}$ states of CBD at the D_{4h} square-planar equilibrium geometry of the $1\,^3A_{2g}$ state. All the spin-flip calculations have been performed with an unrestricted reference and the cc-pVTZ basis set.

Method	Excitation energies (eV)		
	$1\,^3A_{2g}$	$2\,^1A_{1g}$	$1\,^1B_{2g}$
SF-TD-B3LYP[1]	−0.020	0.547	0.486
SF-TD-BH&HLYP[1]	0.048	1.465	1.282
SF-TD-CAM-B3LYP	0.012	0.677	0.595
SF-TD-ωB97X-D	0.005	0.673	0.592
SF-TD-LC-ωPBE08	0.062	0.663	0.570
SF-CIS[2]	0.317	3.125	2.650
EOM-SF-CCSD[3]	0.369	1.824	2.143
EOM-SF-CCSD(fT)[3]	0.163	1.530	1.921
EOM-SF-CCSD(dT)[3]	0.098	1.456	1.853
SF-ADC(2)-s[4]	0.266	1.664	1.910
SF-ADC(2)-x[4]	0.217	1.123	1.799
SF-ADC(3)[4]	0.083	1.621	1.930
SF-BSE@G_0W_0[1]	−0.092	1.189	1.480
SF-dBSE@G_0W_0[1]	0.012	1.507	1.841

[1] This work.
[2] Values from Ref. [94].
[3] Values from Ref. [173].
[4] Values from Ref. [181].

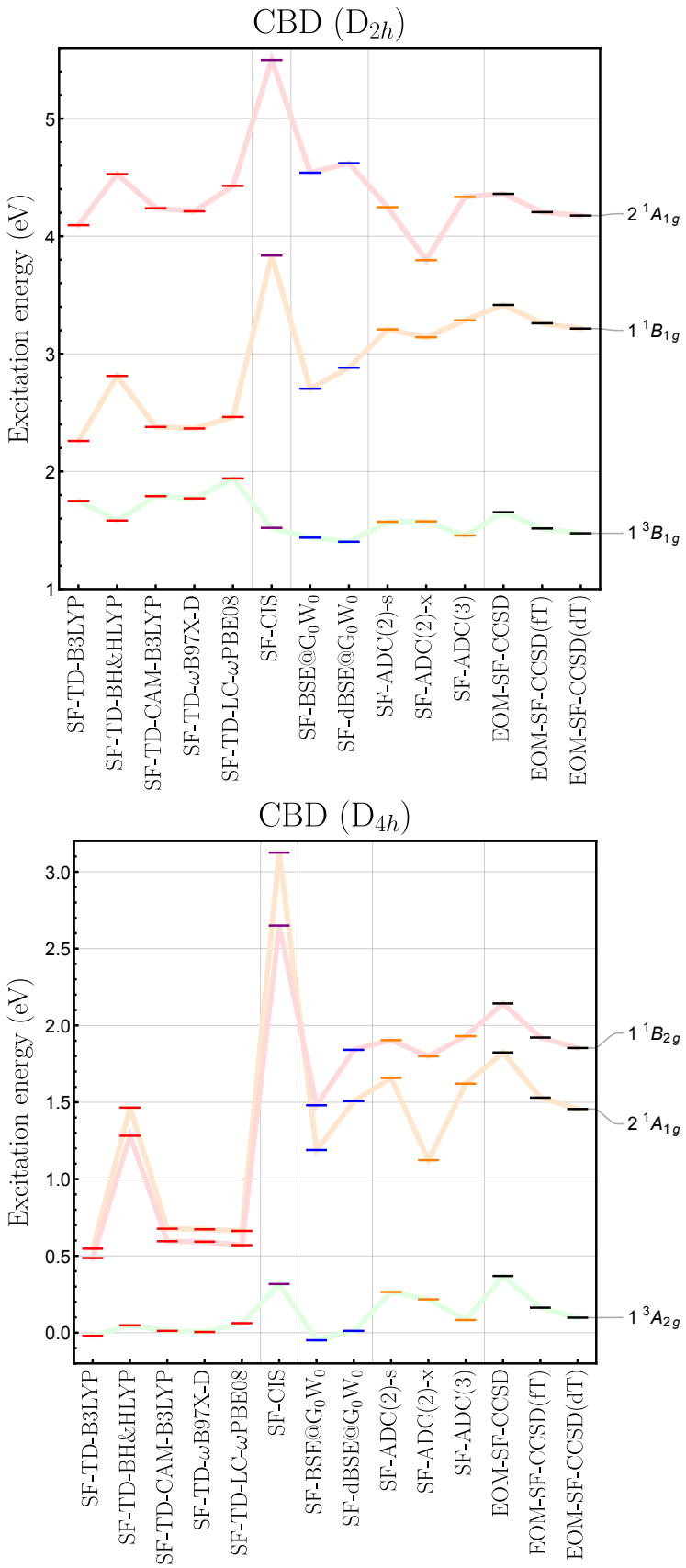

Figure 2.3: Vertical excitation energies of CBD at various levels of theory: SF-TD-DFT (red), SF-CIS (purple), SF-BSE (blue), SF-ADC (orange), and EOM-SF-CCSD (black). Top: $1\,^3B_{1g}$, $1\,^1B_{1g}$, and $2\,^1A_{1g}$ states at the D_{2h} rectangular equilibrium geometry of the $X\,^1A_g$ ground state (see Table 2.2 for the raw data). Bottom: $1\,^3A_{2g}$, $2\,^1A_{1g}$, and $1\,^1B_{2g}$ states at the D_{4h} square-planar equilibrium geometry of the $1\,^3A_{2g}$ state (see Table 2.3 for the raw data). All the spin-flip calculations have been performed with an unrestricted reference and the cc-pVTZ basis set.

Chapter 3

Reference energies for cyclobutadiene: automerization and excited states

This chapter is the subject of the following publication: E. Monino, M. Boggio-Pasqua, A. Scemama, D. Jacquemin, and P. F. Loos.*J. Phys. Chem. A* **126**, 4664 (2022).

Note that the multi-reference (CASSCF, CASPT2, and NEVPT2) calculations were done by Martial Boggio-Pasqua, coupled-cluster (CCSD, CC3, CCSDT, CC4, and CCSDTQ) calculations were done by Denis Jacquemin and selected configuration interaction (sCI) calculations were done by Anthony Scemama.

Cyclobutadiene is a well-known playground for theoretical chemists and is particularly suitable to test ground- and excited-state methods. Indeed, due to its high spatial symmetry, especially at the D_{4h} square geometry but also in the D_{2h} rectangular arrangement, the ground and excited states of cyclobutadiene exhibit multi-configurational characters and single-reference methods, such as standard adiabatic time-dependent density-functional theory (TD-DFT) or standard equation-of-motion coupled-cluster (EOM-CC), are notoriously known to struggle in such situations. In this work, using a large panel of methods and basis sets, we provide an extensive computational study of the automerization barrier (defined as the difference between the square and rectangular ground-state energies) and the vertical excitation energies at D_{2h} and D_{4h} equilibrium structures. In particular, selected configuration interaction (SCI), multi-reference perturbation theory (CASSCF, CASPT2, and NEVPT2), and coupled-cluster (CCSD, CC3, CCSDT, CC4, and CCSDTQ) calculations are performed. The spin-flip formalism, which is known to provide a qualitatively correct description of these diradical states, is also tested within TD-DFT (combined with numerous exchange-correlation functionals) and the algebraic diagrammatic construction [ADC(2)-s, ADC(2)-x, and ADC(3)] schemes. A theoretical best estimate is defined for the automerization barrier and for each vertical transition energy.

3.1 Introduction

Despite the fact that excited states are involved in ubiquitous processes such as photochemistry [267–273], catalysis [274], and solar cells [12], none of the currently

existing methods has shown to provide accurate excitation energies in all scenarios due to the complexity of the process, the size of the systems, the impact of the environment, and many other factors. Indeed, each computational model has its own theoretical and/or technical limitations and the number of possible chemical scenarios is so vast that the design of new excited-state methodologies remains a very active field of theoretical quantum chemistry [25, 58, 79, 85–93, 275, 276].

Speaking of difficult tasks, the cyclobutadiene (CBD) molecule has been a real challenge for both experimental and theoretical chemistry for many decades [277]. Due to its antiaromaticity [278] and large angular strain [279], CBD presents a high reactivity making its synthesis a particularly difficult exercise. In the D_{4h} symmetry, the simple Hückel molecular orbital theory wrongly predicts a triplet ground state (Hund's rule) with two singly-occupied frontier orbitals that are degenerate by symmetry, while state-of-the-art *ab initio* methods correctly predict an open-shell singlet ground state. This degeneracy is lifted by the so-called pseudo Jahn-Teller effect, *i.e.*, by a descent in symmetry (from D_{4h} to D_{2h} point group) via a geometrical distortion of the molecule, leading to a closed-shell singlet ground state in the rectangular geometry (see below). This was confirmed by several experimental studies by Pettis and co-workers [280] and others [281–283].

In the D_{2h} symmetry, the 1^1A_g ground state has a weak multi-configurational character with well-separated frontier orbitals that can be described by single-reference methods. However, in the D_{4h} symmetry, the 1^1B_{1g} ground state is a diradical that has two degenerate singly occupied frontier orbitals. Therefore, one must take into account, at least, two electronic configurations to properly model this multi-configurational scenario. Of course, standard single-reference methods are naturally unable to describe such situations. Interestingly, the 1^1B_{1g} ground state of the square arrangement is a transition state in the automerization reaction between the two rectangular structures (see Fig. 3.1), while the lowest triplet state, 1^3A_{2g}, is a minimum on the triplet potential energy surface in the D_{4h} arrangement. The automerization barrier (AB) is thus defined as the difference between the square and rectangular ground-state energies. The energy of this barrier is estimated, experimentally, in the range of 1.6–10 kcal mol^{-1} [284], while previous state-of-the-art *ab initio* calculations yield values in the 7–9 kcal mol^{-1} range [259, 260, 285, 286].

The lowest-energy excited states of CBD in both symmetries are represented in Fig. 3.1, where we have reported the 1^1A_g and 1^3B_{1g} states for the rectangular geometry and the 1^1B_{1g} and 1^3A_{2g} states for the square one. Due to the energy scale, the higher-energy states (1^1B_{1g} and 2^1A_g for D_{2h} and 1^1A_{1g} and 1^1B_{2g} for D_{4h}) are not shown. Interestingly, the 2^1A_g and 1^1A_{1g} states have a strong contribution from doubly-excited configurations and these so-called double excitations [130] are known to be inaccessible with standard adiabatic time-dependent density-functional theory (TD-DFT) [65, 67, 123, 124, 134–137, 287] and remain challenging for standard hierarchy of EOM-CC methods that are using ground-state Hartree-Fock reference [148, 149, 151, 288].

In order to tackle the problem of multi-configurational character and double excitations, we have explored several approaches. The most evident way is to rely on multi-reference methods, which are naturally designed to address such scenarios. Among these methods, one can mention the complete-active-space self-consistent field (CASSCF) method [85], its second-order perturbatively-corrected variant (CASPT2) [289–291] and the second-order *n*-electron valence state perturbation theory (NEVPT2) formalism [292–294].

Another way to deal with double excitations and multi-reference situations is to use high level truncation of the EOM formalism [246, 295] of CC theory [148, 149, 151,

288, 296]. However, to provide a correct description of these situations, one has to take into account, at the very least, contributions from the triple excitations in the CC expansion [126, 130, 143, 144]. Although multi-reference CC methods have been designed [297–301], they are computationally demanding and remain far from being black-box.

In this context, an interesting alternative to multi-reference and CC methods is provided by selected configuration interaction (SCI) methods [302–315], which are able to provide near full CI (FCI) ground- and excited-state energies of small molecules [93, 130, 133, 143, 145, 316–331] . For example, the *Configuration Interaction using a Perturbative Selection made Iteratively* (CIPSI) method limits the exponential increase of the size of the CI expansion by retaining the most energetically relevant determinants only, using a second-order energetic criterion to select perturbatively determinants in the FCI space [304, 305, 307, 315, 326, 332]. Nonetheless, SCI methods remain very expensive and can be applied to a limited number of situations.

Finally, another option to deal with these chemical scenarios is to rely on the spin-flip formalism, established by Krylov in 2001 [94, 152–154], where one accesses the ground and doubly-excited states via a single (spin-flip) de-excitation and excitation from the lowest triplet state, respectively. One drawback of spin-flip methods is spin contamination (*i.e.*, the artificial mixing of electronic states with different spin multiplicities) due not only to the spin incompleteness in the spin-flip expansion but also to the potential spin contamination of the reference configuration [94]. One can address part of this issue by increasing the excitation order or by complementing the spin-incomplete configuration set with the missing configurations [164–171]. Note that one can quantify the polyradical character associated to a given electronic state using Head-Gordon's index [333] that provides a measure of the number of unpaired electrons [194].

In the present work, we define highly-accurate reference values and investigate the accuracy of each family of computational methods mentioned above on the automerization barrier and the low-lying excited states of CBD at the D_{2h} and D_{4h} ground-state geometries. Computational details are reported in Sec. 3.2. Section 3.3 is devoted to the discussion of our results. Finally, our conclusions are drawn in Sec. 3.4.

3.2 Computational details

3.2.1 Selected configuration interaction calculations

For the SCI calculations, we rely on the CIPSI algorithm implemented in QUANTUM PACKAGE [326], which iteratively select determinants in the FCI space. To treat electronic states on an equal footing, we use a state-averaged formalism where the ground and excited states are expanded with the same set of determinants but with different CI coefficients. Note that the determinant selection for these states are performed simultaneously via the protocol described in Refs. [326, 334].

For a given size of the variational wave function and for each electronic state, the CIPSI energy is the sum of two terms: the variational energy obtained by diagonalization of the CI matrix in the reference space E_{var} and a second-order perturbative correction E_{PT2} which estimates the contribution of the external determinants that are not included in the variational space at a given iteration. The sum of these two energies is, for large enough wave functions, an estimate of the FCI energy of a given state, *i.e.*, $E_{\text{FCI}} \approx E_{\text{var}} + E_{\text{PT2}}$. It is possible to estimate more precisely the FCI energy via an extrapolation procedure, where the variational energy is extrapolated to $E_{\text{PT2}} = 0$ [319]. Excitation energies are then computed as differences of extrapolated

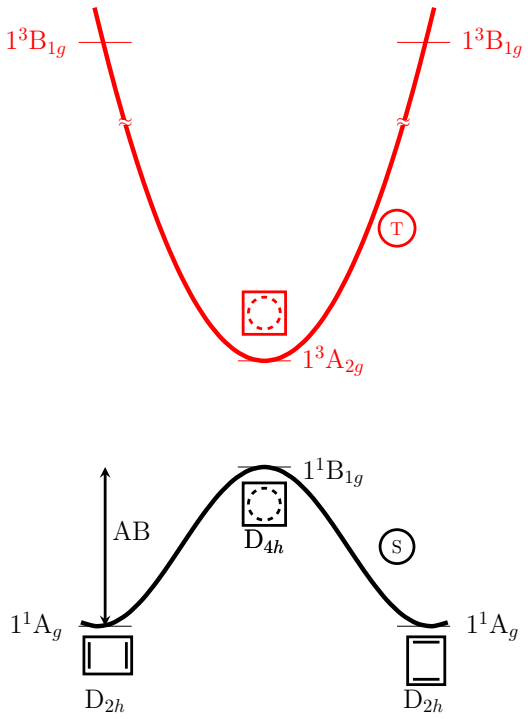

Figure 3.1: Pictorial representation of the ground and lowest excited states of CBD and the properties under investigation. The singlet ground state (S) and triplet (T) properties are colored in black and red, respectively. The automerization barrier (AB) is also represented.

total energies [130, 133, 143, 144, 324]. Additionally, an error bar can be provided thanks to a recent method based on Gaussian random variables that is described in Ref. [145]. This type of extrapolation procedures is now routine in SCI and similar techniques [325, 327, 335].

3.2.2 Coupled-cluster calculations

Coupled-cluster theory provides a hierarchy of methods that yields increasingly accurate ground state energies by ramping up the maximum excitation degree of the cluster operator: [86, 336–340] CC with singles and doubles (CCSD) [336, 341], CC with singles, doubles, and triples (CCSDT) [342, 343], CC with singles, doubles, triples, and quadruples (CCSDTQ) [148, 344, 345], etc. As mentioned above, CC theory can be extended to excited states via the EOM formalism [246, 295], where one diagonalizes the similarity-transformed Hamiltonian in a CI basis of excited determinants yielding the following systematically improvable family of methods for neutral excited states:[148, 149, 151, 245, 246, 288, 296, 342, 346–348] EOM-CCSD, EOM-CCSDT, EOM-CCSDTQ, etc. In the following, we will omit the prefix EOM for the sake of conciseness. Alternatively to the "complete" CC models, one can also employ the CC2 [146, 349], CC3 [146, 350], and CC4 [330, 351, 352] methods which can be seen as cheaper approximations of CCSD, CCSDT, and CCSDTQ by skipping the most expensive terms and avoiding the storage of high-order amplitudes.

Here, we have performed CC calculations using various codes. Typically, CCSD, CCSDT, and CCSDTQ as well as CC3 and CC4 calculations are achieved with CFOUR [352], with which only singlet excited states can be computed (except for CCSD). In some cases, we have also computed (singlet and triplet) excitation energies and

properties (such as the percentage of single excitations involved in a given transition, namely $\%T_1$) at the CC3 level with DALTON [353] and at the CCSDT level with MRCC [354].

To avoid having to perform multi-reference CC calculations or high-level CC calculations in the restricted open-shell or unrestricted formalisms, it is worth mentioning that, for the D_{4h} arrangement, we have considered the lowest *closed-shell* singlet state of A_g symmetry as reference. Hence, the open-shell ground state, 1^1B_{1g}, and the 1^1B_{2g} state appear as a de-excitation and an excitation, respectively. With respect to this closed-shell reference, 1^1B_{1g} has a dominant double excitation character, while 1^1B_{2g} has a dominant single excitation character, hence their contrasting convergence behaviors with respect to the order of the CC expansion (see below).

3.2.3 Multi-reference calculations

State-averaged CASSCF (SA-CASSCF) calculations are performed for vertical transition energies, whereas state-specific CASSCF is used for computing the automerization barrier [355]. For each excited state, a set of state-averaged orbitals is computed by taking into account the excited state of interest as well as the ground state (even if it has a different symmetry). Two active spaces have been considered: (i) a minimal (4e,4o) active space including the valence π orbitals, and (ii) an extended (12e,12o) active space where we have additionally included the σ_{CC} and σ^*_{CC} orbitals. For ionic excited states, like the 1^1B_{1g} state of CBD, it is particularly important to take into account the σ-π coupling [356–358].

On top of this CASSCF treatment, CASPT2 calculations are performed within the RS2 contraction scheme, while the NEVPT2 energies are computed within both the partially contracted (PC) and strongly contracted (SC) schemes [292–294]. Note that PC-NEVPT2 is theoretically more accurate than SC-NEVPT2 due to the larger number of external configurations and greater flexibility. In order to avoid the intruder state problem in CASPT2, a real-valued level shift of 0.3 E_h is set [85, 359], with an additional ionization-potential-electron-affinity (IPEA) shift of 0.25 E_h to avoid systematic underestimation of the vertical excitation energies [360–363]. For the sake of comparison and completeness, for the (4e,4o) active space, we also report (in Appendix C) multi-reference CI calculations including Davidson correction (MRCI+Q) [364, 365]. All these calculations are carried out with MOLPRO [355].

3.2.4 Spin-flip calculations

Within the spin-flip formalism, one considers the lowest triplet state as reference instead of the singlet ground state. Ground-state energies are then computed as sums of the triplet reference state energy and the corresponding de-excitation energy. Likewise, excitation energies with respect to the singlet ground state are computed as differences of excitation energies with respect to the reference triplet state.

Nowadays, spin-flip techniques are broadly accessible thanks to intensive developments in the electronic structure community (see Ref. [94] and references therein). Here, we explore the spin-flip version [181] of the algebraic-diagrammatic construction [75] (ADC) using the standard and extended second-order ADC schemes, SF-ADC(2)-s [79, 264] and SF-ADC(2)-x [79], as well as its third-order version, SF-ADC(3) [79, 84, 266]. These calculations are performed using Q-CHEM 5.4.1 [243]. The spin-flip version of our recently proposed composite approach, namely SF-ADC(2.5) [366], where one simply averages the SF-ADC(2)-s and SF-ADC(3) energies, is also tested in the following.

We have also carried out spin-flip calculations within the TD-DFT framework (SF-TD-DFT) [178]. The B3LYP [43, 45, 50], PBE0 [52, 367] and BH&HLYP global hybrid GGA functionals are considered, which contain 20%, 25%, 50% of exact exchange, respectively. These calculations are labeled as SF-TD-B3LYP, SF-TD-PBE0, and SF-TD-BH&HLYP in the following. Additionally, we have also computed SF-TD-DFT excitation energies using range-separated hybrid (RSH) functionals: CAM-B3LYP (19% of short-range exact exchange and 65% at long range) [368], LC-ωPBE08 (0% of short-range exact exchange and 100% at long range) [55], and ωB97X-V (16.7% of short-range exact exchange and 100% at long range) [369]. Finally, the hybrid meta-GGA functional M06-2X (54% of exact exchange) [370] and the RSH meta-GGA functional M11 (42.8% of short-range exact exchange and 100% at long range) [371] are also employed. Note that all SF-TD-DFT calculations are done within the Tamm-Dancoff approximation [372].

There also exist spin-flip extensions of EOM-CC methods [152, 172–175], and we consider here the spin-flip version of EOM-CCSD, named SF-EOM-CCSD [152]. Additionally, Manohar and Krylov introduced a non-iterative triples correction to EOM-CCSD and extended it to the spin-flip variant [173]. Two types of triples corrections were proposed: (i) EOM-CCSD(dT) that uses the diagonal elements of the similarity-transformed CCSD Hamiltonian, and (ii) EOM-CCSD(fT) where the Hartree-Fock orbital energies are considered instead.

All spin-flip calculations have been performed with Q-CHEM 5.4.1 [243]. Note that symmetry labels may vary as different packages use different standard orientations. Here, we have consistently followed the so-called Mulliken conventions [373].

3.2.5 Theoretical best estimates

When technically possible, each level of theory is tested with four Gaussian basis sets, namely, 6-31+G(d) and aug-cc-pVXZ with X = D, T, and Q [374]. This helps us to assess the convergence of each property with respect to the size of the basis set. More importantly, for each studied quantity (i.e., the automerization barrier and the vertical excitation energies), we provide a theoretical best estimate (TBE) established in the aug-cc-pVTZ basis. These TBEs are defined using extrapolated CCSDTQ/aug-cc-pVTZ values except in a single occasion where the NEVPT2(12,12) value is used.

The extrapolation of the CCSDTQ/aug-cc-pVTZ values is done via a "pyramidal" scheme, where we employ systematically the most accurate level of theory and the largest basis set available. The viability of this scheme lies on the transferability of basis set effects within wave function methods (see below). For example, when CC4/aug-cc-pVTZ and CCSDTQ/aug-cc-pVDZ data are available, we proceed via the following basis set extrapolation:

$$\Delta\tilde{E}^{\text{CCSDTQ}}_{\text{aug-cc-pVTZ}} = \Delta E^{\text{CCSDTQ}}_{\text{aug-cc-pVDZ}} + \left[\Delta E^{\text{CC4}}_{\text{aug-cc-pVTZ}} - \Delta E^{\text{CC4}}_{\text{aug-cc-pVDZ}}\right], \tag{3.1}$$

while, when only CCSDTQ/6-31G+(d) values are available, we further extrapolate the CCSDTQ/aug-cc-pVDZ value as follows:

$$\Delta\tilde{E}^{\text{CCSDTQ}}_{\text{aug-cc-pVDZ}} = \Delta E^{\text{CCSDTQ}}_{\text{6-31G+(d)}} + \left[\Delta E^{\text{CC4}}_{\text{aug-cc-pVDZ}} - \Delta E^{\text{CC4}}_{\text{6-31G+(d)}}\right]. \tag{3.2}$$

If we lack the CC4 data, we can follow the same philosophy and rely on CCSDT (for single excitations) or NEVPT2 (for double excitations). For example,

$$\Delta\tilde{E}^{\text{CC4}}_{\text{aug-cc-pVTZ}} = \Delta E^{\text{CC4}}_{\text{aug-cc-pVDZ}} + \left[\Delta E^{\text{CCSDT}}_{\text{aug-cc-pVTZ}} - \Delta E^{\text{CCSDT}}_{\text{aug-cc-pVDZ}}\right], \tag{3.3}$$

and so on. If neither CC4, nor CCSDT are feasible, then we rely on PC-NEVPT2(12,12). The procedures applied for each extrapolated value are explicitly mentioned as footnote in the tables. Note that, due to error bar inherently linked to the CIPSI calculations (see Sec. 3.2.1), these are mostly used as an additional safety net to further check the convergence of the CCSDTQ estimates. Additional tables gathering these TBEs as well as literature data for the automerization barrier and the vertical excitation energies can be found in Appendix C.

3.3 Results and discussion

3.3.1 Geometries

Two different sets of geometries obtained with different levels of theory are considered for the automerization barrier and the excited states of the CBD molecule. First, because the automerization barrier is obtained as a difference of energies computed at distinct geometries, it is paramount to obtain these at the same level of theory. However, due to the fact that the ground state of the square arrangement is a transition state of singlet open-shell nature, it is technically difficult to optimize the geometry with high-order CC methods. Therefore, we rely on CASPT2(12,12)/aug-cc-pVTZ for both the D_{2h} and D_{4h} ground-state structures. (Note that these optimizations are done without IPEA shift but with a level shift and a state-specific reference CASSCF wave function.) Second, because the vertical transition energies are computed for a particular equilibrium geometry, we can afford to use different methods for the rectangular and square structures. Hence, we rely on CC3/aug-cc-pVTZ to compute the equilibrium geometry of the 1^1A_g state in the rectangular (D_{2h}) arrangement and the restricted open-shell (RO) version of CCSD(T)/aug-cc-pVTZ to obtain the equilibrium geometry of the 1^3A_{2g} state in the square (D_{4h}) arrangement. These two geometries are the lowest-energy equilibrium structure of their respective spin manifold (see Fig. 3.1). The cartesian coordinates of these geometries are provided in Appendix C. Table 3.1 reports the key geometrical parameters obtained at these levels of theory as well as previous geometries computed by Manohar and Krylov at the CCSD(T)/cc-pVTZ level. One notes globally satisfying agreement between the tested methods with variations of the order of 0.01 Å only.

3.3.2 Automerization barrier

The results concerning the automerization barrier are reported in Table 3.2 for various basis sets and shown in Fig. 3.2 for the aug-cc-pVTZ basis. Our TBE with this basis set is 8.93 kcal mol^{-1}, which is in excellent agreement with previous studies [259, 260, 285, 286, 375, 376] (see Appendix C).

First, one can see large variations of the energy barrier at the SF-TD-DFT level, with differences as large as 10 kcal mol^{-1} between the different functionals for a given basis set. Nonetheless, it is clear that the performance of a given functional is directly linked to the amount of exact exchange at short range. Indeed, hybrid functionals with approximately 50% of short-range exact exchange (*e.g.*, BH&HLYP, M06-2X, and M11) perform significantly better than the functionals having a small

Table 3.1: Optimized geometries associated with several states of CBD computed with various levels of theory. Bond lengths are in Å and angles (∠) are in degree.

State	Method	C=C	C−C	C−H	∠H−C=C
D_{2h} (1^1A_g)	CASPT2(12,12)/aug-cc-pVTZ[1]	1.354	1.566	1.077	134.99
	CC3/aug-cc-pVTZ[1]	1.344	1.565	1.076	135.08
	CCSD(T)/cc-pVTZ[2]	1.343	1.566	1.074	135.09
D_{4h} (1^1B_{1g})	CASPT2(12,12)/aug-cc-pVTZ[1]	1.449	1.449	1.076	135.00
D_{4h} (1^3A_{2g})	CASPT2(12,12)/aug-cc-pVTZ[1]	1.445	1.445	1.076	135.00
	RO-CCSD(T)/aug-cc-pVTZ[1]	1.439	1.439	1.075	135.00
	RO-CCSD(T)/cc-pVTZ[2]	1.439	1.439	1.073	135.00

[1] This work.
[2] From Ref. [173].

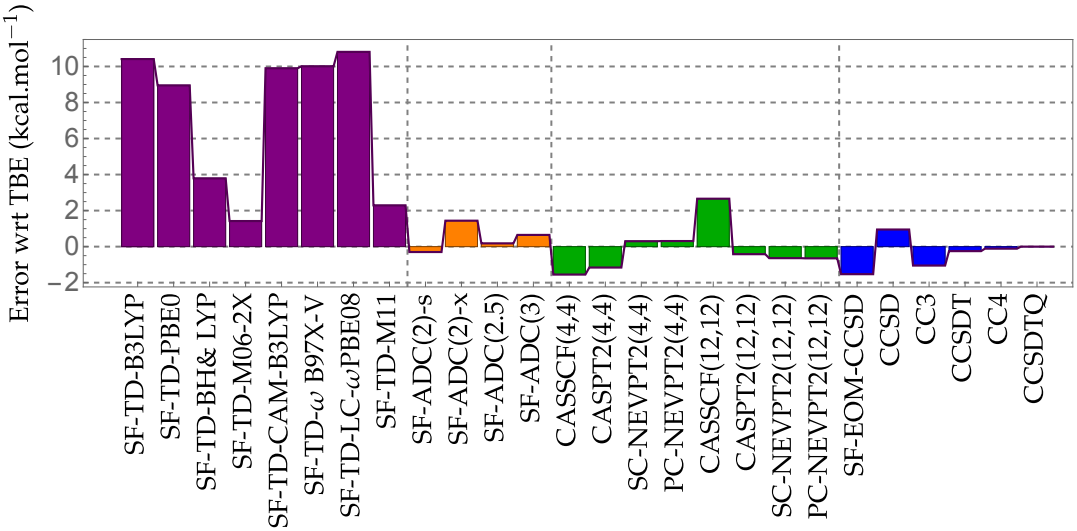

Figure 3.2: Error (with respect to the TBE) in the automerization barrier (in kcal mol^{-1}) of CBD at various levels of theory using the aug-cc-pVTZ basis. See Appendix C for the total energies.

Table 3.2: Automerization barrier (in kcal mol^{-1}) of CBD computed with various computational methods and basis sets. The values in square parenthesis have been obtained by extrapolation via the procedure described in the corresponding footnote. The TBE/aug-cc-pVTZ value is highlighted in bold.

	Basis sets			
Method	6-31+G(d)	aug-cc-pVDZ	aug-cc-pVTZ	aug-cc-pVQZ
SF-TD-B3LYP	18.59	18.64	19.34	19.34
SF-TD-PBE0	17.18	17.19	17.88	17.88
SF-TD-BH&HLYP	11.90	12.02	12.72	12.73
SF-TD-M06-2X	9.32	9.62	10.35	10.37
SF-TD-CAM-B3LYP	18.05	18.10	18.83	18.83
SF-TD-ωB97X-V	18.26	18.24	18.94	18.92
SF-TD-LC-ωPBE08	19.05	18.98	19.74	19.71
SF-TD-M11	11.03	10.25	11.22	11.12
SF-ADC(2)-s	6.69	6.98	8.63	
SF-ADC(2)-x	8.63	8.96	10.37	
SF-ADC(2.5)	7.36	7.76	9.11	
SF-ADC(3)	8.03	8.54	9.58	
SF-EOM-CCSD	5.86	6.27	7.40	
CASSCF(4,4)	6.17	6.59	7.38	7.41
CASPT2(4,4)	6.56	6.87	7.77	7.93
SC-NEVPT2(4,4)	7.95	8.31	9.23	9.42
PC-NEVPT2(4,4)	7.95	8.33	9.24	9.41
CASSCF(12,12)	10.19	10.75	11.59	11.62
CASPT2(12,12)	7.24	7.53	8.51	8.71
SC-NEVPT2(12,12)	7.10	7.32	8.29	8.51
PC-NEVPT2(12,12)	7.12	7.33	8.28	8.49
CCSD	8.31	8.80	9.88	10.10
CC3	6.59	6.89	7.88	8.06
CCSDT	7.26	7.64	8.68	[8.86][1]
CC4	7.40	7.78	[8.82][2]	[9.00][3]
CCSDTQ	7.51	[7.89][4]	[**8.93**][5]	[9.11][6]

[1] Value obtained using CCSDT/aug-cc-pVTZ corrected by the difference between CC3/aug-cc-pVQZ and CC3/aug-cc-pVTZ.
[2] Value obtained using CC4/aug-cc-pVDZ corrected by the difference between CCSDT/aug-cc-pVTZ and CCSDT/aug-cc-pVDZ.
[3] Value obtained using CC4/aug-cc-pVTZ corrected by the difference between CCSDT/aug-cc-pVQZ and CCSDT/aug-cc-pVTZ.
[4] Value obtained using CCSDTQ/6-31+G(d) corrected by the difference between CC4/aug-cc-pVDZ basis and CC4/6-31+G(d).
[5] TBE value obtained using CCSDTQ/aug-cc-pVDZ corrected by the difference between CC4/aug-cc-pVTZ and CC4/aug-cc-pVDZ.
[6] Value obtained using CCSDTQ/aug-cc-pVTZ corrected by the difference between CC4/aug-cc-pVQZ and CC4/aug-cc-pVTZ.

fraction of short-range exact exchange (*e.g.*, B3LYP, PBE0, CAM-B3LYP, ωB97X-V, and LC-ωPBE08). However, they are still off by 1–4 kcal mol^{-1} from the TBE reference value, the most accurate result being obtained with M06-2X. For the RSH functionals, the automerization barrier is much less sensitive to the amount of longe-range exact exchange. Another important feature of SF-TD-DFT is the fast convergence of the energy barrier with the size of the basis set [377]. With the augmented double-ζ basis, the SF-TD-DFT results are basically converged to sub-kcal mol^{-1} accuracy, which is a drastic improvement compared to wave function approaches where this type of convergence is reached with the augmented triple-ζ basis only.

For the SF-ADC family of methods, the energy differences are much smaller with a maximum deviation of 2 kcal mol^{-1} between different versions. In particular, we observe that SF-ADC(2)-s and SF-ADC(3), which respectively scale as $\mathcal{O}(N^5)$ and $\mathcal{O}(N^6)$ (where N is the number of basis functions), under- and overestimate the automerization barrier, making SF-ADC(2.5) a good compromise with an error of only 0.18 kcal mol^{-1} compared to the TBE/aug-cc-pVTZ basis reference value. Nonetheless, at a $\mathcal{O}(N^5)$ computational scaling, SF-ADC(2)-s is particularly accurate, even compared to high-order CC methods (see below). We note that SF-ADC(2)-x [which scales as $\mathcal{O}(N^6)$] is probably not worth its extra cost [as compared to SF-ADC(2)-s] as it overestimates the energy barrier even more than SF-ADC(3). This behavior was previously reported by Dreuw's group [79, 84, 378]. Overall, even with the best exchange-correlation functional, SF-TD-DFT is clearly outperformed by the more expensive SF-ADC models.

We observe that SF-EOM-CCSD/aug-cc-pVTZ tends to underestimate by about 1.5 kcal mol^{-1} the energy barrier compared to the TBE, an observation in agreement with previous results by Manohar and Krylov [173]. This can be alleviated by including the triples correction with SF-EOM-CCSD(fT) and SF-EOM-CCSD(dT)(see Appendix C where we have reported the data from Ref. [173]). We also note that the SF-EOM-CCSD values for the energy barrier are close to the ones obtained with the more expensive (standard) CC3 method, yet less accurate than values computed with the cheaper SF-ADC(2)-s formalism. Note that, in contrast to a previous statement [173], the (fT) correction performs better than the (dT) correction for the energy barrier. However, for the excited states, the situation is reversed (see below).

Concerning the multi-reference approaches with the minimal (4e,4o) active space, the TBEs are bracketed by the CASPT2 and NEVPT2 values that differ by approximately 1.5 kcal mol^{-1} for all bases. In this case, the NEVPT2 values are fairly accurate with differences below half a kcal mol^{-1} compared to the TBEs. The CASSCF results predict an even lower barrier than CASPT2 due to the well known lack of dynamical correlation at the CASSCF level. For the larger (12e,12o) active space, we see larger differences of the order of 3 kcal mol^{-1} (through all the bases) between CASSCF and the second-order variants (CASPT2 and NEVPT2). However, the deviations between CASPT2(12,12) and NEVPT2(12,12) are much smaller than with the minimal active space, with an energy difference of around 0.1–0.2 kcal mol^{-1} for all bases, CASPT2 being slightly more accurate than NEVPT2 in this case. For each basis set, both CASPT2(12,12) and NEVPT2(12,12) are less than a kcal mol^{-1} away from the TBEs. For the two active spaces that we have considered here, the PC- and SC-NEVPT2 schemes provide nearly identical barriers independently of the size of the one-electron basis.

Finally, for the CC family of methods, we observe the usual systematic improvement following the series CCSD $<$ CC3 $<$ CCSDT $<$ CC4 $<$ CCSDTQ, which parallels their increase in computational cost: $\mathcal{O}(N^6)$, $\mathcal{O}(N^7)$, $\mathcal{O}(N^8)$, $\mathcal{O}(N^9)$, and $\mathcal{O}(N^{10})$, respectively. Note that the introduction of the triple excitations is clearly mandatory

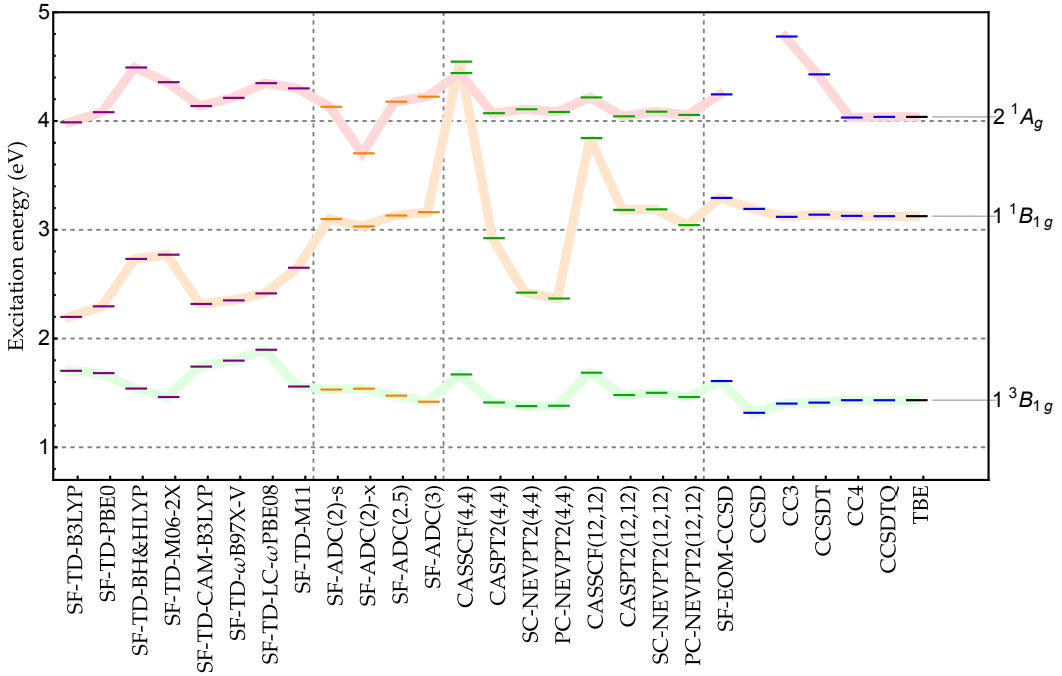

Figure 3.3: Vertical excitation energies of the 1^3B_{1g}, 1^1B_{1g}, and 2^1A_g states at the D_{2h} rectangular equilibrium geometry of the 1^1A_g ground state using the aug-cc-pVTZ basis. See C for the raw data.

to have an accuracy beyond SF-TD-DFT, and we observe that CCSDT is definitely an improvement over its cheaper, approximated version, CC3.

3.3.3 Vertical excitation energies

3.3.3.1 D_{2h} rectangular geometry

Table 3.3 reports, at the D_{2h} rectangular equilibrium geometry of the 1^1A_g ground state, the vertical transition energies associated with the 1^3B_{1g}, 1^1B_{1g}, and 2^1A_g states obtained using the spin-flip formalism, while Table 3.4 gathers the same quantities obtained with the multi-reference, CC, and CIPSI methods. Considering the aug-cc-pVTZ basis, the evolution of the vertical excitation energies with respect to the level of theory is illustrated in Fig. 3.3.

At the CC3/aug-cc-pVTZ level, the percentage of single excitation involved in the 1^3B_{1g}, 1^1B_{1g}, and 2^1A_g are 99%, 95%, and 1%, respectively. Therefore, the two formers are dominated by single excitations, while the latter state corresponds to a genuine double excitation.

First, let us discuss basis set effects at the SF-TD-DFT level (Table 3.3). As expected, these are found to be small and the results are basically converged to the complete basis set limit with the triple-ζ basis, which is definitely not the case for the wave function methods [379]. Regarding now the accuracy of the vertical excitation energies, again, we see that, for 1^3B_{1g} and 1^1B_{1g}, the functionals with the largest amount of short-range exact exchange (*e.g.*, BH&HLYP, M06-2X, and M11) are the most accurate. Functionals with a large share of exact exchange are known to perform best in the SF-TD-DFT framework as the Hartree-Fock exchange term is the only non-vanishing term in the spin-flip block [178]. However, their overall accuracy remains average especially for the singlet states, 1^1B_{1g} and 2^1A_g, with error of the order of 0.2–0.5 eV

Table 3.3: Spin-flip TD-DFT and ADC vertical excitation energies (with respect to the singlet 1^1A_g ground state) of the 1^3B_{1g}, 1^1B_{1g}, and 2^1A_g states of CBD at the D_{2h} rectangular equilibrium geometry of the 1^1A_g ground state.

		Excitation energies (eV)		
Method	Basis	1^3B_{1g}	1^1B_{1g}	2^1A_g
SF-TD-B3LYP	6-31+G(d)	1.706	2.211	3.993
	aug-cc-pVDZ	1.706	2.204	3.992
	aug-cc-pVTZ	1.703	2.199	3.988
	aug-cc-pVQZ	1.703	2.199	3.989
SF-TD-PBE0	6-31+G(d)	1.687	2.314	4.089
	aug-cc-pVDZ	1.684	2.301	4.085
	aug-cc-pVTZ	1.682	2.296	4.081
	aug-cc-pVQZ	1.682	2.296	4.079
SF-TD-BH&HLYP	6-31+G(d)	1.552	2.779	4.428
	aug-cc-pVDZ	1.546	2.744	4.422
	aug-cc-pVTZ	1.540	2.732	4.492
	aug-cc-pVQZ	1.540	2.732	4.415
SF-TD-M06-2X	6-31+G(d)	1.477	2.835	4.378
	aug-cc-pVDZ	1.467	2.785	4.360
	aug-cc-pVTZ	1.462	2.771	4.357
	aug-cc-pVQZ	1.458	2.771	4.352
SF-TD-CAM-B3LYP	6-31+G(d)	1.750	2.337	4.140
	aug-cc-pVDZ	1.745	2.323	4.140
	aug-cc-pVTZ	1.742	2.318	4.138
	aug-cc-pVQZ	1.743	2.319	4.138
SF-TD-ωB97X-V	6-31+G(d)	1.810	2.377	4.220
	aug-cc-pVDZ	1.800	2.356	4.217
	aug-cc-pVTZ	1.797	2.351	4.213
	aug-cc-pVQZ	1.797	2.351	4.213
SF-TD-LC-ωPBE08	6-31+G(d)	1.917	2.445	4.353
	aug-cc-pVDZ	1.897	2.415	4.346
	aug-cc-pVTZ	1.897	2.415	4.348
	aug-cc-pVQZ	1.897	2.415	4.348
SF-TD-M11	6-31+G(d)	1.566	2.687	4.292
	aug-cc-pVDZ	1.546	2.640	4.267
	aug-cc-pVTZ	1.559	2.651	4.300
	aug-cc-pVQZ	1.557	2.650	4.299
SF-ADC(2)-s	6-31+G(d)	1.577	3.303	4.196
	aug-cc-pVDZ	1.513	3.116	4.114
	aug-cc-pVTZ	1.531	3.099	4.131
	aug-cc-pVQZ	1.544	3.101	4.140
SF-ADC(2)-x	6-31+G(d)	1.557	3.232	3.728
	aug-cc-pVDZ	1.524	3.039	3.681
	aug-cc-pVTZ	1.539	3.031	3.703
SF-ADC(2.5)	6-31+G(d)	1.496	3.328	4.219
	aug-cc-pVDZ	1.468	3.148	4.161
	aug-cc-pVTZ	1.475	3.131	4.178
SF-ADC(3)	6-31+G(d)	1.435	3.352	4.242
	aug-cc-pVDZ	1.422	3.180	4.208
	aug-cc-pVTZ	1.419	3.162	4.224
SF-EOM-CCSD	6-31+G(d)	1.663	3.515	4.275
	aug-cc-pVDZ	1.611	3.315	4.216
	aug-cc-pVTZ	1.609	3.293	4.245

Table 3.4: Vertical excitation energies (with respect to the 1^1A_g ground state) of the 1^3B_{1g}, 1^1B_{1g}, and 2^1A_g states of CBD at the D_{2h} rectangular equilibrium geometry of the 1^1A_g ground state. The values in square parenthesis have been obtained by extrapolation via the procedure described in the corresponding footnote. The TBE/aug-cc-pVTZ values are highlighted in bold.

		Excitation energies (eV)		
Method	Basis	1^3B_{1g}	1^1B_{1g}	2^1A_g
CASSCF(4,4)	6-31+G(d)	1.662	4.657	4.439
	aug-cc-pVDZ	1.672	4.563	4.448
	aug-cc-pVTZ	1.670	4.546	4.441
	aug-cc-pVQZ	1.671	4.549	4.440
CASPT2(4,4)	6-31+G(d)	1.440	3.162	4.115
	aug-cc-pVDZ	1.414	2.971	4.068
	aug-cc-pVTZ	1.412	2.923	4.072
	aug-cc-pVQZ	1.417	2.911	4.081
SC-NEVPT2(4,4)	6-31+G(d)	1.407	2.707	4.145
	aug-cc-pVDZ	1.381	2.479	4.109
	aug-cc-pVTZ	1.379	2.422	4.108
	aug-cc-pVQZ	1.384	2.408	4.116
PC-NEVPT2(4,4)	6-31+G(d)	1.409	2.652	4.120
	aug-cc-pVDZ	1.384	2.424	4.084
	aug-cc-pVTZ	1.382	2.368	4.083
	aug-cc-pVQZ	1.387	2.353	4.091
CASSCF(12,12)	6-31+G(d)	1.675	3.924	4.220
	aug-cc-pVDZ	1.685	3.856	4.221
	aug-cc-pVTZ	1.686	3.844	4.217
	aug-cc-pVQZ	1.687	3.846	4.216
CASPT2(12,12)	6-31+G(d)	1.508	3.407	4.099
	aug-cc-pVDZ	1.489	3.256	4.044
	aug-cc-pVTZ	1.480	3.183	4.043
	aug-cc-pVQZ	1.482	3.163	4.047
SC-NEVPT2(12,12)	6-31+G(d)	1.522	3.409	4.130
	aug-cc-pVDZ	1.511	3.266	4.093
	aug-cc-pVTZ	1.501	3.188	4.086
	aug-cc-pVQZ	1.503	3.167	4.088
PC-NEVPT2(12,12)	6-31+G(d)	1.487	3.296	4.103
	aug-cc-pVDZ	1.472	3.141	4.064
	aug-cc-pVTZ	1.462	3.063	4.056
	aug-cc-pVQZ	1.464	3.043	4.059
CCSD	6-31+G(d)	1.346	3.422	
	aug-cc-pVDZ	1.319	3.226	
	aug-cc-pVTZ	1.317	3.192	
	aug-cc-pVQZ	1.323	3.187	
CC3	6-31+G(d)	1.420	3.341	4.658
	aug-cc-pVDZ	1.396	3.158	4.711
	aug-cc-pVTZ	1.402	3.119	4.777
	aug-cc-pVQZ	1.409	3.113	4.774
CCSDT	6-31+G(d)	1.442	3.357	4.311
	aug-cc-pVDZ	1.411	3.175	4.327
	aug-cc-pVTZ	1.411	3.139	4.429
CC4	6-31+G(d)		3.343	4.067
	aug-cc-pVDZ		3.164	4.040
	aug-cc-pVTZ		[3.128][1]	[4.032][2]
CCSDTQ	6-31+G(d)	1.464	3.340	4.073
	aug-cc-pVDZ	[1.433][3]	[3.161][4]	[4.046][4]
	aug-cc-pVTZ	[**1.433**][5]	[**3.125**][6]	[**4.038**][6]
CIPSI	6-31+G(d)	1.486 ± 0.005	3.348 ± 0.024	4.084 ± 0.012
	aug-cc-pVDZ	1.458 ± 0.009	3.187 ± 0.035	4.04 ± 0.04
	aug-cc-pVTZ	1.461 ± 0.030	3.142 ± 0.035	4.03 ± 0.09

[1] Value obtained using CC4/aug-cc-pVDZ corrected by the difference between CCSDT/aug-cc-pVTZ and CCSDT/aug-cc-pVDZ.
[2] Value obtained using CC4/aug-cc-pVDZ corrected by the difference between PC-NEVPT2(12,12)/aug-cc-pVTZ and PC-NEVPT2(12,12)/aug-cc-pVDZ.
[3] Value obtained using CCSDTQ/6-31+G(d) corrected by the difference between CCSDT/aug-cc-pVDZ and CCSDT/6-31+G(d).
[4] Value obtained using CCSDTQ/6-31+G(d) corrected by the difference between CC4/aug-cc-pVDZ and CC4/6-31+G(d).
[5] Value obtained using CCSDTQ/aug-cc-pVDZ corrected by the difference between CCSDT/aug-cc-pVTZ and CCSDT/aug-cc-pVDZ.
[6] TBE value obtained using CCSDTQ/aug-cc-pVDZ corrected by the difference between CC4/aug-cc-pVTZ and CC4/aug-cc-pVDZ.

compared to the TBEs. The triplet state, 1^3B_{1g}, is much better described with errors below 0.1 eV. Surprisingly, for the doubly-excited state, 2^1A_g, the hybrid functionals with a low percentage of exact exchange (B3LYP and PBE0) are the best performers with absolute errors below 0.05 eV. Note that, as evidenced by the data reported in Appendix C, none of these states exhibit a strong spin contamination.

Second, we discuss the various SF-ADC schemes (Table 3.3), *i.e.*, SF-ADC(2)-s, SF-ADC(2)-x, and SF-ADC(3). At the SF-ADC(2)-s level, going from the smallest 6-31+G(d) basis to the largest aug-cc-pVQZ basis induces a small decrease in vertical excitation energies of 0.03 eV (0.06 eV) for the 1^3B_{1g} (2^1A_g) state, while the transition energy of the 1^1B_{1g} state drops more significantly by about 0.2 eV. [The SF-ADC(2)-x and SF-ADC(3) calculations with aug-cc-pVQZ were not feasible with our computational resources.] These basis set effects are fairly transferable to the other wave function methods that we have considered here. This further motivates the "pyramidal" extrapolation scheme that we have employed to produce the TBE values (see Sec. 3.2.5). Again, the extended version, SF-ADC(2)-x, does not seem to be relevant in the present context with much larger errors than the other schemes. Also, as reported previously [366], SF-ADC(2)-s and SF-ADC(3) have mirror error patterns making SF-ADC(2.5) particularly accurate except for the doubly-excited state 2^1A_g where the error with respect to the TBE (0.140 eV) is larger than the SF-ADC(2)-s error (0.093 eV).

Interestingly, we observe that the SF-EOM-CCSD excitation energies are systematically larger than the TBEs by approximately 0.2 eV with a nice consistency throughout the various (singly- and doubly-) excited states. Moreover, SF-EOM-CCSD excitation energies are somehow closer to their SF-ADC(2)-s analogs (with an energy difference of about 0.1 eV) than the other schemes as already noticed by LeFrançois and co-workers [181]. We see that the SF-EOM-CCSD excitations energies for the triplet state are larger of about 0.3 eV compared to the CCSD ones, which was also pointed out in the study of Manohar and Krylov [173]. Again, our SF-EOM-CCSD results are very similar to the ones obtained in previous studies [173, 181]. We can logically expect similar trend for SF-EOM-CCSD(fT) and SF-EOM-CCSD(dT) that lower the excitation energies and tend to be in better agreement with respect to the TBE (see Appendix C). Note that the (dT) correction slightly outperforms the (fT) correction as previously observed [173] and theoretically expected.

Let us now move to the discussion of the results obtained with standard wave function methods that are reported in Table 3.4. Regarding the multi-reference calculations, the most striking result is the poor description of the 1^1B_{1g} ionic state, especially with the (4e,4o) active space where CASSCF predicts this state higher in energy than the 2^1A_g state. Of course, the PT2 correction is able to correct the state ordering problem but cannot provide quantitative excitation energies due to the poor zeroth-order treatment. Another ripple effect of the unreliability of the reference wave function is the large difference between CASPT2 and NEVPT2 that differ by half an eV. This feature is characteristic of the inadequacy of the active space to model such a state. Additional MRCI and MRCI+Q calculations (reported in Appendix C) confirm this. For the two other states, 1^3B_{1g} and 2^1A_g, the errors at the CASPT2(4,4) and NEVPT2(4,4) levels are much smaller (below 0.1 eV). Using a larger active space resolves most of these issues: CASSCF predicts the correct state ordering (though the ionic state is still badly described in term of energetics), CASPT2 and NEVPT2 excitation energies are much closer, and their accuracy is often improved (especially for the triplet and doubly-excited states) although it is difficult to reach chemical accuracy (*i.e.*, an error below 0.043 eV) on a systematic basis.

Finally, for the CC models (Table 3.4), the two states with a large $\%T_1$ value,

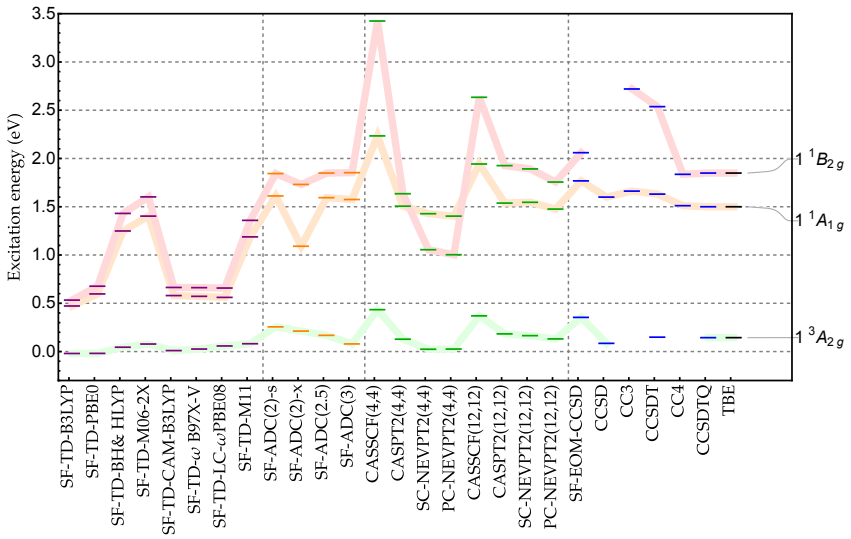

Figure 3.4: Vertical excitation energies (in eV) of the 1^3A_{2g}, 1^1A_{1g}, and 1^1B_{2g} states at the D_{4h} square-planar equilibrium geometry of the 1^3A_{2g} state using the aug-cc-pVTZ basis. See Appendix C for the raw data.

1^3B_{1g} and 1^1B_{1g}, are already extremely accurate at the CC3 level, and systematically improved by CCSDT and CC4. This trend is in line with the observations made on the QUEST database [145]. For the doubly-excited state, 2^1A_g, the convergence of the CC expansion is much slower but it is worth pointing out that the inclusion of approximate quadruples via CC4 is particularly effective, as observed in an earlier work [330]. The CCSDTQ excitation energies (which are used to define the TBEs) are systematically within the error bar of the CIPSI extrapolations, which confirms the outstanding performance of CC methods that include quadruple excitations in the context of excited states.

3.3.3.2 D_{4h} square-planar geometry

In Table 3.5, we report, at the D_{4h} square planar equilibrium geometry of the 1^3A_{2g} state, the vertical transition energies associated with the 1^3A_{2g}, 1^1A_{1g}, and 1^1B_{2g} states obtained using the spin-flip formalism, while Table 3.6 gathers the same quantities obtained with the multi-reference, CC, and CIPSI methods. The vertical excitation energies computed at various levels of theory are depicted in Fig. 3.4 for the aug-cc-pVTZ basis. Unfortunately, due to technical limitations, we could not compute $\%T_1$ values associated with the 1^3A_{2g}, 1^1A_{1g}, and 1^1B_{2g} excited states in the D_{4h} symmetry. However, it is clear from the inspection of the wave function that, with respect to the 1^1B_{1g} ground state, 1^3A_{2g} and 1^1B_{2g} are dominated by single excitations, while 1^1A_{1g} has a strong double excitation character.

As for the previous geometry we start by discussing the SF-TD-DFT results (Table 3.5), and in particular the singlet-triplet gap, *i.e.*, the energy difference between 1^1B_{1g} and 1^3A_{2g}. For all functionals, this gap is small (basically below 0.1 eV while the TBE value is 0.144 eV) but it is worth mentioning that B3LYP and PBE0 incorrectly deliver a negative singlet-triplet gap (hence a triplet ground state at this geometry). Increasing the fraction of exact exchange in hybrids or relying on RSHs (even with a small amount of short-range exact exchange) allows to recover a positive gap and a singlet ground state. At the SF-TD-DFT level, the energy gap between the two singlet excited states, 1^1A_{1g} and 1^1B_{2g}, is particularly small and grows moderately

Table 3.5: Spin-flip TD-DFT and ADC vertical excitation energies (with respect to the singlet 1^1B_{1g} ground state) of the 1^3A_{2g}, 1^1A_{1g}, and 1^1B_{2g} states of CBD at the D_{4h} square-planar equilibrium geometry of the 1^3A_{2g} state.

		Excitation energies (eV)		
Method	Basis	1^3A_{2g}	1^1A_{1g}	1^1B_{2g}
SF-TD-B3LYP	6-31+G(d)	−0.016	0.487	0.542
	aug-cc-pVDZ	−0.019	0.477	0.536
	aug-cc-pVTZ	−0.020	0.472	0.533
	aug-cc-pVQZ	−0.020	0.473	0.533
SF-TD-PBE0	6-31+G(d)	−0.012	0.618	0.689
	aug-cc-pVDZ	−0.016	0.602	0.680
	aug-cc-pVTZ	−0.019	0.597	0.677
	aug-cc-pVQZ	−0.018	0.597	0.677
SF-TD-BH&HLYP	6-31+G(d)	0.064	1.305	1.458
	aug-cc-pVDZ	0.051	1.260	1.437
	aug-cc-pVTZ	0.045	1.249	1.431
	aug-cc-pVQZ	0.046	1.250	1.432
SF-TD-M06-2X	6-31+G(d)	0.102	1.476	1.640
	aug-cc-pVDZ	0.086	1.419	1.611
	aug-cc-pVTZ	0.078	1.403	1.602
	aug-cc-pVQZ	0.079	1.408	1.607
SF-TD-CAM-B3LYP	6-31+G(d)	0.021	0.603	0.672
	aug-cc-pVDZ	0.012	0.585	0.666
	aug-cc-pVTZ	0.010	0.580	0.664
	aug-cc-pVQZ	0.010	0.580	0.664
SF-TD-ωB97X-V	6-31+G(d)	0.040	0.600	0.670
	aug-cc-pVDZ	0.029	0.576	0.664
	aug-cc-pVTZ	0.026	0.572	0.662
	aug-cc-pVQZ	0.026	0.572	0.662
SF-TD-LC-ωPBE08	6-31+G(d)	0.078	0.593	0.663
	aug-cc-pVDZ	0.060	0.563	0.659
	aug-cc-pVTZ	0.058	0.561	0.658
	aug-cc-pVQZ	0.058	0.561	0.659
SF-TD-M11	6-31+G(d)	0.102	1.236	1.374
	aug-cc-pVDZ	0.087	1.196	1.362
	aug-cc-pVTZ	0.081	1.188	1.359
	aug-cc-pVQZ	0.080	1.185	1.357
SF-ADC(2)-s	6-31+G(d)	0.345	1.760	2.096
	aug-cc-pVDZ	0.269	1.656	1.894
	aug-cc-pVTZ	0.256	1.612	1.844
SF-ADC(2)-x	6-31+G(d)	0.264	1.181	1.972
	aug-cc-pVDZ	0.216	1.107	1.760
	aug-cc-pVTZ	0.212	1.091	1.731
SF-ADC(2.5)	6-31+G(d)	0.234	1.705	2.087
	aug-cc-pVDZ	0.179	1.614	1.886
	aug-cc-pVTZ	0.168	1.594	1.849
SF-ADC(3)	6-31+G(d)	0.123	1.650	2.078
	aug-cc-pVDZ	0.088	1.571	1.878
	aug-cc-pVTZ	0.079	1.575	1.853
SF-EOM-CCSD	6-31+G(d)	0.446	1.875	2.326
	aug-cc-pVDZ	0.375	1.776	2.102
	aug-cc-pVTZ	0.354	1.768	2.060

Table 3.6: Vertical excitation energies (with respect to the 1^1B_{1g} ground state) of the 1^3A_{2g}, 1^1A_{1g}, and 1^1B_{2g} states of CBD at the D_{4h} square-planar equilibrium geometry of the 1^3A_{2g} state. The values in square brackets have been obtained by extrapolation via the procedure described in the corresponding footnote. The TBE/aug-cc-pVTZ values are highlighted in bold.

		Excitation energies (eV)		
Method	Basis	1^3A_{2g}	1^1A_{1g}	1^1B_{2g}
CASSCF(4,4)	6-31+G(d)	0.447	2.257	3.549
	aug-cc-pVDZ	0.438	2.240	3.443
	aug-cc-pVTZ	0.434	2.234	3.424
	aug-cc-pVQZ	0.435	2.235	3.427
CASPT2(4,4)	6-31+G(d)	0.176	1.588	1.899
	aug-cc-pVDZ	0.137	1.540	1.708
	aug-cc-pVTZ	0.128	1.506	1.635
	aug-cc-pVQZ	0.128	1.498	1.612
SC-NEVPT2(4,4)	6-31+G(d)	0.083	1.520	1.380
	aug-cc-pVDZ	0.037	1.465	1.140
	aug-cc-pVTZ	0.024	1.428	1.055
	aug-cc-pVQZ	0.024	1.420	1.030
PC-NEVPT2(4,4)	6-31+G(d)	0.085	1.496	1.329
	aug-cc-pVDZ	0.039	1.440	1.088
	aug-cc-pVTZ	0.026	1.403	1.003
	aug-cc-pVQZ	0.026	1.395	0.977
CASSCF(12,12)	6-31+G(d)	0.386	1.974	2.736
	aug-cc-pVDZ	0.374	1.947	2.649
	aug-cc-pVTZ	0.370	1.943	2.634
	aug-cc-pVQZ	0.371	1.945	2.637
CASPT2(12,12)	6-31+G(d)	0.235	1.635	2.170
	aug-cc-pVDZ	0.203	1.588	2.015
	aug-cc-pVTZ	0.183	1.538	1.926
	aug-cc-pVQZ	0.179	1.522	1.898
SC-NEVPT2(12,12)	6-31+G(d)	0.218	1.644	2.143
	aug-cc-pVDZ	0.189	1.600	1.991
	aug-cc-pVTZ	0.165	1.546	1.892
	aug-cc-pVQZ	0.160	1.529	1.862
PC-NEVPT2(12,12)	6-31+G(d)	0.189	1.579	2.020
	aug-cc-pVDZ	0.156	1.530	1.854
	aug-cc-pVTZ	0.131	1.476	1.756
	aug-cc-pVQZ	0.126	1.460	1.727
CCSD	6-31+G(d)	0.148	1.788	
	aug-cc-pVDZ	0.100	1.650	
	aug-cc-pVTZ	0.085	1.600	
	aug-cc-pVQZ	0.084	1.588	
CC3	6-31+G(d)		1.809	2.836
	aug-cc-pVDZ		1.695	2.646
	aug-cc-pVTZ		1.662	2.720
CCSDT	6-31+G(d)	0.210	1.751	2.565
	aug-cc-pVDZ	0.165	1.659	2.450
	aug-cc-pVTZ	0.149	1.631	2.537
CC4	6-31+G(d)		1.604	2.121
	aug-cc-pVDZ		1.539	1.934
	aug-cc-pVTZ		[1.511][1]	[1.836][2]
CCSDTQ	6-31+G(d)	0.205	1.593	2.134
	aug-cc-pVDZ	[0.160][3]	[1.528][4]	[1.947][4]
	aug-cc-pVTZ	[**0.144**][5]	[**1.500**][6]	[**1.849**][6]
CIPSI	6-31+G(d)	0.201 ± 0.003	1.602 ± 0.007	2.13 ± 0.04
	aug-cc-pVDZ	0.157 ± 0.003	1.587 ± 0.005	2.102 ± 0.027
	aug-cc-pVTZ	0.17 ± 0.03	1.63 ± 0.05	

[1] Value obtained using CC4/aug-cc-pVDZ corrected by the difference between CCSDT/aug-cc-pVTZ and CCSDT/aug-cc-pVDZ.
[2] Value obtained using CC4/aug-cc-pVDZ corrected by the difference between PC-NEVPT2(12,12)/aug-cc-pVTZ and PC-NEVPT2(12,12)/aug-cc-pVDZ.
[3] Value obtained using CCSDTQ/6-31+G(d) corrected by the difference between CCSDT/aug-cc-pVDZ and CCSDT/6-31+G(d).
[4] Value obtained using CCSDTQ/6-31+G(d) corrected by the difference between CC4/aug-cc-pVDZ and CC4/6-31+G(d).
[5] TBE value obtained using CCSDTQ/aug-cc-pVDZ corrected by the difference between CCSDT/aug-cc-pVTZ and CCSDT/aug-cc-pVDZ.
[6] TBE value obtained using CCSDTQ/aug-cc-pVDZ corrected by the difference between CC4/aug-cc-pVTZ and CC4/aug-cc-pVDZ.

with the amount of exact exchange at short range. The influence of the exact exchange on the singlet energies is quite significant with an energy difference of the order of 1 eV between the functional with the smallest amount of exact exchange (B3LYP) and the functional with the largest amount (M06-2X). As for the excitation energies computed on the D_{2h} ground-state equilibrium structure and the automerization barrier, the functionals with a large fraction of short-range exact exchange yield more accurate results. Yet, the transition energy to 1^1B_{2g} is off by half an eV compared to the TBE for BH&HLYP and M11, while the doubly-excited state is much closer to the reference value (errors of -0.251 and -0.312 eV for BH&HLYP and M11, respectively). With errors of -0.066, -0.097, and -0.247 eV for 1^3A_{2g}, 1^1A_{1g}, and 1^1B_{2g}, M06-2X is the best performer here. Again, for all the excited states, the basis set effects are extremely small at the SF-TD-DFT level. We emphasize that the $\langle S^2 \rangle$ values reported in Appendix C indicate again that there is no significant spin contamination in these excited states.

Next, we discuss the various ADC schemes (Table 3.5). Globally, we observe similar trends as those noted in Sec. 3.3.3.1. Concerning the singlet-triplet gap, each scheme predicts it to be positive. Although it provides a decent singlet-triplet gap value, SF-ADC(2)-x seems to particularly struggle with the singlet excited states (1^1A_{1g} and 1^1B_{2g}), especially for the doubly-excited state 1^1A_{1g} where it underestimates the vertical excitation energy by 0.4 eV. Again, averaging the SF-ADC(2)-s and SF-ADC(3) transition energies is beneficial in most cases at the exception of 1^1A_{1g}. Although the basis set effects are larger than at the SF-TD-DFT level, they remain quite moderate at the SF-ADC level, and this holds for wave function methods in general. Concerning the SF-EOM-CCSD excitation energies at the D_{4h} square planar equilibrium geometry, very similar conclusions to the ones provided in the previous section dealing with the excitation energies at the D_{2h} rectangular equilibrium geometry can be drawn: (i) SF-EOM-CCSD systematically and consistently overestimates the TBEs by approximately 0.2 eV and is less accurate than SF-ADC(2)-s, (ii) the non-iterative triples corrections tend to give a better agreement with respect to the TBE (see Appendix C), and (iii) the (dT) correction performs better than the (fT) one.

Let us turn to the multi-reference results (Table 3.6). For both active spaces, expectedly, CASSCF does not provide a quantitive energetic description, although it is worth mentioning that the right state ordering is preserved. This is, of course, magnified with the (4e,4o) active space for which the second-order perturbative treatment is unable to provide a satisfying description due to the limited active space. In particular SC-NEVPT2(4,4)/aug-cc-pVTZ and PC-NEVPT2(4,4)/aug-cc-pVTZ underestimate the singlet-triplet gap by 0.072 and 0.097 eV and, more importantly, flip the ordering of 1^1A_{1g} and 1^1B_{2g}. Although 1^1A_{1g} is not badly described, the excitation energy of the ionic state 1^1B_{2g} is off by almost 1 eV. Thanks to the IPEA shift in CASPT2(4,4), the singlet-triplet gap is accurate and the state ordering remains correct but the ionic state is still far from being well described. The (12e,12o) active space significantly alleviates these effects, and, as usual now, the agreement between CASPT2 and NEVPT2 is very much improved for each state, though the accuracy of multi-reference approaches remains questionable for the ionic state with, *e.g.*, an error up to -0.093 eV at the PC-NEVPT2(12,12)/aug-cc-pVTZ level.

Finally, let us analyze the excitation energies computed with various CC models that are gathered in Table 3.6. As mentioned in Sec. 3.2.2, we remind the reader that these calculations are performed by considering the 1^1A_{1g} state as reference, and that, therefore, 1^1B_{1g} and 1^1B_{2g} are obtained as a de-excitation and an excitation, respectively. Consequently, with respect to 1^1A_{1g}, 1^1B_{1g} has a dominant double excitation character, while 1^1B_{2g} have a dominant single excitation character. This

explains why one observes a slower convergence of the transition energies in the case of 1^1B_{1g} as shown in Fig. 3.4. It is clear from the results of Table 3.6 that, if one wants to reach high accuracy with such a computational strategy, it is mandatory to include quadruple excitations. Indeed, at the CCSDT/aug-cc-pVTZ level, the singlet-triplet gap is already very accurate (off by 0.005 eV only) while the excitation energies of the singlet states are still 0.131 and 0.688 eV away from their respective TBE. These deviations drop to 0.011 and −0.013 eV at the CC4/aug-cc-pVTZ level. As a final comment, we can note that the CCSDTQ-based TBEs and the CIPSI results are consistent if one takes into account the extrapolation error (see Sec. 3.2.1).

3.4 Conclusions

In the present study, we have benchmarked a larger number of computational methods on the automerization barrier and the vertical excitation energies of cyclobutadiene in its square (D_{4h}) and rectangular (D_{2h}) geometries, for which we have defined theoretical best estimates based on extrapolated CCSDTQ/aug-cc-pVTZ data.

The main take-home messages of the present work can be summarized as follows:

- Within the SF-TD-DFT framework, we advice to use exchange-correlation (hybrids or range-separated hybrids) with a large fraction of short-range exact exchange. This has been shown to be clearly beneficial for the automerization barrier and the vertical excitation energies computed on both the D_{2h} and D_{4h} equilibrium geometries.

- At the SF-ADC level, we have found that, as expected, the extended scheme, SF-ADC(2)-x, systematically worsen the results compared to the cheaper standard version, SF-ADC(2)-s. Moreover, as previously reported, SF-ADC(2)-s and SF-ADC(3) have opposite error patterns which means that SF-ADC(2.5) emerges as an excellent compromise.

- SF-EOM-CCSD shows similar performance as the cheaper SF-ADC(2)-s formalism, especially for the excitation energies. As previously reported, the two variants including non-iterative triples corrections, SF-EOM-CCSD(dT) and SF-EOM-CCSD(fT), improve the results, the (dT) correction performing slightly better for the vertical excitation energies computed at the D_{2h} and D_{4h} equilibrium geometries.

- For the D_{4h} square planar structure, a faithful energetic description of the excited states is harder to reach at the SF-TD-DFT level because of the strong multi-configurational character. In such scenario, the SF-TD-DFT excitation energies can exhibit errors of the order of 1 eV compared to the TBEs. However, it was satisfying to see that the spin-flip version of ADC can lower these errors to 0.1–0.2 eV.

- Concerning the multi-reference methods, we have found that while NEVPT2 and CASPT2 can provide different excitation energies for the small (4e,4o) active space, the results become highly similar when the larger (12e,12o) active space is considered. From a more general perspective, a significant difference between NEVPT2 and CASPT2 is usually not a good omen and can be seen as a clear warning sign that the active space is too small or poorly chosen. The ionic states remain a struggle for both CASPT2 and NEVPT2, even with the (12e,12o) active space.

- In the context of CC methods, although the inclusion of triple excitations (via CC3 or CCSDT) yields very satisfactory results in most cases, the inclusion of quadruples excitation (via CC4 or CCSDTQ) is mandatory to reach high accuracy (especially in the case of doubly-excited states). Finally, we point out that, considering the error bar related to the CIPSI extrapolation procedure, CCSDTQ and CIPSI yield equivalent excitation energies, hence confirming the outstanding accuracy of CCSDTQ in the context of molecular excited states.

Chapter 4

Unphysical discontinuities, intruder states and regularization in GW methods

This chapter is the subject of the following publication: E. Monino and P. F. Loos. *J. Chem. Phys. (Open Access)* **156**, 231101 (2022).

By recasting the non-linear frequency-dependent GW quasiparticle equation into a linear eigenvalue problem, we explain the appearance of multiple solutions and unphysical discontinuities in various physical quantities computed within the GW approximation. Considering the GW self-energy as an effective Hamiltonian, it is shown that these issues are key signatures of strong correlation in the $(N \pm 1)$-electron states and can be directly related to the intruder state problem. A simple and efficient regularization procedure inspired by the similarity renormalization group is proposed to avoid such issues and speed up convergence of partially self-consistent GW calculations. Note that in this chapter we use chemist's notation for the two-electron integrals.

4.1 Introduction

The GW approximation of many-body perturbation theory [17, 103] allows to compute accurate charged excitation (*i.e.*, ionization potentials, electron affinities and fundamental gaps) in solids and molecules [102, 104, 380, 381]. Its popularity in the molecular electronic structure community is rapidly growing [26, 109, 111, 122, 223, 382–400] thanks to its relatively low computational cost [401–405] and somehow surprising accuracy for weakly-correlated systems [389, 391, 392, 400, 406, 407].

The idea behind the GW approximation is to recast the many-body problem into a set of non-linear one-body equations. The introduction of the self-energy Σ links the non-interacting Green's function G_0 to its fully-interacting version G via the following Dyson equation:

$$G = G_0 + G_0 \Sigma G \tag{4.1}$$

Electron correlation is then explicitly incorporated into one-body quantities via a sequence of self-consistent steps known as Hedin's equations [17].

In recent studies [27, 216, 236, 237, 408], we discovered that one can observe (unphysical) irregularities and/or discontinuities in the energy surfaces of several

key quantities (ionization potential, electron affinity, fundamental and optical gaps, total and correlation energies, as well as excitation energies) even in the weakly-correlated regime. These issues were discovered in Ref. [216] while studying a model two-electron system [409–411] and they were further investigated in Ref. [236], where we provided additional evidences and explanations of these undesirable features in real molecular systems. In particular, we showed that each branch of the self-energy Σ is associated with a distinct quasiparticle solution, and that each switch between solutions implies a significant discontinuity in the quasiparticle energy due to the transfer of weight between two solutions of the quasiparticle equation [236]. Multiple solution issues in GW appears frequently [391, 393, 412] (even at finite temperature [413, 414]), especially for orbitals that are energetically far from the Fermi level, such as in core ionized states [415, 416], and finite-temperature scheme.

In addition to obvious irregularities in potential energy surfaces that hampers the accurate determination of properties such as equilibrium bond lengths and harmonic vibrational frequencies [27, 237], one direct consequence of these discontinuities is the difficulty to converge (partially) self-consistent GW calculations as the self-consistent procedure jumps erratically from one solution to the other even if convergence accelerator techniques such as DIIS [39, 236, 417] or more elaborate schemes [418] are employed. Note in passing that the present issues do not only appear in GW as the T-matrix [30, 73, 419, 420] and second-order Green's function (or second Born) formalisms [70, 74, 421–429] exhibit the same drawbacks.

It was shown that these problems can be tamed by using a static Coulomb-hole plus screened-exchange (COHSEX) [17, 209, 430, 431] self-energy [237] or by considering a fully self-consistent GW scheme [249, 386, 403, 432–437], where one considers not only the quasiparticle solution but also the satellites at each iteration [408]. However, none of these solutions is completely satisfying as a static approximation of the self-energy can induce significant loss in accuracy and fully self-consistent calculations can be quite challenging in terms of implementation and cost.

In this chapter, via an upfolding process of the non-linear GW equation [23], we provide further physical insights into the origin of these discontinuities by highlighting, in particular, the role of intruder states. Inspired by regularized electronic structure theories [438, 439], these new insights allow us to propose a cheap and efficient regularization scheme in order to avoid these issues and speed up convergence of partially self-consistent GW calculations.

Here, for the sake of simplicity, we consider the one-shot G_0W_0 [207–215] but the same analysis can be performed in the case of (partially) self-consistent schemes such as evGW [209, 215, 217–219] (where one updates only the quasiparticle energies) and qsGW [118, 220–224] (where both quasiparticle energies and orbitals are updated at each iteration). Moreover, we consider a Hartree-Fock (HF) starting point but it can be straightforwardly extended to a Kohn-Sham starting point. Throughout this chapter, p and q are general (spatial) orbitals, i, j, k, and l denotes occupied orbitals, a, b, c, and d are vacant orbitals, while m labels single excitations $i \to a$. Atomic units are used throughout.

4.2 Downfolding: The non-linear GW problem

Within the G_0W_0 approximation, in order to obtain the quasiparticle energies and the corresponding satellites, one solve, for each spatial orbital p and assuming real

values of the frequency ω, the following (non-linear) quasiparticle equation

$$\epsilon_p^{\mathrm{HF}} + \Sigma_p^{\mathrm{c}}(\omega) - \omega = 0 \tag{4.2}$$

where ϵ_p^{HF} is the pth HF orbital energy and the correlation part of the G_0W_0 self-energy is constituted by a hole (h) and a particle (p) term as follows

$$\Sigma_p^{\mathrm{c}}(\omega) = \sum_{im} \frac{2(pi|m)^2}{\omega - \epsilon_i^{\mathrm{HF}} + \Omega_m^{\mathrm{RPA}}} + \sum_{am} \frac{2(pa|m)^2}{\omega - \epsilon_a^{\mathrm{HF}} - \Omega_m^{\mathrm{RPA}}} \tag{4.3}$$

Within the Tamm-Dancoff approximation (that we enforce here for the sake of simplicity), the screened two-electron integrals are given by

$$(pq|m) = \sum_{ia} (pq|ia) X_{ia,m}^{\mathrm{RPA}} \tag{4.4}$$

where Ω_m^{RPA} and $\mathbf{X}_m^{\mathrm{RPA}}$ are respectively the mth eigenvalue and eigenvector of the random-phase approximation (RPA) problem, *i.e.*,

$$\mathbf{A}^{\mathrm{RPA}} \cdot \mathbf{X}_m^{\mathrm{RPA}} = \Omega_m^{\mathrm{RPA}} \mathbf{X}_m^{\mathrm{RPA}} \tag{4.5}$$

with

$$A_{ia,jb}^{\mathrm{RPA}} = (\epsilon_a^{\mathrm{HF}} - \epsilon_i^{\mathrm{HF}}) \delta_{ij} \delta_{ab} + (ia|bj) \tag{4.6}$$

and

$$(pq|ia) = \iint \psi_p(\boldsymbol{r}_1) \psi_q(\boldsymbol{r}_1) \frac{1}{|\boldsymbol{r}_1 - \boldsymbol{r}_2|} \psi_i(\boldsymbol{r}_2) \psi_a(\boldsymbol{r}_2) d\boldsymbol{r}_1 d\boldsymbol{r}_2 \tag{4.7}$$

are two-electron integrals over the HF (spatial) orbitals $\psi_p(\boldsymbol{r})$. Because one must compute all the RPA eigenvalues and eigenvectors to construct the self-energy (4.3), the computational cost is $\mathcal{O}(O^3V^3) = \mathcal{O}(K^6)$, where O and V are the number of occupied and virtual orbitals, respectively, and $K = O + V$ is the total number of orbitals.

As a non-linear equation, Eq. (4.2) has many solutions $\epsilon_{p,s}^{GW}$ (where the index s is numbering solutions) and their corresponding weights are given by the value of the following renormalization factor

$$0 \leq Z_{p,s} = \left[1 - \left. \frac{\partial \Sigma_p^{\mathrm{c}}(\omega)}{\partial \omega} \right|_{\omega = \epsilon_{p,s}^{GW}} \right]^{-1} \leq 1 \tag{4.8}$$

In a well-behaved case, one of the solution (the so-called quasiparticle) ϵ_p^{GW} has a large weight Z_p. Note that we have the following important conservation rules [440–442]

$$\sum_s Z_{p,s} = 1 \qquad\qquad \sum_s Z_{p,s} \epsilon_{p,s}^{GW} = \epsilon_p^{\mathrm{HF}} \tag{4.9}$$

which physically shows that the mean-field solution of unit weight is "scattered" by the effect of correlation in many solutions of smaller weights.

In standard GW calculations in solids [103], one assignes a quasparticle peak to the solution of the Dyson equation (4.1) that is associated with the largest value of the spectral function

$$S(\omega) = \frac{1}{\pi} |\mathrm{Im}\, G(\omega)| \tag{4.10}$$

4.3 Upfolding: the linear *GW* problem

The non-linear quasiparticle equation (4.2) can be *exactly* transformed into a larger linear problem via an upfolding process where the 2h1p and 2p1h sectors are upfolded from the 1h and 1p sectors [20–23, 443]. For each orbital p, this yields a linear eigenvalue problem of the form

$$\mathbf{H}^{(p)} \cdot \mathbf{c}(p,s) = \epsilon_{p,s}^{GW} \mathbf{c}(p,s) \tag{4.11}$$

with

$$\mathbf{H}^{(p)} = \begin{pmatrix} \epsilon_p^{\mathrm{HF}} & \boldsymbol{V}_p^{\mathrm{2h1p}} & \boldsymbol{V}_p^{\mathrm{2p1h}} \\ (\boldsymbol{V}_p^{\mathrm{2h1p}})^\intercal & \boldsymbol{C}^{\mathrm{2h1p}} & \mathbf{0} \\ (\boldsymbol{V}_p^{\mathrm{2p1h}})^\intercal & \mathbf{0} & \boldsymbol{C}^{\mathrm{2p1h}} \end{pmatrix} \tag{4.12}$$

where

$$C_{ija,kcl}^{\mathrm{2h1p}} = \left[\left(\epsilon_i^{\mathrm{HF}} + \epsilon_j^{\mathrm{HF}} - \epsilon_a^{\mathrm{HF}} \right) \delta_{jl} \delta_{ac} - 2(ja|cl) \right] \delta_{ik} \tag{4.13}$$

$$C_{iab,kcd}^{\mathrm{2p1h}} = \left[\left(\epsilon_a^{\mathrm{HF}} + \epsilon_b^{\mathrm{HF}} - \epsilon_i^{\mathrm{HF}} \right) \delta_{ik} \delta_{ac} + 2(ai|kc) \right] \delta_{bd} \tag{4.14}$$

and the corresponding coupling blocks read

$$V_{p,klc}^{\mathrm{2h1p}} = \sqrt{2}(pk|cl) \qquad V_{p,kcd}^{\mathrm{2p1h}} = \sqrt{2}(pd|kc) \tag{4.15}$$

The size of this eigenvalue problem is $1 + O^2V + OV^2 = \mathcal{O}(K^3)$, and it has to be solved for each orbital that one wishes to correct. Thus, this step scales as $\mathcal{O}(K^9)$ with conventional diagonalization algorithms. Note, however, that the blocks $\boldsymbol{C}^{\mathrm{2h1p}}$ and $\boldsymbol{C}^{\mathrm{2p1h}}$ do not need to be recomputed for each orbital. Of course, this $\mathcal{O}(K^9)$ scheme is purely illustrative and current state-of-the-art *GW* implementation scales as $\mathcal{O}(K^3)$ thanks to efficient contour deformation and density fitting techniques [405, 412, 444].

It is crucial to understand that diagonalizing $\mathbf{H}^{(p)}$ [see Eq. (4.12)] is completely equivalent to solving the quasiparticle equation (4.2). This can be further illustrated by expanding the secular equation associated with Eq. (4.12)

$$\det\left[\mathbf{H}^{(p)} - \omega \mathbf{1} \right] = 0 \tag{4.16}$$

and comparing it with Eq. (4.2) by setting

$$\begin{aligned} \Sigma_p^{\mathrm{c}}(\omega) = \boldsymbol{V}_p^{\mathrm{2h1p}} \cdot \left(\omega \mathbf{1} - \boldsymbol{C}^{\mathrm{2h1p}} \right)^{-1} \cdot \left(\boldsymbol{V}_p^{\mathrm{2h1p}} \right)^\intercal \\ + \boldsymbol{V}_p^{\mathrm{2p1h}} \cdot \left(\omega \mathbf{1} - \boldsymbol{C}^{\mathrm{2p1h}} \right)^{-1} \cdot \left(\boldsymbol{V}_p^{\mathrm{2p1h}} \right)^\intercal \end{aligned} \tag{4.17}$$

where $\mathbf{1}$ is the identity matrix. Because the renormalization factor (4.8) corresponds to the projection of the vector $\mathbf{c}(p,s)$ onto the reference (or internal) space, the weight of a solution (p,s) is given by the first coefficient of their corresponding eigenvector $\mathbf{c}(p,s)$, *i.e.*,

$$Z_{p,s} = \left[c_1^{(p,s)} \right]^2 \tag{4.18}$$

One can see this downfolding process as the construction of a frequency-dependent effective Hamiltonian where the internal space is composed by a single Slater determinant of the 1h or 1p sector and the external (or outer) space by all the 2h1p and 2p1h

configurations [23, 445, 446]. The main mathematical difference between the two approaches is that, by diagonalizing Eq. (4.12), one has directly access to the internal and external components of the eigenvectors associated with each quasiparticle and satellite, and not only their projection in the reference space as shown by Eq. (4.18).

The element ϵ_p^{HF} of $\mathbf{H}^{(p)}$ [see Eq. (4.12)] corresponds to the (approximate) relative energy of the $(N \pm 1)$-electron reference determinant (compared to the N-electron HF determinant) while the eigenvalues of the blocks $\boldsymbol{C}^{\mathrm{2h1p}}$ and $\boldsymbol{C}^{\mathrm{2p1h}}$, which are $\epsilon_i^{\mathrm{HF}} - \Omega_m^{\mathrm{RPA}}$ and $\varepsilon a\mathrm{HF} + \Omega_m^{\mathrm{RPA}}$ respectively, provide an estimate of the relative energy of the 2h1p and 2p1h determinants. In some situations, one (or several) of these determinants from the external space may become of similar energy than the reference determinant, resulting in a vanishing denominator in the self-energy (4.3). Hence, these two diabatic electronic configurations may cross and form an avoided crossing, and this outer-space determinant may be labeled as an intruder state. As we shall see below, discontinuities, which are ubiquitous in molecular systems, arise in such scenarios.

4.4 An illustrative example

In order to illustrate the appearance and the origin of these multiple solutions, we consider the hydrogen molecule in the 6-31G basis set which corresponds to a two-electron system with four spatial orbitals (one occupied and three virtuals). This example was already considered in our previous work [236] but here we provide further insights on the origin of the appearances of these discontinuities. The downfolded and upfolded G_0W_0 schemes have been implemented in the electronic structure package QuAcK [242] which is freely available at `https://github.com/pfloos/QuAcK`. These calculations are based on restricted HF eigenvalues and orbitals. We denote as $|1\bar{1}\rangle$ the N-electron ground-state Slater determinant where the orbital 1 is occupied by one spin-up and one spin-down electron. Similar notations will be employed for the $(N \pm 1)$-electron configurations.

In Fig. 4.1, we report the variation of the quasiparticle energies of the four orbitals as functions of the internuclear distance $R_{\mathrm{H-H}}$. One can easily diagnose two problematic regions showing obvious discontinuities around $R_{\mathrm{H-H}} = 1.2$ Å for the LUMO+1 ($p = 3$) and $R_{\mathrm{H-H}} = 0.5$ Å for the LUMO+2 ($p = 4$). As thoroughly explained in Ref. [236], if one relies on the linearization of the quasiparticle equation (4.2) to compute the quasiparticle energies, *i.e.*, $\epsilon_p^{GW} \approx \varepsilon p\mathrm{HF} + Z_p \Sigma_p^{\mathrm{c}}(\epsilon_p^{\mathrm{HF}})$, these discontinuities are transformed into irregularities as the renormalization factor cancels out the singularities of the self-energy.

Figure 4.2 shows the evolution of the quasiparticle energy, the energetically close-by satellites and their corresponding weights as functions of $R_{\mathrm{H-H}}$. Let us first look more closely at the region around $R_{\mathrm{H-H}} = 1.2$ Å involving the LUMO+1 (left panel of Fig. 4.2). As one can see, an avoided crossing is formed between two solutions of the quasiparticle equation ($s = 4$ and $s = 5$). Inspection of their corresponding eigenvectors reveals that the $(N+1)$-electron determinants principally involved are the reference 1p determinant $|1\bar{1}3\rangle$ and an excited $(N+1)$-electron determinant of configuration $|12\bar{2}\rangle$ that becomes lower in energy than the reference determinant for $R_{\mathrm{H-H}} > 1.2$ Å. By construction, the quasiparticle solution diabatically follows the reference determinant $|1\bar{1}3\rangle$ through the avoided crossing (thick lines in Fig. 4.2) which is precisely the origin of the energetic discontinuity.

A similar scenario is at play in the region around $R_{\mathrm{H-H}} = 0.5$ Å for the LUMO+2 (right panel of Fig. 4.2) but it now involves three solutions ($s = 5$, $s = 6$, and

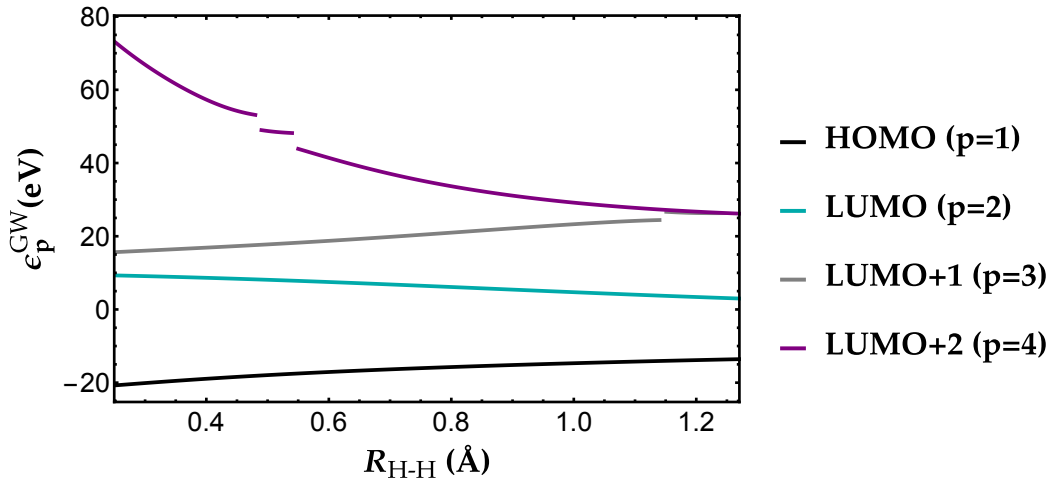

Figure 4.1: Quasiparticle energies ϵ_p^{GW} as functions of the internuclear distance R_{H-H} (in Å) of H_2 at the G_0W_0@HF/6-31G level.

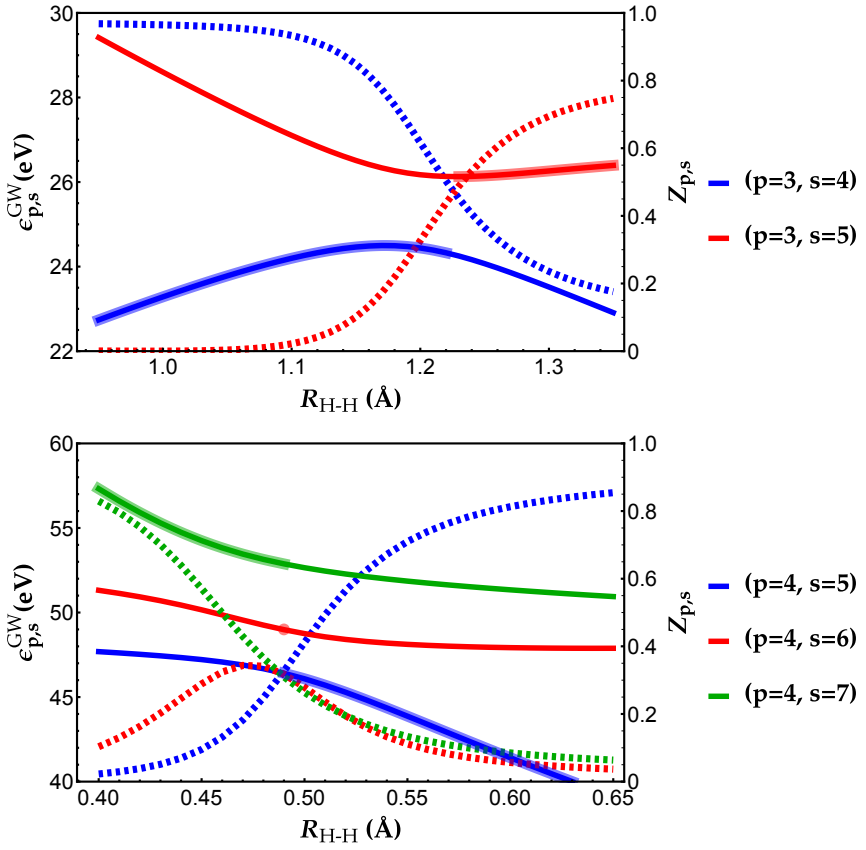

Figure 4.2: Selection of quasiparticle and satellite energies $\epsilon_{p,s}^{GW}$ (solid lines) and their renormalization factor $Z_{p,s}$ (dashed lines) as functions of the internuclear distance R_{H-H} (in Å) for the LUMO+1 ($p = 3$) and LUMO+2 ($p = 4$) orbitals of H_2 at the G_0W_0@HF/6-31G level. The quasiparticle solution (which corresponds to the solution with the largest weight) is represented as a thicker line.

$s = 7$). The electronic configurations of the Slater determinant involved are the $|1\bar{1}4\rangle$ reference determinant as well as two external determinants of configuration $|1\bar{2}3\rangle$ and $|12\bar{3}\rangle$. These states form two avoided crossings in rapid successions, which create two discontinuities in the energy surface (see Fig. 4.1). In this region, although the ground-state wave function is well described by the N-electron HF determinant, a situation that can be safely labeled as single-reference, one can see that the $(N+1)$-electron wave function involves three Slater determinants and can then be labeled as a multi-reference (or strongly-correlated) situation with near-degenerate electronic configurations. Therefore, one can conclude that this downfall of GW is a key signature of strong correlation in the $(N \pm 1)$-electron states that yields a significant redistribution of weights amongst electronic configurations.

4.5 Introducing regularized GW methods

One way to alleviate the issues discussed above and to massively improve the convergence properties of self-consistent GW calculations is to resort to a regularization of the self-energy without altering too much the quasiparticle energies.

From a general perspective, a regularized GW self-energy reads

$$\begin{aligned}\tilde{\Sigma}_p^{\mathrm{c}}(\omega;\eta) = &\sum_{im} 2(pi|m)^2 f_\eta(\omega - \epsilon_i^{\mathrm{HF}} + \Omega_m^{\mathrm{RPA}}) \\ &+ \sum_{am} 2(pa|m)^2 f_\eta(\omega - \epsilon_a^{\mathrm{HF}} - \Omega_m^{\mathrm{RPA}})\end{aligned} \tag{4.19}$$

where various choices for the "regularizer" f_η are possible. The main purpose of f_η is to ensure that $\tilde{\Sigma}_p^{\mathrm{c}}(\omega;\eta)$ remains finite even if one of the denominators goes to zero. The regularized solutions $\tilde{\epsilon}_{p,s}^{GW}$ are then obtained by solving the following regularized quasiparticle equation:

$$\epsilon_p^{\mathrm{HF}} + \tilde{\Sigma}_p^{\mathrm{c}}(\omega;\eta) - \omega = 0 \tag{4.20}$$

Of course, by construction, one must have

$$\lim_{\eta \to 0} \tilde{\Sigma}_p^{\mathrm{c}}(\omega;\eta) = \Sigma_p^{\mathrm{c}}(\omega) \tag{4.21}$$

The most common and well-established way of regularizing Σ is via the simple energy-independent regularizer

$$f_\eta(\Delta) = (\Delta \pm \mathrm{i}\eta)^{-1} \tag{4.22}$$

(with $\eta > 0$) [103, 385, 390, 412], a strategy somehow related to the imaginary shift used in multiconfigurational perturbation theory [447]. Note that this type of broadening is customary in solid-state calculations, hence such regularization is naturally captured in many codes [103]. In practice, an empirical value of η around 100 meV is suggested. Other choices are legitimate like the regularizers considered by Head-Gordon and coworkers within orbital-optimized second-order Møller-Plesset theory (MP2), which have the specificity of being energy-dependent [438, 448]. In this context, the real version of the simple energy-independent regularizer (4.22) has been shown to damage thermochemistry performance and was abandoned [449, 450].

Our investigations have shown that the following energy-dependent regularizer

$$f_\kappa(\Delta) = \frac{1 - e^{-2\Delta^2/\kappa^2}}{\Delta} \tag{4.23}$$

derived from the (second-order) perturbative analysis of the similarity renormalization group (SRG) equations [451–453] by Evangelista [306] is particularly convenient and effective for our purposes. Increasing κ gradually integrates out states with denominators Δ larger than κ while the states with $\Delta \ll \kappa$ are not decoupled from the reference space, hence avoiding intruder state problems [454].

Figure 4.3 compares the non-regularized and regularized quasiparticle energies in the two regions of interest for various η and κ values. It clearly shows how the regularization of the *GW* self-energy diabatically linked the two solutions to get rid of the discontinuities. However, this diabatization is more or less accurate depending on (i) the actual form of the regularizer, and (ii) the value of η or κ. Let us first discuss the simple energy-independent regularizer given by Eq. (4.22) (top panels of Fig. 4.3). Mathematically, in order to link smoothly two solutions, the value of η has to be large enough so that the singularity lying in the complex plane at the avoided crossing is moved to the real axis (see Ref. [455] and references therein). This value is directly linked to the difference in energy between the two states at the avoided crossing, and is thus, by definition, energy-dependent. This is clearly evidenced in Fig. 4.3 where, depending on the value of η, the regularization is more or less effective. For example, around $R_{\mathrm{H-H}} = 1.1$ Å (top-left), a value of 0.1 E_{h} (green curve) is appropriate while at $R_{\mathrm{H-H}} = 0.5$ Å (top-right), this value does not seem to be large enough. Note also that $\eta = 0.1\ E_{\mathrm{h}}$ is significantly larger than the suggested value of 100 meV and if one uses smaller η values, the regularization is clearly inefficient.

Let us now discuss the SRG-based energy-dependent regularizer provided in Eq. (4.23) (bottom panels of Fig. 4.3). For $\kappa = 10\ E_{\mathrm{h}}$, the value is clearly too large inducing a large difference between the two sets of quasiparticle energies (purple curves). For $\kappa = 0.1\ E_{\mathrm{h}}$, we have the opposite scenario where κ is too small and some irregularities remain (green curves). We have found that $\kappa = 1.0\ E_{\mathrm{h}}$ is a good compromise that does not alter significantly the quasiparticle energies while providing a smooth transition between the two solutions. Moreover, although the optimal κ is obviously system-dependent, this value performs well in all scenarios that we have encountered. However, it can be certainly refined for specific applications. For example, in the case of regularized MP2 theory (where one relies on a similar energy-dependent regularizer), a value of $\kappa = 1.1$ have been found to be optimal for noncovalent interactions and transition metal thermochemistry [448].

To further evidence this, Fig. 4.4 reports the difference between regularized (computed at $\kappa = 1.0\ E_{\mathrm{h}}$ with the SRG-based regularizer) and non-regularized quasiparticle energies as functions of $R_{\mathrm{H-H}}$ for each orbital. The principal observation is that, in the absence of intruder states, the regularization induces an error below 10 meV for the HOMO ($p = 1$) and LUMO ($p = 2$), which is practically viable. Of course, in the troublesome regions ($p = 3$ and $p = 4$), the correction brought by the regularization procedure is larger (as it should) but it has the undeniable advantage to provide smooth curves. Similar graphs for $\kappa = 0.1\ E_{\mathrm{h}}$ and $\kappa = 10\ E_{\mathrm{h}}$ [and the simple regularizer given in Eq. (4.22)] are reported in Appendix D, where one clearly sees that the larger the value of κ, the larger the difference between regularized and non-regularizer quasiparticle energies.

As a final example, we report in Fig. 4.5 the ground-state potential energy surface of the F_2 molecule obtained at various levels of theory with the cc-pVDZ basis. In particular, we compute, with and without regularization, the total energy at the Bethe-Salpeter equation (BSE) level [19, 25, 26, 95] within the adiabatic connection fluctuation dissipation formalism [27, 121, 456] following the same protocol as detailed in Ref. [27]. These results are compared to high-level coupled-cluster (CC) calculations extracted from the same work: CC with singles and doubles (CCSD)

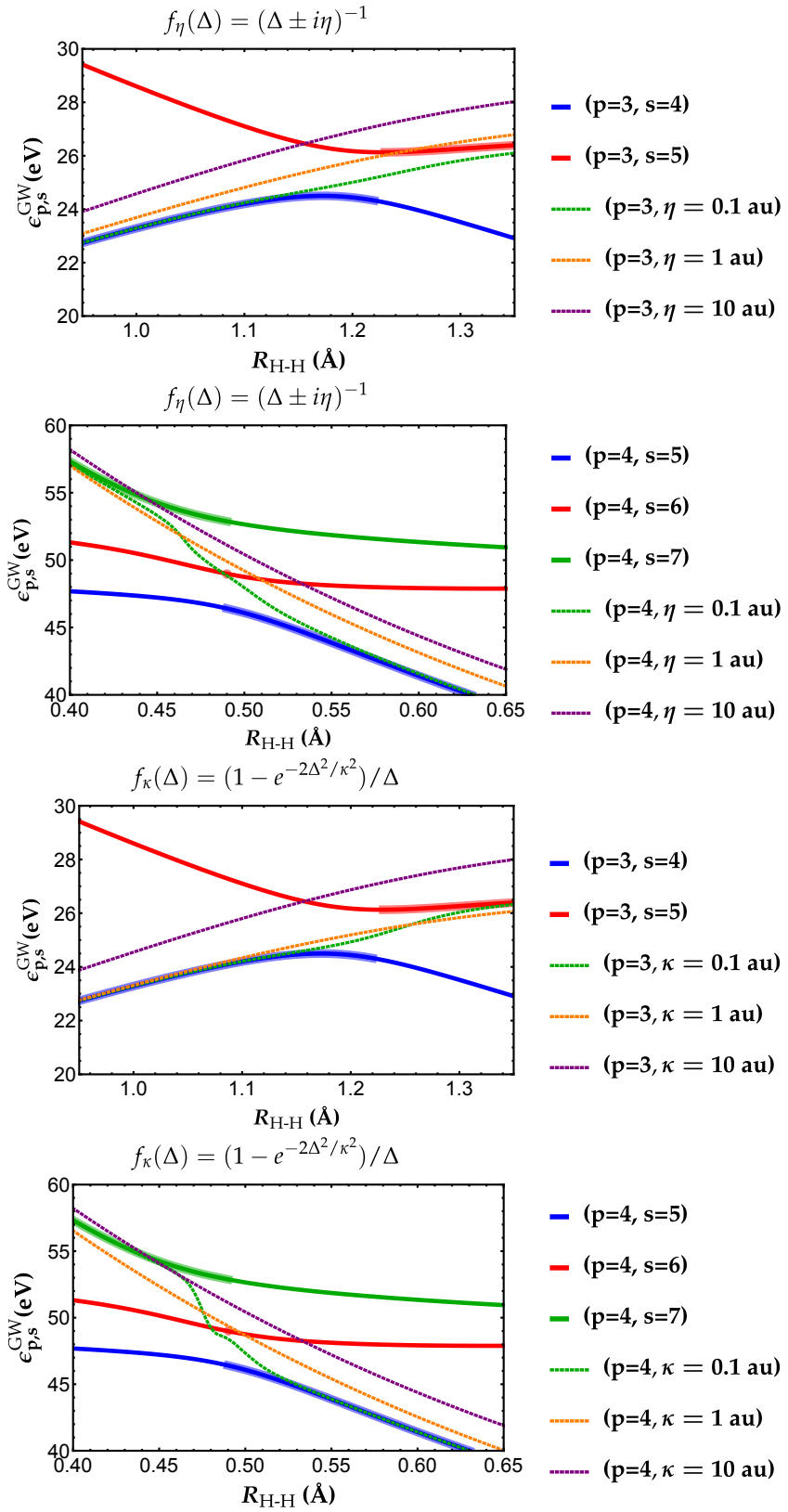

Figure 4.3: Comparison between non-regularized (solid lines) and regularized (dashed lines) energies as functions of the internuclear distance R_{H-H} (in Å) for the LUMO+1 ($p = 3$) and LUMO+2 ($p = 4$) orbitals of H_2 at the G_0W_0@HF/6-31G level. The quasiparticle solution is represented as a thicker line.

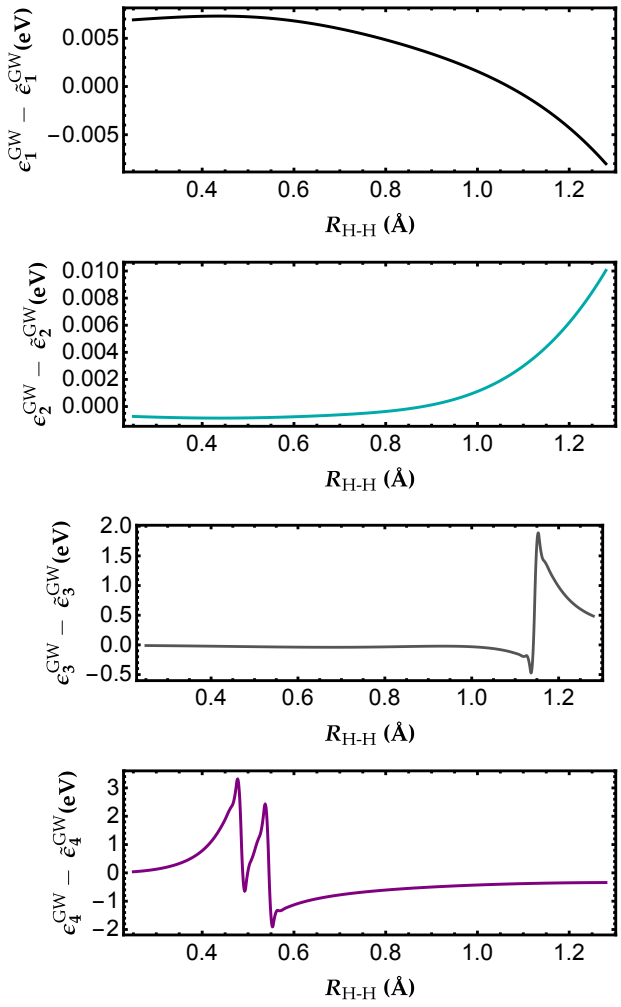

Figure 4.4: Difference between regularized and non-regularized quasiparticle energies $\tilde{\epsilon}_p^{GW} - \epsilon_p^{GW}$ computed with $\kappa = 1\,E_\mathrm{h}$ as functions of the internuclear distance $R_{\mathrm{H-H}}$ (in Å) of H_2 at the G_0W_0@HF/6-31G level. Similar graphs for $\kappa = 0.1\,E_\mathrm{h}$ and $\kappa = 10\,E_\mathrm{h}$ are reported in Appendix D.

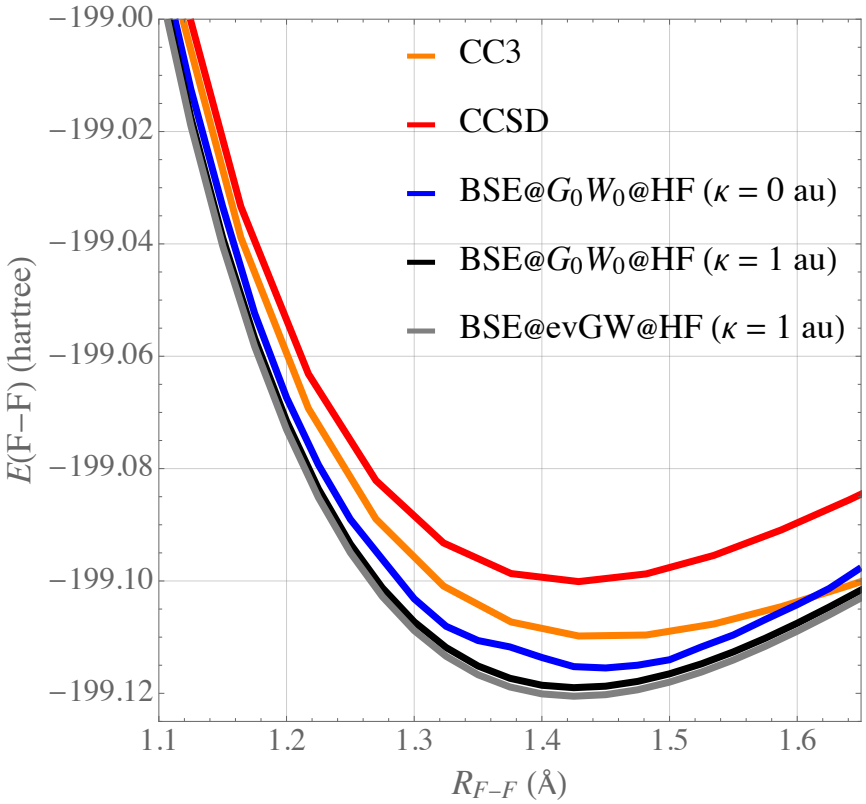

Figure 4.5: Ground-state potential energy surface of F_2 around its equilibrium geometry obtained at various levels of theory with the cc-pVDZ basis set. Similar graphs for $\kappa = 0.1\,E_h$ and $\kappa = 10\,E_h$ are reported in Appendix D.

[341] and the non-perturbative third-order approximate CC method (CC3) [146]. As already shown in Ref. [27], the potential energy surface of F_2 at the BSE@G_0W_0@HF (blue curve) is very "bumpy" around the equilibrium bond length and it is clear that the regularization scheme (black curve computed with $\kappa = 1\,E_h$) allows to smooth it out without significantly altering the overall accuracy. Moreover, while it is extremely challenging to perform self-consistent GW calculations without regularization, it is now straightforward to compute the BSE@evGW@HF potential energy surface (gray curve). For the sake of completeness, similar graphs for $\kappa = 0.1\,E_h$ and $\kappa = 10\,E_h$ are reported in Appendix D. For $\kappa = 0.1\,E_h$, one still has issues. In particular, the BSE@evGW@HF calculations do not converge for numerous values of the internuclear distance. Interestingly, for $\kappa = 10\,E_h$, the smooth BSE@G_0W_0@HF and BSE@evGW@HF curves are superposed, and of very similar quality as CCSD.

4.6 Concluding remarks

In this chapter, we have provided mathematical and physical explanations behind the appearance of multiple solutions and discontinuities in various physical quantities computed within the GW approximation. More precisely, we have evidenced that intruder states are the main cause behind these issues and that this downfall of GW is a key signature of strong correlation. A simple and efficient regularization procedure inspired by the similarity renormalization group has been proposed to remove these discontinuities without altering too much the quasiparticle energies. Moreover, this regularization of the self-energy significantly speeds up the convergence of (partially)

self-consistent *GW* methods. We hope that these new physical insights and technical developments will broaden the applicability of Green's function methods in the molecular electronic structure community and beyond.

Chapter 5

Connections and performances of Green's function methods for charged and neutral excitations

This chapter is the subject of the following publication: E. Monino and P. F. Loos.*J. Chem. Phys.* (submitted).

In recent years, Green's function methods have garnered considerable interest due to their ability to target both charged and neutral excitations. Among them, the well-established *GW* approximation provides accurate ionization potentials and electron affinities and can be extended to neutral excitations using the Bethe-Salpeter equation (BSE) formalism. Here, we investigate the connections between various Green's function methods and evaluate their performance for charged and neutral excitations. Comparisons with other widely-known second-order wave function methods are also reported. Additionally, we calculate the singlet-triplet gap of cycl[3,3,3]azine, a model molecular emitter for thermally activated delayed fluorescence, which has the particularity of having an inverted gap thanks to a substantial contribution from the double excitations. We demonstrate that, within the *GW* approximation, a second-order BSE kernel with dynamical correction is required to predict this distinctive characteristic.

5.1 Green's function methods

Recent developments and investigations in Green's function approaches have generated significant interest within the electronic structure community [81, 103, 457], especially in quantum chemistry [25, 26, 104, 122]. The pillar of Green's function many-body perturbation theory is the one-body Green's function (or electron propagator) [78]. It has the ability to provide the charged excitations (*i.e.*, ionization potentials and electron affinities) of the system in a single calculation as measured in direct or inverse photoemission spectroscopy. This avoids using state-specific methods where one has to perform separate calculations on the neutral and ionized species [458–466].

Obviously, the exact one-body Green's function G is in general unknown but its mean-field Hartree-Fock (HF) version G_{HF} can be linked to the exact one, via a Dyson equation involving a key quantity known as the self-energy Σ, which includes

correlation effects:

$$G(12) = G_{\mathrm{HF}}(12) + \int G_{\mathrm{HF}}(13)\Sigma(34)G(42)d3d4 \tag{5.1}$$

Here, $1 \equiv (\boldsymbol{x}_1, t_1)$ is a composite coordinate gathering spin-space and time variables.

The HF one-body Green's function is given by

$$G_{\mathrm{HF}}(\boldsymbol{x}_1, \boldsymbol{x}_2; \omega) = \sum_i \frac{\psi_i(\boldsymbol{x}_1)\psi_i(\boldsymbol{x}_2)}{\omega - \epsilon_i^{\mathrm{HF}} - i\eta} + \sum_a \frac{\psi_a(\boldsymbol{x}_1)\psi_a(\boldsymbol{x}_2)}{\omega - \epsilon_a^{\mathrm{HF}} + i\eta} \tag{5.2}$$

where $\psi_p(\boldsymbol{x})$ is the pth HF spinorbital and ϵ_p^{HF} its corresponding energy, while η is a positive infinitesimal that we shall set to zero in the remaining of this paper. Throughout this chapter, we assume real orbitals and energies. The indices p, q, r, and s are general spinorbitals, i, j, k, and l denote occupied spinorbitals, a, b, c, and d are vacant spinorbitals, while m and n label single excitations/deexcitations and double electron attachments/detachments, respectively. Here, we systematically consider a HF starting point but the present analysis can be straightforwardly extended to a Kohn-Sham starting point.

Approximations to the self-energy, such as GW [102, 104, 380, 381, 407], are needed to solve the Dyson equation defined in Eq. (5.1). Even though the GW approximation has proven to produce accurate charged excitations in solids [199, 207–210, 467–471] and molecules [25–27, 105–121, 252, 330, 388, 392, 415, 416, 472–481] , it is not the only approximation to the self-energy. Indeed, other approximations exist such as the second-order Green's function (GF2) [20–22, 74, 413, 414, 418, 421, 422, 424–429] , also known as second Born in the condensed matter community [103, 423], the T-matrix [30, 73, 419, 420, 482–492] (or Bethe-Goldstone approximation [441, 442, 493–495]). Going beyond these approximations has been shown to be rather challenging from a computational point of view [389, 419, 430, 441, 442, 483, 484, 496–514]. Moreover, the overall accuracy does not always improve [407, 515]. Here, for the sake of simplicity, we consider only one-shot schemes where one does not self-consistently update the self-energy [207, 208, 210–214], but the same analysis can be performed in the case of (partially) self-consistent schemes [118, 209, 215, 217–224]. Note that by only considering one-shot schemes, we neglect all the diagrammatic contributions stemming from the self-consistency.

Another attractive point concerning Green's function-based techniques is the Bethe-Salpeter equation (BSE) formalism [19, 25, 26, 95] that allows access to the neutral (*i.e.*, optical) excitations of a given system. BSE relies on the two-body Green's function G_2 (or polarization propagator) via its link with the two-body correlation function

$$iL(12;1'2') = -G_2(12;1'2') + G(11')G(22') \tag{5.3}$$

that also satisfies a Dyson equation

$$L(12,1'2') = L_0(12,1'2') + \int L_0(14,1'3)\Xi(35,46)L(62,52')d3d4d5d6 \tag{5.4}$$

with

$$iL_0(12;1'2') = G(12')G(21') \tag{5.5}$$

and where

$$\Xi(13,24) = i\frac{\delta\Sigma(12)}{\delta G(43)} \tag{5.6}$$

is the so-called BSE kernel. As we shall discuss later, like its time-dependent density-functional theory (TD-DFT) cousin [65, 67–69], BSE can be written in the form of Casida-like equations.

Because the BSE kernel is the functional derivative of Σ with respect to G, one can readily see from Eq. (5.6) that Ξ strongly depends on the choice of approximate self-energy. The most popular BSE kernel is based on the GW approximation and leans on the dynamically-screened Coulomb potential W to provide rather accurate neutral excitations for molecular systems [19]. However, one can also rely on kernels based on the T-matrix [30] or GF2 [229, 230, 516].

Undoubtedly, the self-energy and kernel approximations discussed earlier possess inherent limitations, both stemming from their intrinsic nature and the typical methods employed to solve these equations, as well as potential additional approximations involved. For example, unphysical discontinuities in energy surfaces have been recently discovered and studied in the GW approximation [27, 216, 236, 237, 408] but similar observations can be made with the other approximations. The issue can be traced down to the multiple solution character of the quasiparticle equation [236]. This problem of discontinuities can be partially addressed by using linearization of the quasiparticle equation, but irregularities (or "bumps") remain, for example, in potential energy surfaces [236]. One can deal with this issue by using a static Coulomb-hole plus screened-exchange (COHSEX) [17, 209, 237, 430, 431], by adopting a fully self-consistent scheme [249, 386, 403, 408, 432–437, 517], or via regularization techniques [32, 518].

Moreover, the BSE is considered, in general, within the so-called static approximation where the dynamical (*i.e.*, frequency-dependent) BSE kernel is approximated by its static limit. By doing so, the static BSE scheme [29, 140–142, 519], like the adiabatic approximation of TD-DFT [134–138], does not permit the description of double and higher excitations. The endeavor to go beyond the static approximation was first addressed by Strinati for core excitons in semiconductors [18, 19, 199, 467]. Then, using first-order perturbation theory, Rohlfing and co-workers have developed a way to take into account dynamical effects via the plasmon-pole approximation combined with the Tamm-Dancoff approximation (TDA) [200–204, 520–522]. Recently, Loos and Blase [29] proposed a dynamical scheme similar to Rohlfing's that goes beyond the plasmon-pole approximation where the dynamical screening of the Coulomb interaction is computed exactly within the random-phase approximation (RPA) [523–527].

Unfortunately, even though this dynamical scheme allows to dynamically correct the single excitations obtained from the static approach, it does not permit access to double excitations. A way to obtain these higher solutions is to resort to the spin-flip formalism where one considers a higher spin state as a reference [31, 152]. Note, however, that the spin-flip formalism does not give access to all double excitations and is hampered by spin contamination [94, 528].

Recently, Backhouse and Booth have introduced an upfolding version of the non-linear GF2 equations which provides a linear eigenvalue problem of larger dimension [20] (see also Ref. [78]). Bintrim and Berkelbach have extended it to the non-linear GW equations [23]. This linear eigenvalue problem allowed us to understand the role of intruder states in the origin of the energy surface discontinuities [32], as well as the connections between Green's function methods and coupled-cluster theory [529–531]. More importantly, when combined with other computational techniques, the upfolding framework provides a way to significantly lower the computational scaling of these approaches [20–23, 517]. The same concept was also applied to the dynamical BSE eigenvalue problem built from the GW kernel in order to go beyond

the static approximation [24]. This upfolding approach produces a linear eigenvalue problem in an expanded space of single and double excitations, hence direct access to doubly-excited states with, however, limited success in terms of accuracy.

In this work, we investigate both charged and neutral excitations in Secs. 5.2 and 5.3, respectively. We begin by reviewing the equations associated with the GF2 (Sec. 5.2.2), *GW* (Sec. 5.2.3), and *T*-matrix (Sec. 5.2.4) self-energies in various forms. Subsequently, we present and study various static and dynamic BSE kernels based on the GF2 (Sec. 5.3.2), *GW*, (Secs. 5.3.3 and 5.3.4), and *T*-matrix (Sec. 5.3.5) approximations, elucidating their interconnections and similarities with other theories. Computational details are provided in Sec. 5.4. In Sec. 5.5.1, we assess the accuracy of the three different self-energies in calculating the principal ionization potentials of a subset of atoms and molecules taken from the *GW*100 dataset [391]. Section 5.5.2 reports the computation of neutral excitations for another set of molecules using four different kernels within the static approximation. Additionally, we evaluate dynamical corrections through perturbation theory. Our analysis considers various types of excited states, predominantly valence and Rydberg states, and investigates the performance of these kernels based on the specific type of states. Finally, in Sec. 5.5.3, we compute, at various levels of theory, the gap between the first singlet and triplet excited states of cycl[3,3,3]azine, a model light-emitting diode (OLED) emitter for thermally activated delayed fluorescence (TADF), which has the particularity of having an inverted singlet-triplet gap. Our conclusions are presented in Sec. 5.6. Atomic units are consistently employed throughout.

5.2 Charged excitations

5.2.1 Quasiparticle equation

Within the one-shot scheme, in order to obtain the quasiparticle energies and the corresponding satellites, one solve, for each spinorbital p and assuming real values of the frequency ω, the following (non-linear) quasiparticle equation

$$\epsilon_p^{\mathrm{HF}} + \Sigma_{pp}(\omega) - \omega = 0 \tag{5.7}$$

where $\Sigma_{pp}(\omega)$ is a diagonal element of the correlation part of the self-energy. Due to the fact that one is usually interested in the quasiparticle solution, Eq. (5.7) is often linearized around $\omega = \epsilon_p^{\mathrm{HF}}$, *i.e.*,

$$\Sigma_{pp}(\omega) \approx \Sigma_{pp}(\epsilon_p^{\mathrm{HF}}) + (\omega - \epsilon_p^{\mathrm{HF}}) \left.\frac{\partial \Sigma_{pp}(\omega)}{\partial \omega}\right|_{\omega=\epsilon_p^{\mathrm{HF}}} \tag{5.8}$$

which yields

$$\epsilon_p = \epsilon_p^{\mathrm{HF}} + Z_p \Sigma_{pp}(\epsilon_p^{\mathrm{HF}}) \tag{5.9}$$

where

$$Z_p = \left[1 - \left.\frac{\partial \Sigma_{pp}(\omega)}{\partial \omega}\right|_{\omega=\epsilon_p^{\mathrm{HF}}}\right]^{-1} \tag{5.10}$$

is a renormalization factor ($0 \leq Z_p \leq 1$) which represents the spectral weight of the quasiparticle solution.

The non-linear quasiparticle equation (5.7) can be *exactly* transformed into a larger linear problem via the upfolding process mentioned earlier where the 2h1p and 2p1h sectors are upfolded from the 1h and 1p sectors [20–23, 32, 443, 518, 530, 531]. For

each orbital p, this yields a linear eigenvalue problem of the form

$$\mathbf{H}_p \cdot \mathbf{c}_\nu = \epsilon_\nu \mathbf{c}_\nu \tag{5.11}$$

where ν runs over all solutions, quasiparticle and satellites, and with [531]

$$\mathbf{H}_p = \begin{pmatrix} \epsilon_p^{\mathrm{HF}} & \boldsymbol{V}_p^{\mathrm{2h1p}} & \boldsymbol{V}_p^{\mathrm{2p1h}} \\ \left(\boldsymbol{V}_p^{\mathrm{2h1p}}\right)^\dagger & \mathbf{C}^{\mathrm{2h1p}} & \mathbf{0} \\ \left(\boldsymbol{V}_p^{\mathrm{2p1h}}\right)^\dagger & \mathbf{0} & \mathbf{C}^{\mathrm{2p1h}} \end{pmatrix} \tag{5.12}$$

The diagonalization of $\mathbf{H}_p$ is equivalent to solving the quasiparticle equation (5.7). This can be further illustrated by expanding the secular equation associated with Eq. (5.12)

$$\det\left[\mathbf{H}_p - \omega \mathbf{1}\right] = 0 \tag{5.13}$$

and comparing it with Eq. (5.7) by setting

$$\begin{aligned} \Sigma_{pp}(\omega) = \boldsymbol{V}_p^{\mathrm{2h1p}} \cdot \left(\omega \mathbf{1} - \mathbf{C}^{\mathrm{2h1p}}\right)^{-1} \cdot \left(\boldsymbol{V}_p^{\mathrm{2h1p}}\right)^\dagger \\ + \boldsymbol{V}_p^{\mathrm{2p1h}} \cdot \left(\omega \mathbf{1} - \mathbf{C}^{\mathrm{2p1h}}\right)^{-1} \cdot \left(\boldsymbol{V}_p^{\mathrm{2p1h}}\right)^\dagger \end{aligned} \tag{5.14}$$

where $\mathbf{1}$ is the identity matrix.

It can be readily seen from Eq. (5.12) that the hole (h) and particle (p) sectors are potentially coupled. This coupling, which is absent in coupled-cluster theory [529, 530, 532], is critical for generating effective higher-order diagrams in Green's function methods [78].

In the present work, we look at various approximations for the dynamical self-energy $\Sigma_{pp}(\omega)$ and it obviously leads to different expressions for the blocks $\mathbf{C}^{\mathrm{2h1p}}$, $\mathbf{C}^{\mathrm{2p1h}}$, $\boldsymbol{V}_p^{\mathrm{2h1p}}$, and $\boldsymbol{V}_p^{\mathrm{2p1h}}$. In the following, for each approximation, we provide the expression for the self-energy and the different blocks.

5.2.2 GF2 self-energy

Within the GF2 approximation, one only takes into account the direct and exchange second-order diagrams [533], and the self-energy is given by [70, 534, 535]

$$\begin{aligned} \Sigma^{\mathrm{GF2}}(12) = G(12) \int v(13) G(34) G(43) v(42) d3d4 \\ - \int G(13) v(14) G(34) G(42) v(32) d3d4 \end{aligned} \tag{5.15}$$

where $v(12) = |\boldsymbol{r}_1 - \boldsymbol{r}_2|^{-1}$ is the bare Coulomb operator.

In the spinorbital basis, the self-energy is constituted by a hole and a particle term as follows

$$\begin{aligned} \Sigma_{pq}^{\mathrm{GF2}}(\omega) = \frac{1}{2} \sum_{ija} \frac{\langle pa||ij\rangle \ \langle qa||ij\rangle}{\omega + \epsilon_a^{\mathrm{HF}} - \epsilon_i^{\mathrm{HF}} - \epsilon_j^{\mathrm{HF}}} \\ + \frac{1}{2} \sum_{iab} \frac{\langle pi||ab\rangle \ \langle qi||ab\rangle}{\omega + \epsilon_i^{\mathrm{HF}} - \epsilon_a^{\mathrm{HF}} - \epsilon_b^{\mathrm{HF}}} \end{aligned} \tag{5.16}$$

with $\langle pq||rs\rangle = \langle pq|rs\rangle - \langle pq|sr\rangle$ the antisymmetrized two-electron integrals written in Dirac's notation, *i.e.*,

$$\langle pq|rs\rangle = \iint \psi_p(\boldsymbol{x}_1)\psi_q(\boldsymbol{x}_2)v(12)\psi_r(\boldsymbol{x}_1)\psi_s(\boldsymbol{x}_2)d\boldsymbol{x}_1 d\boldsymbol{x}_2 \tag{5.17}$$

As mentioned above, one can rely on an equivalent linear eigenvalue problem [see Eq. (5.12)] where the diagonal blocks are given by [20, 78]

$$C^{\text{2h1p}}_{ija,klc} = \left(-\epsilon^{\text{HF}}_a + \epsilon^{\text{HF}}_i + \epsilon^{\text{HF}}_j\right)\delta_{ik}\delta_{jl}\delta_{ac} \tag{5.18a}$$

$$C^{\text{2p1h}}_{iab,kcd} = \left(-\epsilon^{\text{HF}}_i + \epsilon^{\text{HF}}_a + \epsilon^{\text{HF}}_b\right)\delta_{ik}\delta_{ac}\delta_{bd} \tag{5.18b}$$

and the corresponding coupling blocks read

$$V^{\text{2h1p}}_{p,klc} = \frac{\langle pc||kl\rangle}{\sqrt{2}} \qquad V^{\text{2p1h}}_{p,kcd} = \frac{\langle pk||dc\rangle}{\sqrt{2}} \tag{5.19}$$

Using Eq. (5.14) we can see that one easily retrieves the self-energy expression in Eq. (5.16). As already discussed in the literature [22, 78], it is worth mentioning that we recover the same secular equations as the second-order algebraic-diagrammatic construction [ADC(2)] treatment of the electron propagator in its Dyson form [75–79].

5.2.3 *GW* self-energy

GW is an approximation to Hedin's equations, a set of exact coupled integro-differential equations [17]. Diagrammatically, *GW* takes into account all the direct ring diagrams via a resummation technique [533] and is adequate in the high-density regime where correlation is weak [536, 537]. Therefore, *GW* includes the second-order direct term contained in GF2 but lacks its second-order exchange counterpart. The *GW* approximation is a relatively low computational cost method [401–405, 412, 444] that relies on the dynamically screened Coulomb potential W that is usually computed at the direct (*i.e.*, without exchange) particle-hole RPA (ph-RPA) level. In solids and large molecular systems, screening is usually significant, and the (frequency-dependent) screened Coulomb interaction is noticeably weaker than the (static) bare one. One can also include so-called internal vertex corrections for the calculation of the polarizability. In this case, one talks about test charge-test charge (tc-tc) polarizabilities, and various choices are possible [400, 504, 515, 538–541].

The ph-RPA equations take the form of a non-Hermitian eigenvalue problem written in the basis of single excitations and deexcitations:

$$\begin{pmatrix} \mathbf{A}^{\text{ph}} & \mathbf{B}^{\text{ph}} \\ -\mathbf{B}^{\text{ph}} & -\mathbf{A}^{\text{ph}} \end{pmatrix} \cdot \begin{pmatrix} \boldsymbol{X}^{\text{ph}} & \mathbf{Y}^{\text{ph}} \\ \mathbf{Y}^{\text{ph}} & \boldsymbol{X}^{\text{ph}} \end{pmatrix} = \begin{pmatrix} \boldsymbol{X}^{\text{ph}} & \mathbf{Y}^{\text{ph}} \\ \mathbf{Y}^{\text{ph}} & \boldsymbol{X}^{\text{ph}} \end{pmatrix} \cdot \begin{pmatrix} \boldsymbol{\Omega}^{\text{ph}} & \mathbf{0} \\ \mathbf{0} & -\boldsymbol{\Omega}^{\text{ph}} \end{pmatrix} \tag{5.20}$$

with

$$A^{\text{ph}}_{ia,jb} = (\epsilon^{\text{HF}}_a - \epsilon^{\text{HF}}_i)\delta_{ij}\delta_{ab} + \langle ib|aj\rangle \tag{5.21a}$$

$$B^{\text{ph}}_{ia,jb} = \langle ij|ab\rangle \tag{5.21b}$$

In the absence of instabilities, *i.e.*, when $\mathbf{A}^{\text{ph}} - \mathbf{B}^{\text{ph}}$ is positive definite, the ph-RPA problem reduces to a Hermitian problem of half the size. If one includes exchange in Eq. (5.21a) and (5.21b), one ends up with RPA with exchange (RPAx) which is

equivalent to time-dependent HF (TDHF). Note that TDHF within the TDA, where one removes the coupling between excitations and deexcitations, *i.e.*, $\mathbf{B} = \mathbf{0}$, is equivalent to configuration interaction with singles (CIS) [58].

Within the *GW* approximation, the self-energy is defined by the following simple expression:

$$\Sigma^{GW}(12) = iG(12)W_{\mathrm{c}}(12) \tag{5.22}$$

which clearly justifies the name of this approximation. Here $W_{\mathrm{c}} = W - v$ is the correlation part of the screened Coulomb interaction. In the spinorbital basis, the self-energy reads

$$\Sigma^{GW}_{pq}(\omega) = \sum_{im} \frac{M^{\mathrm{ph}}_{pi,m} M^{\mathrm{ph}}_{qi,m}}{\omega - \epsilon^{\mathrm{HF}}_i + \Omega^{\mathrm{ph}}_m} + \sum_{am} \frac{M^{\mathrm{ph}}_{pa,m} M^{\mathrm{ph}}_{qa,m}}{\omega - \epsilon^{\mathrm{HF}}_a - \Omega^{\mathrm{ph}}_m} \tag{5.23}$$

where the screened two-electron integrals are given by

$$M^{\mathrm{ph}}_{pq,m} = \sum_{ia} \langle pi|qa\rangle \left(\boldsymbol{X}^{\mathrm{ph}} + \boldsymbol{Y}^{\mathrm{ph}}\right)_{ia,m} \tag{5.24}$$

As shown by Bintrim and Berkelbach [23], and more recently by Tölle and Chan [531] (who have been able to eschew the use of the TDA), the blocks $\mathbf{C}^{\mathrm{2h1p}}$ and $\mathbf{C}^{\mathrm{2p1h}}$ defined in Eq. (5.12) are diagonal with elements

$$C^{\mathrm{2h1p}}_{im,im} = \epsilon^{\mathrm{HF}}_i - \Omega^{\mathrm{ph}}_m \qquad C^{\mathrm{2p1h}}_{am,am} = \epsilon^{\mathrm{HF}}_a + \Omega^{\mathrm{ph}}_m \tag{5.25}$$

and the coupling blocks read

$$V^{\mathrm{2h1p}}_{p,im} = M^{\mathrm{ph}}_{pi,m} \qquad V^{\mathrm{2p1h}}_{p,am} = M^{\mathrm{ph}}_{pa,m} \tag{5.26}$$

where $M^{\mathrm{ph}}_{pq,m}$ are the screened integrals of Eq. (5.24). Using the expressions of the different blocks one can, via the inverse process, obtain the expression of the self-energy as described in Eq. (5.14) and recover Eq. (5.23).

Note that an attempt of decoupling the 2h1p and 2p1h spaces within *GW*, as it is done in non-Dyson ADC [80], has been made but with very mitigated results [23].

5.2.4 *T*-matrix self-energy

While *GW* depends on the dynamically screened Coulomb potential *W*, the *T*-matrix approximation relies on the so-called *T*-matrix, which, diagrammatically, corresponds to a resummation of a different class of diagrams known as ladder diagrams [533]. Unlike the two-point quantity *W*, the four-point *T*-matrix is spin-dependent, and mixes the singlet and triplet spin channels in the computation of the self-energy. The *T*-matrix approximation, which contains both second-order diagrams as well as additional higher-order ladder diagrams, is usually preferred to *GW* when the screening is weak or, in other words, in the low-density regime.

While *W* is computed using ph-RPA, the *T*-matrix is computed using the particle-particle (pp) RPA (pp-RPA) problem which is a non-Hermitian eigenvalue problem expressed in the basis of double electron attachments and double electron detachments: [61, 63, 64, 158, 159, 161, 170, 542–545]

$$\begin{pmatrix} \mathbf{C}^{\mathrm{pp}} & \mathbf{B}^{\mathrm{pp/hh}} \\ -\left(\mathbf{B}^{\mathrm{pp/hh}}\right)^{\dagger} & -\boldsymbol{D}^{\mathrm{hh}} \end{pmatrix} \cdot \begin{pmatrix} \boldsymbol{X}^{\mathrm{pp}} & \mathbf{Y}^{\mathrm{hh}} \\ \mathbf{Y}^{\mathrm{pp}} & \boldsymbol{X}^{\mathrm{hh}} \end{pmatrix} = \begin{pmatrix} \boldsymbol{\Omega}^{\mathrm{pp}} & \mathbf{0} \\ \mathbf{0} & \boldsymbol{\Omega}^{\mathrm{hh}} \end{pmatrix} \cdot \begin{pmatrix} \boldsymbol{X}^{\mathrm{pp}} & \mathbf{Y}^{\mathrm{hh}} \\ \mathbf{Y}^{\mathrm{pp}} & \boldsymbol{X}^{\mathrm{hh}} \end{pmatrix} \tag{5.27}$$

where

$$C^{\mathrm{pp}}_{ab,cd} = (\epsilon^{\mathrm{HF}}_a + \epsilon^{\mathrm{HF}}_b)\delta_{ac}\delta_{bd} + \langle ab||cd\rangle \tag{5.28a}$$
$$B^{\mathrm{pp/hh}}_{ab,ij} = \langle ab||ij\rangle \tag{5.28b}$$
$$D^{\mathrm{hh}}_{ij,kl} = -(\epsilon^{\mathrm{HF}}_i + \epsilon^{\mathrm{HF}}_j)\delta_{ik}\delta_{jl} + \langle ij||kl\rangle \tag{5.28c}$$

with the following index restrictions $a < b$, $c < d$, $i < j$, and $k < l$.

Within the T-matrix approximation, the correlation part of the self-energy is

$$\Sigma^{GT}(12) = i \int G(43) T_{\mathrm{c}}(13, 24) d3d4 \tag{5.29}$$

(where T_{c} is the correlation part of the T matrix) and the elements of the self-energy in the spinorbital basis are explicitly given by [73, 419]

$$\Sigma^{GT}_{pq}(\omega) = \sum_{in} \frac{M^{\mathrm{pp}}_{pi,n} M^{\mathrm{pp}}_{qi,n}}{\omega + \epsilon^{\mathrm{HF}}_i - \Omega^{\mathrm{pp}}_n} + \sum_{an} \frac{M^{\mathrm{hh}}_{pa,n} M^{\mathrm{hh}}_{qa,n}}{\omega + \epsilon^{\mathrm{HF}}_a - \Omega^{\mathrm{hh}}_n} \tag{5.30}$$

where the pp and hh versions of the screened two-electron integrals read

$$M^{\mathrm{pp}}_{pq,n} = \sum_{c<d} \langle pq||cd\rangle\, X^{\mathrm{pp}}_{cd,n} + \sum_{k<l} \langle pq||kl\rangle\, Y^{\mathrm{pp}}_{kl,n} \tag{5.31a}$$
$$M^{\mathrm{hh}}_{pq,n} = \sum_{c<d} \langle pq||cd\rangle\, X^{\mathrm{hh}}_{cd,n} + \sum_{k<l} \langle pq||kl\rangle\, Y^{\mathrm{hh}}_{kl,n} \tag{5.31b}$$

Following the upfolding process of Bintrim and Berkelbach [23] together with the generalization of Tölle and Chan [531], in the case of the T-matrix, we have the following diagonal elements for the blocks $\mathbf{C}^{\mathrm{2h1p}}$ and $\mathbf{C}^{\mathrm{2p1h}}$ of Eq. (5.12)

$$C^{\mathrm{2h1p}}_{an,an} = -\epsilon^{\mathrm{HF}}_a + \Omega^{\mathrm{hh}}_n \qquad C^{\mathrm{2p1h}}_{in,in} = -\epsilon^{\mathrm{HF}}_i + \Omega^{\mathrm{pp}}_n \tag{5.32}$$

and the corresponding coupling blocks are

$$V^{\mathrm{2h1p}}_{p,an} = M^{\mathrm{hh}}_{pa,n} \qquad V^{\mathrm{2p1h}}_{p,in} = M^{\mathrm{pp}}_{pi,n} \tag{5.33}$$

where the screened integrals are given by Eqs. (5.31a) and (5.31b).

5.3 Neutral excitations

5.3.1 Bethe-Salpeter equation

Within the BSE formalism, one must solve, in the general setting, a non-linear eigenvalue problem of the form

$$\begin{pmatrix} \mathbf{A}^{\mathrm{BSE}}(\Omega^{\mathrm{BSE}}_\nu) & \mathbf{B}^{\mathrm{BSE}}(\Omega^{\mathrm{BSE}}_\nu) \\ -\mathbf{B}^{\mathrm{BSE}}(-\Omega^{\mathrm{BSE}}_\nu) & -\mathbf{A}^{\mathrm{BSE}}(-\Omega^{\mathrm{BSE}}_\nu) \end{pmatrix} \cdot \begin{pmatrix} \boldsymbol{X}^{\mathrm{BSE}}_\nu \\ \mathbf{Y}^{\mathrm{BSE}}_\nu \end{pmatrix} = \Omega^{\mathrm{BSE}}_\nu \begin{pmatrix} \boldsymbol{X}^{\mathrm{BSE}}_\nu \\ \mathbf{Y}^{\mathrm{BSE}}_\nu \end{pmatrix} \tag{5.34}$$

where the (anti)resonant block $\pm\mathbf{A}^{\mathrm{BSE}}(\omega)$ and the coupling blocks $\pm\mathbf{B}^{\mathrm{BSE}}(\omega)$ are dynamical quantities and the index v runs over single, double, and potentially higher excitations. Of course, their expressions depend on the type of quasiparticles and the

kernel that one considers but they have the following generic expressions

$$A^{\mathrm{BSE}}_{ia,jb}(\omega) = A_{ia,jb} + \Xi_{ia,jb}(\omega) \tag{5.35a}$$
$$B^{\mathrm{BSE}}_{ia,jb}(\omega) = B_{ia,jb} + \Xi_{ia,bj}(\omega) \tag{5.35b}$$

with the following static parts

$$A_{ia,jb} = (\epsilon_a - \epsilon_i)\delta_{ij}\delta_{ab} + \langle ib||aj\rangle \tag{5.36a}$$
$$B_{ia,jb} = \langle ij||ab\rangle \tag{5.36b}$$

where the ϵ_p's are quasiparticle energies and $\Xi_{pq,rs}(\omega)$ is an element of the dynamical correlation kernel computed at a given level of theory. Note that, although these matrices are built in the single excitation and deexcitation manifolds, thanks to the frequency dependence of these quantities, one can potentially access higher excitations.

Again, one can enforce the TDA to obtain a simpler non-linear system

$$\mathbf{A}^{\mathrm{BSE}}(\Omega^{\mathrm{BSE}}_\nu) \cdot \boldsymbol{X}^{\mathrm{BSE}}_\nu = \Omega^{\mathrm{BSE}}_\nu \boldsymbol{X}^{\mathrm{BSE}}_\nu \tag{5.37}$$

Below, we present three different ways of tackling the BSE problem.

First, one can enforce the so-called static approximation where one sets

$$A^{\mathrm{BSE}}_{ia,jb} = A_{ia,jb} + \Xi_{ia,jb} \tag{5.38a}$$
$$B^{\mathrm{BSE}}_{ia,jb} = B_{ia,jb} + \Xi_{ia,bj} \tag{5.38b}$$

to get

$$\begin{pmatrix} \mathbf{A}^{\mathrm{BSE}} & \mathbf{B}^{\mathrm{BSE}} \\ -\mathbf{B}^{\mathrm{BSE}} & -\mathbf{A}^{\mathrm{BSE}} \end{pmatrix} \cdot \begin{pmatrix} \boldsymbol{X}^{\mathrm{BSE}}_m \\ \mathbf{Y}^{\mathrm{BSE}}_m \end{pmatrix} = \Omega^{\mathrm{BSE}}_m \begin{pmatrix} \boldsymbol{X}^{\mathrm{BSE}}_m \\ \mathbf{Y}^{\mathrm{BSE}}_m \end{pmatrix} \tag{5.39}$$

In this case, because of the frequency-independent nature of the static kernel's elements $\Xi_{pq,rs}$, one only accesses single excitations.

Second, one can go beyond the static approximation by using a renormalized first-order perturbative correction to the static BSE excitation energies. (We refer the interested reader to Ref. [29] for a detailed discussion. Here, we only provide the main equations.) This dynamical correction to the static BSE kernel (labeled dBSE in the following) allows us to recover additional relaxation effects coming from higher excitations.

The dBSE excitation energies are then obtained via

$$\Omega^{\mathrm{dBSE}}_m = \Omega^{\mathrm{BSE}}_m + \zeta_m \tilde{\Omega}^{\mathrm{BSE}}_m \tag{5.40}$$

where the Ω^{BSE}_m's are the static (zeroth-order) BSE excitation energies defined in Eq. (5.39) and

$$\tilde{\Omega}^{\mathrm{BSE}}_m = (\boldsymbol{X}^{\mathrm{BSE}}_m)^\dagger \cdot \Delta\boldsymbol{\Xi}(\Omega^{\mathrm{BSE}}_m) \cdot \boldsymbol{X}^{\mathrm{BSE}}_m \tag{5.41}$$

are first-order corrections obtained within the dynamical TDA (*i.e.*, as commonly done, only the resonant block is corrected for dynamical effects) with the renormalization factor

$$\zeta_m = \left[1 - (\boldsymbol{X}^{\mathrm{BSE}}_m)^\dagger \cdot \left.\frac{\partial \Delta\boldsymbol{\Xi}(\omega)}{\partial\omega}\right|_{\omega=\Omega^{\mathrm{BSE}}_m} \cdot \boldsymbol{X}^{\mathrm{BSE}}_m \right]^{-1} \tag{5.42}$$

The generic expression for $\Delta\boldsymbol{\Xi}(\omega)$ is

$$\Delta\Xi_{ia,jb}(\omega) = \tilde{\Xi}_{ia,jb}(\omega) - \Xi_{ia,jb} \tag{5.43}$$

where $\tilde{\Xi}_{ia,jb}(\omega)$ is an element of the so-called effective dynamical kernel. Unlike in the quasiparticle case (see Sec. 5.2.1), this renormalization factor ζ_m is not restricted between 0 and 1. However, it has been found to be close to unity in most cases which indicates the satisfactory convergence properties of the perturbative series [29, 31].

Third, within the TDA, it is also possible to transform the non-linear eigenvalue problem (5.37) into a larger linear problem via an upfolding process where the 2h2p sector is upfolded from the 1h1p sector. The structure (and the dimension) of this matrix $\tilde{\mathbf{H}}$ depends on the nature and origin of the kernel. In the following, we present four different kernels and, for each of them, we provide the corresponding working equations.

5.3.2 Second-order GF2 kernel

We first discuss the BSE correlation kernel based on the GF2 self-energy considered in Eq. (5.15):

$$\Xi^{\mathrm{GF2}}(35,46) = i\frac{\delta\Sigma^{\mathrm{GF2}}(34)}{\delta G(65)} \tag{5.44}$$

To avoid lengthy derivations and expressions, we refer the interested reader to the work of Zhang *et al.* (and particularly to the supplementary material) for the full derivation of the GF2 kernel [229]. Additional details and complements can be found in the work of Rebolini and Toulouse [230, 546].

At the BSE@GF2 level, we have

$$A^{\mathrm{GF2}}_{ia,jb}(\omega) = A^{\mathrm{GF2}}_{ia,jb} + \Xi^{\mathrm{GF2}}_{ia,jb}(\omega) \tag{5.45a}$$
$$B^{\mathrm{GF2}}_{ia,jb}(\omega) = B^{\mathrm{GF2}}_{ia,jb} + \Xi^{\mathrm{GF2}}_{ia,bj}(\omega) \tag{5.45b}$$

with

$$A^{\mathrm{GF2}}_{ia,jb} = (\epsilon^{\mathrm{GF2}}_a - \epsilon^{\mathrm{GF2}}_i)\delta_{ij}\delta_{ab} + \langle ib||aj\rangle \tag{5.46a}$$
$$B^{\mathrm{GF2}}_{ia,jb} = \langle ij||ab\rangle \tag{5.46b}$$

and the elements of the second-order (with respect to the Coulomb interaction) static kernel for the (anti)resonant and coupling blocks are given by the following expression:

$$\begin{aligned}\Xi^{\mathrm{GF2}}_{pq,rs} = &\sum_{kc}\frac{\langle rc||pk\rangle\,\langle kq||cs\rangle}{\epsilon^{\mathrm{GF2}}_c - \epsilon^{\mathrm{GF2}}_k} + \sum_{kc}\frac{\langle rk||pc\rangle\,\langle cq||ks\rangle}{\epsilon^{\mathrm{GF2}}_c - \epsilon^{\mathrm{GF2}}_k} \\ &+ \frac{1}{2}\sum_{kl}\frac{\langle qr||kl\rangle\,\langle lk||sp\rangle}{\epsilon^{\mathrm{GF2}}_k + \epsilon^{\mathrm{GF2}}_l} + \frac{1}{2}\sum_{cd}\frac{\langle qr||cd\rangle\,\langle dc||sp\rangle}{\epsilon^{\mathrm{GF2}}_c + \epsilon^{\mathrm{GF2}}_d}\end{aligned} \tag{5.47}$$

Going beyond the static approximation, the elements of the dynamical kernel for the resonant block are

$$\begin{aligned}\tilde{\Xi}^{\mathrm{GF2}}_{ia,jb}(\omega) = &- \sum_{kc} \frac{\langle jc||ik\rangle \langle ka||cb\rangle}{\omega - (\epsilon^{\mathrm{GF2}}_b + \epsilon^{\mathrm{GF2}}_c - \epsilon^{\mathrm{GF2}}_i - \epsilon^{\mathrm{GF2}}_k)} \\ &- \sum_{kc} \frac{\langle jk||ic\rangle \langle ca||kb\rangle}{\omega - (\epsilon^{\mathrm{GF2}}_a + \epsilon^{\mathrm{GF2}}_c - \epsilon^{\mathrm{GF2}}_j - \epsilon^{\mathrm{GF2}}_k)} \\ &+ \frac{1}{2} \sum_{kl} \frac{\langle aj||kl\rangle \langle lk||bi\rangle}{\omega - (\epsilon^{\mathrm{GF2}}_a + \epsilon^{\mathrm{GF2}}_b - \epsilon^{\mathrm{GF2}}_k - \epsilon^{\mathrm{GF2}}_l)} \\ &+ \frac{1}{2} \sum_{cd} \frac{\langle aj||cd\rangle \langle dc||bi\rangle}{\omega - (\epsilon^{\mathrm{GF2}}_c + \epsilon^{\mathrm{GF2}}_d - \epsilon^{\mathrm{GF2}}_i - \epsilon^{\mathrm{GF2}}_j)}\end{aligned} \tag{5.48}$$

The first two terms in Eqs. (5.47) and (5.48) are ph and hp terms, while the third and fourth ones correspond to hh and pp terms, respectively.

Within the TDA, the upfolding process leads to the following linear eigenvalue problem

$$\tilde{\mathbf{H}}^{\mathrm{GF2}} = \begin{pmatrix} \mathbf{A}^{\mathrm{GF2}} & \boldsymbol{I} + \mathbf{K} & \boldsymbol{J} & \mathbf{K} \\ (\boldsymbol{J} + \boldsymbol{L})^\dagger & \mathbf{C}^{\mathrm{GF2}} & \mathbf{0} & \mathbf{0} \\ \mathbf{K}^\dagger & \mathbf{0} & \mathbf{C}^{\mathrm{GF2}} & \mathbf{0} \\ \boldsymbol{J}^\dagger & \mathbf{0} & \mathbf{0} & \mathbf{C}^{\mathrm{GF2}} \end{pmatrix} \tag{5.49}$$

where, the block $\mathbf{C}^{\mathrm{GF2}}$ is diagonal with elements

$$C^{\mathrm{GF2}}_{ijab,ijab} = \epsilon^{\mathrm{GF2}}_a + \epsilon^{\mathrm{GF2}}_b - \epsilon^{\mathrm{GF2}}_i - \epsilon^{\mathrm{GF2}}_j \tag{5.50}$$

while the various coupling terms read

$$I_{ia,klcd} = +\frac{\delta_{ac}}{\sqrt{2}} \langle di||kl\rangle \tag{5.51a}$$

$$J_{ia,klcd} = -\frac{\delta_{ad}}{\sqrt{2}} \langle ci||kl\rangle \tag{5.51b}$$

$$K_{ia,klcd} = +\frac{\delta_{il}}{\sqrt{2}} \langle dc||ak\rangle \tag{5.51c}$$

$$L_{ia,klcd} = -\frac{\delta_{ik}}{\sqrt{2}} \langle dc||al\rangle \tag{5.51d}$$

Note that, in this case, the upfolded matrix is non-Hermitian and contains three blocks of double excitations (*i.e.*, 2h2p configurations). Therefore, spurious (*i.e.*, non-physical) solutions are expected to appear due to the redundancy of the basis set [140–142]. By downfolding the three subspaces of double excitations onto the space of single excitations, *i.e.*,

$$\begin{aligned}\tilde{\boldsymbol{\Xi}}^{\mathrm{GF2}}(\omega) = &(\boldsymbol{I} + \mathbf{K}) \cdot \left(\omega \mathbf{1} - \mathbf{C}^{\mathrm{GF2}}\right)^{-1} \cdot (\boldsymbol{J} + \boldsymbol{L})^\dagger \\ &+ \boldsymbol{J} \cdot \left(\omega \mathbf{1} - \mathbf{C}^{\mathrm{GF2}}\right)^{-1} \cdot \mathbf{K}^\dagger \\ &+ \mathbf{K} \cdot \left(\omega \mathbf{1} - \mathbf{C}^{\mathrm{GF2}}\right)^{-1} \cdot \boldsymbol{J}^\dagger\end{aligned} \tag{5.52}$$

one recovers exactly the dynamical kernel defined in Eq. (5.48).

Following Bintrim and Berkelbach [24], we attempt to symmetrize $\tilde{\mathbf{H}}^{\mathrm{GF2}}$ and remove the redundant sets of 2h2p configurations by simply defining

$$\tilde{\mathbf{H}}^{\mathrm{GF2}} = \begin{pmatrix} \mathbf{A}^{\mathrm{HF}} & \boldsymbol{V} \\ \boldsymbol{V}^{\dagger} & \mathbf{C}^{\mathrm{HF}} \end{pmatrix} \tag{5.53}$$

with $\boldsymbol{V} = (\boldsymbol{I} + \boldsymbol{J} + \mathbf{K} + \boldsymbol{L})/\sqrt{2}$, and

$$A^{\mathrm{HF}}_{ia,jb} = (\epsilon^{\mathrm{HF}}_a - \epsilon^{\mathrm{HF}}_i)\delta_{ij}\delta_{ab} + \langle ib||aj\rangle \tag{5.54a}$$

$$C^{\mathrm{HF}}_{ijab,ijab} = \epsilon^{\mathrm{HF}}_a + \epsilon^{\mathrm{HF}}_b - \epsilon^{\mathrm{HF}}_i - \epsilon^{\mathrm{HF}}_j \tag{5.54b}$$

In this case, we obtain the dynamical kernel

$$\tilde{\boldsymbol{\Xi}}(\omega) = \boldsymbol{V} \cdot \left(\omega \mathbf{1} - \mathbf{C}^{\mathrm{HF}}\right)^{-1} \cdot \boldsymbol{V}^{\dagger} \tag{5.55}$$

with

$$\begin{aligned}
\tilde{\Xi}^{\mathrm{GF2}}_{ia,jb}(\omega) = &\frac{\delta_{ab}}{2} \sum_{klc} \frac{\langle kl||ic\rangle \langle kl||jc\rangle}{\omega - \left(\epsilon^{\mathrm{HF}}_a + \epsilon^{\mathrm{HF}}_c - \epsilon^{\mathrm{HF}}_k - \epsilon^{\mathrm{HF}}_l\right)} \\
&+ \frac{\delta_{ij}}{2} \sum_{kcd} \frac{\langle ak||cd\rangle \langle bk||cd\rangle}{\omega - \left(\epsilon^{\mathrm{HF}}_c + \epsilon^{\mathrm{HF}}_d - \epsilon^{\mathrm{HF}}_k - \epsilon^{\mathrm{HF}}_i\right)} \\
&- \sum_{kc} \frac{\langle jc||ik\rangle \langle ka||cb\rangle}{\omega - \left(\epsilon^{\mathrm{HF}}_b + \epsilon^{\mathrm{HF}}_c - \epsilon^{\mathrm{HF}}_k - \epsilon^{\mathrm{HF}}_i\right)} \\
&- \sum_{kc} \frac{\langle jk||ic\rangle \langle ca||kb\rangle}{\omega - \left(\epsilon^{\mathrm{HF}}_a + \epsilon^{\mathrm{HF}}_c - \epsilon^{\mathrm{HF}}_k - \epsilon^{\mathrm{HF}}_j\right)} \\
&+ \frac{1}{2} \sum_{kl} \frac{\langle aj||kl\rangle \langle lk||bi\rangle}{\omega - \left(\epsilon^{\mathrm{HF}}_a + \epsilon^{\mathrm{HF}}_b - \epsilon^{\mathrm{HF}}_k - \epsilon^{\mathrm{HF}}_l\right)} \\
&+ \frac{1}{2} \sum_{cd} \frac{\langle aj||cd\rangle \langle dc||bi\rangle}{\omega - \left(\epsilon^{\mathrm{HF}}_c + \epsilon^{\mathrm{HF}}_d - \epsilon^{\mathrm{HF}}_i - \epsilon^{\mathrm{HF}}_j\right)}
\end{aligned} \tag{5.56}$$

where one can see that we recover the four terms of the original dynamical kernel (5.48) with two additional self-energy terms that correspond to partial renormalization of the particle and hole sectors of the self-energy (forward time-ordered diagrams). Therefore, in order to avoid double counting, one must use HF orbital energies instead of GF2 quasiparticle energies in Eq. (5.53). However, the particle (hole) propagator is only renormalized by the 2p1h (2h1p) configurations and not the 2h1p (2p1h) configurations.

The expression (5.56) has a strong connection with the ADC(2) method for the polarization propagator (*i.e.*, for neutral excitations) [75, 79, 378, 547, 548]. Indeed, the blocks $\mathbf{C}^{\mathrm{HF}}$ and $\boldsymbol{V}$ in ADC(2) have identical expressions. However, in ADC(2), the 1h1p block has three additional second-order static terms. By replacing $\mathbf{A}^{\mathrm{HF}}$ by

$\mathbf{A}^{\mathrm{HF}} + \bar{\mathbf{A}}^{\mathrm{GF2}}$ in Eq. (5.53) with

$$\begin{aligned}\bar{A}^{\mathrm{GF2}}_{ia,jb} = \frac{\delta_{ij}}{4}\sum_{klc}\left[\frac{\langle ac||kl\rangle\ \langle kl||bc\rangle}{\epsilon^{\mathrm{HF}}_a - \epsilon^{\mathrm{HF}}_k + \epsilon^{\mathrm{HF}}_c - \epsilon^{\mathrm{HF}}_l} + \frac{\langle ac||kl\rangle\ \langle kl||bc\rangle}{\epsilon^{\mathrm{HF}}_b - \epsilon^{\mathrm{HF}}_k + \epsilon^{\mathrm{HF}}_c - \epsilon^{\mathrm{HF}}_l}\right] \\ + \frac{\delta_{ab}}{4}\sum_{kcd}\left[\frac{\langle cd||ik\rangle\ \langle jk||cd\rangle}{\epsilon^{\mathrm{HF}}_c - \epsilon^{\mathrm{HF}}_i + \epsilon^{\mathrm{HF}}_d - \epsilon^{\mathrm{HF}}_k} + \frac{\langle cd||ik\rangle\ \langle jk||cd\rangle}{\epsilon^{\mathrm{HF}}_c - \epsilon^{\mathrm{HF}}_j + \epsilon^{\mathrm{HF}}_d - \epsilon^{\mathrm{HF}}_k}\right] \\ - \frac{1}{2}\sum_{kc}\left[\frac{\langle ac||ik\rangle\ \langle jk||bc\rangle}{\epsilon^{\mathrm{HF}}_a - \epsilon^{\mathrm{HF}}_i + \epsilon^{\mathrm{HF}}_c - \epsilon^{\mathrm{HF}}_k} + \frac{\langle ac||ik\rangle\ \langle jk||bc\rangle}{\epsilon^{\mathrm{HF}}_b - \epsilon^{\mathrm{HF}}_j + \epsilon^{\mathrm{HF}}_c - \epsilon^{\mathrm{HF}}_k}\right]\end{aligned} \tag{5.57}$$

one ends up with exactly the ADC(2) secular equations. Although static, the first two terms are particularly crucial as they complete the renormalization of the HF orbital energies via the introduction of the missing backward time-ordered diagrams.

5.3.3 First-order *GW* kernel

Within the *GW* approximation, using the self-energy defined in Eq. (5.22), the BSE kernel reads [98, 100, 102, 549]

$$\begin{aligned} i\frac{\delta\Sigma^{GW}(34)}{\delta G(65)} &= -\frac{\delta(G(34)W_{\mathrm{c}}(34)}{\delta G(65)} \\ &= -W_{\mathrm{c}}(34)\frac{\delta G(34)}{\delta G(65)} - G(34)\frac{\delta W_{\mathrm{c}}(34)}{\delta G(65)} \\ &= \Xi^{GW}(35,46) + \Theta^{GW}(35,46)\end{aligned} \tag{5.58}$$

and it is common practice to neglect Θ^{GW} [18, 19, 199, 225, 467]. (We shall come back to this point later on.) Thus, one gets the following static kernel elements [19]

$$\Xi^{GW}_{pq,rs} = 2\sum_m \frac{M^{\mathrm{ph}}_{pr,m}M^{\mathrm{ph}}_{qs,m}}{\Omega^{\mathrm{ph}}_m} \tag{5.59}$$

As for the GF2 case, it is possible to go beyond the static approximation by taking into account the dynamical structure of W, that is [31],

$$\begin{aligned}\tilde{\Xi}^{GW}_{ia,jb}(\omega) = -\sum_m \frac{M^{\mathrm{ph}}_{ij,m}M^{\mathrm{ph}}_{ab,m}}{\omega - (\epsilon^{GW}_b - \epsilon^{GW}_i + \Omega^{\mathrm{ph}}_m)} \\ -\sum_m \frac{M^{\mathrm{ph}}_{ij,m}M^{\mathrm{ph}}_{ab,m}}{\omega - (\epsilon^{GW}_a - \epsilon^{GW}_j + \Omega^{\mathrm{ph}}_m)}\end{aligned} \tag{5.60}$$

By removing the screening effects from *GW*, *i.e.*, by performing the following substitutions, $\Omega^{\mathrm{ph}}_m \to \epsilon^{\mathrm{HF}}_a - \epsilon^{\mathrm{HF}}_i$ and $M^{\mathrm{ph}}_{pq,m} \to \langle pi|qa\rangle$, one recovers the two ph terms of Eq. (5.48), without, of course, the exchange part.

As shown in Ref. [24], at the BSE@*GW* level, the upfolding process yields

$$\tilde{\mathbf{H}}^{GW} = \begin{pmatrix} \mathbf{A}^{GW} & \boldsymbol{J}^{\mathrm{ph}} & \mathbf{K}^{\mathrm{ph}} \\ \left(\mathbf{K}^{\mathrm{ph}}\right)^{\dagger} & \mathbf{C}^{GW} & \mathbf{0} \\ \left(\boldsymbol{J}^{\mathrm{ph}}\right)^{\dagger} & \mathbf{0} & \mathbf{C}^{GW} \end{pmatrix} \tag{5.61}$$

with the usual static expression for the 1h1p part

$$A^{GW}_{ia,jb} = (\epsilon^{GW}_a - \epsilon^{GW}_i)\delta_{ij}\delta_{ab} + \langle ib||aj\rangle \tag{5.62}$$

a diagonal 2h2p block with elements

$$C^{GW}_{iam,iam} = \Omega^{\text{ph}}_m + \epsilon^{GW}_a - \epsilon^{GW}_i \tag{5.63}$$

and coupling blocks that read

$$J^{\text{ph}}_{ia,kcm} = -\delta_{ac} M^{\text{ph}}_{ik,m} \tag{5.64a}$$
$$K^{\text{ph}}_{ia,kcm} = +\delta_{ik} M^{\text{ph}}_{ac,m} \tag{5.64b}$$

Again, $\tilde{\mathbf{H}}^{GW}$ is a non-Hermitian matrix with two sets of double excitations. By downfolding we get

$$\begin{aligned}\tilde{\Xi}^{GW}(\omega) = \boldsymbol{J}^{\text{ph}} \cdot \left(\omega\mathbf{1} - \mathbf{C}^{GW}\right)^{-1} \cdot \left(\mathbf{K}^{\text{ph}}\right)^{\dagger} \\ + \mathbf{K}^{\text{ph}} \cdot \left(\omega\mathbf{1} - \mathbf{C}^{GW}\right)^{-1} \cdot \left(\boldsymbol{J}^{\text{ph}}\right)^{\dagger}\end{aligned} \tag{5.65}$$

which gives us back the dynamical kernel (5.60). As proposed by Bintrim and Berkelbach [24], one can also symmetrize $\tilde{\mathbf{H}}^{GW}$ and remove the additional 2h2p block by defining

$$\bar{\mathbf{H}}^{GW} = \begin{pmatrix} \mathbf{A}^{\text{HF}} + \bar{\mathbf{A}}^{GW} & \boldsymbol{J}^{\text{ph}} + \mathbf{K}^{\text{ph}} \\ \left(\boldsymbol{J}^{\text{ph}} + \mathbf{K}^{\text{ph}}\right)^{\dagger} & \bar{\mathbf{C}}^{GW} \end{pmatrix} \tag{5.66}$$

with

$$\bar{C}^{GW}_{iam,iam} = \Omega^{\text{ph}}_m + \epsilon^{\text{HF}}_a - \epsilon^{\text{HF}}_i \tag{5.67}$$

but, again, the resulting dynamical kernel

$$\bar{\Xi}^{GW}(\omega) = \left(\boldsymbol{J}^{\text{ph}} + \mathbf{K}^{\text{ph}}\right) \cdot \left(\omega\mathbf{1} - \bar{\mathbf{C}}^{GW}\right)^{-1} \cdot \left(\boldsymbol{J}^{\text{ph}} + \mathbf{K}^{\text{ph}}\right)^{\dagger} \tag{5.68}$$

contains additional self-energy terms:

$$\begin{aligned}\bar{\Xi}^{GW}_{ia,jb}(\omega) = \delta_{ab} \sum_{km} \frac{M^{\text{ph}}_{ik,m} M^{\text{ph}}_{jk,m}}{\omega - (\epsilon^{\text{HF}}_a - \epsilon^{\text{HF}}_k + \Omega^{\text{ph}}_m)} \\ + \delta_{ij} \sum_{cm} \frac{M^{\text{ph}}_{ac,m} M^{\text{ph}}_{bc,m}}{\omega - (\epsilon^{\text{HF}}_c - \epsilon^{\text{HF}}_i + \Omega^{\text{ph}}_m)} \\ - \sum_{m} \frac{M^{\text{ph}}_{ij,m} M^{\text{ph}}_{ab,m}}{\omega - (\epsilon^{\text{HF}}_b - \epsilon^{\text{HF}}_i + \Omega^{\text{ph}}_m)} \\ - \sum_{m} \frac{M^{\text{ph}}_{ij,m} M^{\text{ph}}_{ab,m}}{\omega - (\epsilon^{\text{HF}}_a - \epsilon^{\text{HF}}_j + \Omega^{\text{ph}}_m)}\end{aligned} \tag{5.69}$$

It has been found to severely affect the excitation energies due to the lack of backward time-ordered diagrams in the self-energy [24]. Hence, inspired by the ADC(2) expression, one could consider adding the missing self-energy terms (which correspond to

the inclusion of the backward time-ordered diagrams) by defining the elements of $\bar{\mathbf{A}}^{GW}$ in Eq. (5.66) as

$$\begin{aligned} \bar{A}^{GW}_{ia,jb} = \frac{\delta_{ij}}{2} \sum_{km} \left[\frac{M^{\mathrm{ph}}_{ak,m} M^{\mathrm{ph}}_{bk,m}}{\epsilon^{\mathrm{HF}}_a - \epsilon^{\mathrm{HF}}_k + \Omega^{\mathrm{ph}}_m} + \frac{M^{\mathrm{ph}}_{ak,m} M^{\mathrm{ph}}_{bk,m}}{\epsilon^{\mathrm{HF}}_b - \epsilon^{\mathrm{HF}}_k + \Omega^{\mathrm{ph}}_m} \right] \\ - \frac{\delta_{ab}}{2} \sum_{cm} \left[\frac{M^{\mathrm{ph}}_{ic,m} M^{\mathrm{ph}}_{jc,m}}{\epsilon^{\mathrm{HF}}_i - \epsilon^{\mathrm{HF}}_c - \Omega^{\mathrm{ph}}_m} + \frac{M^{\mathrm{ph}}_{ic,m} M^{\mathrm{ph}}_{jc,m}}{\epsilon^{\mathrm{HF}}_j - \epsilon^{\mathrm{HF}}_c - \Omega^{\mathrm{ph}}_m} \right] \end{aligned} \tag{5.70}$$

One can then solely rely on HF orbital energies in the previous expressions, instead of the GW quasiparticles [24]. The study of the performance of this new scheme is left for future work.

5.3.4 Second-order GW kernel

As mentioned above, it is customary to neglect the functional derivative $\delta W_{\mathrm{c}}/\delta G$ in the expression of the GW kernel [see Eq. (5.58)]. However, a second-order GW kernel, Θ^{GW}, that takes into account this additional term has been recently derived by Yamada *et al.* [550] and tested on the Thiel benchmark set [551–554] within the plasmon-pole approximation. In the following, we refer to this scheme as BSE2@GW.

The second-order GW kernel is naturally divided into two terms as follows:

$$\begin{aligned} \Theta^{GW}(35,46) = iG(35)G(64)W(34)W(56) \\ + iG(35)G(64)W(36)W(54) \end{aligned} \tag{5.71}$$

Contrary to Ξ^{GW} which corresponds to the screening of the exchange term, the two additional second-order terms included in Θ^{GW} screen the direct term. As a consequence, BSE2@GW only alters the excitation energies of the singlet excited states, while triplet states remain unaffected by this second-order correction.

In the spinorbital basis, we obtain the following static kernel elements:

$$\begin{aligned} \Theta^{GW}_{pq,rs} = \sum_{kc} \frac{W_{rk,pc} W_{qc,sk}}{\epsilon^{GW}_c - \epsilon^{GW}_k} + \sum_{kc} \frac{W_{rc,pk} W_{qk,sc}}{\epsilon^{GW}_c - \epsilon^{GW}_k} \\ + \sum_{kl} \frac{W_{qr,kl} W_{kl,ps}}{\epsilon^{GW}_k + \epsilon^{GW}_l} - \sum_{cd} \frac{W_{qr,cd} W_{cd,ps}}{\epsilon^{GW}_c + \epsilon^{GW}_d} \end{aligned} \tag{5.72}$$

where

$$W_{pq,rs} = -\langle pq|rs\rangle + \Xi^{GW}_{pq,rs} \tag{5.73}$$

are the elements of the dynamically-screened Coulomb potential in its static limit, while the elements of the dynamical kernel for the resonant block are [550]

$$\begin{aligned}\tilde{\Theta}^{GW}_{ia,jb}(\omega) = &- \sum_{kc} \frac{W_{ac,bk} W_{jk,ic}}{\omega - \left(\epsilon^{GW}_a + \epsilon^{GW}_c - \epsilon^{GW}_k - \epsilon^{GW}_j\right)} \\ &- \sum_{kc} \frac{W_{ak,bc} W_{ki,cj}}{\omega - \left(\epsilon^{GW}_c + \epsilon^{GW}_b - \epsilon^{GW}_i - \epsilon^{GW}_k\right)} \\ &+ \sum_{cd} \frac{W_{aj,cd} W_{cd,ib}}{\omega - \left(\epsilon^{GW}_c + \epsilon^{GW}_d - \epsilon^{GW}_j - \epsilon^{GW}_i\right)} \\ &+ \sum_{kl} \frac{W_{aj,kl} W_{kl,ib}}{\omega - \left(\epsilon^{GW}_a + \epsilon^{GW}_b - \epsilon^{GW}_k - \epsilon^{GW}_l\right)}\end{aligned} \tag{5.74}$$

where one readily sees that hp, ph, pp, and hh contributions are included at the BSE2@GW level. As for the GF2 kernel (see Sec. 5.3.2), one can easily derive an upfolded version of this second-order kernel.

5.3.5 First-order T-matrix kernel

Another possible BSE kernel can be constructed using the T-matrix self-energy [see Eq. (5.29)]. A detailed study of this kernel is performed in Ref. [30]. Following a similar derivation as the GW kernel, one gets at the BSE@GT level

$$\begin{aligned}\Xi^{GT}(35,46) &= i\frac{\delta \Sigma^{GT}(34)}{\delta G(65)} = -\frac{\delta (G(87) T_{\mathrm{c}}(37,48))}{\delta G(65)} \\ &= -T_{\mathrm{c}}(37,48)\frac{\delta G(87)}{\delta G(65)} - G(87)\frac{\delta T_{\mathrm{c}}(37,48)}{\delta G(65)} \\ &= -T_{\mathrm{c}}(35,46)\end{aligned} \tag{5.75}$$

where again we neglect the functional derivative $\delta T_{\mathrm{c}}/\delta G$. (To be best of our knowledge, a second-order expression of the T-matrix kernel has not yet been derived.)

The elements of the static T-matrix kernel are given by [73]

$$\Xi^{GT}_{pq,rs} = -\sum_n \frac{M^{\mathrm{pp}}_{pq,n} M^{\mathrm{pp}}_{rs,n}}{\Omega^{\mathrm{pp}}_n} + \sum_n \frac{M^{\mathrm{hh}}_{pq,n} M^{\mathrm{hh}}_{rs,n}}{\Omega^{\mathrm{hh}}_n} \tag{5.76}$$

where the expressions for the screened integrals have already been established in Sec. 5.2.4.

Going beyond the static approximation, one gets the dynamical T-matrix kernel [30]

$$\begin{aligned}\tilde{\Xi}^{GT}_{ia,jb}(\omega) = &\sum_n \frac{M^{\mathrm{pp}}_{aj,n} M^{\mathrm{pp}}_{bi,n}}{\omega - (\Omega^{\mathrm{pp}}_n - \epsilon^{GT}_i - \epsilon^{GT}_j)} \\ &+ \sum_n \frac{M^{\mathrm{hh}}_{aj,n} M^{\mathrm{hh}}_{bi,n}}{\omega - (\epsilon^{GT}_a + \epsilon^{GT}_b - \Omega^{\mathrm{hh}}_n)}\end{aligned} \tag{5.77}$$

It is interesting to note that, by removing the resummation effect of the T-matrix, *i.e.*, by performing the following substitutions, $\Omega^{\mathrm{pp}}_n \to \epsilon^{\mathrm{HF}}_a + \epsilon^{\mathrm{HF}}_b$, $\Omega^{\mathrm{hh}}_n \to \epsilon^{\mathrm{HF}}_i + \epsilon^{\mathrm{HF}}_j$,

$M^{\mathrm{pp}}_{pq,m} \to \langle pq||cd\rangle$, and $M^{\mathrm{hh}}_{pq,m} \to \langle pq||ij\rangle$, one recovers both the direct and exchange parts of the pp and hh terms from Eq. (5.48).

The upfolding process gives us

$$\tilde{\mathbf{H}}^{GT} = \begin{pmatrix} \mathbf{A}^{GT} & \mathbf{K}^{\mathrm{pp}} & \boldsymbol{I}^{\mathrm{hh}} \\ (\boldsymbol{L}^{\mathrm{pp}})^{\dagger} & \mathbf{C}^{\mathrm{pp}} & \mathbf{0} \\ (\boldsymbol{J}^{\mathrm{hh}})^{\dagger} & \mathbf{0} & \mathbf{C}^{\mathrm{hh}} \end{pmatrix} \tag{5.78}$$

with

$$A^{GT}_{ia,jb} = (\epsilon^{GT}_a - \epsilon^{GT}_i)\delta_{ij}\delta_{ab} + \langle ib||aj\rangle \tag{5.79}$$

and the following expressions for the diagonal blocks $\mathbf{C}^{\mathrm{pp}}$ and $\mathbf{C}^{\mathrm{hh}}$

$$C^{\mathrm{pp}}_{ijn,ijn} = \Omega^{\mathrm{pp}}_n - \epsilon^{GT}_i - \epsilon^{GT}_j \tag{5.80a}$$

$$C^{\mathrm{hh}}_{abn,abn} = \epsilon^{GT}_a + \epsilon^{GT}_b - \Omega^{\mathrm{hh}}_n \tag{5.80b}$$

while the coupling blocks read

$$I^{\mathrm{hh}}_{ia,cdn} = \delta_{ac} M^{\mathrm{hh}}_{di,n} \qquad J^{\mathrm{hh}}_{ia,cdn} = \delta_{ad} M^{\mathrm{hh}}_{ci,n} \tag{5.81a}$$

$$K^{\mathrm{pp}}_{ia,kln} = \delta_{il} M^{\mathrm{pp}}_{ak,n} \qquad L^{\mathrm{pp}}_{ia,kln} = \delta_{ik} M^{\mathrm{pp}}_{al,n} \tag{5.81b}$$

By downfolding Eq. (5.78), we obtain

$$\begin{aligned} \tilde{\boldsymbol{\Xi}}^{GT}(\omega) = \mathbf{K}^{\mathrm{pp}} \cdot (\omega\mathbf{1} - \mathbf{C}^{\mathrm{pp}})^{-1} \cdot (\boldsymbol{L}^{\mathrm{pp}})^{\dagger} \\ + \boldsymbol{I}^{\mathrm{hh}} \cdot \left(\omega\mathbf{1} - \mathbf{C}^{\mathrm{hh}}\right)^{-1} \cdot \left(\boldsymbol{J}^{\mathrm{hh}}\right)^{\dagger} \end{aligned} \tag{5.82}$$

which gives back the dynamical kernel (5.77). Symmetrizing Eq. (5.78) has been revealed to be challenging, and we have not found any satisfying form.

5.4 Computational Details

All systems investigated in this study possess a closed-shell singlet ground state, and thus we employ the restricted formalism exclusively. As mentioned earlier, we initiate all calculations from HF orbitals and energies. We focus on two sets of atoms and molecules: one set pertains to charged excitations, where we solely consider the principal ionization potentials (IPs), while the other set concerns neutral excitations, where we compute singlet and triplet vertical excitation energies. In all calculations, the positive infinitesimal η is set to zero.

The first set comprises 20 atoms and molecules from the *GW*100 test set [391], denoted as *GW*20, previously explored in Refs. [28, 515]. We adopt the geometries for the *GW*20 set from Ref. [391]. Calculations of IPs are performed using three different schemes: GF2, *GW*, and *GT*. All occupied and virtual orbitals are corrected. For each scheme, we compute the linearized solution of the quasiparticle equation by solving Eq. (5.9) and the dynamical solution by employing Newton's method starting from the linearized solution. The results presented in Appendix E indicate that the linearization procedure has minimal impact on the *GW* and *GT* quasiparticles energies, while it improves the accuracy of GF2. Consequently, all quasiparticle energies are obtained via linearization of quasiparticle equation [see Eq. (5.9)]. It is important to note that the *GW* and *GT* calculations are carried out without the TDA

for the calculation of W and T, respectively. As reference data, we rely on CCSD(T) IPs computed in the same basis.

The second set comprises 7 molecules as considered in Ref. [29]. The corresponding geometries are extracted from the same work. Singlet and triplet transition energies are computed using the aug-cc-pVTZ basis via BSE utilizing the quasiparticle energies and kernels from the three different approximations under consideration (GF2, *GW*, and *GT*). For each scheme (BSE@GF2, BSE@*GW*, BSE2@*GW*, and BSE@*GT*), we also incorporate their respective dynamical corrections, named dBSE@GF2, dBSE@*GW*, dBSE2@*GW*, and dBSE@*GT*. To facilitate comparison, we also perform TDHF and CIS calculations. Our results are benchmarked against the theoretical best estimates (TBEs) from Ref. [29], from which we also extract transition energies computed using various second-order methods: CIS(D) [262, 263], ADC(2) [79, 264], CC2 [265], and EOM-CCSD [246, 341].

Here, we detail the strategy for the computation of neutral excitations within the BSE formalism. First, we solve the linearized quasiparticle equation [see Eq. (5.9)] to obtain the quasiparticle solutions. Then, for the static calculations, we solve the eigenvalue problem of Eq. (5.39) using the various static kernels. Finally, for the dynamic corrections, we compute the corrected excitation energies using Eqs. (**??**) and (**??**) and the corresponding dynamical kernels.

Various statistical quantities with respect to the reference values [CCSD(T) for IPs and TBEs for transition energies] are reported: mean absolute error (MAE), mean signed error (MSE), root-mean-square error (RMSE), and maximum error (Max). All static and dynamic BSE calculations, as well as CIS and TDHF calculations, are performed using the freely available software QUACK, which can be found on GITHUB [242].

5.5 Results and discussion

5.5.1 Ionization potentials

The IPs of the *GW*20 set using the different approximations of the self-energy are reported in Table 5.1, where we also report the HF values. It clearly shows the superiority of the *GW* approximation for the calculation of IPs compared to the GF2 approximation. Indeed, we can see that the different statistical errors associated with *GW* (MAE and MSE of 0.28 eV and 0.23 eV, respectively) are much smaller than the ones of GF2 (MAE and MSE of 0.56 eV and -0.55 eV, respectively). For example, we have a maximum error of 1.60 eV for GF2 whereas *GW* has a maximum error of 0.85 eV. We can note that the *GT* approximation (MAE and MSE of 0.26 eV and -0.18 eV, respectively) presents a similar MAE and maximum error as *GW*, while its MSE has also a similar magnitude but opposite sign. An analogous conclusion was reached by Zhang and coworkers for larger systems [73]. Note also that similar trends on ionization potentials were found by Bruneval *et al.* [407]

5.5.2 Vertical transition energies

The results of our calculations for vertical transition energies using the aug-cc-pVTZ basis set are summarized in Tables 5.2 and 5.3 for the singlet and triplet excited states, respectively. They also report separate statistical errors for different classes of singlet and triplet excitations: valence (Val.) and Rydberg (Ryd.) excited states.

As expected, both CIS and TDHF exhibit large statistical errors compared to the TBEs. It is well known that TDHF provides a poor description of triplet excitations,

Table 5.1: Principal IPs (in eV) of the *GW*20 set computed with various approximations using the cc-pVTZ basis.

Mol.	HF	GF2	*GW*	*GT*	ΔCCSD(T)
He	24.97	24.54	24.58	24.77	24.53
Ne	23.01	20.13	21.40	21.02	21.30
H_2	16.17	16.31	16.49	16.26	16.40
Li_2	4.95	5.19	5.35	5.04	5.23
LiH	8.20	7.99	8.16	8.14	7.99
HF	17.53	14.72	16.18	15.63	15.98
Ar	16.06	15.39	15.70	15.49	15.53
H_2O	13.75	11.52	12.81	12.24	12.53
LiF	12.92	9.81	11.38	10.95	11.39
HCl	12.95	12.40	12.75	12.48	12.59
BeO	10.50	8.38	9.78	9.21	9.98
CO	15.35	14.17	15.03	14.44	14.21
N_2	17.23	15.09	17.09	15.70	15.49
CH_4	14.84	14.11	14.75	14.28	14.38
BH_3	13.56	13.25	13.65	13.30	13.28
NH_3	11.61	10.18	11.15	10.62	10.78
BF	11.00	11.02	11.29	10.92	11.09
BN	11.52	10.99	11.70	11.12	11.99
SH_2	10.46	10.15	10.46	10.15	10.32
F_2	18.09	14.26	16.31	15.38	15.68
MAE	0.81	0.56	0.28	0.26	
MSE	0.70	-0.55	0.23	-0.18	
RMSE	1.04	0.80	0.36	0.34	
Max	2.41	1.60	0.85	0.87	

Table 5.2: Singlet excitation energies (in eV) of various molecules computed using the aug-cc-pVTZ basis set at different levels of theory. The dynamically-corrected BSE transition energies (dBSE) are reported in parentheses. CT stands for charge transfer. The statistical descriptors associated with the errors with respect to the reference values are also reported for the entire dataset and separately for valence (Val.) and Rydberg (Ryd.) excited states.

Mol.	Nature	CIS	TDHF	BSE@GF2		BSE@*GW*		BSE2@*GW*		BSE@*GT*		CIS(D)	ADC(2)	CC2	CCSD	TBE
HCl	CT	8.32	8.27	8.17	(7.99)	8.30	(8.19)	8.48	(8.36)	7.56	(7.52)	6.07	7.97	7.96	7.91	7.84
H_2O	Ryd.	8.69	8.64	7.13	(7.01)	8.09	(8.01)	8.24	(8.14)	7.12	(7.08)	7.62	7.18	7.23	7.60	7.17
	Ryd.	10.36	10.31	8.71	(8.66)	9.80	(9.72)	9.91	(9.84)	8.88	(8.84)	9.41	8.84	8.89	9.36	8.92
	Ryd.	10.96	10.93	9.49	(9.36)	10.42	(10.35)	10.53	(10.45)	9.55	(9.51)	9.99	9.52	9.58	9.96	9.52
N_2	Val.	9.95	9.70	9.83	(9.28)	10.42	(9.99)	11.28	(10.74)	7.89	(7.78)	9.66	9.48	9.44	9.41	9.34
	Val.	8.43	7.86	10.72	(9.69)	10.11	(9.66)	11.35	(10.70)	8.18	(8.02)	10.31	10.26	10.32	10.00	9.88
	Val.	8.98	8.68	11.28	(10.34)	10.75	(10.33)	11.45	(10.86)	8.47	(8.36)	10.85	10.79	10.86	10.44	10.29
	Ryd.	14.48	14.46	12.30	(12.29)	13.60	(13.57)	13.61	(13.57)	12.71	(12.68)	13.67	12.99	12.83	13.15	12.98
	Ryd.	14.95	14.87	14.19	(14.07)	13.98	(13.94)	14.08	(14.03)	13.69	(13.66)	13.64	13.32	13.15	13.43	13.03
	Ryd.	14.42	13.98	12.84	(12.84)	13.98	(13.91)	14.13	(14.08)	13.16	(13.11)	13.75	13.07	12.89	13.26	13.09
	Ryd.	13.56	13.54	12.99	(12.96)	14.24	(14.21)	14.30	(14.27)	13.54	(13.47)	14.52	14.00	13.96	13.67	13.46
CO	Val.	9.00	8.72	9.40	(8.84)	9.54	(9.20)	10.15	(9.74)	7.63	(7.53)	8.78	8.69	8.64	8.59	8.49
	Val.	9.61	9.25	10.11	(9.43)	10.25	(9.91)	11.27	(10.79)	8.62	(8.52)	10.13	10.03	10.30	9.99	9.92
	Val.	10.02	9.82	10.39	(9.83)	10.72	(10.40)	11.23	(10.77)	8.80	(8.72)	10.41	10.30	10.60	10.12	10.06
	Ryd.	12.12	12.08	11.04	(11.00)	11.88	(11.85)	11.86	(11.83)	11.16	(11.13)	11.48	11.32	11.11	11.22	10.95
	Ryd.	12.72	12.71	11.72	(11.65)	12.39	(12.37)	12.45	(12.42)	11.81	(11.80)	11.71	11.83	11.63	11.75	11.52
	Ryd.	12.82	12.81	11.69	(11.62)	12.37	(12.32)	12.46	(12.41)	11.68	(11.67)	12.06	12.03	11.83	11.96	11.72
C_2H_2	Val.	6.27	5.90	7.95	(7.33)	7.37	(7.05)	8.09	(7.67)	5.72	(5.63)	7.28	7.24	7.26	7.15	7.10
	Val.	6.61	6.42	8.15	(7.59)	7.74	(7.46)	8.17	(7.81)	5.94	(5.87)	7.62	7.56	7.59	7.48	7.44
C_2H_4	Ryd.	7.15	7.13	7.41	(7.31)	7.64	(7.62)	7.69	(7.66)	7.01	(6.98)	7.35	7.34	7.29	7.42	7.39
	Val.	7.72	7.37	8.36	(8.11)	8.19	(8.04)	8.34	(8.31)	7.02	(6.97)	7.95	7.91	7.92	8.02	7.93
	Ryd.	7.74	7.73	8.04	(7.97)	8.29	(8.26)	8.35	(8.35)	7.64	(7.61)	8.01	7.99	7.95	8.08	8.08
CH_2O	Val.	4.57	4.39	4.82	(4.26)	5.03	(4.68)	5.66	(5.17)	2.78	(2.68)	4.04	3.92	4.07	4.01	3.98
	Ryd.	8.59	8.59	6.36	(6.40)	7.87	(7.85)	7.87	(7.88)	7.11	(7.09)	6.64	6.50	6.56	7.23	7.23
	Ryd.	9.41	9.40	7.50	(7.45)	8.76	(8.72)	8.83	(8.79)	7.87	(7.85)	7.56	7.53	7.57	8.12	8.13
	Ryd.	9.53	9.58	7.39	(7.41)	8.85	(8.84)	8.85	(8.86)	8.12	(8.11)	8.16	7.47	7.52	8.21	8.23
	Ryd.	10.02	10.02	7.40	(7.37)	8.87	(8.85)	8.92	(8.89)	8.00	(7.99)	8.04	7.99	8.04	8.65	8.67
	Val.	9.82	9.57	10.00	(9.34)	10.19	(9.77)	11.00	(10.48)	7.54	(7.44)	9.38	9.17	9.32	9.28	9.22
	Val.	9.72	9.21	9.95	(9.82)	10.06	(9.82)	10.39	(10.14)	8.38	(8.31)	9.08	9.46	9.54	9.67	9.43
MAE		0.92	0.94	0.52	(0.35)	0.64	(0.50)	0.96	(0.76)	0.69	(0.74)	0.43	0.24	0.25	0.15	
MSE		0.54	0.38	0.15	(-0.13)	0.64	(0.48)	0.96	(0.76)	-0.60	(-0.66)	0.14	0.02	0.03	0.14	
RMSE		1.06	1.09	0.63	(0.47)	0.71	(0.58)	1.06	(0.82)	0.92	(0.98)	0.55	0.33	0.33	0.20	
Max		1.92	2.02	1.27	(1.30)	1.08	(0.91)	1.94	(1.40)	1.82	(1.93)	1.77	0.76	0.71	0.44	
MAE	Val.	0.63	0.74	0.66	(0.23)	0.61	(0.32)	1.27	(0.84)	1.34	(1.44)	0.26	0.17	0.23	0.09	
MSE	Val.	-0.20	-0.52	0.66	(0.06)	0.61	(0.27)	1.27	(0.84)	-1.34	(-1.44)	0.20	0.14	0.23	0.09	
RMSE	Val.	0.75	0.94	0.70	(0.26)	0.69	(0.41)	1.35	(0.91)	1.37	(1.47)	0.30	0.22	0.30	0.11	
Max	Val.	1.45	2.02	0.99	(0.49)	1.08	(0.71)	1.94	(1.40)	1.82	(1.93)	0.56	0.50	0.57	0.24	
MAE	Ryd.	1.16	1.12	0.43	(0.45)	0.68	(0.64)	0.75	(0.71)	0.23	(0.23)	0.47	0.30	0.27	0.19	
MSE	Ryd.	1.09	1.04	-0.24	(-0.30)	0.68	(0.64)	0.75	(0.71)	-0.07	(-0.09)	0.22	-0.07	-0.13	0.19	
RMSE	Ryd.	1.26	1.22	0.59	(0.59)	0.73	(0.69)	0.80	(0.76)	0.31	(0.31)	0.54	0.41	0.36	0.25	
Max	Ryd.	1.92	1.84	1.27	(1.30)	0.95	(0.91)	1.07	(1.00)	0.67	(0.68)	1.06	0.76	0.71	0.44	

Table 5.3: Triplet excitation energies (in eV) of various molecules computed using the aug-cc-pVTZ basis set at different levels of theory. The dynamically-corrected BSE transition energies (dBSE) are reported in parentheses. The statistical descriptors associated with the errors with respect to the reference values are also reported for the entire dataset and separately for valence (Val.) and Rydberg (Ryd.) excited states.

Mol.	Nature	CIS	TDHF	BSE@GF2		BSE@*GW*		BSE@*GT*		CIS(D)	ADC(2)	CC2	CCSD	TBE
H_2O	Ryd.	8.00	7.88	7.02	(6.80)	7.62	(7.48)	6.60	(6.54)	7.25	6.86	6.91	7.20	6.92
	Ryd.	10.01	9.88	8.68	(8.60)	9.61	(9.50)	8.65	(8.58)	9.24	8.72	8.77	9.20	8.91
	Ryd.	10.10	9.87	9.33	(9.09)	9.81	(9.67)	8.82	(8.75)	9.54	9.15	9.20	9.49	9.30
N_2	Val.	6.16	3.36	8.88	(7.41)	8.03	(7.38)	6.17	(5.91)	8.20	8.15	8.19	7.66	7.70
	Val.	7.95	7.57	9.04	(8.10)	8.66	(8.10)	6.30	(6.12)	8.33	8.20	8.19	8.09	8.01
	Val.	7.23	5.72	9.94	(8.67)	9.04	(8.48)	7.11	(6.90)	9.30	9.25	9.30	8.91	8.87
	Val.	8.43	7.86	10.91	(9.88)	10.11	(9.66)	7.99	(7.85)	10.29	10.23	10.29	9.83	9.66
CO	Val.	5.81	5.22	7.59	(6.45)	6.80	(6.25)	4.99	(4.76)	6.51	6.45	6.42	6.36	6.28
	Val.	7.68	6.21	8.80	(7.71)	8.57	(8.07)	7.02	(6.81)	8.63	8.54	8.72	8.34	8.45
	Val.	8.61	7.71	9.58	(8.68)	9.39	(8.96)	7.78	(7.62)	9.44	9.33	9.56	9.23	9.27
	Val.	9.61	9.25	10.24	(9.56)	10.25	(9.91)	8.49	(8.39)	10.10	10.01	10.27	9.81	9.80
	Ryd.	11.13	11.03	10.86	(10.71)	11.17	(11.07)	10.48	(10.41)	10.98	10.83	10.60	10.71	10.47
C_2H_2	Val.	4.51	2.16	7.09	(6.13)	5.83	(5.32)	4.18	(3.99)	5.79	5.75	5.76	5.45	5.53
	Val.	5.41	4.44	7.60	(6.81)	6.64	(6.24)	4.97	(4.83)	6.62	6.57	6.60	6.41	6.40
	Val.	6.27	5.90	8.05	(7.43)	7.37	(7.05)	5.66	(5.57)	7.31	7.27	7.29	7.12	7.08
C_2H_4	Val.	3.61	0.76	6.15	(5.20)	4.96	(4.50)	3.15	(2.07)	4.62	4.59	4.59	4.46	4.54
	Ryd.	6.92	6.88	7.40	(7.25)	7.46	(7.42)	6.83	(6.07)	7.26	7.23	7.19	7.29	7.23
	Ryd.	7.65	7.62	8.04	(7.96)	8.23	(8.19)	7.58	(7.17)	7.97	7.95	7.91	8.03	7.98
CH_2O	Val.	3.75	3.40	4.52	(3.83)	4.28	(3.88)	2.17	(2.02)	3.58	3.46	3.59	3.56	3.58
	Val.	4.88	1.95	5.96	(4.31)	6.32	(5.76)	4.26	(4.03)	6.27	6.20	6.30	5.97	6.06
	Ryd.	8.25	8.17	6.32	(6.28)	7.60	(7.56)	6.79	(6.75)	6.66	6.39	6.44	7.08	7.06
MAE		0.82	1.65	0.72	(0.39)	0.41	(0.27)	1.10	(1.33)	0.27	0.21	0.24	0.10	
MSE		-0.34	-1.25	0.61	(-0.11)	0.41	(0.06)	-1.10	(-1.33)	0.23	0.10	0.14	0.05	
RMSE		0.92	2.10	0.88	(0.54)	0.46	(0.33)	1.25	(1.48)	0.31	0.27	0.30	0.13	
Max		1.64	4.34	1.61	(1.75)	0.70	(0.60)	1.80	(2.47)	0.63	0.67	0.63	0.29	
MAE	Val.	0.83	2.12	0.95	(0.47)	0.36	(0.19)	1.50	(1.74)	0.27	0.21	0.27	0.06	
MSE	Val.	-0.81	-2.12	0.94	(-0.08)	0.36	(-0.12)	-1.50	(-1.74)	0.27	0.20	0.27	-0.00	
RMSE	Val.	0.96	2.52	1.06	(0.62)	0.40	(0.23)	1.51	(1.76)	0.31	0.26	0.32	0.08	
Max	Val.	1.64	4.34	1.61	(1.75)	0.70	(0.39)	1.80	(2.47)	0.63	0.57	0.63	0.17	
MAE	Ryd.	0.78	0.70	0.25	(0.24)	0.52	(0.43)	0.31	(0.51)	0.26	0.21	0.16	0.16	
MSE	Ryd.	0.60	0.49	-0.03	(-0.17)	0.52	(0.43)	-0.30	(-0.51)	0.15	-0.11	-0.12	0.16	
RMSE	Ryd.	0.85	0.75	0.34	(0.34)	0.55	(0.46)	0.34	(0.62)	0.32	0.30	0.25	0.19	
Max	Ryd.	1.19	1.11	0.74	(0.78)	0.70	(0.60)	0.48	(1.16)	0.51	0.67	0.62	0.29	

often leading to triplet instabilities [58, 555]. One notices that TDHF is particularly bad at valence excitations. On the other hand, CIS provides a more balanced description of singlets and triplets, thanks to error cancellation.

In Appendix E, we report additional TDHF calculations using the GF2, *GW*, and *GT* quasiparticles (without their corresponding kernel) instead of HF orbital energies. These calculations, referred to as TDHF@GF2, TDHF@*GW*, and TDHF@*GT*, allow us to observe the effects of different kernels and quasiparticles on the excitation energies. We find that the sole introduction of quasiparticle energies does not improve the description of singlet excitations. It should be noted that these calculations for triplet excitations resulted in instabilities and are not shown.

The inclusion of the corresponding BSE kernel significantly improves the description of both singlet and triplet excitations. This highlights the key role of the excitonic effect (*i.e.*, the attractive interaction of the excited electron and the hole left behind), which is captured by the BSE kernel and is crucial for an accurate description of neutral excitations. Importantly, BSE@GF2 (MAE and MSE of 0.52 eV and 0.15 eV, respectively) provides better excitation energies for singlet states compared to BSE@*GW* (MAE and MSE of 0.64 eV), as indicated by their respective statistical descriptors. This observation suggests that the versatility of the GF2 kernel, which contains ph, hp, pp, and hh terms, is a key factor behind its superior performance in describing singlet excitations (see Sec. 5.3.2). However, these trends might be different for larger chemical systems where screening effects become predominant. Furthermore, while BSE@GF2 exhibits a similar accuracy to the second-order method CIS(D) for singlet excitations, BSE@*GW* outperforms BSE@GF2 for triplet excitations. Another notable observation is that the static GF2 kernel provides a better description of Rydberg excitations compared to valence states. Conversely, the static *GW* kernel performs better for valence than Rydberg excitations. These hold for both singlet and triplet transitions. A last point worth highlighting is the contrasted performance of BSE@*GT* for the two classes of excitations: while the accuracy of BSE@*GT* is poor for the valence states (MAEs of 1.34 eV and 1.50 eV for singlets and triplets, respectively), it can be considered accurate for Rydberg transitions (MAEs of 0.23 eV and 0.31 eV for singlets and triplets, respectively), where the excited-state density is much lower than the ground-state one, a situation where ladder diagrams are known to be relevant (see Sec. 5.2.4).

By taking into account the dynamical corrections, we observe an overall improvement in the description of both singlet and triplet excitations, except at the BSE@*GT* level. From a general point of view, as previously mentioned and analyzed in Refs. [29], Rydberg excitations are less affected by dynamical effects than valence excitations across all BSE kernels. For singlet excitations, dBSE@GF2 outperforms CIS(D), especially for singlet valence excitations where its performance surpasses that of all second-order methods, except for EOM-CCSD, which is known to be highly accurate for small molecular systems [143, 145]. Although dBSE@*GW* shows an improvement compared to its static version, it does not reach the accuracy of dBSE@GF2 or second-order methods. However, for triplet excitations, dBSE@*GW* is on par with CIS(D), ADC(2), CC2, and EOM-CCSD, while dBSE@GF2 falls short of the accuracy of CIS(D). In particular, for triplet valence excitations, dBSE@*GW* outperforms all second-order methods, except EOM-CCSD. For these small molecular systems, both at the static and dynamic levels, the second-order scheme BSE2@*GW* does not bring any improvement upon its first-order version.

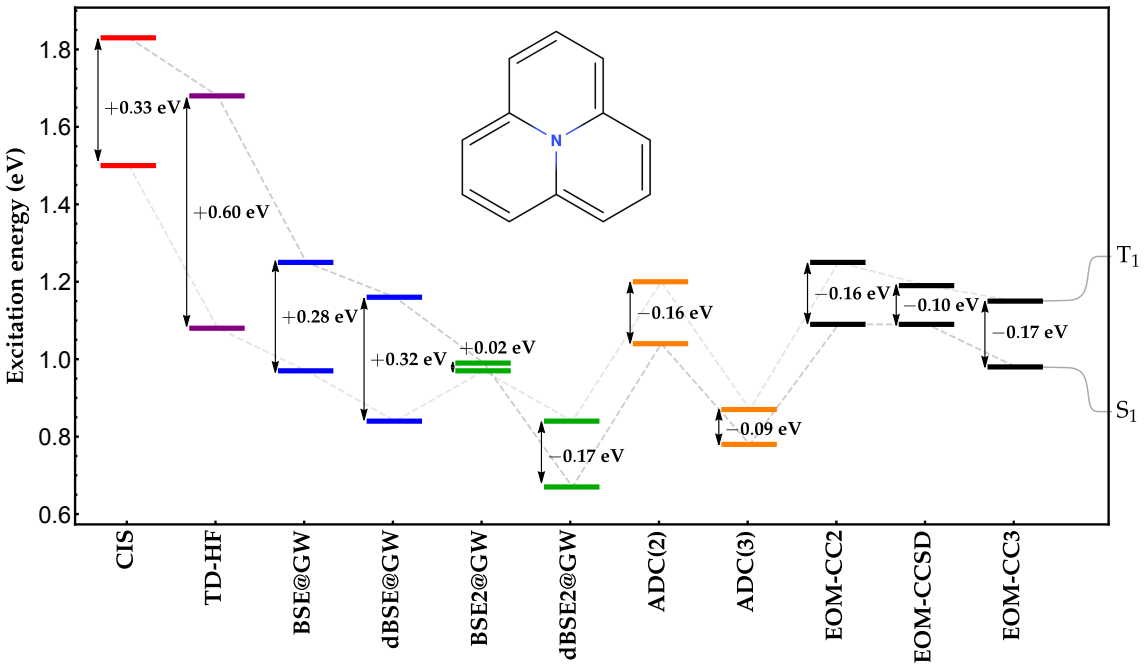

Figure 5.1: Evolution of the lowest singlet and triplet vertical excitation energies (in eV) of cycl[3,3,3]zine evaluated with different computational methods using the cc-pVDZ basis.

Table 5.4: Lowest singlet and triplet vertical excitation energies, E_S and E_T, and resulting singlet-triplet gap ΔE_{ST} (in eV) of cycl[3,3,3]zine computed at various levels of theory using the cc-pVDZ basis. The percentage of single excitations involved in each transition, $\%T_1$, computed at the EOM-CC3 level is reported in parenthesis.

Method	E_S	E_T	ΔE_{ST}
CIS	1.83	1.50	+0.33
TDHF	1.68	1.08	+0.60
BSE@*GW*	1.25	0.97	+0.28
dBSE@*GW*	1.16	0.84	+0.32
BSE2@*GW*	0.99	0.97	+0.02
dBSE2@*GW*	0.67	0.84	-0.17
CIS(D)	1.07	1.37	-0.30
ADC(2)	1.04	1.20	-0.16
ADC(3)	0.78	0.87	-0.09
EOM-CC2	1.09	1.25	-0.16
EOM-CCSD	1.09	1.19	-0.10
EOM-CC3	0.98 (87%)	1.15 (96%)	-0.17

5.5.3 Singlet-triplet gap of cycl[3,3,3]zine

Molecules with an inverted singlet-triplet gap (*i.e.*, where the lowest singlet excited state is lower in energy than the lowest triplet state) are of particular interest in TADF [556, 557] because they can harness both singlet and triplet excitons for emission, thereby enhancing the efficiency of OLEDs [558, 559]. Thanks to this inverted gap, the system can undergo efficient reverse intersystem crossing, a process in which the population from the triplet state can be thermally activated and transferred back to the singlet state, resulting in delayed fluorescence.

Recently, such systems have been scrutinized at different computational levels, including TD-DFT and second-order wave function methods, such as CIS(D), ADC(2), and EOM-CCSD [560–566]. In particular, de Silva has shown that this inversion requires a substantial contribution from the double excitations [560]. This explains why adiabatic TD-DFT is not able to reproduce this particular feature, and second- or higher-order methods are required where double excitations are explicitly treated.

Following the computational protocol of Ref. [560], we compute the lowest singlet and triplet excitation energies, E_S and E_T, as well as the corresponding singlet-triplet gap, ΔE_{ST}, of cycl[3,3,3]zine (see Fig. 5.1), a model molecular emitter for TADF, with the cc-pVDZ basis at various levels of theory. The geometry of cycl[3,3,3]zine has been optimized at the B3LYP/cc-pVDZ level and is reported in Appendix E for the sake of completeness. Additionally, we have been able to compute the singlet-triplet gap with third-order methods such as ADC(3) [79, 84, 266] and EOM-CC3 [146, 147].

Our results are gathered in Table 5.4 and shown in Fig. 5.1. As expected, the BSE@*GW* and BSE2@*GW* calculations do not produce an inverted singlet-triplet gap due to the static nature of the kernel. Because the dynamical correction of the singlet and triplet excitation energies cancel each other pretty much exactly, dBSE@*GW* yields the same state ordering. However, the second-order dynamical *GW* kernel (which only corrects singlet states as explained in Sec. 5.3.4) faithfully predicts this inversion although the corresponding excitation energies are underestimated compared to other approaches, except ADC(3), which is known to exhibit this trend [366]. Interestingly, ADC(2), EOM-CC2, EOM-CC3, and BSE2@*GW* yield essentially the same value, while EOM-CCSD and ADC(3) slightly underestimate the gap. Because the percentage of single excitations involved in these two valence transitions (%T_1, see Table 5.4) is high (although not negligible for the singlet state), the EOM-CC3 value is likely to be accurate [145]. Note that, because of the poor quality of the GF2 quasiparticle energies, we could not compute excitation energies at the (d)BSE@GF2 level as spurious poles appeared in the BSE kernel.

5.6 Concluding remarks

In this study, our focus was on examining the relationships between different Green's function methods, specifically exploring various approximations for the self-energy (GF2, *GW*, and *GT*) and their corresponding BSE kernels at the static and dynamic levels. Additionally, we extended the upfolding process, previously confined to the GF2 and *GW* frameworks, to the *T*-matrix approximation. The introduction of this upfolding framework allowed us to uncover connections between GF2 and the ADC(2) scheme concerning both charged and neutral excitations, and to propose new directions for the development of accurate kernels at the *GW* level.

Subsequently, we applied these three distinct approximations to calculate the principal IPs and vertical transition energies for both singlet and triplet states of small molecules. Our findings can be summarized as follows:

- Confirming previous knowledge, the *GW* approximation surpasses the GF2 method in accurately calculating IPs, emphasizing the significance of screening even in small molecular systems.
- The *T*-matrix approximation exhibits comparable accuracy to *GW*, although it falls slightly short.
- For the singlet excited states of small molecules, the GF2 kernel generally outperforms its *GW* counterpart. Conversely, for triplet excitations, BSE@*GW* provides more accurate vertical excitation energies.
- Importantly, our investigations highlight the sensitivity of BSE kernels to the nature of the excited states. For example, BSE@*GT* is poor for valence states while it is accurate for Rydberg transitions.
- Overall, except in the *T*-matrix approximation, dynamical corrections are almost systematically beneficial.

It is important to note that these conclusions are drawn specifically for small molecules, and it would be intriguing to explore if similar trends persist in larger systems. Moreover, it is worth mentioning that because we only rely on one-shot schemes, the quality of our results strongly depends on the starting point (HF orbitals). It is clear that more accurate results can be obtained using partially self-consistent schemes or by tuning the starting point using an adequate exchange-correlation functional.

To initiate our pursuit of this objective, we examined the capability of our various schemes to replicate the inversion of the singlet-triplet gap in cycl[3,3,3]zine, a prototypical molecular emitter for TADF. With the exception of one case, we observed that all static and dynamic BSE-based schemes failed to reproduce this unique characteristic. The only exception was the dynamically-corrected BSE2@*GW* scheme, which yielded a gap value consistent with that obtained from EOM-CC3 calculations. This observation effectively highlights the significance of higher-order terms and dynamic effects within the BSE formalism, and we anticipate that these findings will stimulate further advancements in this area of research.

Chapter 6

qcmath: Mathematica modules for electronic structure calculations

In this chapter, we present a quantum chemistry software for electronic structure calculations based on the Wolfram Mathematica language. This software aims to take advantage of the powerful symbolic nature of Mathematica to help newcomers in quantum chemistry easily develop their ideas.

6.1 Introduction

Quantum chemistry methods are highly compatible with computer utilization, owing to the matrix formulation of quantum mechanics, which leverages the power of linear algebra packages like BLAS and LAPACK. As a result, a wide array of quantum chemistry software is currently available, encompassing both free and commercial options. These software packages cater to specific methods or offer a diverse range of methodologies, utilizing various types of basis functions, among other features. A considerable number of quantum chemistry codes exist, covering a comprehensive range of methods. For a comprehensive list of these codes, refer to Wikipedia's page on quantum chemistry and solid-state physics software.

Regrettably, despite the efficient design of many of these software packages, they can be challenging to comprehend as they often employ low-level programming languages. Moreover, these programs are not primarily intended for educational purposes or for facilitating understanding. This is precisely where QCMATH comes into play. QCMATH aims to assist newcomers in the field of quantum chemistry by providing a user-friendly platform for developing ideas and codes. It is worth noting that certain software packages utilize higher-level programming languages, which can enhance code comprehension. As for QCMATH, it is a compilation of MATHEMATICA modules specifically designed for conducting electronic structure calculations.

Before delving into the specifics of QCMATH, let us provide an overview of the MATHEMATICA environment. MATHEMATICA is a comprehensive software system developed by Wolfram Research, initially conceptualized by Stephen Wolfram. It boasts a wide range of built-in libraries that can be utilized for diverse purposes. One of its key strengths lies in its ability to perform computer algebra operations, such as derivatives, integrals, and expression simplifications. Furthermore, MATHEMATICA enables the numerical evaluation of these expressions. Another notable feature is its

advanced plotting capabilities, supporting intricate visualizations of functions in one, two, and three dimensions. Numerous books offer extensive examples of MATHEMATICA's applications across various domains. With its versatility, MATHEMATICA has become a powerful tool employed in numerous scientific fields, including education, research, and industry.

MATHEMATICA comprises two main components: the kernel and the front end. The kernel interprets expressions and generates result expressions, which can then be displayed using the front end. The original front end takes the form of a notebook interface, facilitating the creation and editing of notebook documents that can contain code, plaintext, images, and graphics. QCMATH, specifically, relies on these notebook documents. It is important to note that QCMATH is **not** primarily designed for computational efficiency but rather focuses on providing a user-friendly environment.

6.2 Installation guide

The QCMATH software can be downloaded on GITHUB as a git repository

```
git clone https://github.com/LCPQ/qcmath.git
```

Then, one must define the variable `QCMATH_ROOT` and install PySCF using `pip`

```
pip install pyscf
```

PySCF is used for the computation of one- and two-electron integrals. Here is the list of the requirements to use QCMATH:

- Linux OS
- Wolfram Mathematica $\geq$ 12.1
- PySCF
- Python $\geq$ 3.6.0
- Numpy $\geq$ 1.13

Note that the version of Python and Numpy is fixed by PySCF.

6.3 Quick start

Before running any QCMATH calculation, we need to define the working directory as

```
SetDirectory[NotebookDirectory[]];
path=Directory[];
py="your_path_to_python"
NotebookEvaluate[path<>"/src/Main/Main.nb"]
```

To streamline the execution of other notebooks and prevent the need for directory changes, the first line of code sets the working directory as the directory containing the notebook. This ensures a seamless evaluation process. Following that, the second line establishes the variable `path` as the current directory, which corresponds to the working directory. The third line designates the path to your Python installation,

allowing for appropriate configuration. Lastly, the main notebook is evaluated, with the inclusion of the `path` variable to locate the correct directory. This approach ensures smooth execution and seamless integration of the required files.

Once this first step is done, one can run a QCMATH calculation as follows

```
qcmath[molecule_name,basis_set,methods]
```

To invoke the QCMATH module, use the keyword `qcmath` followed by three arguments. These arguments are either strings or a list of strings. The first argument is the name of the molecule to be studied, represented as a string. For example, in the case of the H_2 molecule, it would be specified as `"H2"`. The second argument corresponds to the basis set and is also provided as a string. For instance, in the example of the 6-31G basis set, it would be specified as `"6-31g"`. In summary, taking the example of the H_2 molecule in the 6-31G basis set using the restricted Hartree-Fock method, the QCMATH module call would resemble the following code:

```
qcmath["H2","6-31g",{"RHF"}]
```

The molecular geometry is specified in a .xyz file in the mol directory while the basis set file is in the basis directory.

Additional options can be specified, such as the charge and spin multiplicity of the molecule. If these options are not explicitly stated, the default values are zero for the charge (neutral) and singlet state for the spin multiplicity. Furthermore, options related to different methods can also be specified, but we will discuss them in the upcoming section. It is worth noting that most of the presented methods offer both spin and spatial orbital implementations. You can choose between them using the keyword `"spinorbital"`, with the default value being `False` (indicating spatialorbital as the default choice). For a comprehensive list of all available options, including charge, spin multiplicity, and method-related choices, please refer to the `Main/default_options.nb` notebook. This notebook presents the options in the form of a dictionary, providing a convenient reference for configuring and customizing the calculations.

6.4 User guide

The QCMATH software is currently undergoing active development. The features discussed below are currently available, and they represent the initial roadmap for the software's future. This User Guide provides a comprehensive introduction to the underlying theoretical concepts and showcases the functionalities offered by these methods [70, 81, 103, 567, 568]. It serves as a valuable resource to gain insights into the theoretical background and explore the capabilities that will be incorporated into QCMATH as it continues to evolve.

6.4.1 Ground state calculations

Hartree-Fock

In the context of the Hartree-Fock (HF) approximation, the electronic wave function is expressed as a Slater determinant comprising N one-electron orbitals [70]. Within the restricted HF (RHF) formalism, the Roothaan-Hall equations come into play, given by $\boldsymbol{F} \cdot \boldsymbol{C} = \boldsymbol{S} \cdot \boldsymbol{C} \cdot \boldsymbol{\varepsilon}$. Here, $\boldsymbol{F}$ represents the Fock matrix, $\boldsymbol{C}$ denotes the matrix of orbital coefficients, $\boldsymbol{S}$ stands for the matrix representing atomic orbital overlaps, and $\boldsymbol{\varepsilon}$ is a diagonal matrix containing the orbital energies. Since the Fock matrix relies on the

orbital coefficients $\boldsymbol{C}$, which are obtained from the Fock matrix itself, these equations necessitate a self-consistent solution. To facilitate this process, various options can be specified to customize the calculations and achieve desired outcomes:

1. an initial guess for the Fock matrix needs to be diagonalized to give the MO coefficients and this initial guess is described by the keyword `"guess_type"`
   - `"guess_type"→"core"` (default) corresponds to the core Hamiltonian defined as $\boldsymbol{H}^{\mathrm{c}} = \boldsymbol{T} + \boldsymbol{V}$ where $\boldsymbol{T}$ is the kinetic energy matrix and $\boldsymbol{V}$ is the external potential.
   - `"guess_type"→"huckel"` corresponds to the Hückel Hamiltonian
   - `"guess_type"→"random"` corresponds to random MO coefficients
2. converging HF calculation
   - `"maxSCF"`: maximum number of iterations, by default `"maxSCF"→100`
   - `"threshHF"`: threshold for the HF to converge, by default `"threshHF"→` 10^{-7}
   - `"DIIS"`: we can use the Direct Inversion in the Iterative Subspace (DIIS) where the Fock matrix is extrapolated at each iteration using the ones of the previous iterations, by default `"DIIS"→True`
   - `"n_DIIS"`: by default `"n_DIIS"→5`
   - `"level_shift"`: a level shift increases the gap between the occupied and virtual orbitals, it can help to converge the SCF process for systems with a small HOMO-LUMO gap, by default `"level_shift"→0.0` eV
3. orthogonalization matrix with the keyword `"ortho_type"`
   - `"ortho_type"→"lowdin"` (default): Löwdin orthogonalization
   - `"ortho_type"→"canonical"`: Canonical orthogonalization
4. print supplementary information about the calculation with the keyword `"verbose"`
   - `"verbose"→False` by default, if `"verbose"→True` then more information about the CPU timing and additional quantities are printed. Note that this option is available for most methods in qcmath.

Two flavors of Hartree-Fock (HF) are available in qcmath: restricted HF (RHF) and unrestricted HF (UHF). To run a UHF calculation, one simply does

```
qcmath["H2","6-31g",{"UHF"}]
```

Møller-Plesset (MP) perturbation theory

The second-order Møller-Plesset (MP2) correlation energy is defined by

$$E_c^{\mathrm{MP2}} = \frac{1}{4}\sum_{ij}^{\mathrm{occ}}\sum_{ab}^{\mathrm{vir}} \frac{|\langle ij||ab\rangle|^2}{\varepsilon_i^{\mathrm{HF}} + \varepsilon_j^{\mathrm{HF}} - \varepsilon_a^{\mathrm{HF}} - \varepsilon_b^{\mathrm{HF}}} \tag{6.1}$$

where $\langle pq||rs\rangle = \langle pq|rs\rangle - \langle pq|sr\rangle$ are antisymmetrized two-electron integrals (in Dirac notations) in the spinorbital basis and the $\varepsilon_p^{\mathrm{HF}}$'s are the HF orbital energies.

From here on, $i, j, \ldots$ are occupied spinorbitals, $a, b, \ldots$ denote virtual (unoccupied) spinorbitals, and p, q, r, and s indicate arbitrary (orthonormal) spinorbitals. Since MP2 needs HF quantities, first, a HF calculation needs to be done. This is automatically taken into account by QCMATH and an MP2 calculation can be done using

```
qcmath["H2","6-31g",{"RHF","MP2"}]
```

or

```
qcmath["H2","6-31g",{"MP2"}]
```

Note that in the last case, a RHF is performed by default so if one wants to rely on a UHF reference, one has to run

```
qcmath["H2","6-31g",{"UHF","MP2"}]
```

6.4.2 Charged excitations

Methods based on the one-body Green's function offer a means to describe charged excitations, namely, the ionization potentials (IPs) and electron affinities (EAs) of a system [81, 103, 457, 533]. This particular aspect forms the heart of QCMATH, with a diverse range of methods, approximations, and options available. To ensure clarity and coherence, this section is organized as follows: Firstly, we provide a brief introduction to the general equations that depend on the degree of (partial) self-consistency. These general equations are shared among the three self-energy approximations implemented in QCMATH: the second-order Green's function (GF2), the *GW* approximation, and the *T*-matrix approximation. By outlining these common equations, we establish a foundational understanding of the framework. Subsequently, we present the specific expressions corresponding to each of the self-energy approximations. This breakdown allows for a comprehensive exploration of the distinct methodologies incorporated in QCMATH, enabling users to leverage the most suitable approach for their research goals.

Three levels of (partial) self-consistency are available in QCMATH:

- the one-shot scheme where quasiparticles and satellites are obtained by solving, for each orbital p, the frequency-dependent quasiparticle equation

$$\omega = \varepsilon_p^{\mathrm{HF}} + \Sigma_{pp}^c(\omega) \tag{6.2}$$

  where the diagonal approximation is used. Because we are, most of the time, interested in the quasiparticle solution we can use the linearized quasiparticle equation

$$\varepsilon_p^{\mathrm{QP}} = \varepsilon_p^{\mathrm{HF}} + Z_p \Sigma_{pp}^c(\varepsilon_p^{\mathrm{HF}}) \tag{6.3}$$

  where the renormalization factor Z_p is defined as

$$Z_p = \left[1 - \frac{\partial \Sigma_{pp}(\omega)}{\partial \omega}\bigg|_{\omega=\varepsilon_p^{\mathrm{HF}}}\right]^{-1} \tag{6.4}$$

- the eigenvalue scheme where we iterate on the quasiparticle solutions of Eq (6.3) that are used to build the self-energy Σ_{pp}^c (and Z_p)
- the quasiparticle scheme where an effective Fock matrix built from a frequency-independent Hermitian self-energy as [31]

$$\tilde{F}_{pq} = F_{pq} + \tilde{\Sigma}_{pq} \tag{6.5}$$

where

$$\tilde{\Sigma}_{pq} = \frac{1}{2}\left[\Sigma^c_{pq}(\varepsilon_p^{\mathrm{HF}}) + \Sigma^c_{qp}(\varepsilon_p^{\mathrm{HF}})\right] \tag{6.6}$$

Note that the whole self-energy is computed for this last scheme.

The non-linear Eq (6.2) can be exactly transformed in a linear eigenvalue problem by use of the upfolding process [20, 23, 32]. For each orbital p, this yields a linear eigenvalue problem of the form

$$\mathbf{H}_p \cdot \mathbf{c}_\nu = \epsilon_\nu^{\mathrm{QP}} \mathbf{c}_\nu \tag{6.7}$$

where ν runs overall solutions, quasiparticles, and satellites and with [531]

$$\mathbf{H}_p = \begin{pmatrix} \epsilon_p^{\mathrm{HF}} & \boldsymbol{V}_p^{\mathrm{2h1p}} & \boldsymbol{V}_p^{\mathrm{2p1h}} \\ (\boldsymbol{V}_p^{\mathrm{2h1p}})^\intercal & \boldsymbol{C}^{\mathrm{2h1p}} & \mathbf{0} \\ (\boldsymbol{V}_p^{\mathrm{2p1h}})^\intercal & \mathbf{0} & \boldsymbol{C}^{\mathrm{2p1h}} \end{pmatrix} \tag{6.8}$$

Note that the different blocks will depend on the approximated self-energy. Now that the general equations have been set, we can turn to the self-energy approximations. Three different approximations are available in QCMATH: the second-order Green's function (GF2), the *GW* approximation, and the T-matrix approximation. For each approximation the three partially self-consistent schemes and the upfolding process are available. Note also that, regularization parameters are available in QCMATH.

Second-order Green's function (GF2) approximation

The GF2 correlation self-energy is closely related to MP2 and is given by the following expression

$$\Sigma^{\mathrm{GF2}}_{pq}(\omega) = \frac{1}{2}\sum_{ija} \frac{\langle pa||ij\rangle \langle qa||ij\rangle}{\omega + \epsilon_a^{\mathrm{HF}} - \epsilon_i^{\mathrm{HF}} - \epsilon_j^{\mathrm{HF}}} + \frac{1}{2}\sum_{iab} \frac{\langle pi||ab\rangle \langle qi||ab\rangle}{\omega + \epsilon_i^{\mathrm{HF}} - \epsilon_a^{\mathrm{HF}} - \epsilon_b^{\mathrm{HF}}} \tag{6.9}$$

Keywords need to be specified for the different schemes:

- `"G0F2"`: run a one-shot calculation
- `"evGF2"`: run an eigenvalue calculation
- `"qsGF2"`: run a quasiparticle calculation
- `"upfG0F2"`: run an upfolded calculation

Example of a one-shot calculation

```
qcmath["H2","6-31g",{"G0F2"}]
```

Note that here, an RHF calculation is done by default.

GW approximation

The *GW* correlation self-energy is given by

$$\Sigma^{GW}_{pq}(\omega) = \sum_{im} \frac{M^{\mathrm{ph}}_{pi,m} M^{\mathrm{ph}}_{qi,m}}{\omega - \epsilon_i^{\mathrm{HF}} + \Omega_m^{\mathrm{ph}}} + \sum_{am} \frac{M^{\mathrm{ph}}_{pa,m} M^{\mathrm{ph}}_{qa,m}}{\omega - \epsilon_a^{\mathrm{HF}} - \Omega_m^{\mathrm{ph}}} \tag{6.10}$$

where the screened two-electron integrals are given by

$$M^{\mathrm{ph}}_{pq,m} = \sum_{ia} \langle pi|qa\rangle \left(\boldsymbol{X}^{\mathrm{ph}} + \boldsymbol{Y}^{\mathrm{ph}}\right)_{ia,m} \tag{6.11}$$

with $\boldsymbol{X}^{\mathrm{ph}}$ and $\boldsymbol{Y}^{\mathrm{ph}}$ are the eigenvectors and excitations energies Ω^{ph}_m are the eigenvalues of the ph-dRPA problem that is discussed in Section 6.4.3. Keywords for the method argument need to be specified for the different schemes:

- `"G0W0"`: run a one-shot calculation
- `"evGW"`: run an eigenvalue calculation
- `"qsGW"`: run a quasiparticle calculation
- `"upfG0W0"`: run an upfolded calculation

Example of an eigenvalue calculation

```
qcmath["H2","6-31g",{"evGW"}]
```

Note that here, an RHF calculation is done by default.

T-matrix approximation

The T-matrix correlation self-energy is given by

$$\Sigma^{GT}_{pq}(\omega) = \sum_{in} \frac{M^{\mathrm{pp}}_{pi,n} M^{\mathrm{pp}}_{qi,n}}{\omega + \epsilon^{\mathrm{HF}}_i - \Omega^{\mathrm{pp}}_n} + \sum_{an} \frac{M^{\mathrm{hh}}_{pa,n} M^{\mathrm{hh}}_{qa,n}}{\omega + \epsilon^{\mathrm{HF}}_a - \Omega^{\mathrm{hh}}_n} \tag{6.12}$$

where the pp and hh versions of the screened two-electron integrals read

$$M^{\mathrm{pp}}_{pq,n} = \sum_{c<d} \langle pq||cd\rangle \, X^{\mathrm{pp}}_{cd,n} + \sum_{k<l} \langle pq||kl\rangle \, Y^{\mathrm{pp}}_{kl,n} \tag{6.13a}$$

$$M^{\mathrm{hh}}_{pq,n} = \sum_{c<d} \langle pq||cd\rangle \, X^{\mathrm{hh}}_{cd,n} + \sum_{k<l} \langle pq||kl\rangle \, Y^{\mathrm{hh}}_{kl,n} \tag{6.13b}$$

The components $X^{\mathrm{pp}/hh}_{cd,n}$ and $Y^{\mathrm{pp}/hh}_{kl,n}$ and excitation energies $\Omega^{\mathrm{pp}/hh}_n$ are the double addition/removal eigenvector components and eigenvalues, respectively, of the pp-RPA eigenvalue problem discussed in Section 6.4.3. Keywords for the method argument need to be specified for the different schemes:

- `"G0T0"`: run a one-shot calculation
- `"evGT"`: run an eigenvalue calculation
- `"qsGT"`: run a quasiparticle calculation
- `"upfG0T0"`: run an upfolded calculation

Example of a quasiparticle calculation

```
qcmath["H2","6-31g",{"qsGT"}]
```

Note that here, an RHF calculation is done by default.

6.4.3 Neutral excitations

Within QCMATH, the computation of excitation energies utilizes methods formulated as a Casida-like equation [131]. This equation is an eigenvalue equation that serves as a fundamental component in linear response theory. It plays a pivotal role in various approaches, including time-dependent density functional theory (TD-DFT) [69], the random phase approximation (RPA), and the Bethe-Salpeter equation (BSE) [103]. In this section, we begin by exploring the RPA method and distinguishing between different variations within this framework. By examining these different flavors of the RPA method, we gain insights into their unique characteristics and applicability. Subsequently, we delve into the discussion of the BSE method. This method represents another important approach for computing excitation energies, with its distinct theoretical foundations and computational considerations. By exploring the BSE method, users can gain a comprehensive understanding of its principles and its role within QCMATH. Note that when the spatial orbital implementation of a method is available, then we can use the `"singlet"` and/or `"triplet"` keywords to compute only singlet and/or triplet states.

Particle-hole random-phase approximation (ph-RPA)

The traditional RPA can be found under different names like RPAx or ph-RPA [61]. We choose to call it ph-RPA to make the difference with the particle-particle RPA (pp-RPA). The ph-RPA problem takes the form of the following Casida-like equation

$$\begin{pmatrix} \mathbf{A}^{\text{ph}} & \mathbf{B}^{\text{ph}} \\ -\mathbf{B}^{\text{ph}} & -\mathbf{A}^{\text{ph}} \end{pmatrix} \cdot \begin{pmatrix} \boldsymbol{X}^{\text{ph}} & \mathbf{Y}^{\text{ph}} \\ \mathbf{Y}^{\text{ph}} & \boldsymbol{X}^{\text{ph}} \end{pmatrix} = \begin{pmatrix} \boldsymbol{X}^{\text{ph}} & \mathbf{Y}^{\text{ph}} \\ \mathbf{Y}^{\text{ph}} & \boldsymbol{X}^{\text{ph}} \end{pmatrix} \cdot \begin{pmatrix} \boldsymbol{\Omega}^{\text{ph}} & \mathbf{0} \\ \mathbf{0} & -\boldsymbol{\Omega}^{\text{ph}} \end{pmatrix} \tag{6.14}$$

where Ω_m is the diagonal matrix of the excitation energies, $\boldsymbol{X}^{\text{ph}}$ and $\mathbf{Y}^{\text{ph}}$ matrices are the transition coefficients, and the matrix elements are defined as

$$A^{\text{ph}}_{ia,jb} = (\epsilon^{\text{HF}}_a - \epsilon^{\text{HF}}_i)\delta_{ij}\delta_{ab} + \langle ib||aj\rangle \tag{6.15}$$

$$B^{\text{ph}}_{ia,jb} = \langle ij||ab\rangle \tag{6.16}$$

Now, from these equations, different approximations arise:

- if we only take the direct term for the antisymmetrized two-electron integrals we end up with the direct ph-RPA (ph-dRPA), this is the one used in the *GW* approximation
- if we use the Tamm–Dancoff approximation (TDA) that sets $\boldsymbol{B}^{\text{ph}} = \mathbf{0}$, we end up with the ph-TDA approach

Note that TDA can be used with the ph-RPA flavor and gives ph-dTDA. Ground state correlation energy can be computed with

$$E_c^{\text{ph-RPA}} = \frac{1}{2}\left(\sum_m \Omega_m^{\text{ph}} - \text{Tr}(A^{\text{ph}})\right) \tag{6.17}$$

Keywords for the method argument need to be specified for the different approaches and options:

- `"RPAx"`: run a ph-RPA calculation
- `"RPA"`: run a ph-dRPA calculation

The option `"TDA"` can be set to `True`, by default `"TDA"`→`False`.

Particle-particle random-phase approximation (pp-RPA)

The particle-particle RPA (pp-RPA) problem considers the excitation energies of the $(N+2)$- and $(N-2)$-electron systems [61]. It is also defined by a slightly different eigenvalue problem than ph-RPA:

$$\begin{pmatrix} \mathbf{C}^{\text{pp}} & \mathbf{B}^{\text{pp/hh}} \\ -\left(\mathbf{B}^{\text{pp/hh}}\right)^{\dagger} & -\boldsymbol{D}^{\text{hh}} \end{pmatrix} \cdot \begin{pmatrix} \boldsymbol{X}^{\text{pp}} & \mathbf{Y}^{\text{hh}} \\ \mathbf{Y}^{\text{pp}} & \boldsymbol{X}^{\text{hh}} \end{pmatrix} = \begin{pmatrix} \boldsymbol{\Omega}^{\text{pp}} & \mathbf{0} \\ \mathbf{0} & \boldsymbol{\Omega}^{\text{hh}} \end{pmatrix} \cdot \begin{pmatrix} \boldsymbol{X}^{\text{pp}} & \mathbf{Y}^{\text{hh}} \\ \mathbf{Y}^{\text{pp}} & \boldsymbol{X}^{\text{hh}} \end{pmatrix} \tag{6.18}$$

where $\boldsymbol{\Omega}^{\text{pp/hh}}$ are the diagonal matrices of the double addition/removal excitation energies, labeled by n, and the matrix elements are defined as

$$C^{\text{pp}}_{ab,cd} = (\epsilon^{\text{HF}}_a + \epsilon^{\text{HF}}_b)\delta_{ac}\delta_{bd} + \langle ab||cd\rangle \tag{6.19a}$$

$$B^{\text{pp/hh}}_{ab,ij} = \langle ab||ij\rangle \tag{6.19b}$$

$$D^{\text{hh}}_{ij,kl} = -(\epsilon^{\text{HF}}_i + \epsilon^{\text{HF}}_j)\delta_{ik}\delta_{jl} + \langle ij||kl\rangle \tag{6.19c}$$

The $\boldsymbol{X}^{\text{pp/hh}}$ and $\mathbf{Y}^{\text{pp/hh}}$ are the double addition/removal transition coefficients matrices. In the same way we did for the ph-RPA, we can obtain the correlation energy at the pp-RPA level using [63, 64]

$$E_c^{\text{pp-RPA}} = \frac{1}{2}\left(\sum_n \Omega_n^{\text{pp}} - \sum_n \Omega_n^{\text{hh}} - \text{Tr}\boldsymbol{C}^{\text{pp}} - \text{Tr}\boldsymbol{D}^{\text{hh}}\right) \tag{6.20}$$

The keyword to use the pp-RPA is `pp-RPA`. Note that TDA is also available with the option `"TDA"`→`True`.

Bethe-Salpeter equation (BSE)

The Bethe-Salpeter equation (BSE) is detailed in Section 1.8.3 of Chapter 1 and is related to the two-body Green's function (2-GF) [19]. The central quantity is the so-called BSE kernel defined as the functional derivative of the self-energy with respect to the 1-GF. As exposed in Section 6.4.2, there are several approximations of the self-energy and each one of them leads to a different BSE approximation. The common central equation is the following eigenvalue equation

$$\begin{pmatrix} \mathbf{A}^{\text{BSE}} & \mathbf{B}^{\text{BSE}} \\ -\mathbf{B}^{\text{BSE}} & -\mathbf{A}^{\text{BSE}} \end{pmatrix} \cdot \begin{pmatrix} \boldsymbol{X}^{\text{BSE}}_m \\ \mathbf{Y}^{\text{BSE}}_m \end{pmatrix} = \Omega^{\text{BSE}}_m \begin{pmatrix} \boldsymbol{X}^{\text{BSE}}_m \\ \mathbf{Y}^{\text{BSE}}_m \end{pmatrix} \tag{6.21}$$

where the BSE matrix elements depend on the choice of the BSE kernel (see Chapter 5). To run a BSE calculation we have first to specify the approximation for the self-energy with the method argument and the keyword for this option is `"BSE"`→`True`. Note that in general a BSE calculation is done in the static approximation, which is the equivalent of the adiabatic approximation in TD-DFT. It is possible to take into account dynamical effects using first-order perturbation theory [29] using the option `"dBSE"`→`True`. This dynamical correction is applicable for all the different BSE kernels available in qcmath. Note that this dynamical correction is only available in TDA with the option `"dTDA"`.

6.5 Programmer guide

As mentioned in the first section, one of the primary objectives of QCMATH is to enable newcomers in quantum chemistry to explore and advance their ideas through coding. Therefore, it is crucial to allow them to incorporate their methods into QCMATH. To facilitate this process, we have developed a notebook example called `module_example.nb` to guide users step-by-step. The following outlines the different stages involved in adding a new method to QCMATH:

1. The new method needs to be implemented in its notebook
2. add your method in the `src/utils/list_method.nb` and specify the dependencies (ex: if post-HF method then dependency= `"RHF"`)
3. add default options in `src/Main/default_options.nb` if needed
4. add a call to your method in `src/Main/Main.nb` as

```
NameNewMethod="NameNewMethod"
If[ToDoModules[NameNewMethod]["Do"] == True,
  NotebookEvaluate[path<>"/src/"<>NameNewMethod<>".nb"
     ];

PrintTemporary[Style[NameNewMethod<>" calculation...",
    Bold, Orange]];
{time, outputsNewMethod} = Timing[NewMethod[arguments,
    options]];

If[verbose == True,
  Print["CPU time for "<>NameNewMethod<>" calculation=
      ", time]];
];
```

Each new method notebook needs to be divided into (potentially) three modules. The first part reads the input and the options, then call either the spin or spatial orbitals module, and finally returns the associated output. Then the two other modules are devoted to the implementation of the new method in spin and spatial orbitals. Note that if your method is, for example, only implemented in spatial orbitals then your notebook will be divided into only two parts. This information can be found in `module_example.nb`.

Conclusion

The goal of this thesis was the study of Green's function methods for the computation of charged (*i.e.*, ionization potentials and electron affinities) and neutral (optical) excitations in molecules. The one-body Green's function can provide the charged excitations of the system in a single calculation. This great feature permits to avoid to perform separate calculations on the neutral and ionized species. The Bethe-Salpeter equation (BSE) formalism, which relies on the two-body Green's function, allows access to the neutral excitations of a given system.

To do so, this thesis was divided into four parts. In the first chapter of this thesis, we have laid the foundations by presenting the core methods of quantum chemistry: the Hartree-Fock (HF) approximation and Kohn-Sham density functional theory (KS-DFT). We then used linear response theory to review the time-dependent HF (TDHF) approximation and the time-dependent DFT (TD-DFT) method. We have then presented the basic of many-body perturbation theory and reviewed Green's function methods to obtain charged excitations with the self-energy and neutral excitations with the Bethe-Salpeter equation (BSE) formalism.

The second part of this thesis focused on the application of Green's function and other quantum chemistry methods for the computation of neutral excitations in molecules. Like adiabatic time-dependent density-functional theory (TD-DFT), the Bethe-Salpeter equation (BSE) formalism of many-body perturbation theory, in its static approximation, is "blind" to double (and higher) excitations. So, we applied the spin-flip *ansatz* which considers the lowest triplet state as the reference configuration instead of the singlet ground state to the BSE formalism to access double excitations. We also took into account dynamical corrections to the static BSE optical excitations via renormalized perturbative treatment. To illustrate the performance of the developed spin-flip BSE formalism we have computed excited-state energies of the beryllium atom, the hydrogen molecule at various bond lengths, and cyclobutadiene in its rectangular and square-planar geometries. We have shown that the spin-flip BSE formalism can accurately model double excitations and seems to surpass systematically its spin-flip TD-DFT parent. This contributes to show that the BSE formalism is a solid alternative to TD-DFT for the study of molecular excited states.

Then, we have focused on the cyclobutadiene (CBD) molecule, a well-known playground for theoretical chemists and particularly suitable to test ground- and excited-state methods. Indeed, due to its high spatial symmetry, the ground and excited states of CBD exhibit multi-configurational characters and single-reference methods, such as standard adiabatic time-dependent density-functional theory (TD-DFT) or standard equation-of-motion coupled-cluster (EOM-CC), struggle to describe such states. We have used a large panel of methods to provide an extensive computational study of the automerization barrier, defined as the difference between the square and rectangular ground-state energies and the vertical excitation energies of both structures. We have performed selected configuration interaction (SCI), multireference perturbation theory (CASSCF, CASPT2, and NEVPT2), and coupled-cluster (CCSD, CC3, CCSDT, CC4, and CCSDTQ) calculations. We have tested the spin-flip

formalism, which is known to provide a qualitatively correct description of these diradical states, within TD-DFT and the algebraic diagrammatic construction [ADC(2)-s, ADC(2)-x, and ADC(3)]. A theoretical best estimate is defined for the automerization barrier and each vertical transition energy. We have seen that SF-EOM-CCSD and SF-ADC(2)-s show similar accuracies and that the SF-ADC(2)-x scheme, as expected, does not provide an improvement on the different results. In the case of the square CBD, SF-TD-DFT displayed its limitations in the description of excited states due to the strong multiconfigurational character. However, the spin-flip version of ADC showed much better results. Finally, this study of the CBD molecule confirmed the outstanding accuracy of CCSDTQ in the context of molecular excited states.

In the third part of this thesis, we studied the features of Green's function methods. We first studied and explained the appearance of multiple solutions and unphysical discontinuities in various physical quantities computed within the *GW* approximation. This was done by recasting the non-linear frequency-dependent *GW* quasiparticle equation into a linear eigenvalue problem. We looked at the H_2 molecule to display the appearance of such multiple solutions problem. We have seen that these issues are key signatures of strong correlation in the $(N \pm 1)$-electron states and can be directly related to the intruder state problem. We then proposed a simple and efficient regularization procedure inspired by the similarity renormalization group (SRG) to avoid such issues and speed up the convergence of partially self-consistent *GW* calculations. Note that, a very recent work by people in our group went further by applying the flow equation of SRG to the *GW* approximation in its quasiparticle scheme (qsGW) [518]. By doing so, they obtained a renormalized Fock matrix and screened two-electron integrals. This leads to an alternative Hermitian and intruder-state-free self-energy that can be used in the context of qs*GW* calculations and which is called SRG-qs*GW*.

Then, we have investigated the connections between various Green's function methods and evaluate their performance for charged and neutral excitations. We have compared it with other widely-known second-order wave function methods. We have specifically explored various approximations for the self-energy (GF2, *GW*, and *GT*) and their corresponding BSE kernels at the static and dynamic levels. The second-order GW kernel, usually neglected, was also considered. We confirmed previous knowledge, the *GW* approximation surpasses the GF2 method in accurately calculating IPs, emphasizing the significance of screening even in small molecular systems. Importantly, our investigations highlighted the sensitivity of BSE kernels to the nature of the excited states. For example, BSE@*GT* is poor for valence states while it is accurate for Rydberg transitions. We also examined the capability of our various schemes to replicate the inversion of the singlet-triplet gap in cycl[3,3,3]zine, a prototypical molecular emitter for TADF. Except for one case, we observed that all static and dynamic BSE-based schemes failed to reproduce this unique characteristic. The only exception was the dynamically-corrected BSE2@*GW* scheme (i.e. the second-order *GW* kernel), which yielded a gap value consistent with that obtained from EOM-CC3 calculations. This observation effectively highlighted the significance of higher-order terms and dynamic effects within the BSE formalism.

In this thesis's last part, we presented a quantum chemistry software for electronic structure calculations based on the Wolfram Mathematica language. This software aims to take advantage of the powerful symbolic nature of Mathematica to help newcomers in quantum chemistry easily develop their ideas. The capabilities of this software can be summarized in three sections, first, ground-state calculations can be done using Hartree-Fock in both restricted and unrestricted formalisms or perturbation theory with Møller-Plesset. Secondly, we can compute charged excitations using

various approximations of the self-energy (GF2, GW, and GT) and finally, we can use their corresponding kernels to have access to neutral excitations with the BSE formalism.

A few perspectives of this work can be listed. For the second part of this thesis, on the computation of neutral excitations in molecules, further improvements could be obtained thanks to a better choice of the starting orbitals and their energies by using KS-DFT orbitals and energies. Moreover, we could use the different BSE kernels seen in the third part of the thesis to investigate their performances for these molecular systems. In the case of CBD, we could also use the spin-flip BSE formalism with the different BSE kernels to compare its performance against its spin-flip TD-DFT parent. It would also be interesting to derive the second-order BSE kernel at the T-matrix level to see if we can obtain the inversion of the singlet-triplet gap of the cycl[3,3,3]zine molecule.

The most interesting perspectives are in the third part. Indeed, as discussed in Chapter 5, different connections exist between the self-energy approximations and hence the BSE kernels. A particularly striking point is the similarities between the different BSE kernels. Indeed, we have seen that by removing the screening effect from GW and GT we recover the different terms of the GF2 kernel (up to an exchange part in the two-electron integrals). Moreover, we have seen that BSE@GT is quite accurate for Rydberg transitions where the excited-state density is much lower than the ground-state one. This is a situation where ladder diagrams are known to be relevant. On the other hand, BSE@GW exhibits a good description of valence excitations especially when taking into account dynamical corrections. Furthermore, the GF2 kernel showed accurate results for the computation of neutral excitations. Thus, it would be quite interesting to be able to build a screened version of the GF2 kernel based on the GW and GT kernels, especially considering that screening becomes more important for large molecules with many electrons.

An obvious idea is to combine the two self-energies (GW and GT) and then build the corresponding BSE kernel. By doing so, it would be particularly interesting to see the performances of these hypothetical self-energy and kernel for charged and neutral excitations. Note that combining GW and GT is not a new idea and is still an active research area in physics [419, 569–571]. As already mentioned in a previous work [419], it exists different ways of combining correlation channels by preventing the double counting problem [484, 499]. The fluctuating exchange (FLEX) approximation of Bickers *et* al. [483, 498] that starts from GF2 and sums all contributions from the third order in each channel separately. Unfortunately, by doing so, we do not have access to mixed diagrams. Note that beyond FLEX approaches have been proposed [482, 485, 486]. It is also possible to couple ph and pp channels on an equal footing which leads to parquet theory that relies on diagrams [484, 572]. It is worth mentioning that a straightforward combination of the ph and pp channels, that are present in GW and GT through the ph-RPA and pp-RPA problems, where the double-counting terms are removed was already explored [569]. Unfortunately, this scheme is not successful regarding molecular dissociations. We can also mention the work of Romaniello *et* al. that derived the coupling of GW and GT channels on an equal footing starting from exact many-body equations in the case of the exactly solvable Hubbard molecule [419]. Work from Degroote [570] uses the Faddeev partitioning [573] to combine in a diagrammatic way the correlation channels.

Unfortunately, many of these methods and approximations rely on complicated diagrammatic approaches, which we did not talk about in this thesis, and it would be good to use non-diagrammatic ways to do this combination. This is a topic that we

would like to continue to work on and we hope that the upfolding formalism could help us in the pursuit of this objective.

For the QCMATH software, we could think of extending its capabilities by implementing different flavors of CI and CC methods for ground- and excited states. We could also think of not only focusing on energies but also on properties like oscillator strengths, dipole moments, etc. Due to the power of MATHEMATICA, it would be relatively easy and interesting to implement DFT methods with various exchange-correlation functionals. Moreover, an extension to excited states with TD-DFT would be easy considering the similarities of the matrix expressions with the BSE formalism that is already implemented in QCMATH. We also hope to implement new CC methods, especially at the equation-of-motion CC level where our group has recently designed an automatic equation generator based on MATHEMATICA, named EOMCCGEN [574].

Appendix A

Löwdin partitioning technique

Here, one explains briefly the principle of the Löwdin partitioning technique. One starts from an eigenvalue problem

$$\boldsymbol{H} \cdot \boldsymbol{c} = \omega \boldsymbol{c} \tag{A.1}$$

that is a large linear system with $\mathcal{N}$ solutions where $\boldsymbol{H}$ is the Hamiltonian matrix, $\boldsymbol{c}$ is the matrix of eigenvectors and ω represent an eigenvalue. One can always split the matrices $\boldsymbol{H}$ and $\boldsymbol{c}$ in such way that one obtains the following eigenvalue problem

$$\begin{pmatrix} \overbrace{\boldsymbol{H}_1}^{\mathcal{N}_1 \times \mathcal{N}_1} & \boldsymbol{h}_{12} \\ \boldsymbol{h}_{21} & \underbrace{\boldsymbol{H}_2}_{\mathcal{N}_2 \times \mathcal{N}_2} \end{pmatrix} \cdot \begin{pmatrix} \boldsymbol{c}_1 \\ \boldsymbol{c}_2 \end{pmatrix} = \omega \begin{pmatrix} \boldsymbol{c}_1 \\ \boldsymbol{c}_2 \end{pmatrix} \tag{A.2}$$

where $\mathcal{N} = \mathcal{N}_1 + \mathcal{N}_2$. Then, by doing the matrix multiplication one gets

$$\textbf{Row \#2:} \quad \boldsymbol{h}_{21} \cdot \boldsymbol{c}_1 + \boldsymbol{H}_2 \cdot \boldsymbol{c}_2 = \omega \boldsymbol{c}_2 \quad \Rightarrow \quad \boldsymbol{c}_2 = (\omega \mathbf{1} - \boldsymbol{H}_2)^{-1} \cdot \boldsymbol{h}_{21} \cdot \boldsymbol{c}_1 \tag{A.3}$$

$$\textbf{Row \#1:} \quad \boldsymbol{H}_1 \cdot \boldsymbol{c}_1 + \boldsymbol{h}_{12} \cdot \boldsymbol{c}_2 = \omega \boldsymbol{c}_1 \quad \Rightarrow \quad \tilde{\boldsymbol{H}}_1(\omega) \cdot \boldsymbol{c}_1 = \omega \boldsymbol{c}_1 \tag{A.4}$$

with $\tilde{\boldsymbol{H}}_1(\omega) \cdot \boldsymbol{c}_1 = \omega \boldsymbol{c}_1$, a smaller non-linear system with the same number $\mathcal{N}$ of solutions. So, by using the Löwdin partitioning technique and starting from a large linear eigenvalue problem one gets a smaller but non-linear system with the same number of solutions where $\tilde{\boldsymbol{H}}_1(\omega)$ is an effective Hamiltonian defined as

$$\boxed{\tilde{\boldsymbol{H}}_1(\omega) = \boldsymbol{H}_1 + \boldsymbol{h}_{12} \cdot (\omega \mathbf{1} - \boldsymbol{H}_2)^{-1} \cdot \boldsymbol{h}_{21}} \tag{A.5}$$

where one assumes the existence of the inverse matrix $(\omega \mathbf{1} - \boldsymbol{H}_2)^{-1}$. Then, one can rely on some approximations to solve this non-linear system with an example of a static approximation with $\omega = 0$

$$\tilde{\boldsymbol{H}}_1(\omega = 0) = \boldsymbol{H}_1 - \boldsymbol{h}_{12} \cdot \boldsymbol{H}_2^{-1} \cdot \boldsymbol{h}_{21} \tag{A.6}$$

that gives a smaller linear system but with only $\mathcal{N}_1$ solutions.

Appendix B

Supporting information for Chapter 2

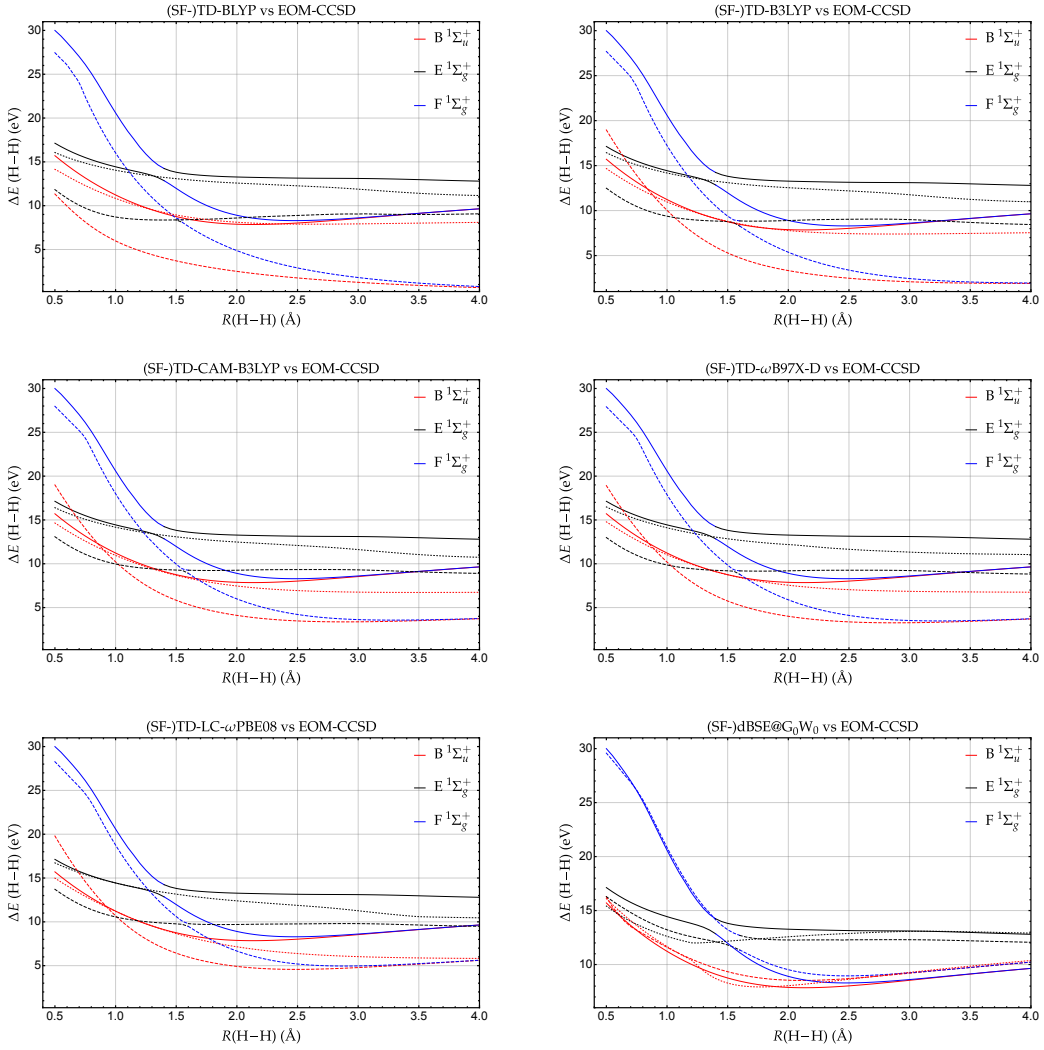

Figure B.1: Excitation energies with respect to the $X\,^1\Sigma_g^+$ ground state of the $B\,^1\Sigma_u^+$ (red), $E\,^1\Sigma_g^+$ (black), and $F\,^1\Sigma_g^+$ (blue) states of H_2 obtained with the cc-pVQZ basis at various levels of theory. The reference EOM-CCSD excitation energies are represented as solid lines, while the results obtained with and without spin-flip are represented as dashed and dotted lines, respectively. All the spin-conserved and spin-flip calculations have been performed with an unrestricted reference.

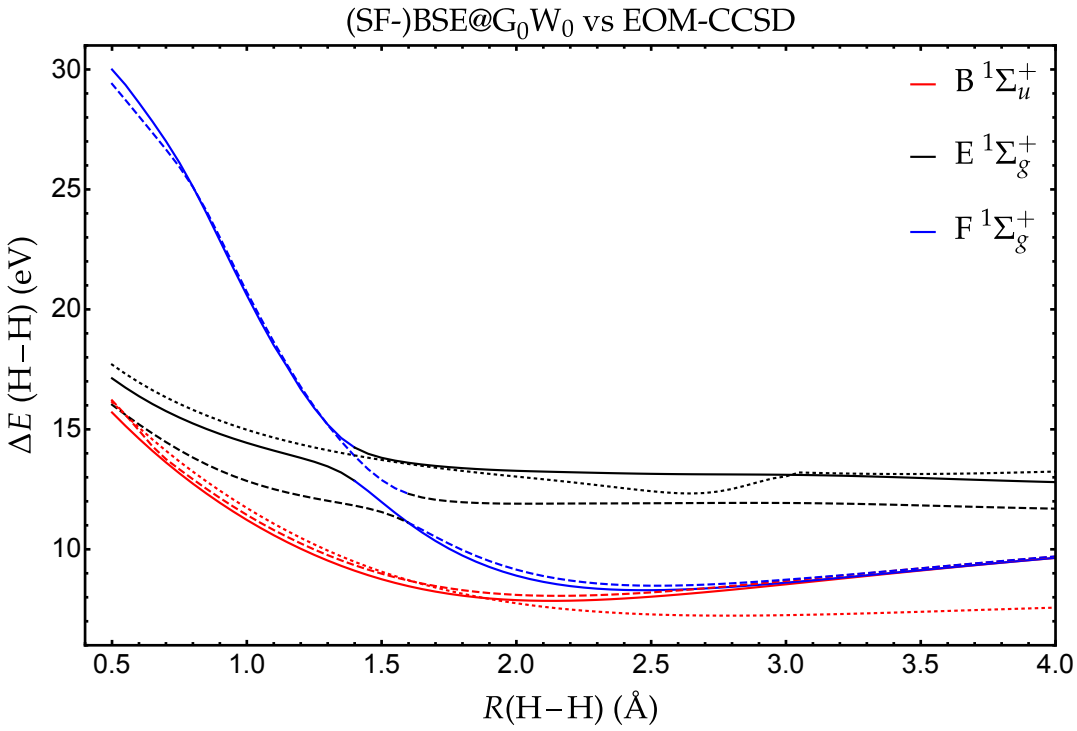

Figure B.2: Excitation energies with respect to the $X\,^1\Sigma_g^+$ ground state of the $B\,^1\Sigma_u^+$ (red), $E\,^1\Sigma_g^+$ (black), and $F\,^1\Sigma_g^+$ (blue) states of H_2 obtained with the cc-pVQZ basis at the (SF-)BSE level of theory. The reference EOM-CCSD excitation energies are represented as solid lines, while the results obtained with and without spin-flip are represented as dashed and dotted lines, respectively. In this case, the spin-conserved calculations have been performed with a restricted reference while the spin-flip calculations have been performed with an unrestricted reference.

	CIS		BH&HLYP		BSE@G_0W_0		EOM-CCSD	
R(H−H) (Å)	$B\,^1\Sigma_u^+$	$E\,^1\Sigma_g^+$	$B\,^1\Sigma_u^+$	$E\,^1\Sigma_g^+$	$B\,^1\Sigma_u^+$	$E\,^1\Sigma_g^+$	$B\,^1\Sigma_u^+$	$E\,^1\Sigma_g^+$
0.5	15.942	17.398	15.253	16.896	15.535	16.135	15.703	16.737
0.6	14.791	16.579	14.180	16.199	14.767	15.073	14.610	16.056
0.7	13.745	15.891	13.339	15.614	14.108	14.120	13.621	15.491
0.8	12.800	15.311	12.514	15.122	13.236	13.591	12.735	15.017
0.9	11.943	14.815	11.766	14.699	12.444	13.126	11.938	14.615
1.0	11.163	14.389	11.088	14.334	11.722	12.733	11.224	14.270
1.1	10.454	14.025	10.474	14.020	11.068	12.410	10.587	13.962
1.2	9.810	13.712	9.919	13.750	10.477	12.132	10.023	13.648
1.3	9.369	13.401	9.421	13.515	9.470	12.139	9.531	13.201
1.4	9.128	13.262	8.977	13.309	8.743	12.211	9.108	14.241
1.5	8.986	13.180	8.585	13.127	8.299	12.300	8.753	13.814
1.6	8.911	13.125	8.241	12.966	8.054	12.395	8.463	13.606
1.7	8.884	13.085	7.943	12.824	7.946	12.482	8.236	13.475
1.8	8.894	13.058	7.687	12.699	7.928	12.563	8.067	13.383
1.9	8.931	13.041	7.468	12.593	7.970	12.641	7.951	13.317
2.0	8.989	13.033	7.283	12.502	8.049	12.714	7.881	13.272
2.1	9.063	13.031	7.128	12.421	8.151	12.783	7.852	13.239
2.2	9.149	13.031	7.000	12.343	8.267	12.845	7.858	13.212
2.3	9.243	13.031	6.895	12.265	8.391	12.901	7.892	13.187
2.4	9.344	13.031	6.810	12.186	8.520	12.951	7.949	13.164
2.5	9.448	13.032	6.743	12.109	8.650	12.997	8.024	13.145
2.6	9.556	13.037	6.690	12.030	8.779	13.042	8.112	13.133
2.7	9.666	13.043	6.650	11.946	8.908	13.084	8.211	13.125
2.8	9.776	13.050	6.621	11.851	9.035	13.123	8.316	13.120
2.9	9.887	13.056	6.600	11.744	9.161	13.154	8.427	13.115
3.0	9.998	13.057	6.586	11.627	9.283	13.174	8.541	13.106
3.1	10.109	13.053	6.578	11.505	9.403	13.183	8.656	13.091
3.2	10.219	13.043	6.575	11.383	9.521	13.181	8.773	13.069
3.3	10.328	13.027	6.575	11.266	9.637	13.169	8.888	13.041
3.4	10.435	13.006	6.579	11.158	9.751	13.150	9.003	13.008
3.5	10.541	12.983	6.586	11.062	9.862	13.126	9.116	12.972
3.6	10.645	12.958	6.594	10.977	9.971	13.100	9.227	12.935
3.7	10.748	12.933	6.604	10.905	10.077	13.073	9.335	12.899
3.8	10.848	12.908	6.615	10.846	10.181	13.047	9.440	12.863
3.9	10.947	12.884	6.626	10.798	10.282	13.023	9.542	12.830
4.0	11.043	12.861	6.638	10.761	10.380	13.000	9.642	12.800

Table B.1: Excitation energies with respect to the $X\,^1\Sigma_g^+$ ground state of the $B\,^1\Sigma_u^+$ and $E\,^1\Sigma_g^+$ states of H_2 obtained with the cc-pVQZ basis at the CIS, TD-BH&HLYP, BSE@G_0W_0, and EOM-CCSD levels of theory.

	SF-CIS			SF-BH&HLYP			SF-BSE@G_0W_0			EOM-CCSD		
R(H−H) (Å)	$B\,^1\Sigma_u^+$	$E\,^1\Sigma_g^+$	$F\,^1\Sigma_g^+$	$B\,^1\Sigma_u^+$	$E\,^1\Sigma_g^+$	$F\,^1\Sigma_g^+$	$B\,^1\Sigma_u^+$	$E\,^1\Sigma_g^+$	$F\,^1\Sigma_g^+$	$B\,^1\Sigma_u^+$	$E\,^1\Sigma_g^+$	$F\,^1\Sigma_g^+$
0.5	14.829	15.279	28.726	17.276	13.506	27.846	16.208	16.026	29.398	15.703	17.126	29.997
0.6	14.057	14.694	27.528	15.523	12.674	26.696	14.953	15.206	28.044	14.610	16.380	28.608
0.7	13.385	14.227	26.27	13.916	11.978	25.396	13.759	14.469	26.668	13.621	15.760	27.011
0.8	12.784	13.849	24.801	12.469	11.414	23.715	12.920	13.824	25.101	12.735	15.244	25.114
0.9	12.228	13.535	22.906	11.191	10.965	21.235	12.141	13.284	23.004	11.938	14.808	22.869
1.0	11.710	13.273	20.834	10.086	10.617	18.824	11.434	12.849	20.725	11.224	14.437	20.591
1.1	11.233	13.054	18.885	9.144	10.353	16.693	10.803	12.507	18.643	10.587	14.114	18.502
1.2	10.804	12.869	17.164	8.350	10.155	14.838	10.246	12.241	16.776	10.023	13.811	16.680
1.3	10.427	12.704	15.700	7.679	10.003	13.233	9.756	12.023	15.185	9.531	13.456	15.200
1.4	10.106	12.526	14.516	7.112	9.873	11.863	9.336	11.821	13.884	9.108	14.241	12.853
1.5	9.843	12.262	13.663	6.630	9.709	10.751	8.984	11.554	12.889	8.753	13.814	11.971
1.6	9.636	13.198	11.831	6.222	10.108	9.266	8.696	12.310	11.105	8.463	13.606	11.096
1.7	9.483	13.006	11.320	5.877	9.932	8.524	8.468	12.066	10.520	8.236	13.475	10.347
1.8	9.379	12.933	10.855	5.587	9.878	7.810	8.296	11.962	9.968	8.067	13.383	9.739
1.9	9.317	12.913	10.481	5.347	9.862	7.189	8.175	11.916	9.510	7.951	13.317	9.262
2.0	9.293	12.922	10.197	5.150	9.867	6.665	8.099	11.902	9.152	7.881	13.272	8.902
2.1	9.301	12.943	9.995	4.991	9.882	6.230	8.065	11.903	8.885	7.852	13.239	8.642
2.2	9.334	12.968	9.862	4.867	9.895	5.873	8.063	11.908	8.698	7.858	13.212	8.466
2.3	9.388	12.988	9.784	4.772	9.901	5.585	8.089	11.911	8.576	7.892	13.187	8.358
2.4	9.457	13.005	9.752	4.703	9.902	5.357	8.137	11.915	8.508	7.949	13.164	8.305
2.5	9.538	12.987	9.754	4.657	9.901	5.180	8.204	11.919	8.483	8.024	13.145	8.296
2.6	9.628	12.971	9.783	4.628	9.901	5.045	8.284	11.924	8.492	8.112	13.133	8.319
2.7	9.725	12.968	9.833	4.614	9.900	4.946	8.374	11.930	8.527	8.211	13.125	8.368
2.8	9.825	12.972	9.898	4.612	9.896	4.876	8.473	11.933	8.583	8.316	13.120	8.436
2.9	9.928	12.979	9.975	4.621	9.886	4.829	8.576	11.934	8.654	8.427	13.115	8.517
3.0	10.033	12.986	10.060	4.637	9.867	4.802	8.682	11.930	8.734	8.541	13.106	8.609
3.1	10.139	12.989	10.152	4.659	9.839	4.789	8.788	11.921	8.821	8.656	13.091	8.708
3.2	10.244	12.987	10.247	4.686	9.803	4.789	8.894	11.905	8.913	8.773	13.069	8.811
3.3	10.345	12.979	10.350	4.717	9.763	4.798	8.998	11.884	9.009	8.888	13.041	8.917
3.4	10.445	12.966	10.454	4.751	9.721	4.814	9.103	11.857	9.107	9.003	13.008	9.024
3.5	10.546	12.949	10.558	4.787	9.679	4.837	9.206	11.829	9.207	9.116	12.972	9.132
3.6	10.646	12.930	10.660	4.825	9.640	4.864	9.306	11.800	9.310	9.227	12.935	9.238
3.7	10.746	12.910	10.760	4.864	9.605	4.894	9.405	11.771	9.411	9.335	12.899	9.343
3.8	10.845	12.889	10.859	4.903	9.573	4.927	9.503	11.743	9.510	9.440	12.863	9.446
3.9	10.942	12.868	10.956	4.943	9.547	4.961	9.600	11.717	9.608	9.542	12.830	9.546
4.0	11.038	12.848	11.051	4.982	9.524	4.996	9.696	11.693	9.703	9.642	12.800	9.644

Table B.2: Excitation energies with respect to the $X\,^1\Sigma_g^+$ ground state of the $B\,^1\Sigma_u^+$, $E\,^1\Sigma_g^+$, and $F\,^1\Sigma_g^+$ states of H_2 obtained with the cc-pVQZ basis at the SF-CIS, SF-TD-BH&HLYP, SF-BSE@G_0W_0, and EOM-CCSD levels of theory. All the spin-conserved and spin-flip calculations have been performed with an unrestricted reference.

	SF-CIS			SF-BH&HLYP			SF-BSE@G_0W_0		
R(H−H) (Å)	$B\,^1\Sigma_u^+$	$E\,^1\Sigma_g^+$	$F\,^1\Sigma_g^+$	$B\,^1\Sigma_u^+$	$E\,^1\Sigma_g^+$	$F\,^1\Sigma_g^+$	$B\,^1\Sigma_u^+$	$E\,^1\Sigma_g^+$	$F\,^1\Sigma_g^+$
0.5	0.047	0.983	0.987	0.893	0.975	1.000	0.190	0.977	0.994
0.6	0.074	0.985	0.966	0.842	0.973	1.000	0.072	0.978	0.983
0.7	0.106	0.988	0.900	0.778	0.972	0.925	0.112	0.979	0.926
0.8	0.137	0.990	0.703	0.694	0.971	0.482	0.138	0.980	0.712
0.9	0.162	0.992	0.418	0.592	0.969	0.177	0.160	0.981	0.365
1.0	0.178	0.993	0.249	0.485	0.968	0.143	0.174	0.982	0.203
1.1	0.185	0.993	0.178	0.388	0.967	0.141	0.180	0.983	0.149
1.2	0.185	0.989	0.153	0.310	0.965	0.145	0.179	0.981	0.132
1.3	0.182	0.973	0.158	0.256	0.960	0.151	0.174	0.971	0.140
1.4	0.176	0.920	0.208	0.219	0.943	0.168	0.169	0.934	0.175
1.5	0.171	0.757	0.374	0.196	0.848	0.264	0.164	0.797	0.318
1.6	0.166	0.640	0.495	0.182	0.678	0.434	0.160	0.617	0.502
1.7	0.162	0.807	0.333	0.173	0.880	0.232	0.157	0.817	0.308
1.8	0.161	0.881	0.266	0.168	0.925	0.188	0.156	0.896	0.237
1.9	0.161	0.917	0.238	0.166	0.941	0.174	0.157	0.931	0.210
2.0	0.163	0.937	0.227	0.166	0.949	0.168	0.159	0.949	0.120
2.1	0.167	0.949	0.223	0.167	0.954	0.166	0.162	0.960	0.197
2.2	0.172	0.956	0.225	0.170	0.957	0.166	0.167	0.966	0.199
2.3	0.179	0.961	0.228	0.172	0.959	0.168	0.173	0.970	0.203
2.4	0.187	0.963	0.233	0.175	0.960	0.170	0.180	0.973	0.208
2.5	0.195	0.965	0.240	0.179	0.961	0.173	0.187	0.974	0.214
2.6	0.205	0.964	0.247	0.183	0.962	0.176	0.195	0.974	0.221
2.7	0.215	0.963	0.254	0.186	0.962	0.179	0.203	0.973	0.228
2.8	0.225	0.960	0.262	0.190	0.961	0.183	0.211	0.970	0.235
2.9	0.235	0.955	0.270	0.194	0.961	0.187	0.220	0.966	0.244
3.0	0.245	0.950	0.278	0.198	0.959	0.191	0.229	0.960	0.252
3.1	0.255	0.943	0.286	0.201	0.958	0.194	0.239	0.954	0.260
3.2	0.265	0.936	0.293	0.204	0.956	0.198	0.248	0.947	0.268
3.3	0.274	0.929	0.300	0.207	0.954	0.201	0.256	0.941	0.275
3.4	0.282	0.921	0.307	0.210	0.952	0.204	0.263	0.935	0.281
3.5	0.290	0.914	0.313	0.212	0.951	0.206	0.270	0.930	0.286
3.6	0.297	0.908	0.318	0.214	0.949	0.209	0.276	0.925	0.291
3.7	0.304	0.901	0.323	0.215	0.948	0.210	0.281	0.920	0.295
3.8	0.310	0.896	0.327	0.216	0.946	0.212	0.285	0.917	0.297
3.9	0.315	0.891	0.330	0.217	0.946	0.213	0.289	0.914	0.299
4.0	0.319	0.887	0.333	0.217	0.945	0.214	0.291	0.912	0.301

Table B.3: Expectation value of the spin operator $\langle \hat{S}^2 \rangle$ of the $B\,^1\Sigma_u^+$, $E\,^1\Sigma_g^+$, and $F\,^1\Sigma_g^+$ states of H_2 obtained with the cc-pVQZ basis at the SF-CIS, SF-TD-BH&HLYP, SF-BSE@G_0W_0, and EOM-CCSD levels of theory. All the spin-conserved and spin-flip calculations have been performed with an unrestricted reference.

Appendix C

Supporting information for Chapter 3

C.1 Geometries

Below, we provide the Cartesian coordinates (in Å) of the geometries that are employed in this work.

- D_{2h} rectangular equilibrium geometry of the 1^1A_g ground state computed at the CASPT2(12,12)/aug-cc-pVTZ level:

C	0.0000000000	-0.6769380253	-0.7827569236
C	0.0000000000	-0.6769380253	0.7827569236
C	0.0000000000	0.6769380253	0.7827569236
C	0.0000000000	0.6769380253	-0.7827569236
H	0.0000000000	-1.4379809006	-1.5441628360
H	0.0000000000	-1.4379809006	1.5441628360
H	0.0000000000	1.4379809006	1.5441628360
H	0.0000000000	1.4379809006	-1.5441628360

- D_{4h} square planar equilibrium geometry of the 1^1B_{1g} ground state computed at the CASPT2(12,12)/aug-cc-pVTZ level:

C	1.0248323754	0.0000000000	0.0000000000
C	0.0000000000	-1.0248323754	0.0000000000
C	-1.0248323754	0.0000000000	0.0000000000
C	0.0000000000	1.0248323754	0.0000000000
H	2.1005277359	0.0000000000	0.0000000000
H	0.0000000000	-2.1005277359	0.0000000000
H	-2.1005277359	0.0000000000	0.0000000000
H	0.0000000000	2.1005277359	0.0000000000

- D_{2h} rectangular equilibrium geometry of the 1^1A_g ground state computed at the CC3/aug-cc-pVTZ level:

C	-0.78248546	-0.67208001	0.00000000
C	0.78248546	-0.67208001	0.00000000
C	-0.78248546	0.67208001	0.00000000
C	0.78248546	0.67208001	0.00000000
H	-1.54227765	-1.43404123	-0.00000000
H	1.54227765	-1.43404123	0.00000000
H	-1.54227765	1.43404123	0.00000000
H	1.54227765	1.43404123	-0.00000000

- D_{4h} square planar equilibrium geometry of the 1^3A_{2g} state computed at the (RO)-CCSD(T)/aug-cc-pVTZ level:

```
C             0.000000    1.017702    0.000000
C             1.017702   -0.000000    0.000000
C            -1.017702    0.000000    0.000000
C            -0.000000   -1.017702    0.000000
H             0.000000    2.092429    0.000000
H             2.092429   -0.000000    0.000000
H            -0.000000   -2.092429    0.000000
H            -2.092429    0.000000    0.000000
```

C.2 Tables

		D_{2h} excitation energies (eV)			D_{4h} excitation energies (eV)		
Method	AB	1^3B_{1g}(99%)	1^1B_{1g}(95%)	2^1A_g(1%)	1^3A_{2g}	1^1A_{1g}	1^1B_{2g}
SF-TD-B3LYP	10.41	0.270	−0.926	−0.050	−0.164	−1.028	−1.316
SF-TD-PBE0	8.95	0.249	−0.829	0.043	−0.163	−0.903	−1.172
SF-TD-BH&HLYP	3.79	0.107	−0.393	0.454	−0.099	−0.251	−0.418
SF-TD-M06-2X	1.42	0.029	−0.354	0.319	−0.066	−0.097	−0.247
SF-TD-CAM-B3LYP	9.90	0.309	−0.807	0.100	−0.134	−0.920	−1.185
SF-TD-ωB97X-V	10.01	0.364	−0.774	0.175	−0.118	−0.928	−1.187
SF-TD-LC-ωPBE08	10.81	0.464	−0.710	0.310	−0.086	−0.939	−1.191
SF-TD-M11	2.29	0.126	−0.474	0.262	−0.063	−0.312	−0.490
SF-ADC(2)-s	−0.30	0.098	−0.026	0.093	0.112	0.112	−0.005
SF-ADC(2)-x	1.44	0.106	−0.094	−0.335	0.068	−0.409	−0.118
SF-ADC(2.5)	0.18	0.042	0.006	0.140	0.024	0.094	0.000
SF-ADC(3)	0.65	−0.014	0.037	0.186	−0.065	0.075	0.004
SF-EOM-CCSD	−1.53	0.176	0.168	0.207	0.210	0.268	0.211
CASSCF(4,4)	−1.55	0.237	1.421	0.403	0.290	0.734	1.575
CASPT2(4,4)	−1.16	−0.021	−0.202	0.034	−0.016	0.006	−0.214
SC-NEVPT2(4,4)	0.30	−0.054	−0.703	0.070	−0.120	−0.072	−0.794
PC-NEVPT2(4,4)	0.31	−0.051	−0.757	0.045	−0.118	−0.097	−0.846
MRCI(4,4)		0.135	0.553	0.232	0.127	0.324	0.566
MRCI(4,4)+Q		0.086	0.217	0.121	0.075	0.167	0.205
CASSCF(12,12)	2.66	0.253	0.719	0.179	0.226	0.443	0.785
CASPT2(12,12)	−0.42	0.047	0.058	0.005	0.039	0.038	0.077
SC-NEVPT2(12,12)	−0.64	0.068	0.063	0.048	0.021	0.046	0.043
PC-NEVPT2(12,12)	−0.65	0.029	−0.062	0.018	−0.013	−0.024	−0.093
CCSD	0.95	−0.116	0.067		−0.059	0.100	
CC3	−1.05	−0.031	−0.006	0.739		0.162	0.871
CCSDT	−0.25	−0.022	0.014	0.391	0.005	0.131	0.688
CC4	−0.11	0.000	0.003	0.105		0.011	−0.013
CCSDTQ	0.00		0.000	0.000	0.000	0.000	0.000
TBE	[**8.93**][1]	[**1.433**][2]	[**3.125**][1]	[**4.038**][1]	[**0.144**][2]	[**1.500**][1]	[**1.849**][1]
Literature	8.53[3]	1.573[3]	3.208[3]	4.247[3]	0.266[3]	1.664[3]	1.910[3]
	10.35[4]	1.576[4]	3.141[4]	3.796[4]	0.217[4]	1.123[4]	1.799[4]
	9.58[5]	1.456[5]	3.285[5]	4.334[5]	0.083[5]	1.621[5]	1.930[5]
	7.50[6]	1.654[6]	3.416[6]	4.360[6]	0.369[6]	1.824[6]	2.143[6]
	9.36[7]	1.516[7]	3.260[7]	4.205[7]	0.163[7]	1.530[7]	1.921[7]
	9.91[8]	1.475[8]	3.215[8]	4.176[8]	0.098[8]	1.456[8]	1.853[8]
		1.403[9]	3.120[9]	4.127[9]	0.023[9]	1.406[9]	1.751[9]
					0.062[10]		
					0.219[11]		

[1] Value obtained using CCSDTQ/aug-cc-pVDZ corrected by the difference between CC4/aug-cc-pVTZ and CC4/aug-cc-pVDZ.
[2] Value obtained using CCSDTQ/aug-cc-pVDZ corrected by the difference between CCSDT/aug-cc-pVTZ and CCSDT/aug-cc-pVDZ.
[3] Value obtained from Ref. [181] at the SF-ADC(2)-s/cc-pVTZ level with the geometry obtained at the CCSD(T)/cc-pVTZ level.
[4] Value obtained from Ref. [181] at the SF-ADC(2)-x/cc-pVTZ level with the geometry obtained at the CCSD(T)/cc-pVTZ level.
[5] Value obtained from Ref. [181] at the SF-ADC(3)/cc-pVTZ level with the geometry obtained at the CCSD(T)/cc-pVTZ level.
[6] Value obtained from Ref. [173] at the SF-EOM-CCSD/cc-pVTZ level with the geometry obtained at the CCSD(T)/cc-pVTZ level.
[7] Value obtained from Ref. [173] at the SF-EOM-CCSD(fT)/cc-pVTZ level with the geometry obtained at the CCSD(T)/cc-pVTZ level.
[8] Value obtained from Ref. [173] at the SF-EOM-CCSD(dT)/cc-pVTZ level with the geometry obtained at the CCSD(T)/cc-pVTZ level.
[9] Value obtained from Ref. [575] at the EOM-DEA-CCSD/cc-pVTZ level with the geometry obtained at the CCSD(T)/cc-pVTZ level.
[10] Value obtained from Ref. [576] at the DEA-EOM-CC(3p-1h)/cc-pVDZ level with the geometry obtained at the CCSD/cc-pVDZ level.
[11] Value obtained from Ref. [576] at the DEA-EOM-CC(4p-2h)/cc-pVDZ level with the geometry obtained at the CCSD/cc-pVDZ level.

Table C.1: Energy differences between the states computed with various methods and the reference TBE values. Note that AB stands for the automerization barrier and is reported in kcal mol^{-1}. The numbers reported in parenthesis are the percentage of single excitations involved in the transition (%T_1) calculated at the CC3/aug-cc-pVTZ level. The values between square brackets have been obtained by extrapolation via the procedure described in the corresponding footnote.

Level of theory	Automerization barrier (kcal mol^{-1})	Reference
CCSDTQ/aug-cc-pVTZ	8.93	This work
ic-MRCISD+Q/cc-pVTZ	8.93	Ref. [286]
Mk-MRCCSD/cc-pVTZ	10.09	Ref. [286]
Mk-MRCCSD(T)/cc-pVTZ	8.56	Ref. [286]
SUCCSD/cc-pVTZ	8.7	Ref. [259]
MkCCSD/cc-pVTZ	9.6	Ref. [259]
RMRCCSD(T)/cc-pVTZ	9.5	Ref. [259]
MRCISD/cc-pVTZ	8.4	Ref. [285]
MRCISD + Q/cc-pVTZ	8.8	Ref. [285]
MRAQCC/cc-pVTZ	8.9	Ref. [285]
CCSDt/cc-pVTZ	9.5	Ref. [260]
CCSD(T)-h/cc-pVTZ	6.8	Ref. [260]
CC(t;3)/cc-pVTZ	10.0	Ref. [260]
CC(P;Q)/cc-pVDZ	8.65	Ref. [375]

Table C.2: Automerization energy (in kcal mol^{-1}) of CBD computed at various levels of theory.

	$\langle S^2 \rangle$ for D_{2h} geometry			$\langle S^2 \rangle$ for D_{4h} geometry		
Method	1^3B_{1g}	1^1B_{1g}	2^1A_g	1^3A_{2g}	1^1A_{1g}	1^1B_{2g}
SF-TD-B3LYP	1.989	0.030	0.017	2.007	0.014	0.012
SF-TD-PBE0	2.001	0.021	0.019	2.009	0.018	0.012
SF-TD-BH&HLYP	2.017	0.026	0.041	2.020	0.021	0.018
SF-TD-M06-2X	2.014	0.017	0.040	2.014	0.015	0.012
SF-TD-CAM-B3LYP	1.990	0.033	0.024	2.008	0.013	0.012
SF-TD-ωB97X-V	1.986	0.035	0.024	2.008	0.012	0.010
SF-TD-LC-ωPBE08	1.984	0.044	0.031	2.012	0.015	0.012
SF-TD-M11	2.011	0.023	0.045	2.012	0.016	0.014

Table C.3: $\langle S^2 \rangle$ values for the different excited states computed at the SF-TD-DFT/aug-cc-pVTZ level for the D_{2h} and D_{4h} structures.

Method	Basis	Excitation energies (eV)		
		1^3B_{1g}	1^1B_{1g}	2^1A_g
CASSCF(4,4)	6-31+G(d)	1.662	4.657	4.439
	aug-cc-pVDZ	1.672	4.563	4.448
	aug-cc-pVTZ	1.670	4.546	4.441
	aug-cc-pVQZ	1.671	4.549	4.440
CASPT2(4,4)	6-31+G(d)	1.440	3.162	4.115
	aug-cc-pVDZ	1.414	2.971	4.068
	aug-cc-pVTZ	1.412	2.923	4.072
	aug-cc-pVQZ	1.417	2.911	4.081
SC-NEVPT2(4,4)	6-31+G(d)	1.407	2.707	4.145
	aug-cc-pVDZ	1.381	2.479	4.109
	aug-cc-pVTZ	1.379	2.422	4.108
	aug-cc-pVQZ	1.384	2.408	4.116
PC-NEVPT2(4,4)	6-31+G(d)	1.409	2.652	4.120
	aug-cc-pVDZ	1.384	2.424	4.084
	aug-cc-pVTZ	1.382	2.368	4.083
	aug-cc-pVQZ	1.387	2.353	4.091
MRCI(4,4)	6-31+G(d)	1.564	3.802	4.265
	aug-cc-pVDZ	1.558	3.670	4.254
	aug-cc-pVTZ	1.568	3.678	4.270
	aug-cc-pVQZ	1.574	3.681	4.280
MRCI(4,4)+Q	6-31+G(d)	1.525	3.515	4.165
	aug-cc-pVDZ	1.510	3.347	4.142
	aug-cc-pVTZ	1.519	3.342	4.159
	aug-cc-pVQZ	1.525	3.342	4.169
CASSCF(12,12)	6-31+G(d)	1.675	3.924	4.220
	aug-cc-pVDZ	1.685	3.856	4.221
	aug-cc-pVTZ	1.686	3.844	4.217
	aug-cc-pVQZ	1.687	3.846	4.216
CASPT2(12,12)	6-31+G(d)	1.508	3.407	4.099
	aug-cc-pVDZ	1.489	3.256	4.044
	aug-cc-pVTZ	1.480	3.183	4.043
	aug-cc-pVQZ	1.482	3.163	4.047
SC-NEVPT2(12,12)	6-31+G(d)	1.522	3.409	4.130
	aug-cc-pVDZ	1.511	3.266	4.093
	aug-cc-pVTZ	1.501	3.188	4.086
	aug-cc-pVQZ	1.503	3.167	4.088
PC-NEVPT2(12,12)	6-31+G(d)	1.487	3.296	4.103
	aug-cc-pVDZ	1.472	3.141	4.064
	aug-cc-pVTZ	1.462	3.063	4.056

Table C.4: Vertical excitation energies (with respect to the 1^1A_g ground state) obtained with multireference methods for the 1^3B_{1g}, 1^1B_{1g}, and 2^1A_g states of CBD at the D_{2h} rectangular equilibrium geometry of the 1^1A_g ground state.

		Excitation energies (eV)		
Method	Basis	1^3A_{2g}	1^1A_{1g}	1^1B_{2g}
CASSCF(4,4)	6-31+G(d)	0.447	2.257	3.549
	aug-cc-pVDZ	0.438	2.240	3.443
	aug-cc-pVTZ	0.434	2.234	3.424
	aug-cc-pVQZ	0.435	2.235	3.427
CASPT2(4,4)	6-31+G(d)	0.176	1.588	1.899
	aug-cc-pVDZ	0.137	1.540	1.708
	aug-cc-pVTZ	0.128	1.506	1.635
	aug-cc-pVQZ	0.128	1.498	1.612
SC-NEVPT2(4,4)	6-31+G(d)	0.083	1.520	1.380
	aug-cc-pVDZ	0.037	1.465	1.140
	aug-cc-pVTZ	0.024	1.428	1.055
	aug-cc-pVQZ	0.024	1.420	1.030
PC-NEVPT2(4,4)	6-31+G(d)	0.085	1.496	1.329
	aug-cc-pVDZ	0.039	1.440	1.088
	aug-cc-pVTZ	0.026	1.403	1.003
	aug-cc-pVQZ	0.026	1.395	0.977
MRCI(4,4)	6-31+G(d)	0.297	1.861	2.571
	aug-cc-pVDZ	0.273	1.823	2.419
	aug-cc-pVTZ	0.271	1.824	2.415
	aug-cc-pVQZ	0.273	1.825	2.413
MRCI(4,4)+Q	6-31+G(d)	0.260	1.728	2.272
	aug-cc-pVDZ	0.225	1.669	2.073
	aug-cc-pVTZ	0.219	1.667	2.054
	aug-cc-pVQZ	0.220	1.667	2.048
CASSCF(12,12)	6-31+G(d)	0.386	1.974	2.736
	aug-cc-pVDZ	0.374	1.947	2.649
	aug-cc-pVTZ	0.370	1.943	2.634
	aug-cc-pVQZ	0.371	1.945	2.637
CASPT2(12,12)	6-31+G(d)	0.235	1.635	2.170
	aug-cc-pVDZ	0.203	1.588	2.015
	aug-cc-pVTZ	0.183	1.538	1.926
	aug-cc-pVQZ	0.179	1.522	1.898
SC-NEVPT2(12,12)	6-31+G(d)	0.218	1.644	2.143
	aug-cc-pVDZ	0.189	1.600	1.991
	aug-cc-pVTZ	0.165	1.546	1.892
	aug-cc-pVQZ	0.160	1.529	1.862
PC-NEVPT2(12,12)	6-31+G(d)	0.189	1.579	2.020
	aug-cc-pVDZ	0.156	1.530	1.854
	aug-cc-pVTZ	0.131	1.476	1.756
	aug-cc-pVQZ	0.126	1.460	1.727

Table C.5: Vertical excitation energies (with respect to the 1^1B_{1g} ground state) obtained with multireference methods for the 1^3A_{2g}, 1^1A_{1g}, and 1^1B_{2g} states of CBD at the D_{4h} square-planar equilibrium geometry of the 1^3A_{2g} state. The values in square brackets have been obtained by extrapolation via the procedure described in the corresponding footnote. The TBE/aug-cc-pVTZ values are highlighted in bold.

Appendix D

Supporting information for Chapter 4

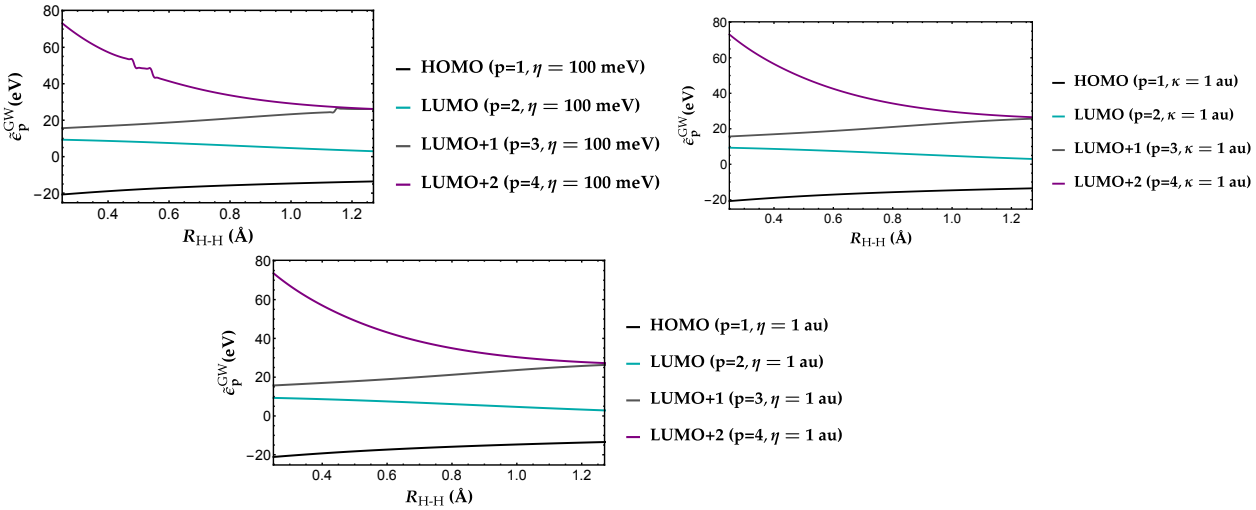

Figure D.1: Regularized quasiparticle energies $\tilde{\epsilon}_p^{GW}$ as functions of the internuclear distance $R_{\mathrm{H-H}}$ (in Å) of H_2 at the G_0W_0@HF/6-31G level for $\eta = 100\,\mathrm{meV}$ (top), $\eta = 1\,E_\mathrm{h}$ (center), and $\kappa = 1\,E_\mathrm{h}$ (bottom).

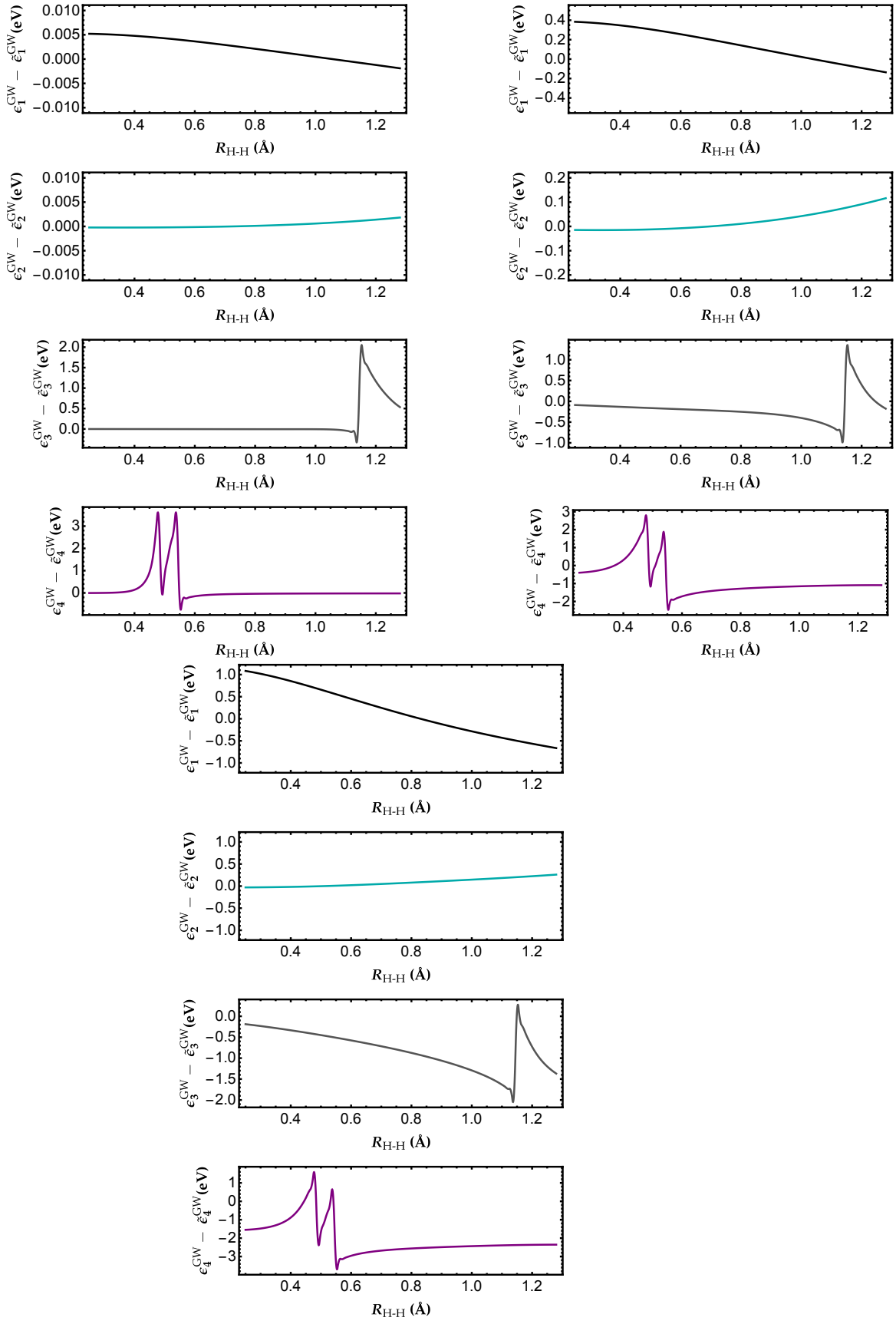

Figure D.2: Difference between non-regularized and regularized quasiparticle energies $\varepsilon pGW - \tilde{\epsilon}_p^{GW}$ computed with $\eta = 0.1\,E_h$ (left), $\eta = 1\,E_h$ (center), and $\eta = 10\,E_h$ (right) as functions of the internuclear distance R_{H-H} (in Å) of H_2 at the G_0W_0@HF/6-31G level.

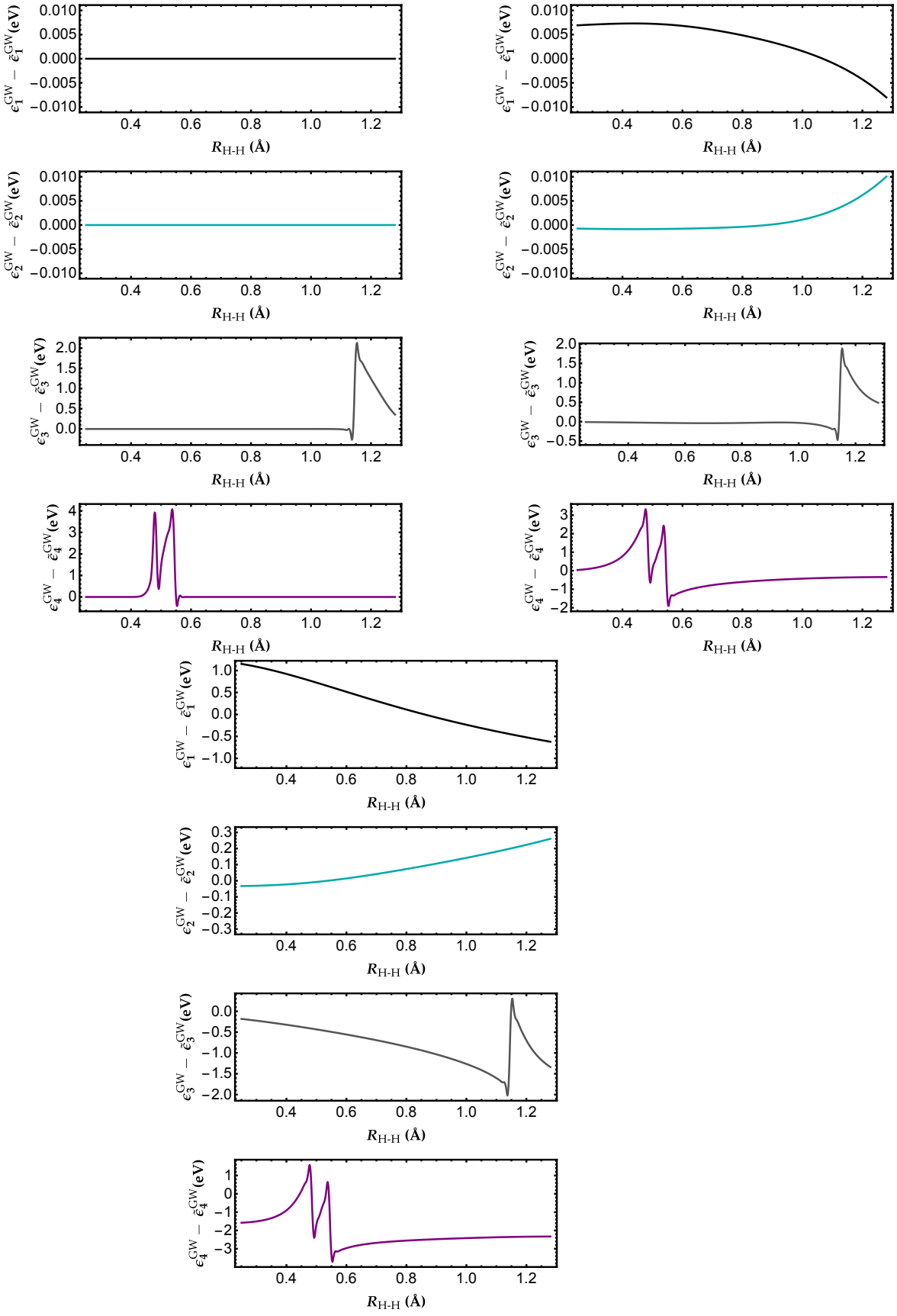

Figure D.3: Difference between non-regularized and regularized quasiparticle energies $\epsilon_p^{GW} - \tilde{\epsilon}_p^{GW}$ computed with computed with $\kappa = 0.1\,E_h$ (left), $\kappa = 1\,E_h$ (center), and $\kappa = 10\,E_h$ (right) as functions of the internuclear distance R_{H-H} (in Å) of H_2 at the G_0W_0@HF/6-31G level.

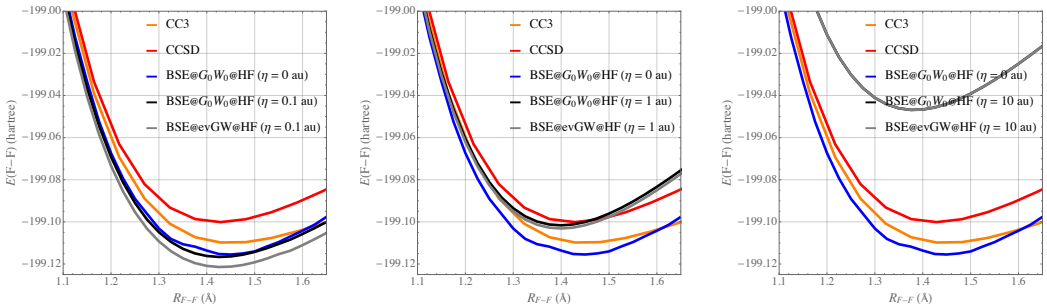

Figure D.4: Ground-state potential energy surface of F_2 around its equilibrium geometry obtained at various levels of theory with the cc-pVDZ basis set for $\eta = 0.1\,E_h$ (left), $\eta = 1\,E_h$ (center), and $\eta = 10\,E_h$ (right).

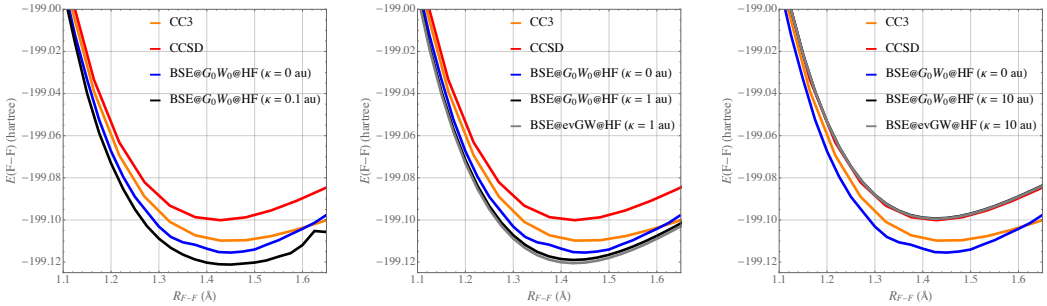

Figure D.5: Ground-state potential energy surface of F_2 around its equilibrium geometry obtained at various levels of theory with the cc-pVDZ basis set for $\kappa = 0.1\,E_h$ (left), $\kappa = 1\,E_h$ (center), and $\kappa = 10\,E_h$ (right). For $\kappa = 0.1\,E_h$, the BSE@evGW@HF calculations do not converge for numerous values of R_{F-F} and are not shown in this figure. For $\kappa = 10\,E_h$, the black and gray curves are superposed.

Appendix E

Supporting information for Chapter 5

E.1 Charged excitations

Mol.	GF2	linGF2	*GW*	lin*GW*	*GT*	lin*GT*	ΔCCSD(T)
He	24.40	24.41	24.35	24.36	24.56	24.56	24.33
Ne	19.65	19.83	20.82	20.88	20.46	20.54	20.89
H_2	16.16	16.16	16.25	16.25	16.13	16.13	16.27
Li_2	5.14	5.12	5.27	5.24	4.98	4.98	5.20
LiH	7.85	7.87	7.95	7.97	8.06	8.06	7.86
HF	14.04	14.32	15.48	15.55	15.00	15.09	15.44
Ar	15.10	15.14	15.36	15.38	15.27	15.29	15.29
H_2O	10.76	11.03	12.11	12.17	11.63	11.72	11.96
LiF	8.79	9.40	10.62	10.78	10.40	10.53	10.95
HCl	12.06	12.11	12.36	12.38	12.20	12.22	12.27
BeO	7.59	8.21	9.37	9.47	8.94	9.04	9.89
CO	13.79	13.93	14.65	14.69	14.13	14.18	13.91
N_2	14.47	14.77	15.82	15.90	15.24	15.34	15.13
CH_4	13.82	13.89	14.41	14.43	14.06	14.09	14.21
BH_3	13.03	13.06	13.35	13.36	13.13	13.14	13.14
NH_3	9.54	9.73	10.56	10.60	10.13	10.19	10.33
BF	10.88	10.89	11.11	11.10	10.78	10.78	10.92
BN	10.63	10.77	11.35	11.36	10.86	10.90	11.80
SH_2	9.80	9.84	10.07	10.08	9.88	9.89	9.96
F_2	13.45	14.08	15.81	15.94	14.92	15.13	15.37
MAE	0.72	0.54	0.24	0.25	0.29	0.26	
MSE	-0.71	-0.53	0.10	0.14	-0.22	-0.17	
RMSD	1.03	0.77	0.32	0.33	0.39	0.35	
Max	2.30	1.68	0.75	0.78	0.96	0.90	

Table E.1: Principal IPs (in eV) of the *GW*20 set computed at various levels of theory with linearization (lin) or without using the cc-pVDZ basis.

E.2 Neutral excitations

Mol.	Nature	CIS	TDHF	TDHF@GF2	BSE@GF2		TDHF@*GW*	BSE@*GW*		TDHF@*GT*	BSE@*GT*		TBE
HCl	CT	8.32	8.27	7.19	8.17	(7.99)	7.68	8.30	(8.19)	7.37	7.56	(7.52)	7.84
H_2O	Ryd.	8.69	8.64	6.08	7.13	(7.01)	7.46	8.09	(8.01)	6.92	7.12	(7.08)	7.17
	Ryd.	10.36	10.31	7.80	8.71	(8.66)	9.15	9.80	(9.72)	8.61	8.88	(8.84)	8.92
	Ryd.	10.96	10.93	8.62	9.49	(9.36)	9.94	10.42	(10.35)	9.35	9.55	(9.51)	9.52
N_2	Val.	9.95	9.70	6.71	9.83	(9.28)	8.05	10.42	(9.99)	7.33	7.89	(7.78)	9.34
	Val.	8.43	7.86	7.50	10.72	(9.69)	7.53	10.11	(9.66)	7.14	8.18	(8.02)	9.88
	Val.	8.98	8.68	8.34	11.28	(10.34)	8.37	10.75	(10.33)	7.99	8.47	(8.36)	10.29
	Ryd.	14.48	14.46	12.03	12.30	(12.29)	13.36	13.60	(13.57)	12.71	12.71	(12.68)	12.98
	Ryd.	14.95	14.87	13.77	14.19	(14.07)	13.70	13.98	(13.94)	13.30	13.69	(13.66)	13.03
	Ryd.	14.42	13.98	13.63	12.84	(12.84)	13.36	13.98	(13.91)	12.79	13.16	(13.11)	13.09
	Ryd.	13.56	13.54	12.71	12.99	(12.96)	14.16	14.24	(14.21)	13.61	13.54	(13.47)	13.46
CO	Val.	9.00	8.72	6.77	9.40	(8.84)	7.65	9.54	(9.20)	7.11	7.63	(7.53)	8.49
	Val.	9.61	9.25	7.48	10.11	(9.43)	8.27	10.25	(9.91)	7.79	8.62	(8.52)	9.92
	Val.	10.02	9.82	8.08	10.39	(9.83)	8.85	10.72	(10.40)	8.38	8.80	(8.72)	10.06
	Ryd.	12.12	12.08	10.83	11.04	(11.00)	11.59	11.88	(11.85)	11.12	11.16	(11.13)	10.95
	Ryd.	12.72	12.71	11.49	11.72	(11.65)	12.26	12.39	(12.37)	11.78	11.81	(11.80)	11.52
	Ryd.	12.82	12.81	11.35	11.69	(11.62)	12.12	12.37	(12.32)	11.63	11.68	(11.67)	11.72
C_2H_2	Val.	6.27	5.90	5.12	7.95	(7.33)	5.54	7.37	(7.05)	5.02	5.72	(5.63)	7.10
	Val.	6.61	6.42	5.68	8.15	(7.59)	6.09	7.74	(7.46)	5.58	5.94	(5.87)	7.44
C_2H_4	Ryd.	7.15	7.13	7.03	7.41	(7.31)	7.45	7.64	(7.62)	6.91	7.01	(6.98)	7.39
	Val.	7.72	7.37	6.56	8.36	(8.11)	7.17	8.19	(8.04)	6.53	7.02	(6.97)	7.93
	Ryd.	7.74	7.73	7.68	8.04	(7.97)	8.07	8.29	(8.26)	7.49	7.64	(7.61)	8.08
CH_2O	Val.	4.57	4.39	1.38	4.82	(4.26)	2.99	5.03	(4.68)	2.15	2.78	(2.68)	3.98
	Ryd.	8.59	8.59	6.32	6.36	(6.40)	7.75	7.87	(7.85)	7.02	7.11	(7.09)	7.23
	Ryd.	9.41	9.40	7.08	7.50	(7.45)	8.52	8.76	(8.72)	7.78	7.87	(7.85)	8.13
	Ryd.	9.53	9.58	7.36	7.39	(7.41)	8.81	8.85	(8.84)	8.09	8.12	(8.11)	8.23
	Ryd.	10.02	10.02	7.22	7.40	(7.37)	8.75	8.87	(8.85)	7.95	8.00	(7.99)	8.67
	Val.	9.82	9.57	8.08	10.00	(9.34)	7.74	10.19	(9.77)	6.89	7.54	(7.44)	9.22
	Val.	9.72	9.21	7.61	9.95	(9.82)	8.46	10.06	(9.82)	7.81	8.38	(8.31)	9.43
MAE		0.92	0.94	1.24	0.52	(0.35)	0.79	0.64	(0.50)	0.98	0.69	(0.74)	
MSE		0.54	0.38	-1.16	0.15	(-0.13)	-0.35	0.64	(0.48)	-0.93	-0.60	(-0.66)	
RMSE		1.06	1.09	1.45	0.63	(0.47)	0.98	0.71	(0.58)	1.30	0.92	(0.98)	
Max		1.92	2.02	2.63	1.27	(1.30)	2.35	1.08	(0.91)	2.74	1.82	(1.93)	

Table E.2: Singlet excitation energies (in eV) of various molecules computed using the aug-cc-pVTZ basis set at different levels of theory. The dynamically-corrected BSE transition energies (dBSE) are reported in parentheses.

E.3 Geometry

Below, we provide the Cartesian coordinates (in Å) of the cycl[3,3,3]zine molecule optimized at the B3LYP/cc-pVDZ level:

N	0.000000	0.009080	0.000000
C	1.224802	0.716230	0.000000
C	-1.224802	0.716230	0.000000
C	2.437473	-0.010534	0.000000
C	-2.437473	-0.010534	0.000000
H	3.363630	0.562441	0.000000
H	-3.363630	0.562441	0.000000
C	1.201735	2.129808	0.000000
C	-1.201735	2.129808	0.000000
H	2.161023	2.645400	0.000000
H	-2.161023	2.645400	0.000000
C	0.000000	2.821547	0.000000
H	0.000000	3.914218	0.000000
C	0.000000	-1.405179	0.000000
C	2.435666	-1.397141	0.000000
C	-2.435666	-1.397141	0.000000
H	3.381943	-1.943483	0.000000
H	-3.381943	-1.943483	0.000000
C	1.235729	-2.091996	0.000000
C	-1.235729	-2.091996	0.000000
H	1.202592	-3.180558	0.000000
H	-1.202592	-3.180558	0.000000

Résumé en français

L'interaction entre la lumière et la matière est omniprésente dans la nature, et de nombreux exemples peuvent être cités. Parmi ceux-ci, on peut mentionner la photosynthèse, qui est un processus utilisé par les plantes, les algues et certaines bactéries. Elle capture la lumière du soleil pour convertir le dioxyde de carbone (CO_2) et l'eau (H_2O) de l'air et du sol en dioxygène (O_2) ainsi qu'en énergie chimique sous forme de glucose. Un autre exemple biologique qui souligne l'interaction entre la lumière et les molécules est le processus de la vision qui se déroule dans la rétine de l'œil. En effet, dans le processus de la vision, la lumière est absorbée par un pigment dans l'œil et entraîne une réaction d'isomérisation du pigment. Cette réaction est le début du processus visuel. De nombreuses autres applications importantes existent dans de nombreux domaines différents, comme dans le domaine énergétique avec la conversion de la lumière du soleil en courant électrique dans les cellules photovoltaïques ou la photocatalyse. Bien sûr, de nombreux autres exemples d'applications peuvent être donnés, mais ces quelques exemples montrent que la compréhension de l'interaction entre la lumière et les molécules est fondamentale dans de nombreux domaines pertinents de la physique, de la chimie et de la biologie.

De nos jours, la simulation numérique est un outil très important non seulement en chimie, mais dans la science en général. Elle permet aux scientifiques de modéliser et d'étudier des systèmes ou des phénomènes complexes qui sont difficiles ou impossibles à étudier directement. En effet, grâce aux simulations, les scientifiques peuvent explorer des environnements hostiles tels que l'espace ou des environnements à température et pression extrêmes. Cela permet de faire des prédictions, de tester des hypothèses et d'obtenir des informations dans différents domaines scientifiques. Cependant, l'interaction entre la lumière et les molécules est un problème complexe qui donne lieu à différents mécanismes possibles tels que l'absorption, l'émission ou la diffusion. Dans cette thèse, nous nous intéressons uniquement au cas de l'absorption des photons et nous nous concentrons sur deux processus, l'excitation neutre et l'ionisation. Le processus d'ionisation se produit lorsque le photon absorbé a suffisamment d'énergie pour extraire un électron de la molécule, tandis qu'une excitation neutre promeut un électron d'un état électronique occupé à un état excité.

Notez que lorsqu'une molécule est excitée à partir de sa géométrie à l'état fondamental, la géométrie de l'état excité peut se détendre. Tout d'abord, un électron absorbe un photon et est promu de l'état électronique et vibratoire à l'état fondamental à sa géométrie d'équilibre vers un état excité à la même géométrie. Ensuite, la structure moléculaire relaxe (et se déplace le long de l'axe horizontal) vers la géométrie d'équilibre de l'état excité. Ensuite, l'électron se désexcite vers l'état électronique fondamental à la géométrie d'équilibre de l'état excité. Enfin, la géométrie de la molécule se détend vers l'état électronique et vibratoire fondamental à sa géométrie d'équilibre. Malheureusement, tous ces processus sont extrêmement difficiles à modéliser, et dans cette thèse, nous nous concentrons uniquement sur les énergies d'excitation verticales, ce qui signifie que nous ne prenons pas en compte la relaxation des géométries.

Chapitre 1

Dans ce chapitre, nous posons le cadre sur lequel repose cette thèse en présentant de nombreuses méthodes de chimie quantique qui sont utilisées tout au long de cette étude. La liste des méthodes évoquées dans ce chapitre est la suivante :

- Approximation Hartree-Fock qui consiste à réécrire l'équation de Schrödinger en N équations monoélectroniques. Dans cette approximation la fonction d'onde électronique est écrite comme un déterminant de Slater de N orbitales occupées. Cette dernière est appelée approximation de champ moyen car on introduit un potentiel effectif à un électron qui est un potentiel moyen subi par un électron en raison de la présence des $(N-1)$ autres électrons. On considère cette méthode dans sa forme restreinte (RHF) où les spinorbitales sont contraintes d'avoir la même fonction spatiale pour les électrons α et β ainsi que son formalisme non restreint (UHF) où les spinorbitales ont des fonctions spatiales différentes pour les spins α et β.

- Théorie de la fonctionnelle de la densité (DFT) où la quantité de base n'est pas la fonction d'onde mais la densité électronique. On s'intéresse au formalisme Kohn-Sham (KS) qui montre des similitudes avec la théorie HF car les électrons sont traités comme des particules indépendantes se déplaçant dans le champ moyen de tous les autres.

- En appliquant la théorie de la réponse linéaire à la méthode Hartree-Fock on obtient un problème aux valeurs propres nommé Hartree-Fock dépendant du temps (TDHF) ou approximation random-phase (RPAx). Lorsqu'on l'applique au formalisme Kohn-Sham de la DFT on obtient également un problème aux valeurs propres nommé DFT dépendant du temps (TD-DFT). Lorsque les matrices correspondants à chacun des problèmes sont diagonalisées elles donnent accès aux excitations neutres de la molécule.

- Ensuite, on se tourne vers la théorie des perturbations où l'idée principale est de séparer l'Hamiltonien en deux parties, une partie non perturbée dont on connait les valeurs et vecteurs propres et une autre partie qui joue le rôle de la perturbation. Dans un premier temps on se tourne vers la théorie des perturbations de Rayleigh et Schrödinger qui nous conduit à la méthode M$\acute{}$oller Plesset qui considére l'Hamiltonien Hartree-Fock comme Hamiltonien non perturbé. Finalement, on considère la théorie des perturbations basée sur la fonction de Green qui nous permet d'obtenir les excitations chargées et neutres d'une molécule. Les excitations chargées sont obtenues grâce à la fonction de Green à un corps en introduisant le potentiel de "self-energy" tandis que les excitations neutres sont obtenues grâce à la fonction de Green à deux corps. Il est intéressant de noter que dans le cas des excitations neutres on obtient un problème aux valeurs propres similaire à celui rencontré en TD-DFT avec un noyau différent. Dans ce chapitre, on étudie plusieurs approximations pour le potentiel de "self-energy".

Chapitre 2

Comme la théorie de la fonctionnelle de la densité dépendante du temps adiabatique (TD-DFT), le formalisme de l'équation de Bethe-Salpeter (BSE) de la théorie de perturbation à plusieurs corps, dans son approximation statique, est "aveugle"

aux excitations doubles (et supérieures), qui sont omniprésentes, par exemple, dans les molécules conjuguées telles que les polyènes. Ici, nous appliquons l'*ansatz* de l'inversion de spin (ou spin-flip), qui considère l'état triplet le plus bas comme la configuration de référence au lieu de l'état singulet fondamental, au formalisme BSE afin d'accéder, en particulier, aux excitations doubles. Le schéma présent est basé sur une version non restreinte de l'approximation *GW* utilisée pour calculer les excitations chargées et le potentiel de Coulomb écranté requis pour les calculs BSE. Les corrections dynamiques aux excitations optiques statiques BSE sont prises en compte par une généralisation non restreinte de notre traitement perturbatif (renormalisé) récemment développé. La performance du formalisme BSE avec renversement de spin est illustrée par le calcul des énergies des états excités de l'atome de béryllium (Be), de la molécule d'hydrogène (H_2) à différentes longueurs de liaison, et du cyclobutadiène (CBD) dans ses géométries rectangulaire et plan carré.

Atome de béryllium

Dans un premier exemple, nous considérons le cas simple de l'atome de béryllium, dont la configuration de l'état fondamental ^1S est $1s^2 2s^2$, dans une petite base (6-31G) qui a été étudié par Krylov dans deux de ses tout premiers articles sur les méthodes d'inversion de spin. Les énergies d'excitation correspondant aux premières excitations singulet et triplet simples $2s \rightarrow 2p$ avec des symétries spatiales P, ainsi qu'aux premières excitations doubles singulet et triplet $2s^2 \rightarrow 2p^2$ avec des symétries spatiales D et P (respectivement), sont représentées dans la figure E.1.

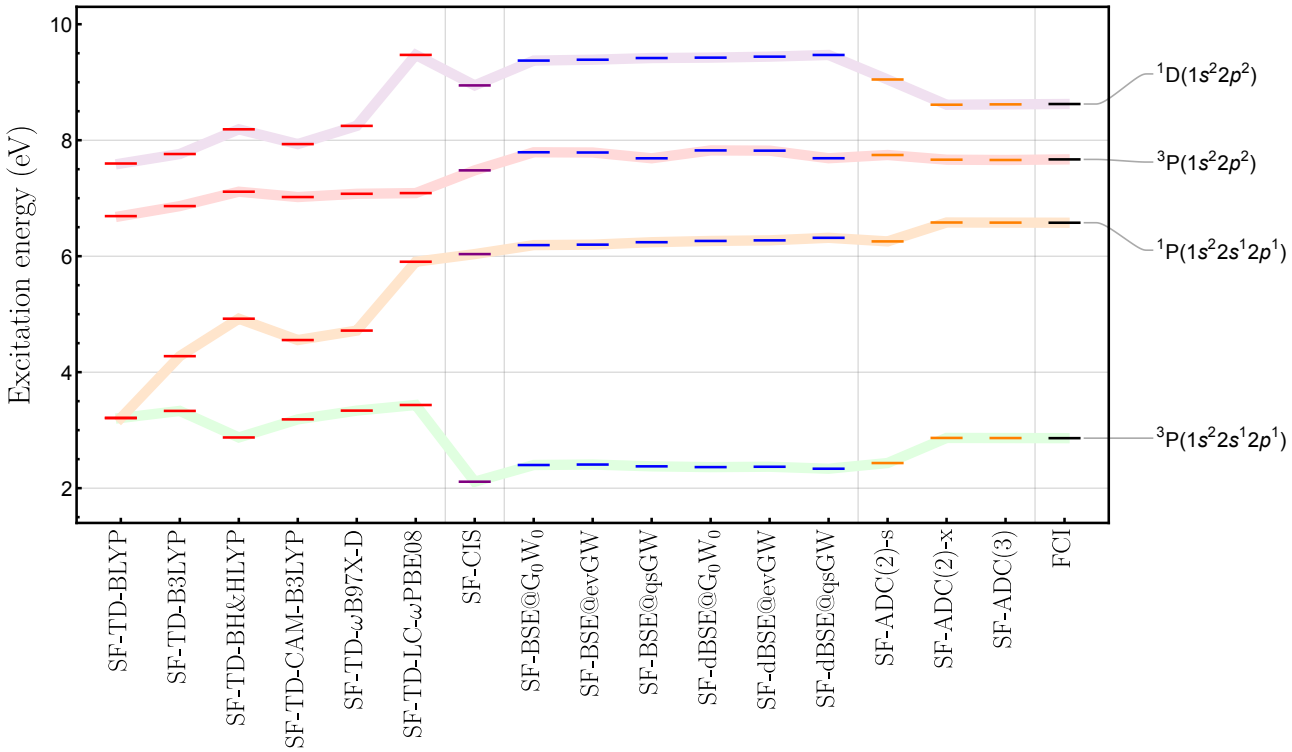

Figure E.1: Les énergies d'excitation (en eV) par rapport à l'état fondamental singulet $^1S(1s^2 2s^2)$ de Be obtenues avec la base 6-31G aux différents niveaux de théorie sont les suivantes: SF-TD-DFT (rouge), SF-CIS (violet), SF-BSE (bleu), SF-ADC (orange), FCI (noir) Tous les calculs d'inversion de spin ont été réalisés avec une référence non restreinte.

Sur le côté gauche de la figure E.1, nous rapportons les énergies d'excitation SF-TD-DFT (lignes rouges) obtenues avec les fonctionnelles BLYP, B3LYP et BH&HLYP, qui correspondent à une augmentation de l'échange exact de 0% à 50%. Les états $^3P(1s^2 2s^1 2p^1)$ et $^1P(1s^2 2s^1 2p^1)$ sont dégénérés au niveau de SF-TD-BLYP. En effet, en raison de l'absence de termes de couplage dans le bloc d'inversion de spin des équations SF-TD-DFT, leurs énergies d'excitation sont données par la différence d'énergie entre les orbitales $2s$ et $2p$ et les deux états sont fortement contaminés par le spin. L'inclusion de l'échange exact, comme dans SF-TD-B3LYP et SF-TD-BH&HLYP, lève cette dégénérescence et améliore la description des deux états. Cependant, l'énergie d'excitation SF-TD-BH&HLYP de l'état $^1P(1s^2 2s^1 2p^1)$ diffère encore de 1.6 eV par rapport à la référence FCI. Pour les autres états, l'accord entre SF-TD-BH&HLYP et FCI est significativement amélioré. Les calculs de TD-DFT avec inversion de spin réalisés avec CAM-B3LYP et ωB97X-D sont seulement légèrement plus précis que leurs homologues hybrides globaux, tandis que SF-TD-LC-ωPBE08 présente des améliorations plus significatives même si cela n'atteint pas la précision de SF-(d)BSE.

La partie centrale de la figure E.1 montre les résultats SF-(d)BSE (lignes bleues) ainsi que les énergies d'excitation SF-CIS (lignes violettes). Tous ces calculs sont effectués avec 100% d'échange exact, avec l'inclusion supplémentaire de la corrélation dans le cas de SF-BSE et SF-dBSE grâce à l'introduction du dépistage statique et dynamique, respectivement. Dans l'ensemble, les énergies d'excitation SF-CIS et SF-BSE se rapprochent de la référence FCI plus que celles de SF-TD-DFT, sauf pour l'état triplet le plus bas où l'énergie d'excitation SF-TD-BH&HLYP est plus précise, probablement grâce à une compensation d'erreur. À l'exception de l'état ^1D, SF-BSE améliore SF-CIS avec une contribution assez faible des effets dynamiques supplémentaires inclus dans le schéma SF-dBSE. Il est à noter que l'échange exact semble purifier le spin de l'état $^3P(1s^2 2s^1 2p^1)$ tandis que les états singulets au niveau de SF-BSE sont légèrement plus contaminés par le spin que leurs homologues SF-CIS.

La figure 2.1 regroupe également les résultats obtenus aux niveaux SF-(d)BSE@evGW partiellement auto-cohérent et SF-(d)BSE@qsGW entièrement auto-cohérent. Les énergies d'excitation SF-(d)BSE sont assez stables par rapport au schéma sous-jacent GW, ce qui illustre bien que les états propres UHF sont en fait un excellent point de départ dans ce cas particulier.

Le côté droit de la figure E.1 illustre les performances des méthodes SF-ADC. Fait intéressant, SF-BSE et SF-ADC(2)-s ont des précisions assez similaires, à l'exception de l'état ^1D où SF-ADC(2)-s a clairement l'avantage sur SF-BSE. Enfin, SF-ADC(2)-x et SF-ADC(3) donnent des énergies d'excitation très proches de la référence FCI pour ce système simple, avec des améliorations significatives pour l'état triplet le plus bas ^3P et l'état doublement excité ^1D. Bien que (d)BSE et ADC(2)-s présentent des similitudes théoriques évidentes, nous tenons à mentionner qu'ils ne sont pas strictement identiques car ADC(2) inclut des contributions clés d'échange du second ordre qui ne sont pas incluses au niveau GW, même dans le cas de schémas plus élaborés tels que evGW et qsGW.

Molécule d'hydrogène

Dans notre deuxième exemple, nous étudions la dissociation de la molécule H_2, qui est un système prototype pour tester de nouvelles méthodes de structure électronique et, en particulier, leur précision en présence d'une forte corrélation. L'état fondamental X, $^1\Sigma_g^+$ de H_2 a une configuration électronique $(1\sigma_g)^2$. La variation des énergies d'excitation associées aux trois premiers états excités singulets par rapport à

l'allongement de la liaison H−H est particulièrement intéressante ici. Le plus bas état simple excité B, $^1\Sigma_u^+$ a une configuration $(1\sigma_g)(1\sigma_u)$, tandis que l'état simple excité E, $^1\Sigma_g^+$ et l'état doublement excité F, $^1\Sigma_g^+$ ont des configurations $(1\sigma_g)(2\sigma_g)$ et $(1\sigma_u)^2$, respectivement. Parce que ces deux derniers états excités interagissent fortement et forment un croisement évité autour de $R(\mathrm{H}-\mathrm{H}) = 1.4$ Å, ils sont généralement appelés état EF, $^1\Sigma_g^+$. Il convient de noter que ce croisement évité n'est pas visible avec des méthodes sans inversion de spin restreintes aux excitations simples (comme CIS, TD-DFT et BSE), car elles sont "aveugles" aux excitations doubles. Trois méthodes, dans leurs versions standard et avec inversion de spin, sont étudiées ici (CIS, TD-BH&HLYP et BSE) et sont comparées aux énergies d'excitation de référence EOM-CCSD (équivalentes à FCI dans le cas de H_2). Tous ces calculs sont effectués avec la base cc-pVQZ.

Le panneau supérieur de la figure E.2 montre les énergies d'excitation CIS (lignes en pointillés) et SF-CIS (lignes en tirets) en fonction de $R(\mathrm{H}-\mathrm{H})$. Les énergies d'excitation de référence EOM-CCSD sont représentées par des lignes pleines. Nous observons que CIS et SF-CIS décrivent mal l'état B, $^1\Sigma_u^+$ dans la limite de dissociation avec une erreur supérieure à 1 eV, tandis que CIS, contrairement à SF-CIS, est beaucoup plus précis autour de la géométrie d'équilibre. Des observations similaires peuvent être faites pour l'état E, $^1\Sigma_g^+$ avec une bonne description au niveau de CIS pour toutes les longueurs de liaison. SF-CIS ne décrit pas avec précision l'état E, $^1\Sigma_g^+$ avant le croisement évité

Cyclobutadiène

Le cyclobutadiène (CBD) est un exemple intéressant car les propriétés électroniques de son état fondamental peuvent être modifiées en déformant sa géométrie. Dans son état fondamental, le CBD peut avoir différentes géométries, comme une géométrie rectangulaire D_{2h} dans l'état singulet A_g ou une géométrie carrée D_{4h} dans l'état triplet A_{2g}. Dans la géométrie rectangulaire D_{2h} de l'état singulet A_g, l'orbitale moléculaire la plus haute occupée (HOMO) et l'orbitale moléculaire la plus basse non occupée (LUMO) ne sont pas dégénérées, et l'état fondamental singulet peut être considéré comme une référence unique avec des orbitales doublement occupées bien définies. Cependant, dans la géométrie carrée D_{4h} de l'état triplet A_{2g}, la HOMO et la LUMO sont strictement dégénérées, et l'état électronique fondamental, qui est toujours de nature singulet avec une symétrie spatiale B_{1g} (violant ainsi la règle de Hund), est fortement multiréférence avec des orbitales occupées de manière singulet (état ouvert singulet). Dans ce cas, les méthodes à référence unique échouent généralement. Néanmoins, l'état triplet le plus bas de symétrie $^3A_{2g}$ reste de nature à référence unique et constitue donc un point de départ parfait pour les calculs d'inversion de spin.

Les géométries optimisées D_{2h} et D_{4h} des états ^1A_g et $^3A_{2g}$ du CBD ont été obtenues au niveau CCSD(T)/cc-pVTZ. Toutes ces valeurs ont été obtenues avec une référence UHF, tout comme les calculs SF-BSE réalisés ici. Tous ces résultats sont présentés dans la figure E.3.

Pour chaque géométrie, trois états excités sont étudiés :

- les états 1, $^3B_{1g}$, 1, $^1B_{1g}$ et 2, ^1A_g de la géométrie D_{2h} ;
- les états 1, $^3A_{2g}$, 2, $^1A_{1g}$ et 1, $^1B_{2g}$ de la géométrie D_{4h}.

Il est important de mentionner que l'état 2, $^1A_{1g}$ de la géométrie rectangulaire a un caractère significatif d'excitation double et est donc difficilement décrit par des

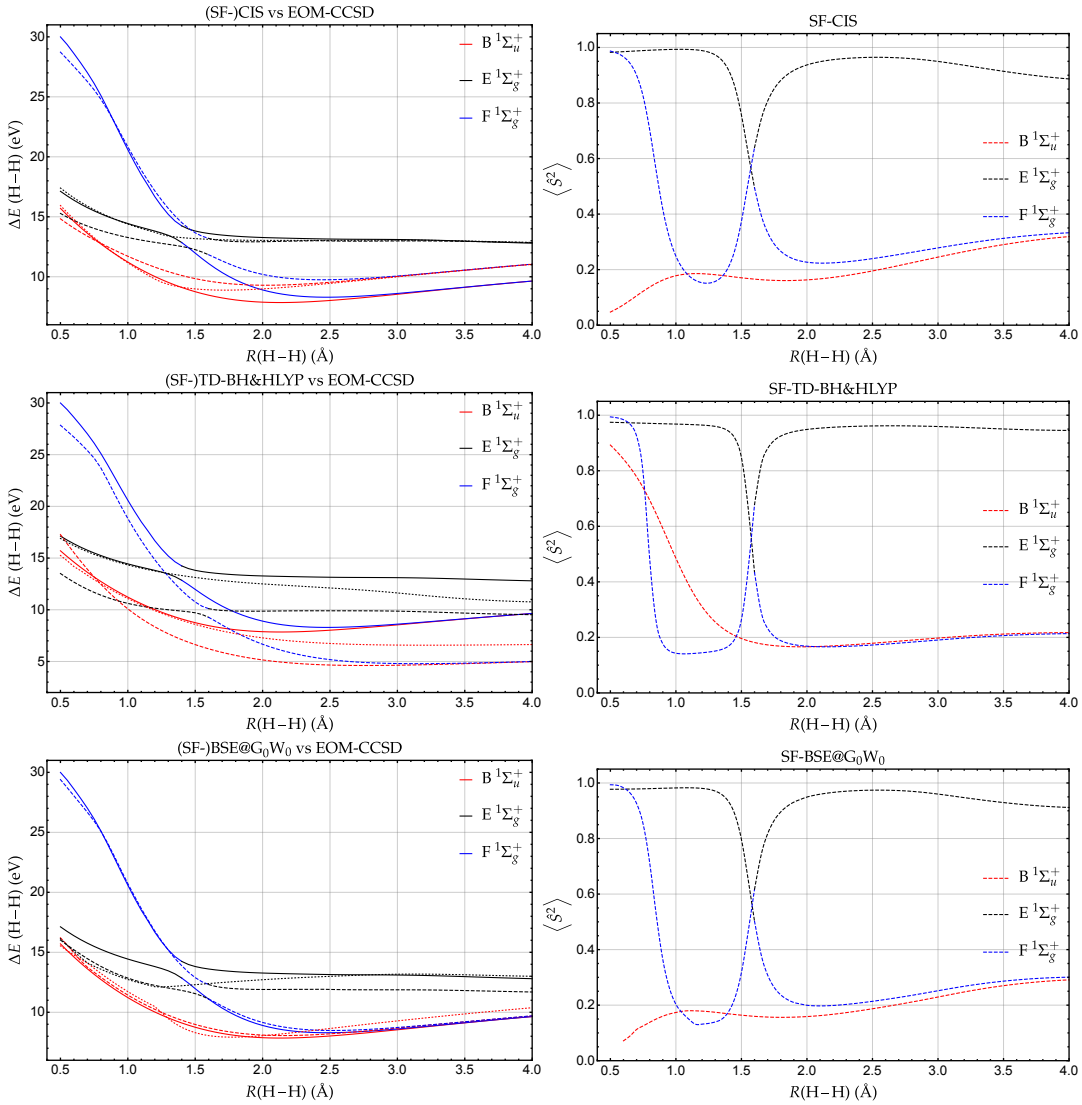

Figure E.2: Énergies d'excitation par rapport à l'état fondamental X, $^1\Sigma_g^+$ (gauche) et valeur d'attente de l'opérateur de spin $\langle \hat{S}^2 \rangle$ (droite) des états B, $^1\Sigma_u^+$ (rouge), E, $^1\Sigma_g^+$ (noir) et F, $^1\Sigma_g^+$ (bleu) de H_2 obtenues avec la base cc-pVQZ aux niveaux de théorie (SF-)CIS (en haut), (SF-)TD-BH&HLYP (au milieu) et (SF-)BSE (en bas). Les énergies d'excitation de référence EOM-CCSD sont représentées par des lignes continues, tandis que les résultats obtenus avec et sans inversion de spin sont représentés par des lignes en pointillés et en tirets, respectivement. Tous les calculs conservant le spin et les calculs avec inversion de spin ont été effectués avec une référence non restreinte.

méthodes du second ordre (telles que CIS(D), ADC(2), CC2 ou EOM-CCSD) et reste un défi réel pour les méthodes du troisième ordre (comme ADC(3), CC3 ou EOM-CCSDT).

En comparant les résultats actuels SF-BSE@G_0W_0 pour la géométrie rectangulaire au niveau ADC le plus précis, c'est-à-dire SF-ADC(3), on obtient une différence d'énergie d'excitation de 0.017 eV pour l'état $1,^3 B_{1g}$. Cette différence augmente à 0.572 eV pour l'état $1,^1 B_{1g}$ puis diminue à 0.212 eV pour l'état $2,^1 A_g$. Dans l'ensemble, l'ajout de corrections dynamiques via le schéma SF-dBSE@G_0W_0 n'améliore pas la précision des énergies d'excitation (par rapport à SF-ADC(3)) avec des erreurs de

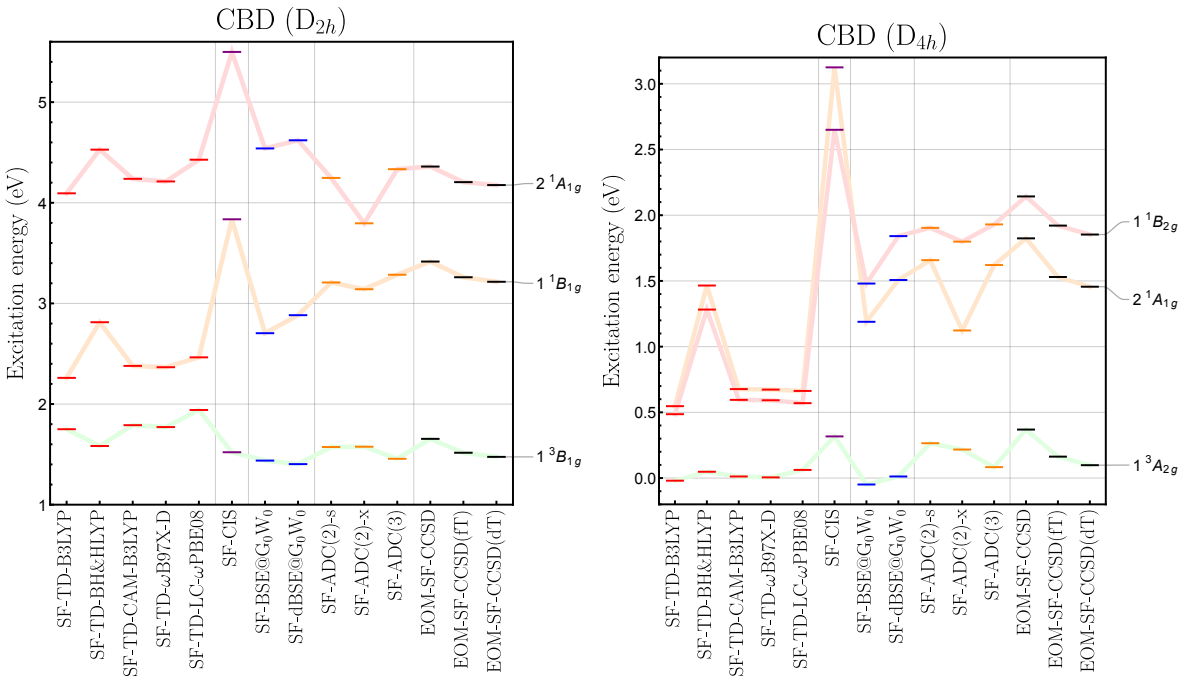

Figure E.3: Excitations verticales pour le CBD à différents niveaux de théorie : SF-TD-DFT (rouge), SF-CIS (violet), SF-BSE (bleu), SF-ADC (orange), and EOM-SF-CCSD (noir). Gauche: états $1\,^3B_{1g}$, $1\,^1B_{1g}$, and $2\,^1A_{1g}$ à la géométrie d'équilibre rectangulaire D_{2h} de l'état fondamental $X\,^1A_g$. Droite: états $1\,^3A_{2g}$, $2\,^1A_{1g}$ et $1\,^1B_{2g}$ à la géométrie d'équilibre plan-carée D_{4h} de l'état $1\,^3A_{2g}$. Tous les calculs d'inversion de spin ont été réalisés avec une référence non restreinte et avec la base cc-pVTZ.

0.052, 0.393 et 0.293 eV pour les états $1,^3B_{1g}$, $1,^1B_{1g}$ et $2,^1A_g$, respectivement.

Pour la géométrie carrée, on constate qu'au niveau SF-BSE@G_0W_0, les deux premiers états sont inversés avec l'état triplet $1,^3B_{1g}$ inférieur à l'état singulet $1,^1A_g$. La même observation peut être faite au niveau SF-TD-B3LYP. Cela est certainement dû à la mauvaise référence Hartree-Fock qui manque de corrélation des spins opposés, et ce problème pourrait être potentiellement atténué en utilisant un meilleur point de départ pour le calcul *GW*. Néanmoins, il est satisfaisant de constater que l'ajout de la correction dynamique dans SF-dBSE@G_0W_0 améliore non seulement l'accord avec SF-ADC(3), mais permet également de retrouver le bon ordre des états. Ainsi, le CBD constitue un excellent exemple pour lequel des corrections dynamiques sont nécessaires pour obtenir la bonne chimie au niveau SF-BSE.

Une autre caractéristique intéressante est l'ordre incorrect des états $2,^1A_{1g}$ et $1,^1B_{2g}$ aux niveaux SF-B3LYP, SF-BH&HLYP et SF-CIS, qui donne le premier plus élevé en énergie que le second. Ce problème n'apparaît pas aux niveaux SF-BSE, SF-ADC et SF-EOM-SF-CCSD. Ici encore, on n'observe pas d'amélioration claire en utilisant des RSH (range-separated hybrids) au lieu des hybrides globaux (BH&HLYP semble particulièrement performant dans le cas du CBD), bien qu'il soit intéressant de mentionner que les calculs SF-TD-DFT basés sur les RSH fournissent des excitations précises pour l'excitation double $1,^1A_g \rightarrow 2,^1A_g$ dans la géométrie D_{2h}.

Conclusion

Dans ce chapitre, nous avons présenté l'extension de l'approche BSE (Bethe-Salpeter Equation) de la théorie de perturbation à plusieurs corps au formalisme d'inversion

de spin afin d'accéder aux excitations doubles dans des systèmes moléculaires. Les calculs d'inversion de spin présentés ici reposent sur une version non restreinte de l'approximation *GW* et du formalisme BSE, avec, en plus de cela, une correction dynamique aux excitations optiques BSE statiques via une généralisation non restreinte de notre traitement perturbatif renormalisé récemment développé. En prenant comme exemples l'atome de béryllium (Be), la dissociation de la molécule d'hydrogène (H_2) et le cyclobutadiène (CBD) dans deux géométries différentes, nous avons montré que le formalisme BSE d'inversion de spin peut modéliser avec précision les excitations doubles et semble dépasser systématiquement son prédécesseur TD-DFT d'inversion de spin. Des améliorations supplémentaires pourraient être obtenues grâce à un meilleur choix des orbitales de départ et de leurs énergies, et nous espérons étudier cela dans un prochain article. Des techniques pour atténuer la contamination de spin dans le formalisme BSE d'inversion de spin seront également explorées dans un avenir proche. Nous espérons que ces nouveaux résultats encourageants stimuleront de nouveaux développements autour du formalisme BSE pour l'établir davantage en tant qu'alternative *ab initio* précieuse à la TD-DFT pour l'étude des états excités moléculaires.

Chapitre 3

Le cyclobutadiène est un terrain de jeu bien connu pour les chimistes théoriciens et est particulièrement adapté pour tester les méthodes d'états fondamentaux et excités. En effet, en raison de sa haute symétrie spatiale, notamment dans la géométrie carrée D_{4h} mais aussi dans l'arrangement rectangulaire D_{2h}, les états fondamentaux et excités du cyclobutadiène présentent des caractères multi-configurationnels, et les méthodes à référence unique, telles que la théorie de la fonctionnelle de la densité dépendante du temps adiabatique standard (TD-DFT) ou la théorie couplée aux équations de mouvement coupled-cluster (EOM-CC), sont connues pour avoir des difficultés dans de telles situations. Dans ce travail, en utilisant un large éventail de méthodes et de jeux de bases, nous proposons une étude computationnelle approfondie de la barrière d'automérisation (définie comme la différence entre les énergies des états fondamentaux rectangulaire et carré) et des énergies d'excitation verticales aux structures d'équilibre D_{2h} et D_{4h}. En particulier, des calculs d'interaction de configuration sélectionnée (SCI), de théorie de perturbation à référence multiple (CASSCF, CASPT2 et NEVPT2) et de coupled-cluster (CCSD, CC3, CCSDT, CC4 et CCSDTQ) sont réalisés. Le formalisme de l'inversion de spin, qui est connu pour fournir une description qualitativement correcte de ces états diradicaux, est également testé dans le cadre de la TD-DFT (combinée avec de nombreuses fonctionnelles d'échange-corrélation) et des schémas de construction diagrammatique algébrique [ADC(2)-s, ADC(2)-x et ADC(3)]. Une meilleure estimation théorique est définie pour la barrière d'automérisation et pour chaque énergie de transition verticale. Dans cette étude, nous avons comparé un plus grand nombre de méthodes de calcul pour la barrière d'automérisation et les énergies d'excitation verticales du cyclobutadiène dans ses géométries carrée (D_{4h}) et rectangulaire (D_{2h}). Nous avons défini des estimations théoriques basées sur des données CCSDTQ/aug-cc-pVTZ extrapolées comme étant les meilleures.

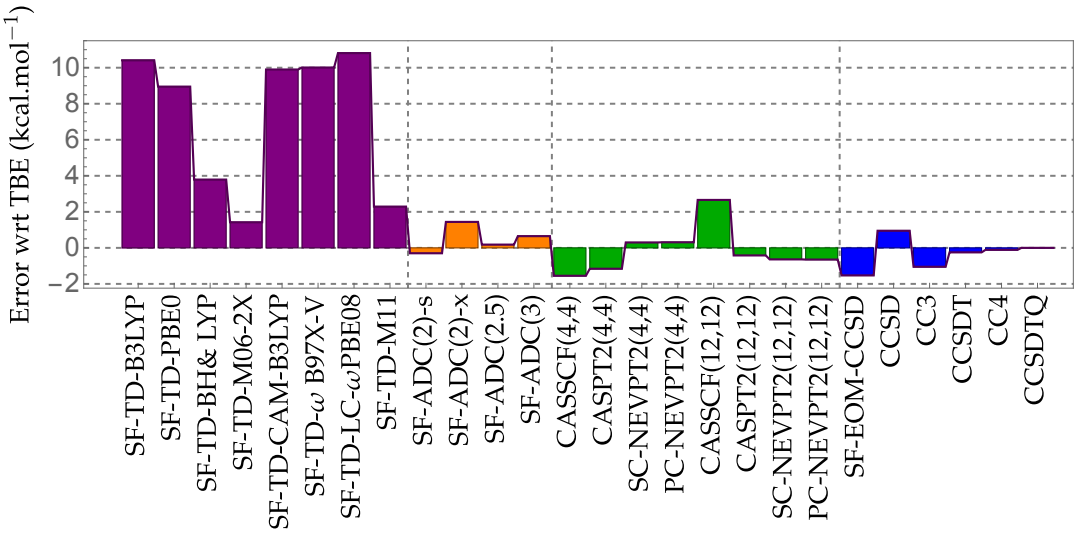

Figure E.4: Erreur (par rapport à la TBE) dans la barrière d'automérisation (en kcal mol^{-1}) du CBD à différents niveaux de théorie en utilisant la base aug-cc-pVTZ. Voir l'annexe C pour les énergies totales.

Barrière d'automerisation

Les résultats concernant la barrière d'automérisation sont rapportés dans le tableau 3.2 pour différents ensembles de bases et présentés dans la figure 3.2 pour la base aug-cc-pVTZ. Notre TBE avec cet ensemble de base est 8.93 kcal mol^{-1}, ce qui est en excellent accord avec de précédentes études (voir annexe C).

Premièrement, on peut voir de grandes variations de la barrière d'énergie au niveau SF-TD-DFT, avec des différences aussi grandes que 10 kcal mol^{-1} entre les différentes fonctionnelles pour un ensemble de base donné. Néanmoins, il est clair que la performance d'une fonctionnelle donnée est directement liée à la quantité d'échange exact à courte distance. En effet, les fonctionnelles hybrides avec environ 50% d'échange exact à courte portée (

exemple, BH&HLYP, M06-2X et M11) fonctionnent nettement mieux que les fonctionnelles ayant une petite fraction d'échange exact à courte portée (

exemple, B3LYP, PBE0, CAM-B3LYP, ωB97X-V et LC-ωPBE08). Cependant, ils sont toujours éloignés de 1–4 kcal mol^{-1} de la valeur de référence TBE, le résultat le plus précis étant obtenu avec M06-2X. Pour les fonctionnelles RSH, la barrière d'automérisation est beaucoup moins sensible à la quantité d'échange exact à longue portée. Une autre caractéristique importante de SF-TD-DFT est la convergence rapide de la barrière énergétique avec la taille de l'ensemble de base. Avec la base double-ζ augmentée, les résultats SF-TD-DFT sont fondamentalement convergés vers une précision sous-kcal mol^{-1}, ce qui est une amélioration drastique par rapport aux approches de fonction d'onde où ce type de convergence est atteint avec l'augmentation base triple-ζ uniquement.

Pour la famille de méthodes SF-ADC, les différences d'énergie sont beaucoup plus faibles avec un écart maximum de 2 kcal mol^{-1} entre les différentes versions. En particulier, nous observons que SF-ADC(2)-s et SF-ADC(3), qui évoluent respectivement comme $\mathcal{O}(N^5)$ et $\mathcal{O}(N^6)$ (où N est le nombre de fonctions de base), sous-estime et surestime la barrière d'automérisation, faisant de SF-ADC(2.5) un bon compromis avec une erreur de seulement 0.18 kcal mol^{-1} par rapport au TBE/aug-cc -valeur de référence de base pVTZ. Néanmoins, à une mise à l'échelle de calcul

$\mathcal{O}(N^5)$, SF-ADC(2)-s est particulièrement précis, même par rapport aux méthodes CC d'ordre élevé (voir ci-dessous). Nous notons que SF-ADC(2)-x [qui s'échelonne comme $\mathcal{O}(N^6)$] ne vaut probablement pas son coût supplémentaire [par rapport à SF-ADC(2)-s] car il surestime le barrière énergétique encore plus que SF-ADC(3). Dans l'ensemble, même avec la meilleure fonction de corrélation d'échange, SF-TD-DFT est clairement surpassé par les modèles SF-ADC plus chers.

Nous observons que SF-EOM-CCSD/aug-cc-pVTZ a tendance à sous-estimer d'environ 1.5 kcal mol^{-1} la barrière énergétique par rapport au TBE. Cela peut être atténué en incluant la correction des triplets avec SF-EOM-CCSD(fT) et SF-EOM-CCSD(dT) (voir l'annexe C. Nous notons également que les valeurs SF-EOM-CCSD pour la barrière énergétique sont proches de celles obtenues avec la méthode CC3 plus coûteuse (standard), mais moins précises que les valeurs calculées avec le formalisme moins cher SF-ADC(2)-s. Notez que la correction (fT) est plus performante que la correction (dT) pour la barrière d'énergie. Cependant, pour les états excités, la situation est inversée (voir ci-dessous).

Concernant les approches multi-références avec l'espace actif minimal (4e,4o), les TBEs sont encadrés par les valeurs CASPT2 et NEVPT2 qui diffèrent d'environ 1.5 kcal mol^{-1} pour toutes les bases. Dans ce cas, les valeurs NEVPT2 sont assez précises avec des différences inférieures à un demi kcal mol^{-1} par rapport aux TBE. Les résultats du CASSCF prédisent une barrière encore plus faible que le CASPT2 en raison du manque bien connu de corrélation dynamique au niveau du CASSCF. Pour le plus grand espace actif (12e,12o), nous voyons des différences plus importantes de l'ordre de 3 kcal mol^{-1} (à travers toutes les bases) entre CASSCF et les variantes de second ordre (CASPT2 et NEVPT2). Cependant, les écarts entre CASPT2(12,12) et NEVPT2(12,12) sont beaucoup plus faibles qu'avec l'espace actif minimal, avec une différence d'énergie d'environ 0.1–0.2 kcal mol^{-1} pour toutes les bases, CASPT2 étant légèrement plus précis que NEVPT2 dans ce cas. Pour chaque ensemble de base, CASPT2(12,12) et NEVPT2(12,12) sont à moins d'un kcal mol^{-1} des TBE. Pour les deux espaces actifs que nous avons considérés ici, les schémas PC- et SC-NEVPT2 fournissent des barrières presque identiques indépendamment de la taille de la base à un électron.

Enfin, pour la famille de méthodes CC, nous observons l'amélioration systématique habituelle suivant la série CCSD $<$ CC3 $<$ CCSDT $<$ CC4 $<$ CCSDTQ, qui est parallèle à leur augmentation de coût : $\mathcal{O}(N^6)$, $\mathcal{O}(N^7)$, $\mathcal{O}(N^8)$, $\mathcal{O}(N^9)$ et $\mathcal{O}(N^{10})$, respectivement. Notez que l'introduction des triples excitations est clairement obligatoire pour avoir une précision au-delà de SF-TD-DFT, et nous observons que CCSDT est définitivement une amélioration par rapport à sa version approchée moins chère, CC3.

Énergies d'excitations verticales

Géométrie rectangulaire D_{2h}

En considérant la base aug-cc-pVTZ, l'évolution des énergies d'excitation verticales par rapport au niveau de la théorie est illustrée sur la Fig. 3.3.

Au niveau CC3/aug-cc-pVTZ, le pourcentage d'excitation unique impliquée dans 1^3B_{1g}, 1^1B_{1g} et 2^1A_g est de 99%, 95% et 1%, respectivement. Par conséquent, les deux premiers sont dominés par des excitations simples, tandis que le dernier état correspond à une véritable double excitation.

Tout d'abord, discutons des effets de base au niveau SF-TD-DFT. Comme prévu, ceux-ci s'avèrent petits et les résultats convergent essentiellement vers la limite de

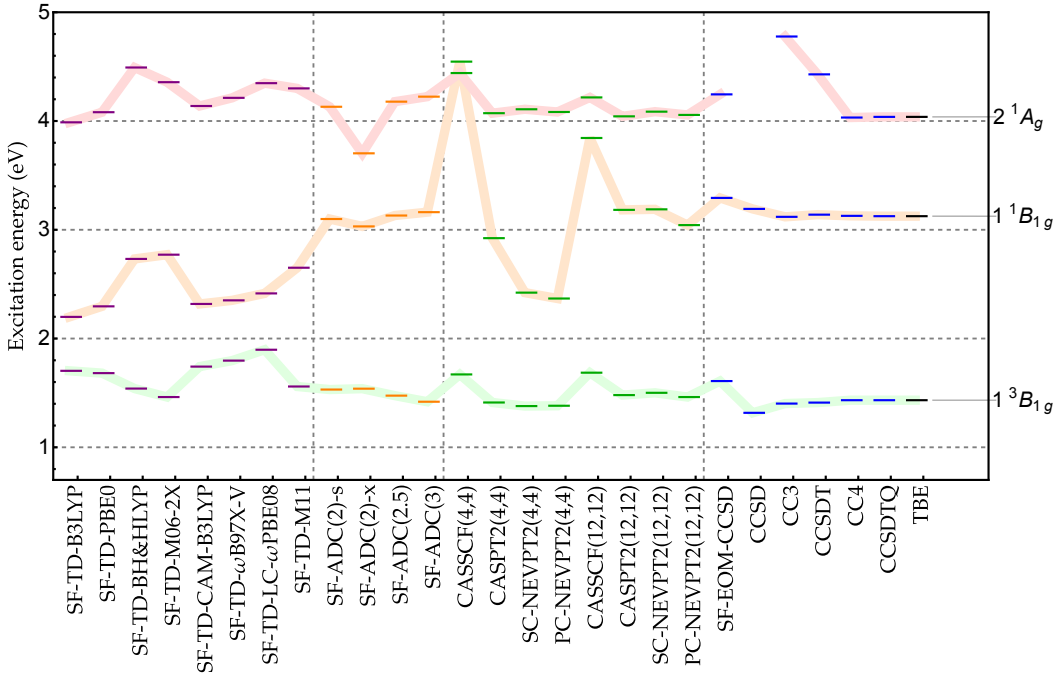

Figure E.5: Énergies d'excitation verticales des états 1^3B_{1g}, 1^1B_{1g} et 2^1A_g à la géométrie d'équilibre rectangulaire D_{2h} de l'état fondamental 1^1A_g en utilisant la base aug-cc-pVTZ. Voir C pour les données brutes.

l'ensemble de base complet avec la base triple-ζ, ce qui n'est certainement pas le cas pour les méthodes de fonction d'onde. En ce qui concerne maintenant la précision des énergies d'excitation verticales, encore une fois, nous voyons que, pour 1^3B_{1g} et 1^1B_{1g}, les fonctionnelles avec la plus grande quantité d'échange exact à courte portée (

exemple, BH&HLYP, M06-2X , et M11) sont les plus précis. Les fonctionnelles avec une grande part d'échange exact sont connues pour fonctionner le mieux dans le cadre SF-TD-DFT car le terme d'échange Hartree-Fock est le seul terme non nul dans le bloc d'inversion de spin. Cependant, leur précision globale reste moyenne surtout pour les états singulets, 1^1B_{1g} et 2^1A_g, avec une erreur de l'ordre de 0.2–0.5 eV par rapport aux TBE. L'état triplet, 1^3B_{1g}, est beaucoup mieux décrit avec des erreurs inférieures à 0.1 eV. Étonnamment, pour l'état doublement excité, 2^1A_g, les fonctionnelles hybrides avec un faible pourcentage d'échange exact (B3LYP et PBE0) sont les plus performantes avec des erreurs absolues inférieures à 0.05 eV. Notez que, comme en témoignent les données rapportées dans l'annexe C, aucun de ces états ne présente une forte contamination de spin.

Deuxièmement, nous discutons des différents schémas SF-ADC (tableau 3.3), *i.e.*, SF-ADC(2)-s, SF-ADC(2)-x et SF-ADC(3). Au niveau du SF-ADC(2)-s, le passage de la plus petite base 6-31+G(d) à la plus grande base aug-cc-pVQZ induit une légère diminution des énergies d'excitation verticales de 0.03 eV (0.06 eV) pour l'état 1^3B_{1g} (2^1A_g), tandis que l'énergie de transition de l'état 1^1B_{1g} chute plus significativement d'environ 0.2 eV. [Les calculs SF-ADC(2)-x et SF-ADC(3) avec aug-cc-pVQZ n'étaient pas réalisables avec nos ressources de calcul.] Ces effets d'ensemble de base sont assez transférables aux autres méthodes de fonction d'onde que nous avons considérées ici. Ceci motive davantage le schéma d'extrapolation "pyramidale" que nous avons utilisé pour produire les valeurs TBE (voir Sec. 3.2.5). Encore une fois, la version étendue, SF-ADC(2)-x, ne semble pas pertinente dans le contexte actuel avec des

erreurs beaucoup plus importantes que les autres schémas. De plus SF-ADC(2)-s et SF-ADC (3) ont des modèles d'erreur miroir rendant SF-ADC (2.5) particulièrement précis, sauf pour l'état à double excitation twoAg où l'erreur par rapport au TBE (0.140 eV) est supérieure à l'erreur SF-ADC(2)-s (0.093 eV).

Fait intéressant, nous observons que les énergies d'excitation SF-EOM-CCSD sont systématiquement plus grandes que les TBE d'environ 0.2 eV avec une belle cohérence dans les différents états excités (simple et double). De plus, les énergies d'excitation SF-EOM-CCSD sont en quelque sorte plus proches de leurs analogues SF-ADC(2)-s (avec une différence d'énergie d'environ 0.1 eV) que les autres schémas. Nous voyons que les énergies des excitations SF-EOM-CCSD pour l'état triplet sont plus grandes d'environ 0.3 eV par rapport à celles du CCSD. On peut logiquement s'attendre à une tendance similaire pour SF-EOM-CCSD(fT) et SF-EOM-CCSD(dT) qui abaissent les énergies d'excitation et tendent à être en meilleur accord par rapport au TBE (voir annexe C). On peut noter que la correction (dT) surpasse légèrement la correction (fT) comme théoriquement attendu.

Concernant les calculs multi-références, le résultat le plus frappant est la mauvaise description de l'état ionique 1^1B_{1g}, en particulier avec l'espace actif (4e,4o) où CASSCF prédit cet état plus élevé en énergie que l'état 2^1A_g. Bien sûr, la correction PT2 est capable de corriger le problème d'ordre d'état mais ne peut pas fournir d'énergies d'excitation quantitatives en raison du mauvais traitement d'ordre zéro. Un autre effet d'entraînement du manque de fiabilité de la fonction d'onde de référence est la grande différence entre CASPT2 et NEVPT2 qui diffèrent d'un demi-eV. Cette caractéristique est caractéristique de l'insuffisance de l'espace actif pour modéliser un tel état. Des calculs MRCI et MRCI+Q supplémentaires (rapportés à l'annexe C) le confirment. Pour les deux autres états, 1^3B_{1g} et 2^1A_g, les erreurs aux niveaux CASPT2(4,4) et NEVPT2(4,4) sont beaucoup plus faibles (inférieures à 0.1 eV). L'utilisation d'un espace actif plus grand résout la plupart de ces problèmes : CASSCF prédit le bon ordre d'état (bien que l'état ionique soit encore mal décrit en termes d'énergétique), les énergies d'excitation CASPT2 et NEVPT2 sont beaucoup plus proches, et leur précision est souvent améliorée (surtout pour les états triplet et doublement excité) bien qu'il soit difficile d'atteindre une précision chimique (,est-à-dire une erreur inférieure à 0.043 eV) de manière systématique.

Enfin, pour les modèles CC, les deux états à grande valeur $\%T_1$, 1^3B_{1g} et 1^1B_{1g}, sont déjà extrêmement précis au niveau CC3, et systématiquement amélioré par CCSDT et CC4. Pour l'état doublement excité, 2^1A_g, la convergence de l'expansion CC est beaucoup plus lente mais il convient de souligner que l'inclusion de quadruples approximatifs via CC4 est particulièrement efficace. Les énergies d'excitation CCSDTQ (qui sont utilisées pour définir les TBE) sont systématiquement dans la barre d'erreur des extrapolations CIPSI, ce qui confirme les performances exceptionnelles des méthodes CC qui incluent des excitations quadruples dans le cadre d'états excités.

D_{4h} square-planar geometry

Les énergies d'excitation verticales calculées à différents niveaux de théorie sont représentées sur la figure E.6 pour la base aug-cc-pVTZ. Comme pour la géométrie précédente, nous commençons par discuter des résultats SF-TD-DFT (tableau 3.5), et en particulier de l'écart singulet-triplet, *i.e.*, la différence d'énergie entre 1^1B_{1g} et Atwog. Pour toutes les fonctionnelles, cet écart est faible (essentiellement inférieur à 0.1 eV alors que la valeur TBE est 0.144 eV) mais il convient de mentionner que B3LYP et PBE0 délivrent à tort un singulet négatif- trou de triplet (d'où un état fondamental de triplet à cette géométrie). Augmenter la fraction d'échange exact dans les hybrides

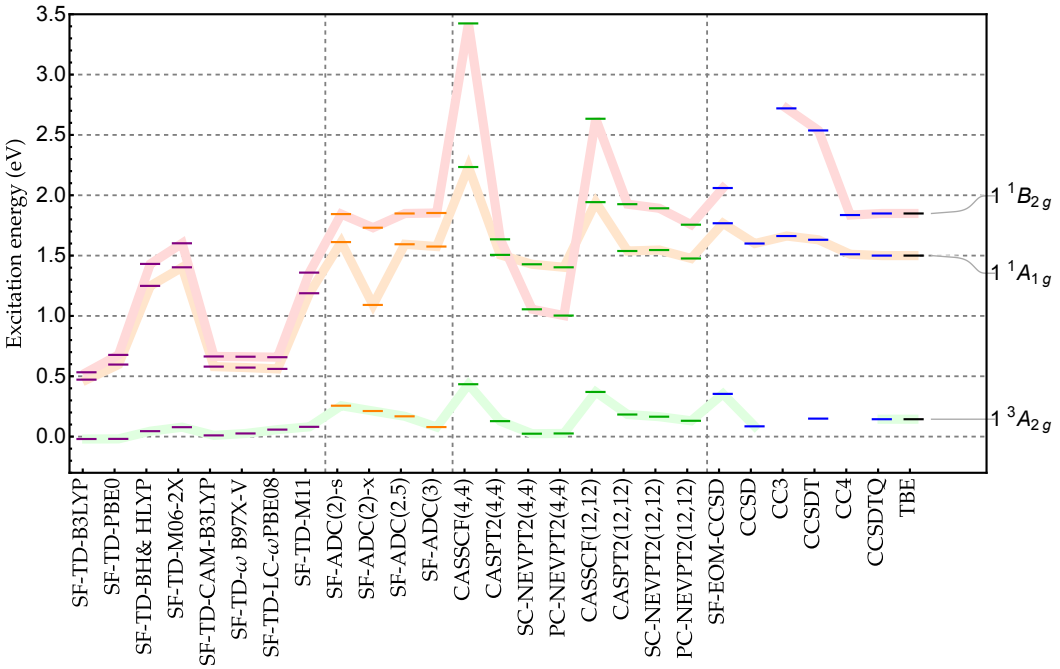

Figure E.6: Énergies d'excitation verticales (en eV) des états 1^3A_{2g}, 1^1A_{1g} et 1^1B_{2g} à la géométrie d'équilibre plan carré D_{4h} de l'état 1^3A_{2g} en utilisant le base aug-cc-pVTZ. Voir l'annexe C pour les données brutes.

ou s'appuyer sur les RSH (même avec une petite quantité d'échange exact à courte portée) permet de récupérer un écart positif et un état fondamental singulet. Au niveau SF-TD-DFT, l'écart d'énergie entre les deux états excités singulet, 1^1A_{1g} et 1^1B_{2g}, est particulièrement petit et croît modérément avec la quantité d'échange exact à courte distance. L'influence de l'échange exact sur les énergies singulet est assez importante avec une différence d'énergie de l'ordre de 1 eV entre la fonctionnelle avec le moins d'échange exact (B3LYP) et la fonctionnelle avec le plus grand montant (M06-2X). En ce qui concerne les énergies d'excitation calculées sur la structure d'équilibre de l'état fondamental D_{2h} et la barrière d'automérisation, les fonctionnelles avec une grande fraction d'échange exact à courte portée donnent des résultats plus précis. Pourtant, l'énergie de transition vers 1^1B_{2g} est décalée d'un demi eV par rapport au TBE pour BH&HLYP et M11, tandis que l'état doublement excité est beaucoup plus proche de la valeur de référence (erreurs de -0.251 et -0.312 eV pour BH&HLYP et M11, respectivement). Avec des erreurs de -0.066, -0.097 et -0.247 eV pour 1^3A_{2g}, 1^1A_{1g} et 1^1B_{2g}, M06 -2X est le meilleur interprète ici. Encore une fois, pour tous les états excités, les effets de l'ensemble de base sont extrêmement faibles au niveau SF-TD-DFT. Nous soulignons que les valeurs $\langle S^2 \rangle$ rapportées dans l'annexe C indiquent à nouveau qu'il n'y a pas de contamination de spin significative dans ces états excités.

Ensuite, nous discutons des différents schémas ADC. Concernant l'écart singulet-triplet, chaque schéma le prédit positif. Bien qu'il fournisse une valeur décente d'écart singulet-triplet, SF-ADC(2)-x semble particulièrement lutter avec les états excités singulet (1^1A_{1g} et 1^1B_{2g}), en particulier pour l'état doublement excité 1^1A_{1g} où il sous-estime l'énergie d'excitation verticale de 0.4 eV. Encore une fois, la moyenne des énergies de transition SF-ADC(2)-s et SF-ADC(3) est bénéfique dans la plupart des cas à l'exception de 1^1A_{1g}. Bien que les effets de l'ensemble de base soient plus importants qu'au niveau SF-TD-DFT, ils restent assez modérés au niveau SF-ADC, et cela vaut pour les méthodes de fonction d'onde en général. Concernant

les énergies d'excitation SF-EOM-CCSD à la géométrie d'équilibre plan carré D_{4h}, des conclusions très similaires à celles fournies dans la section précédente traitant des énergies d'excitation à la géométrie d'équilibre rectangulaire D_{2h} peuvent être tirées : (i) SF-EOM-CCSD surestime systématiquement et systématiquement les TBE d'environ 0.2 eV et est moins précis que SF-ADC(2)-s, (ii) les corrections de triplets non itératives ont tendance à donner un meilleur accord par rapport au TBE (voir annexe C), et (iii) la correction (dT) est plus performante que celle (fT).

Passons aux résultats multi-références (Table 3.6). Pour les deux espaces actifs, comme on pouvait s'y attendre, CASSCF ne fournit pas de description énergétique quantitative, bien qu'il convient de mentionner que le bon ordre d'état est préservé. Ceci est bien sûr amplifié avec l'espace actif (4e,4o) pour lequel le traitement perturbatif de second ordre est incapable de fournir une description satisfaisante en raison de l'espace actif limité. En particulier, SC-NEVPT2(4,4)/aug-cc-pVTZ et PC-NEVPT2(4,4)/aug-cc-pVTZ sous-estiment l'écart singulet-triplet de 0.072 et 0.097 eV et, plus important encore, inversez l'ordre de 1^1A_{1g} et 1^1B_{2g}. Bien que 1^1A_{1g} ne soit pas mal décrit, l'énergie d'excitation de l'état ionique 1^1B_{2g} est décalée de presque 1 eV. Grâce au décalage IPEA dans CASPT2(4,4), l'écart singulet-triplet est précis et l'ordre des états reste correct mais l'état ionique est encore loin d'être bien décrit. L'espace actif (12e,12o) atténue considérablement ces effets et, comme d'habitude maintenant, l'accord entre CASPT2 et NEVPT2 est très nettement amélioré pour chaque état, bien que la précision des approches multi-références reste discutable pour l'état ionique avec, emphe.g., une erreur jusqu'à -0.093 eV au niveau PC-NEVPT2(12,12)/aug-cc-pVTZ.

Enfin, analysons les énergies d'excitation calculées avec différents modèles CC. Nous rappelons au lecteur que ces calculs sont effectués en considérant l'état 1^1A_{1g} comme référence, et que, par conséquent, 1^1B_{1g} et 1^1B_{2g} sont respectivement obtenus comme une désexcitation et une excitation. Par conséquent, par rapport à 1^1A_{1g}, 1^1B_{1g} a un caractère dominant de double excitation, tandis que 1^1B_{2g} a un caractère dominant d'excitation simple. Ceci explique pourquoi on observe une convergence plus lente des énergies de transition dans le cas de 1^1B_{1g} comme le montre la Fig. 3.4. Il ressort des résultats du tableau 3.6 que, si l'on veut atteindre une grande précision avec une telle stratégie de calcul, il est obligatoire d'inclure des excitations quadruples. En effet, au niveau CCSDT/aug-cc-pVTZ, l'écart singulet-triplet est déjà très précis (off by 0.005 eV seulement) alors que les énergies d'excitation des états singulet sont encore 0.131 et 0.688 eV loin de leur TBE respectif. Ces écarts chutent à 0.011 et -0.013 eV au niveau CC4/aug-cc-pVTZ. Enfin, notons que les TBE basés sur le CCSDTQ et les résultats du CIPSI sont cohérents si l'on tient compte de l'erreur d'extrapolation.

Conclusion

Les principaux messages clés de cette étude peuvent être résumés comme suit :

- Dans le cadre du cadre SF-TD-DFT, nous recommandons d'utiliser des échanges-corrélations (hybrides ou hybrides à séparation de portée) avec une grande fraction d'échange exact à courte portée. Cela s'est avéré clairement bénéfique pour la barrière d'automérisation et les énergies d'excitation verticales calculées pour les géométries d'équilibre D_{2h} et D_{4h}.

- Au niveau SF-ADC, nous avons constaté que, comme prévu, le schéma étendu, SF-ADC(2)-x, détériore systématiquement les résultats par rapport à la version standard moins coûteuse, SF-ADC(2)-s. De plus, comme précédemment

rapporté, SF-ADC(2)-s et SF-ADC(3) présentent des erreurs opposées, ce qui signifie que SF-ADC(2.5) émerge comme un excellent compromis.

- SF-EOM-CCSD montre des performances similaires à celles du formalisme moins coûteux SF-ADC(2)-s, en particulier pour les énergies d'excitation. Comme précédemment rapporté, les deux variantes comprenant des corrections triples non itératives, SF-EOM-CCSD(dT) et SF-EOM-CCSD(fT), améliorent les résultats, la correction (dT) donnant de légèrement meilleurs résultats pour les énergies d'excitation verticales calculées pour les géométries d'équilibre D_{2h} et D_{4h}.

- Pour la structure carrée D_{4h}, il est plus difficile d'obtenir une description énergétique fidèle des états excités au niveau de la SF-TD-DFT en raison du fort caractère multi-configurationnel. Dans un tel scénario, les énergies d'excitation SF-TD-DFT peuvent présenter des erreurs de l'ordre de 1 eV par rapport aux estimations théoriques. Cependant, il est satisfaisant de constater que la version d'inversion de spin de l'ADC peut réduire ces erreurs à $0.1 - 0.2$ eV.

- En ce qui concerne les méthodes multi-références, nous avons constaté que bien que NEVPT2 et CASPT2 puissent fournir des énergies d'excitation différentes pour le petit espace actif (4e,4o), les résultats deviennent très similaires lorsque le plus grand espace actif (12e,12o) est considéré. D'un point de vue plus général, une différence significative entre NEVPT2 et CASPT2 n'est généralement pas un bon signe et peut être considérée comme un avertissement clair que l'espace actif est trop petit ou mal choisi. Les états ioniques restent difficiles à traiter pour CASPT2 et NEVPT2, même avec le plus grand espace actif (12e,12o).

- Dans le contexte des méthodes de CC, bien que l'inclusion des excitations triples (via CC3 ou CCSDT) donne des résultats très satisfaisants dans la plupart des cas, l'inclusion des excitations quadruples (via CC4 ou CCSDTQ) est nécessaire pour atteindre une grande précision (surtout dans le cas des états doublement excités). Enfin, nous soulignons qu'en tenant compte de la marge d'erreur liée à la procédure d'extrapolation CIPSI, CCSDTQ et CIPSI fournissent des énergies d'excitation équivalentes, confirmant ainsi l'exceptionnelle précision de CCSDTQ dans le contexte des états excités moléculaires.

Chapitre 4

En reformulant l'équation des quasi-particules *GW* dépendante de la fréquence non linéaire en un problème aux valeurs propres linéaire, nous expliquons l'apparition de solutions multiples et de discontinuités non physiques dans différentes grandeurs physiques calculées dans l'approximation *GW*. En considérant la "self-energy" *GW* comme un hamiltonien effectif, il est démontré que ces problèmes sont des signatures clés d'une forte corrélation dans les états $(N \pm 1)$-électroniques et peuvent être directement liés au problème d'état parasite. Une procédure de régularisation simple et efficace, inspirée par le groupe de renormalisation de similarité, est proposée pour éviter de tels problèmes et accélérer la convergence des calculs *GW* partiellement auto-cohérents.

Un exemple illustratif

Afin d'illustrer l'apparition et l'origine de ces solutions multiples, nous considérons la molécule d'hydrogène dans l'ensemble de base 6-31G qui correspond à un système

à deux électrons avec quatre orbitales spatiales (une occupée et trois virtuelles). Ces calculs sont basés sur des valeurs propres et des orbitales HF restreintes. Nous notons $|1\bar{1}\rangle$ le déterminant de Slater de l'état fondamental de l'électron N où l'orbitale 1 est occupée par un électron de spin-up et un électron de spin-down. Des notations similaires seront utilisées pour les configurations d'électrons $(N \pm 1)$.

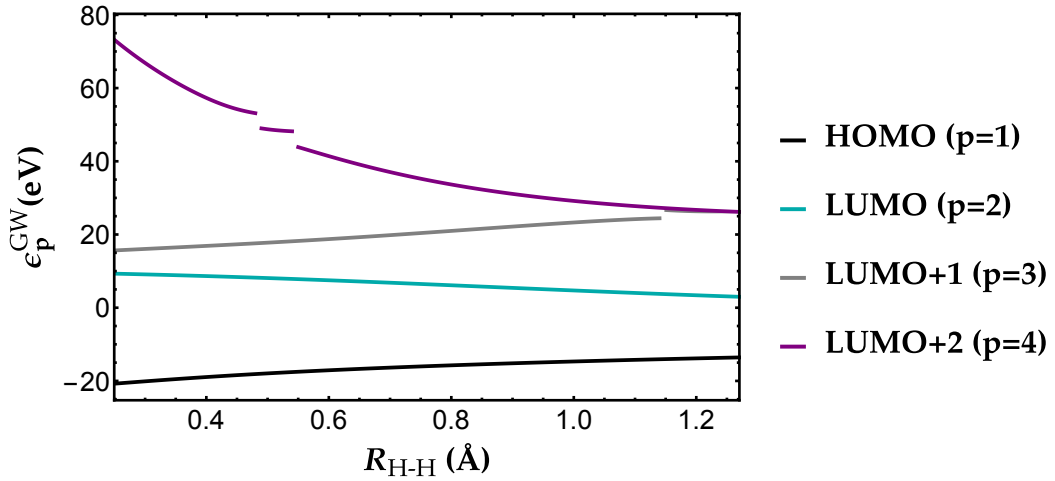

Figure E.7: Énergies des quasi-particules ϵ_p^{GW} en fonction de la distance internucléaire R_{H-H} (en Å) de H_2 au G_0W_0@HF/6-31G niveau.

Sur la Fig. E.7, nous rapportons la variation des énergies des quasiparticules des quatre orbitales en fonction de la distance internucléaire R_{H-H}. On peut facilement diagnostiquer deux régions problématiques montrant des discontinuités évidentes autour de $R_{H-H} = 1.2$ Å pour le LUMO+1 ($p = 3$) et $R_{H-H} = 0.5$ Å pour le LUMO+2 ($p = 4$). Si l'on s'appuie sur la linéarisation de l'équation des quasiparticules pour calculer les énergies des quasiparticules, *i.e.*, ϵ_p^{GW} *environ*ϵpHF $+ Z_p\Sigma_p^c(\epsilon_p^{HF})$, ces discontinuités se transforment en irrégularités car le facteur de renormalisation annule les singularités de la "self-energy".

La figure E.8 montre l'évolution de l'énergie des quasiparticules, des satellites énergétiquement proches et de leurs poids correspondants en fonction de R_{H-H}. Regardons d'abord de plus près la région autour de $R_{H-H} = 1.2$ Å impliquant le LUMO+1 (panneau de gauche de la Fig. E.8). Comme on peut le voir, un croisement évité se forme entre deux solutions de l'équation des quasiparticules ($s = 4$ et $s = 5$). L'examen de leurs vecteurs propres correspondants révèle que les déterminants électroniques $(N + 1)$ principalement impliqués sont le déterminant de référence 1p $|1\bar{1}3\rangle$ et un $(N + 1)$ déterminant excité de configuration électronique $|12\bar{2}\rangle$ qui devient plus faible en énergie que le déterminant de référence pour $R_{H-H} > 1.2$ Å. Par construction, la solution de quasiparticules suit diabatiquement le déterminant de référence $|1\bar{1}3\rangle$ par le croisement évité (traits épais sur la Fig. E.8) qui est précisément à l'origine de la discontinuité énergétique.

Un scénario similaire est en jeu dans la région autour de $R_{H-H} = 0.5$ Å pour le LUMO+2 (panneau de droite de la Fig. E.8) mais il implique maintenant trois solutions ($s = 5$, $s = 6$ et $s = 7$). Les configurations électroniques du déterminant de Slater impliquées sont le déterminant de référence $|1\bar{1}4\rangle$ ainsi que deux déterminants externes de configuration $|1\bar{2}3\rangle$ et $|12\bar{3}\rangle$. Ces états forment deux croisements évités en successions rapides, qui créent deux discontinuités dans la surface d'énergie (voir Fig. E.8). Dans cette région, bien que la fonction d'onde de l'état fondamental soit bien décrite par le déterminant HF de l'électron N, une situation qui peut être

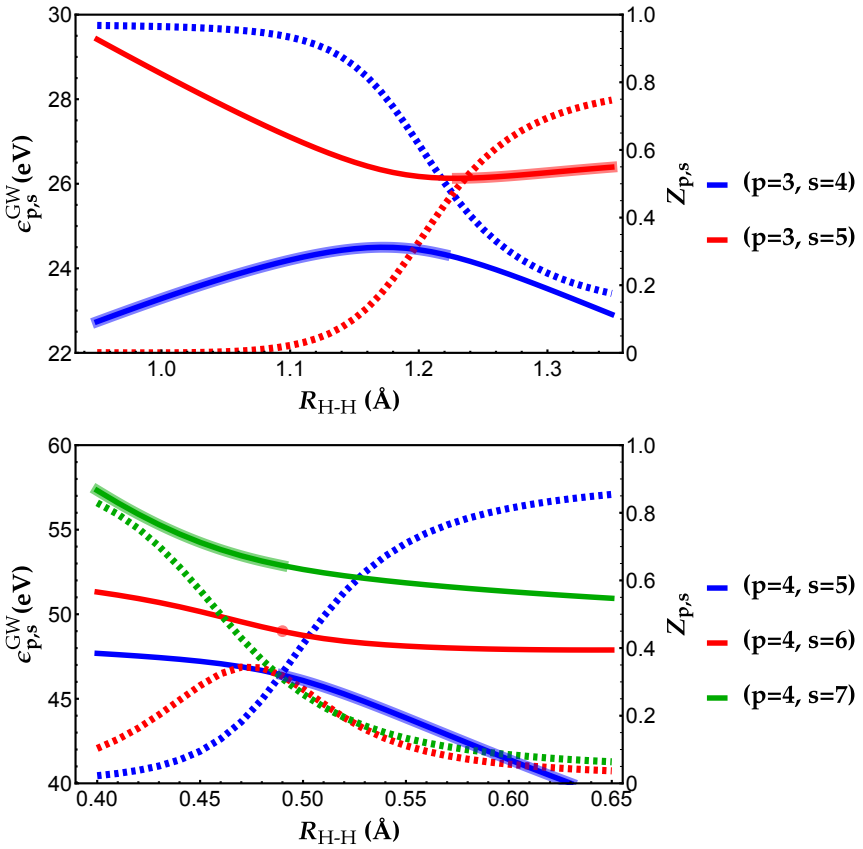

Figure E.8: Sélection des énergies des quasiparticules et des satellites $\epsilon^{GW}_{p,s}$ (traits pleins) et leur facteur de renormalisation $Z_{p,s}$ (traits pointillés) en fonction de la distance internucléaire $R_{\text{H}-\text{H}}$ (dans Å) pour les orbitales LUMO+1 ($p = 3$) et LUMO+2 ($p = 4$) de H_2 au G_0W_0@HF / Niveau 6-31G. La solution de quasiparticules (qui correspond à la solution avec le plus grand poids) est représentée par une ligne plus épaisse.

étiquetée en toute sécurité comme une référence unique, on peut voir que le $(N+1)$ -la fonction d'onde électronique implique trois déterminants de Slater et peut alors être qualifiée de situation multi-références (ou fortement corrélée) avec des configurations électroniques quasi dégénérées. Par conséquent, on peut conclure que cette chute de *GW* est une signature clé d'une forte corrélation dans les états d'électrons $(N \pm 1)$ qui produit une redistribution significative des poids entre les configurations électroniques.

Introduction des méthodes *GW* régularisées

La figure E.9 compare les énergies des quasiparticules non régularisées et régularisées dans les deux régions d'intérêt pour diverses valeurs η et κ. Elle montre clairement comment la régularisation de la "self-energy" *GW* a lié diabatiquement les deux solutions pour s'affranchir des discontinuités. Cependant, cette diabatisation est plus ou moins précise selon (i) la forme réelle du régularisateur, et (ii) la valeur de η ou κ.

Discutons d'abord du simple régularisateur indépendant de l'énergie (panneaux du haut de la Fig. 4.3). Mathématiquement, pour lier harmonieusement deux solutions, la valeur de η doit être suffisamment grande pour que la singularité située dans le plan complexe au croisement évité soit déplacée vers l'axe réel. Cette valeur est directement liée à la différence d'énergie entre les deux états au croisement évité, et est donc, par définition, dépendante de l'énergie. Ceci est clairement mis en évidence sur la Fig. E.9 où, selon la valeur de η, la régularisation est plus ou moins efficace. Par exemple, autour de $R_{\mathrm{H-H}} = 1.1$ Å (en haut à gauche), une valeur de $0.1\,E_{\mathrm{h}}$ (courbe verte) est appropriée tandis qu'à $R_{\mathrm{H-H}} = 0.5$ Å (en haut à droite), cette valeur ne semble pas assez grande. Notez également que $\eta = 0.1\,E_{\mathrm{h}}$ est nettement supérieur à la valeur suggérée de 100 meV et si l'on utilise des valeurs η plus petites, la régularisation est clairement inefficace.

Discutons maintenant du régularisateur dépendant de l'énergie basé sur SRG (panneaux inférieurs de la Fig. E.9). Pour $\kappa = 10\,E_{\mathrm{h}}$, la valeur est clairement trop grande induisant une grande différence entre les deux ensembles d'énergies des quasiparticules (courbes violettes). Pour $\kappa = 0.1\,E_{\mathrm{h}}$, nous avons le scénario inverse où κ est trop petit et certaines irrégularités subsistent (courbes vertes). Nous avons trouvé que $\kappa = 1.0\,E_{\mathrm{h}}$ est un bon compromis qui ne modifie pas significativement les énergies des quasiparticules tout en assurant une transition douce entre les deux solutions. De plus, bien que le κ optimal dépende évidemment du système, cette valeur fonctionne bien dans tous les scénarios que nous avons rencontrés. Cependant, il peut certainement être affiné pour des applications spécifiques.

Conclusion

Dans ce chapitre, nous avons fourni des explications mathématiques et physiques sur l'apparition de multiples solutions et de discontinuités dans diverses quantités physiques calculées dans l'approximation *GW*. Plus précisément, nous avons montré que les états intrus sont la principale cause de ces problèmes et que cette limitation du *GW* est une signature clé d'une forte corrélation. Une procédure de régularisation simple et efficace inspirée du groupe de renormalisation de similarité a été proposée pour éliminer ces discontinuités sans altérer trop les énergies des quasi-particules. De plus, cette régularisation de l'auto-énergie accélère considérablement la convergence des méthodes *GW* (partiellement) auto-cohérentes. Nous espérons que ces nouvelles perspectives physiques et ces développements techniques élargiront l'applicabilité des

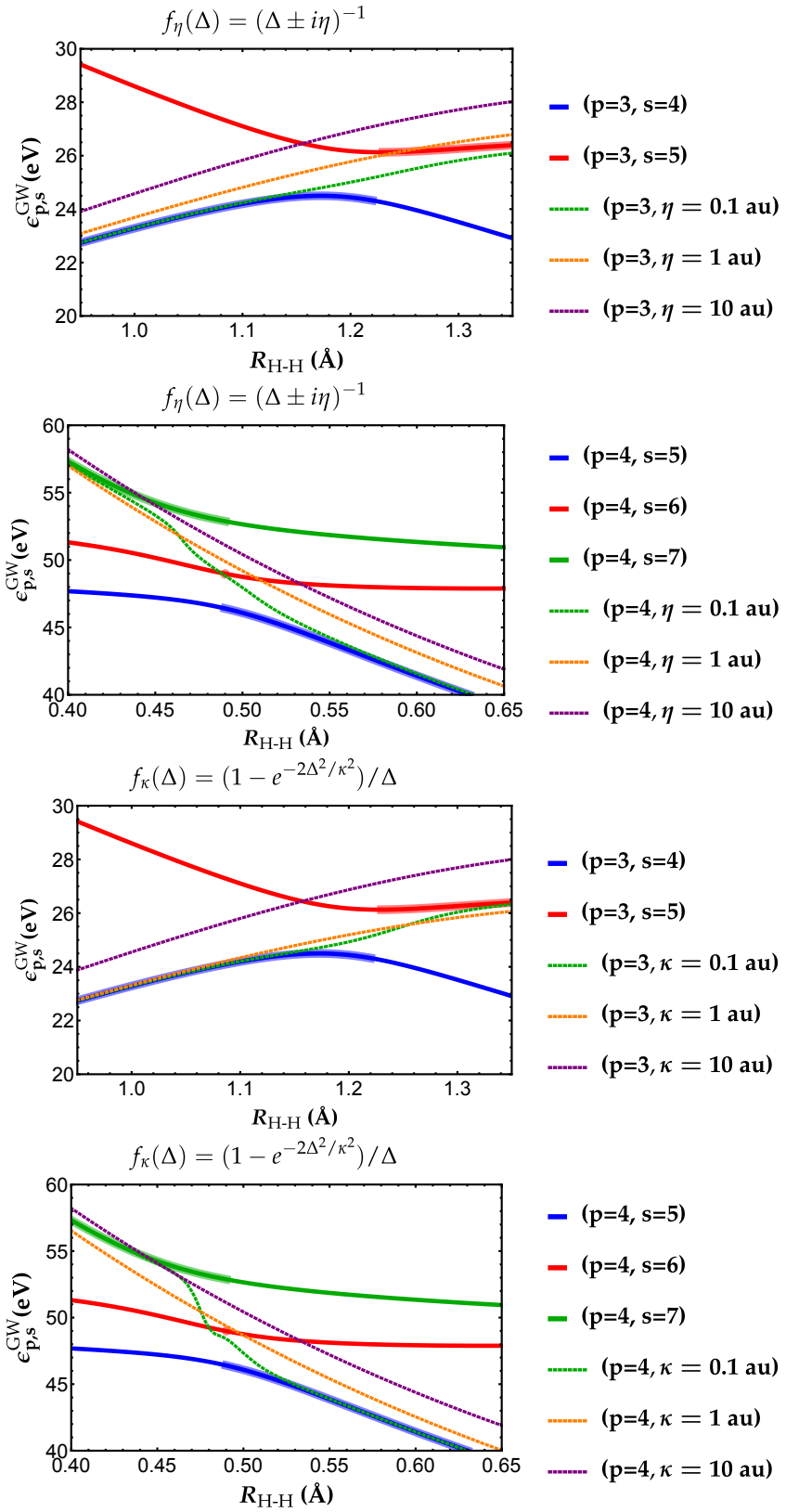

Figure E.9: Comparaison entre les énergies non régularisées (traits pleins) et régularisées (traits pointillés) en fonction de la distance internucléaire $R_{\mathrm{H-H}}$ (en Å) pour les orbitales LUMO+1 ($p = 3$) et LUMO+2 ($p = 4$) de H_2 au niveau G_0W_0@HF/6-31G. La solution de quasiparticules est représentée par une ligne plus épaisse.

méthodes de la fonction de Green dans la communauté de la structure électronique moléculaire et au-delà.

Chapitre 5

Ces dernières années, les méthodes basées sur les fonctions de Green ont suscité un intérêt considérable en raison de leur capacité à cibler à la fois les excitations chargées et neutres. Parmi elles, l'approximation bien établie *GW* fournit des potentiels d'ionisation et des affinités électroniques précis et peut être étendue aux excitations neutres en utilisant le formalisme de l'équation de Bethe-Salpeter (BSE). Dans cette étude, nous examinons les liens entre différentes méthodes des fonctions de Green et évaluons leurs performances pour les excitations chargées et neutres. Des comparaisons avec d'autres méthodes de fonctions d'onde de second ordre largement connues sont également présentées. De plus, nous calculons l'écart singulet-triplet du cycl[3,3,3]azine, un émetteur moléculaire modèle pour la fluorescence retardée activée thermiquement, qui a la particularité d'avoir un écart inversé grâce à une contribution substantielle des excitations doubles. Nous démontrons que, dans l'approximation *GW*, un noyau BSE de second ordre avec correction dynamique est nécessaire pour prédire cette caractéristique distinctive.

Écart singulet-triplet de cycl[3,3,3]zine

Les molécules avec un écart singulet-triplet inversé (c'est-à-dire où l'état excité singulet le plus bas a une énergie plus élevée que l'état triplet le plus bas) présentent un intérêt particulier dans le processus TADF car elles peuvent exploiter à la fois les excitons singulet et triplet pour l'émission, améliorant ainsi l'efficacité des OLED. Grâce à cet écart inversé, le système peut subir un croisement intersystème inverse efficace, un processus dans lequel la population de l'état triplet peut être thermiquement activée et transférée à l'état singulet, ce qui entraîne une fluorescence retardée.

Récemment, ces systèmes ont été examinés à différents niveaux de calcul, y compris TD-DFT et les méthodes de fonction d'onde du second ordre, telles que CIS(D), ADC(2) et EOM-CCSD. Cette inversion nécessite une contribution substantielle des doubles excitations. Cela explique pourquoi la TD-DFT adiabatique n'est pas capable de reproduire cette caractéristique particulière, et des méthodes de second ordre ou d'ordre supérieur sont nécessaires lorsque les doubles excitations sont explicitement traitées. Nous calculons les plus basses énergies d'excitation singulet et triplet, E_S et E_T, ainsi que l'écart singulet-triplet correspondant, ΔE_{ST}, de cycl[3,3,3]zine (voir Fig. E.10), un émetteur moléculaire modèle pour TADF, avec la base cc-pVDZ à différents niveaux théoriques. La géométrie de la cycl[3,3,3]zine a été optimisée au niveau B3LYP/cc-pVDZ et est rapportée en annexe E par souci d'exhaustivité. De plus, nous avons pu calculer l'écart singulet-triplet avec des méthodes du troisième ordre telles que ADC(3).

Nos résultats sont présentés dans la Fig. E.10. Comme prévu, les calculs BSE@*GW* et BSE2@*GW* ne produisent pas d'écart singulet-triplet inversé en raison de la nature statique du noyau. Parce que la correction dynamique des énergies d'excitation singulet et triplet s'annulent à peu près exactement, dBSE@*GW* donne le même ordre d'état. Cependant, le noyau dynamique de second ordre *GW* (qui ne corrige que les états singulets) prédit fidèlement cette inversion bien que les énergies d'excitation correspondantes soient sous-estimées par rapport aux autres approches, sauf ADC(3), qui est connu pour présenter cette tendance. Fait intéressant, ADC(2), EOM-CC2,

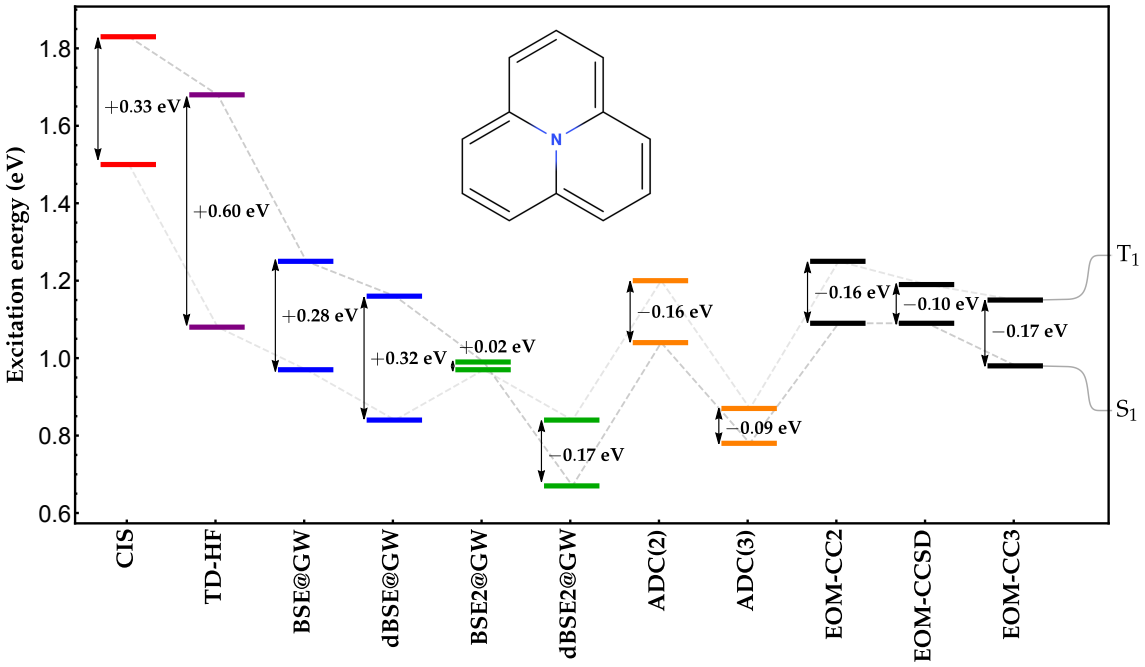

Figure E.10: Évolution des énergies d'excitation verticale singulet et triplet les plus basses (en eV) de cycl[3,3,3]zine évaluées avec différentes méthodes de calcul utilisant la base cc-pVDZ.

EOM-CC3 et BSE2@*GW* donnent essentiellement la même valeur, tandis que EOM-CCSD et ADC(3) sous-estiment légèrement l'écart. Étant donné que le pourcentage d'excitations simples impliquées dans ces deux transitions de valence (%T_1) est élevé (bien que non négligeable pour l'état singulet), la valeur EOM-CC3 est susceptible d'être précise.

Conclusion

Dans cette étude, notre objectif était d'examiner les relations entre différentes méthodes de la fonction de Green, en explorant spécifiquement diverses approximations pour l'auto-énergie (GF2, *GW* et *GT*) et leurs noyaux correspondants de l'équation de Bethe-Salpeter (BSE) aux niveaux statique et dynamique.

Dans la poursuite de cet objectif, nous avons examiné la capacité de nos différentes méthodes à reproduire l'inversion de l'écart singulet-triplet dans le cycl[3,3,3]zine, un émetteur moléculaire prototypique pour le TADF (thermally activated delayed fluorescence). À l'exception d'un cas, nous avons observé que toutes les méthodes basées sur la BSE, statiques et dynamiques, n'ont pas réussi à reproduire cette caractéristique unique. La seule exception était le schéma BSE2@*GW* corrigé dynamiquement, qui a donné une valeur d'écart cohérente avec celle obtenue à partir de calculs EOM-CC3. Cette observation met en évidence l'importance des termes d'ordre supérieur et des effets dynamiques dans la formalisme de la BSE, et nous espérons que ces résultats stimuleront de nouveaux progrès dans ce domaine de recherche.

Chapitre 6

Les méthodes de chimie quantique sont hautement compatibles avec l'utilisation d'ordinateur grâce à la formulation matricielle de la mécanique quantique, qui tire

parti de la puissance des bibliothèques d'algèbre linéaire comme BLAS et LAPACK. Par conséquent, un large éventail de logiciels de chimie quantique est actuellement disponible, comprenant à la fois des options gratuites et commerciales. Ces logiciels sont adaptés à des méthodes spécifiques ou offrent une gamme diversifiée de méthodologies, utilisant divers types de fonctions de base, entre autres fonctionnalités. Un nombre considérable de codes de chimie quantique existent, couvrant une large gamme de méthodes. Pour une liste complète de ces codes, consultez la page Wikipedia sur les logiciels de chimie quantique et de physique de l'état solide.

Malheureusement, malgré la conception efficace des nombreux logiciels, ils peuvent être difficiles à comprendre car ils utilisent souvent des langages de programmation de bas niveau. De plus, ces programmes ne sont pas principalement destinés à des fins pédagogiques ou à faciliter la compréhension. C'est précisément là que QCMATH intervient. QCMATH vise à aider les nouveaux venus dans le domaine de la chimie quantique en fournissant une plateforme facile à utiliser pour développer des idées et des codes. Il convient de noter que certains logiciels utilisent des langages de programmation de haut niveau, ce qui peut améliorer la compréhension du code. En ce qui concerne QCMATH, il s'agit d'une compilation de modules MATHEMATICA spécialement conçus pour effectuer des calculs de structure électronique.

Avant d'entrer dans les détails spécifiques de QCMATH, on donne un aperçu de l'environnement MATHEMATICA. MATHEMATICA est un système logiciel complet développé par Wolfram Research, initialement conceptualisé par Stephen Wolfram. Il dispose d'une large gamme de bibliothèques intégrées qui peuvent être utilisées à des fins diverses. L'un de ses points forts réside dans sa capacité à effectuer des opérations d'algèbre informatique, telles que les dérivées, les intégrales et les simplifications d'expressions. De plus, MATHEMATICA permet l'évaluation numérique de ces expressions. Une autre fonctionnalité notable est ses capacités avancées de tracé, qui prennent en charge des visualisations complexes de fonctions en une, deux et trois dimensions. De nombreux livres offrent de nombreux exemples d'applications de MATHEMATICA dans différents domaines. Avec sa polyvalence, MATHEMATICA est devenu un outil puissant utilisé dans de nombreux domaines scientifiques, notamment l'éducation, la recherche et l'industrie.

MATHEMATICA comprend deux composants principaux : le noyau et l'interface utilisateur (front end). Le noyau interprète les expressions et génère des expressions résultantes, qui peuvent ensuite être affichées à l'aide de l'interface utilisateur. L'interface utilisateur d'origine prend la forme d'une interface de type bloc-notes, facilitant la création et la modification de documents bloc-notes pouvant contenir du code, du texte, des images et des graphiques. QCMATH, en particulier, repose sur ces documents bloc-notes. Il est important de noter que QCMATH n'est **pas** principalement conçu pour l'efficacité informatique, mais se concentre plutôt sur la fourniture d'un environnement facile à utiliser. Un grand nombre des méthodes évoquées dans cette thèse sont implémentées dans QCMATH. La liste de celles-ci peut être dressée comme suit :

- Calculs de l'état fondamental :
    1. Hartree-Fock (HF) restreint et non restreint
    2. Théorie des perturbations de Moller-Plesset (MP)
- Calculs d'excitations chargées :
    1. fonction de Green (GF) de deuxième ordre
    2. approximation *GW*

3. approximation T-matrix

- Calculs d'excitations neutres
  1. approximation random-phase (RPA)
  2. equation Bethe-Salpeter (BSE)

Conclusion

Quelques perspectives de ce travail peuvent être mentionnées. Pour la deuxième partie de cette thèse, sur le calcul des excitations neutres dans les molécules, des améliorations supplémentaires pourraient être obtenues grâce à un meilleur choix des orbitales de départ et de leurs énergies en utilisant les orbitales et les énergies KS-DFT. De plus, nous pourrions utiliser les différents noyaux BSE vus dans la troisième partie de la thèse pour étudier leurs performances pour ces systèmes moléculaires. Dans le cas de CBD, nous pourrions également utiliser le formalisme BSE avec inversion de spin et les différents noyaux BSE pour comparer ses performances à celles de son parent TD-DFT avec inversion de spin. Il serait également intéressant de dériver le noyau BSE du second ordre au niveau de la matrice T afin de voir si nous pouvons obtenir l'inversion de l'écart singulet-triplet de la molécule cycl[3,3,3]zine.

Les perspectives les plus intéressantes se trouvent dans la troisième partie. En effet, comme discuté dans le chapitre 5, il existe des liens entre les approximations de la "self-energy" et donc les noyaux BSE. Un point particulièrement frappant est la similitude entre les différents noyaux BSE. En effet, nous avons vu que en supprimant l'effet d'écrantage de GW et GT, nous retrouvons les différents termes du noyau GF2 (à l'exception d'une partie d'échange dans les intégrales à deux électrons). De plus, nous avons vu que BSE@GT est assez précis pour les transitions de Rydberg où la densité d'états excitée est beaucoup plus faible que celle de l'état fondamental. Il s'agit d'une situation où les diagrammes en échelle sont connus pour être pertinents. D'autre part, BSE@GW présente une bonne description des excitations de valence, en particulier lorsqu'on prend en compte les corrections dynamiques. De plus, le noyau GF2 a montré des résultats précis pour le calcul des excitations neutres. Il serait donc très intéressant de pouvoir construire une version écrantée du noyau GF2 basée sur les noyaux GW et GT, en particulier compte tenu du fait que l'écrantage devient plus important pour les grandes molécules avec de nombreux électrons.

Une idée évidente est de combiner les deux "self-energy" (GW et GT) et de construire ensuite le noyau BSE correspondant. Ce faisant, il serait particulièrement intéressant de voir les performances de ces "self-energy" et de ce noyau hypothétiques pour les excitations chargées et neutres. Notez que la combinaison de GW et GT n'est pas une idée nouvelle et reste un domaine de recherche actif en physique [419, 569–571]. Comme mentionné dans une précédente étude [419], il existe différentes façons de combiner les chaînes de corrélation en évitant le problème de double comptage [484, 499]. L'approximation d'échange fluctuant (FLEX) de Bickers *et* al. [483, 498] qui part de GF2 et somme toutes les contributions du troisième ordre dans chaque chaîne séparément. Malheureusement, en procédant ainsi, nous n'avons pas accès aux diagrammes mixtes. Notez que des approches au-delà de FLEX ont été proposées [482, 485, 486]. Il est également possible de coupler les chaînes ph et pp sur un pied d'égalité, ce qui conduit à la théorie des parquets qui repose sur des diagrammes [484, 572]. Il est important de mentionner qu'une combinaison directe des chaînes ph et pp, qui sont présentes dans GW et GT à travers les problèmes ph-RPA et pp-RPA, où les termes de double comptage sont éliminés, a déjà été explorée [569].

Malheureusement, ce schéma n'est pas concluant pour les dissociations moléculaires. Nous pouvons également mentionner le travail de Romaniello *et* al. qui a dérivé le couplage des chaînes *GW* et *GT* sur un pied d'égalité en partant des équations exactes à plusieurs corps dans le cas de la molécule de Hubbard exactement soluble [419]. Degroote [570] a quant à lui utilisé la partition de Faddeev [573] pour combiner de manière diagrammatique les chaînes de corrélation.

Malheureusement, bon nombre de ces méthodes et approximations reposent sur des approches diagrammatiques complexes, que nous n'avons pas abordées dans cette thèse, et il serait bon d'utiliser des méthodes non diagrammatiques pour effectuer cette combinaison. C'est un sujet sur lequel nous souhaitons continuer à travailler et nous espérons que le formalisme de dépliage pourrait nous aider dans la poursuite de cet objectif.

Pour le logiciel QCMATH, nous pourrions envisager d'étendre ses capacités en implémentant différentes variantes de méthodes CI et CC pour les états fondamentaux et excités. Nous pourrions également envisager de ne pas nous concentrer uniquement sur les énergies, mais aussi sur des propriétés telles que les forces d'oscillateur, les moments dipolaires, etc. Grâce à la puissance de MATHEMATICA, il serait relativement aisé et intéressant d'implémenter des méthodes DFT avec différentes fonctionnelles d'échange-corrélation. De plus, une extension aux états excités avec TD-DFT serait facile compte tenu des similitudes des expressions matricielles avec le formalisme BSE déjà implémenté dans QCMATH. Nous espérons également implémenter de nouvelles méthodes CC, en particulier au niveau de l'équation d'état CC où notre groupe a récemment conçu un générateur d'équations automatique basé sur MATHEMATICA, nommé EOMCCGEN [574].

Bibliography

[1]R. E. Blankenship, *The basic principles of photosynthetic energy storage* (John Wiley & Sons, Ltd, 2002).

[2]T. Mirkovic, E. E. Ostroumov, J. M. Anna, R. van Grondelle, Govindjee, and G. D. Scholes, "Light absorption and energy transfer in the antenna complexes of photosynthetic organisms", Chem. Rev. **117**, 249–293 (2017).

[3]S. I. Allakhverdiev, *Photosynthesis: A new approach to the molecular, cellular, and organismal levels* (John Wiley & Sons, Ltd, 2015).

[4]C. Schnedermann, X. Yang, M. Liebel, K. M. Spillane, J. Lugtenburg, I. Fernández, A. Valentini, I. Schapiro, M. Olivucci, P. Kukura, and R. A. Mathies, "Evidence for a vibrational phase-dependent isotope effect on the photochemistry of vision", Nature Chem **10**, 449–455 (2018).

[5]S. Gozem, M. Huntress, I. Schapiro, R. Lindh, A. A. Granovsky, C. Angeli, and M. Olivucci, "Dynamic electron correlation effects on the ground state potential energy surface of a retinal chromophore model", J. Chem. Theory Comput. **8**, 4069–4080 (2012).

[6]N. Ferré and M. Olivucci, "Probing the rhodopsin cavity with reduced retinal models at the CASPT2//CASSCF/AMBER Level of Theory", J. Am. Chem. Soc. **125**, 6868–6869 (2003).

[7]M. Garavelli, T. Vreven, P. Celani, F. Bernardi, M. A. Robb, and M. Olivucci, "Photoisomerization path for a realistic retinal chromophore model: The nonatetraeniminium cation", J. Am. Chem. Soc. **120**, 1285–1288 (1998).

[8]T. Vreven, F. Bernardi, M. Garavelli, M. Olivucci, M. A. Robb, and H. B. Schlegel, "Ab initio photoisomerization dynamics of a simple retinal chromophore model", J. Am. Chem. Soc. **119**, 12687–12688 (1997).

[9]Y. Cui, P. Zhu, X. Liao, and Y. Chen, "Recent advances of computational chemistry in organic solar cell research", J. Mater. Chem. C **8**, 15920–15939 (2020).

[10]F. Arkan and M. Izadyar, "Quantum chemistry study on the anthropomorphic molecules: characterization, photovoltaic properties, and application", J. Iran. Chem. Soc. **20**, 47–55 (2023).

[11]R. Aqil Shehzad, K. Ayub, M. Al-Buriahi, N. Alfryyan, H. Somaily, S. Alomairy, and J. Iqbal, "Quantum chemical approach to study tipstap derivatives with anticipated minimized crystal roughness for photovoltaic application with estimated pce of over 20%", Solar Energy **237**, 96–107 (2022).

[12]J. L. Delgado, P.-A. Bouit, S. Filippone, M. Herranz, and N. Martín, "Organic photovoltaics: A chemical approach", Chem. Comm. **46**, 4853 (2010).

[13]S. Rhatigan and M. Nolan, *Insights into photocatalysis from computational chemistry* (John Wiley & Sons, Ltd, 2021) Chap. 6, pp. 127–154.

[14]M. Kılıç and Z. Çınar, "A quantum mechanical approach to TiO2 photocatalysis", Journal of Advanced Oxidation Technologies **12**, 37–46 (2009).

[15]G. Green, "An essay on the application of mathematical analysis to the theories of electricity and magnetism", in , edited by N. M. Ferrers, Cambridge Library Collection - Mathematics (Cambridge University Press, 2014), 1–82.

[16]E. E. Salpeter and H. A. Bethe, "A relativistic equation for bound-state problems", Phys. Rev. **84**, 1232–1242 (1951).

[17]L. Hedin, "New method for calculating the one-particle Green's function with application to the electron-gas problem", Phys. Rev. **139**, A796 (1965).

[18]G. Strinati, "Effects of dynamical screening on resonances at inner-shell thresholds in semiconductors", Phys. Rev. B **29**, 5718 (1984).

[19]G. Strinati, "Application of the Green's functions method to the study of the optical properties of semiconductors", Riv. Nuovo Cimento **11**, 1–86 (1988).

[20]O. J. Backhouse and G. H. Booth, "Efficient excitations and spectra within a perturbative renormalization approach", J. Chem. Theory Comput. **16**, 6294–6304 (2020).

[21]O. J. Backhouse, M. Nusspickel, and G. H. Booth, "Wave function perspective and efficient truncation of renormalized second-order perturbation theory", J. Chem. Theory Comput. **16**, 1090–1104 (2020).

[22]O. J. Backhouse, A. Santana-Bonilla, and G. H. Booth, "Scalable and predictive spectra of correlated molecules with moment truncated iterated perturbation theory", J. Phys. Chem. Lett. **12**, 7650–7658 (2021).

[23]S. J. Bintrim and T. C. Berkelbach, "Full-frequency GW without frequency", J. Chem. Phys. **154**, 041101 (2021).

[24]S. J. Bintrim and T. C. Berkelbach, "Full-frequency dynamical Bethe–Salpeter equation without frequency and a study of double excitations", J. Chem. Phys. **156**, 044114 (2022).

[25]X. Blase, I. Duchemin, D. Jacquemin, and P.-F. Loos, "The Bethe–Salpeter equation formalism: From physics to chemistry", J. Phys. Chem. Lett. **11**, 7371–7382 (2020).

[26]X. Blase, I. Duchemin, and D. Jacquemin, "The Bethe–Salpeter equation in chemistry: relations with TD-DFT, applications and challenges", Chem. Soc. Rev. **47**, 1022–1043 (2018).

[27]P.-F. Loos, A. Scemama, I. Duchemin, D. Jacquemin, and X. Blase, "Pros and Cons of the Bethe–Salpeter Formalism for Ground-State Energies", J. Phys. Chem. Lett. **11**, 3536–3545 (2020).

[28]P. F. Loos, B. Pradines, A. Scemama, E. Giner, and J. Toulouse, "A density-based basis-set incompleteness correction for GW methods", J. Chem. Theory Comput. **16**, 1018–1028 (2020).

[29]P.-F. Loos and X. Blase, "Dynamical correction to the Bethe–Salpeter equation beyond the plasmon-pole approximation", J. Chem. Phys. **153**, 114120 (2020).

[30]P.-F. Loos and P. Romaniello, "Static and dynamic Bethe–Salpeter equations in the T-matrix approximation", J. Chem. Phys. **156**, 164101 (2022).

[31]E. Monino and P.-F. Loos, "Spin-conserved and spin-flip optical excitations from the Bethe–Salpeter equation formalism", J. Chem. Theory Comput. **17**, 2852–2867 (2021).

[32]E. Monino and P.-F. Loos, "Unphysical discontinuities, intruder states and regularization in GW methods", J. Chem. Phys. **156**, 231101 (2022).

[33]M. Born and R. Oppenheimer, "Zur Quantentheorie der Molekeln", Ann. Phys. **389**, 457–484 (1927).

[34]F. W. J. Olver, D. W. Lozier, R. F. Boisvert, and C. W. Clark, *NIST Handbook of Mathematical Functions*, eds (Cambridge University Press, Cambridge ; New York, 2010).

[35]D. R. Hartree, "The Wave Mechanics of an Atom with a Non-Coulomb Central Field. Part I. Theory and Methods", Proc. Camb. Philos. Soc. **24**, 89 (1928).

[36]W. Pauli, "Über den Zusammenhang des Abschlusses der Elektronengruppen im Atom mit der Komplexstruktur der Spektren", Z Phys. **31**, 765–783 (1925).

[37]J. C. Slater, "The Theory of Complex Spectra", Phys. Rev. **34**, 1293–1322 (1929).

[38]V. Fock, "Näherungsmethode zur Lösung des quantenmechanischen Mehrkörperproblems", Z. Physik **61**, 126–148 (1930).

[39]P. Pulay, "Improved SCF convergence acceleration", J. Comput. Chem. **3**, 556–560 (1982).

[40]P. Hohenberg and W. Kohn, "Inhomogeneous electron gas", Phys. Rev. **136**, B864–B871 (1964).

[41]W. Kohn and L. J. Sham, "Self-consistent equations including exchange and correlation effects", Phys. Rev. **140**, A1133–A1138 (1965).

[42]J. P. Perdew, A. Ruzsinszky, J. Tao, V. N. Staroverov, G. E. Scuseria, and G. I. Csonka, "Prescription for the design and selection of density functional approximations: More constraint satisfaction with fewer fits", J. Chem. Phys. **123**, 062201 (2005).

[43]A. D. Becke, "Density-functional exchange-energy approximation with correct asymptotic behavior", Phys. Rev. A **38**, 3098–3100 (1988).

[44]J. P. Perdew, K. Burke, and M. Ernzerhof, "Generalized Gradient Approximation Made Simple", Phys. Rev. Lett. **77**, 3865–3868 (1996).

[45]C. Lee, W. Yang, and R. G. Parr, "Development of the Colle–Salvetti correlation-energy formula into a functional of the electron density", Phys. Rev. B **37**, 785 (1988).

[46]A. D. Becke, "Correlation energy of an inhomogeneous electron gas: A coordinate-space model", J. Chem. Phys. **88**, 1053–1062 (1988).

[47]Y. Zhao and D. G. Truhlar, "A new local density functional for main-group thermochemistry, transition metal bonding, thermochemical kinetics, and noncovalent interactions", J. Chem. Phys. **125**, 194101 (2006).

[48]J. Sun, B. Xiao, and A. Ruzsinszky, "Communication: Effect of the orbital-overlap dependence in the meta generalized gradient approximation", J. Chem. Phys. **137**, 051101 (2012).

[49]J. Sun, R. Haunschild, B. Xiao, I. W. Bulik, G. E. Scuseria, and J. P. Perdew, "Semilocal and hybrid meta-generalized gradient approximations based on the understanding of the kinetic-energy-density dependence", J. Chem. Phys. **138**, 044113 (2013).

[50]A. D. Becke, "Density-functional thermochemistry. III. The role of exact exchange", J. Chem. Phys. **98**, 5648–5652 (1993).

[51]A. D. Becke, "A new mixing of Hartree–Fock and local density-functional theories", J. Chem. Phys. **98**, 1372–1377 (1993).

[52]C. Adamo and V. Barone, "Toward reliable density functional methods without adjustable parameters: The PBE0 model", J. Chem. Phys. **110**, 6158–6170 (1999).

[53]J. D. Chai and M. Head-Gordon, "Long-range corrected hybrid density functionals with damped Atom–Atom dispersion corrections", Phys. Chem. Chem. Phys. **10**, 6615–6620 (2008).

[54]T. Yanai, D. P. Tew, and N. C. Handy, "A new hybrid exchange–correlation functional using the Coulomb-Attenuating method (CAM-B3LYP)", Chem. Phys. Lett. **393**, 51–57 (2004).

[55]E. Weintraub, T. M. Henderson, and G. E. Scuseria, "Long-range-corrected hybrids based on a new model exchange hole", J. Chem. Theory Comput. **5**, 754–762 (2009).

[56]S. Grimme, "Semiempirical hybrid density functional with perturbative second-order correlation", J. Chem. Phys. **124**, 034108 (2006).

[57]A. Karton, A. Tarnopolsky, J.-F. Lamère, G. C. Schatz, and J. M. L. Martin, "Highly Accurate First-Principles Benchmark Data Sets for the Parametrization and Validation of Density Functional and Other Approximate Methods. Derivation of a Robust, Generally Applicable, Double-Hybrid Functional for Thermochemistry and Thermochemical Kinetics", J. Phys. Chem. A **112**, 12868–12886 (2008).

[58]A. Dreuw and M. Head-Gordon, "Single-Reference ab Initio Methods for the Calculation of Excited States of Large Molecules", Chem. Rev. **105**, 4009–4037 (2005).

[59]P. A. M. Dirac, Proc. Cambridge Philos. Soc. **26**, 376 (1930).

[60]A. L. Fetter and J. D. Walecka, *Quantum Theory of Many-Particle Systems* (Courier Corporation, Mar. 2012).

[61]P. Ring and P. Schuck, *The nuclear many-body problem* (Springer, 2004).

[62]G. E. Scuseria, T. M. Henderson, and D. C. Sorensen, "The ground state correlation energy of the random phase approximation from a ring coupled cluster doubles approach", J. Chem. Phys. **129**, 231101 (2008).

[63]G. E. Scuseria, T. M. Henderson, and I. W. Bulik, "Particle-particle and quasiparticle random phase approximations: Connections to coupled cluster theory", J. Chem. Phys. **139**, 104113 (2013).

[64]D. Peng, S. N. Steinmann, H. van Aggelen, and W. Yang, "Equivalence of particle-particle random phase approximation correlation energy and ladder-coupled-cluster doubles", J. Chem. Phys. **139**, 104112 (2013).

[65]E. Runge and E. K. U. Gross, "Density-functional theory for time-dependent systems", Phys. Rev. Lett. **52**, 997–1000 (1984).

[66]E. K. U. Gross and N. T. Maitra, "Introduction to TDDFT", in *Fundamentals of time-dependent density functional theory*, edited by M. A. Marques, N. T. Maitra, F. M. Nogueira, E. Gross, and A. Rubio (Springer Berlin Heidelberg, Berlin, Heidelberg, 2012), pp. 53–99.

[67]M. E. Casida, "Time-dependent density functional response theory for molecules", in , edited by D. P. Chong, Recent Advances in Density Functional Methods (World Scientific, Singapore, 1995), pp. 155–192.

[68]M. Petersilka, U. J. Gossmann, and E. K. U. Gross, "Excitation energies from time-dependent density-functional theory", Phys. Rev. Lett. **76**, 1212 (1996).

[69]C. Ullrich, *Time-dependent density-functional theory: concepts and applications*, Oxford Graduate Texts (Oxford University Press, New York, 2012).

[70] A. Szabo and N. S. Ostlund, *Modern quantum chemistry* (McGraw-Hill, New York, 1989).

[71] Chr. Møller and M. S. Plesset, "Note on an approximation treatment for many-electron systems", Phys. Rev. **46**, 618–622 (1934).

[72] V. Galitskii and A. Migdal, "Application of quantum field theory methods to the many body problem", Sov. Phys. JETP **7**, 96 (1958).

[73] D. Zhang, N. Q. Su, and W. Yang, "Accurate Quasiparticle Spectra from the T-Matrix Self-Energy and the Particle–Particle Random Phase Approximation", J. Phys. Chem. Lett. **8**, 3223–3227 (2017).

[74] S. Hirata, A. E. Doran, P. J. Knowles, and J. V. Ortiz, "One-particle many-body Green's function theory: Algebraic recursive definitions, linked-diagram theorem, irreducible-diagram theorem, and general-order algorithms", J. Chem. Phys. **147**, 044108 (2017).

[75] J. Schirmer, "Beyond the random-phase approximation: A new approximation scheme for the polarization propagator", Phys. Rev. A **26**, 2395–2416 (1982).

[76] J. Schirmer, L. S. Cederbaum, and O. Walter, "New approach to the one-particle Green's function for finite Fermi systems", Phys. Rev. A **28**, 1237–1259 (1983).

[77] J. Schirmer and A. Barth, "Higher-order approximations for the particle-particle propagator", Z. Phys. A **317**, 267–279 (1984).

[78] J. Schirmer, *Many-body methods for atoms, molecules and clusters* (Springer, 2018).

[79] A. Dreuw and M. Wormit, "The algebraic diagrammatic construction scheme for the polarization propagator for the calculation of excited states", Wiley Interdiscip. Rev. Comput. Mol. Sci. **5**, 82–95 (2015).

[80] J. Schirmer, A. B. Trofimov, and G. Stelter, "A non-Dyson third-order approximation scheme for the electron propagator", J. Chem. Phys. **109**, 4734–4744 (1998).

[81] A. L. Fetter and J. D. Waleck, *Quantum theory of many particle systems* (McGraw Hill, San Francisco, 1971).

[82] S. Banerjee and A. Y. Sokolov, "Non-dyson algebraic diagrammatic construction theory for charged excitations in solids", J. Chem. Theory Comput. **18**, 5337–5349 (2022).

[83] S. Banerjee and A. Y. Sokolov, "Algebraic diagrammatic construction theory for simulating charged excited states and photoelectron spectra", J. Chem. Theory Comput. **19**, 3037–3053 (2023).

[84] P. H. P. Harbach, M. Wormit, and A. Dreuw, "The third-order algebraic diagrammatic construction method (ADC(3)) for the polarization propagator for closed-shell molecules: Efficient implementation and benchmarking", J. Chem. Phys. **141**, 064113 (2014).

[85] B. O. Roos, K. Andersson, M. P. Fulscher, P.-A. Malmqvist, and L. Serrano-Andrés, "Multiconfigurational perturbation theory: Applications in electronic spectroscopy", in, Vol. XCIII, edited by I. Prigogine and S. A. Rice, Adv. Chem. Phys. (Wiley, New York, 1996), pp. 219–331.

[86] P. Piecuch, K. Kowalski, I. S. O. Pimienta, and M. J. Mcguire, "Recent advances in electronic structure theory: Method of moments of coupled-cluster equations and renormalized coupled-cluster approaches", Int. Rev. Phys. Chem. **21**, 527–655 (2002).

[87] A. I. Krylov, "Spin-flip equation-of-motion coupled-cluster electronic structure method for a description of excited states, bond breaking, diradicals, and triradicals", Acc. Chem. Res. **39**, 83–91 (2006).

[88] K. Sneskov and O. Christiansen, "Excited state coupled cluster methods", WIREs Comput. Mol. Sci. **2**, 566–584 (2012).

[89] L. González, D. Escudero, and L. Serrano-Andrès, "Progress and challenges in the calculation of electronic excited states", ChemPhysChem **13**, 28–51 (2012).

[90] A. D. Laurent and D. Jacquemin, "TD-DFT benchmarks: A review", Int. J. Quantum Chem. **113**, 2019–2039 (2013).

[91] C. Adamo and D. Jacquemin, "The calculations of excited-state properties with time-dependent density functional theory", Chem. Soc. Rev. **42**, 845–856 (2013).

[92] S. Ghosh, P. Verma, C. J. Cramer, L. Gagliardi, and D. G. Truhlar, "Combiningwave function methods with density functional theory for excited states", Chem. Rev. **118**, 7249–7292 (2018).

[93] P. F. Loos, A. Scemama, and D. Jacquemin, "The quest for highly-accurate excitation energies: a computational perspective", J. Phys. Chem. Lett. **11**, 2374–2383 (2020).

[94] D. Casanova and A. I. Krylov, "Spin-flip methods in quantum chemistry", Phys. Chem. Chem. Phys. **22**, 4326 (2020).

[95] E. E. Salpeter and H. A. Bethe, "A relativistic equation for bound-state problems", Phys. Rev. **84**, 1232 (1951).

[96] L. J. Sham and T. M. Rice, "Many-particle derivation of the effective-mass equation for the wannier exciton", Phys. Rev. **144**, 708–714 (1966).

[97] C. Delerue, M. Lannoo, and G. Allan, "Excitonic and quasiparticle gaps in si nanocrystals", Phys. Rev. Lett. **84**, 2457–2460 (2000).

[98] S. Albrecht, L. Reining, R. Del Sole, and G. Onida, "Ab initio calculation of excitonic effects in the optical spectra of semiconductors", Phys. Rev. Lett. **80**, 4510–4513 (1998).

[99] M. Rohlfing and S. G. Louie, "Electron-hole excitations in semiconductors and insulators", Phys. Rev. Lett. **81**, 2312–2315 (1998).

[100] L. X. Benedict, E. L. Shirley, and R. B. Bohn, "Optical absorption of insulators and the electron-hole interaction: An ab initio calculation", Phys. Rev. Lett. **80**, 4514–4517 (1998).

[101] J.-W. van der Horst, P. A. Bobbert, M. A. J. Michels, G. Brocks, and P. J. Kelly, "Ab initio calculation of the electronic and optical excitations in polythiophene: effects of intra- and interchain screening", Phys. Rev. Lett. **83**, 4413–4416 (1999).

[102] G. Onida, L. Reining, and A. Rubio, "Electronic excitations: Density-functional versus many-body green's function approaches", Rev. Mod. Phys. **74**, 601–659 (2002).

[103] R. M. Martin, L. Reining, and D. M. Ceperley, *Interacting electrons: Theory and computational approaches* (Cambridge University Press, 2016).

[104] D. Golze, M. Dvorak, and P. Rinke, "The GW compendium: A practical guide to theoretical photoemission spectroscopy", Front. Chem. **7**, 377 (2019).

[105] M. Rohlfing and S. G. Louie, "Optical excitations in conjugated polymers", Phys. Rev. Lett. **82**, 1959–1962 (1999).

[106]J.-W. van der Horst, P. A. Bobbert, M. A. J. Michels, G. Brocks, and P. J. Kelly, "Ab initio calculation of the electronic and optical excitations in polythiophene: Effects of intra- and interchain screening", Phys. Rev. Lett. **83**, 4413–4416 (1999).

[107]P. Puschnig and C. Ambrosch-Draxl, "Suppression of electron-hole correlations in 3D polymer materials", Phys. Rev. Lett. **89**, 056405 (2002).

[108]M. L. Tiago, J. E. Northrup, and S. G. Louie, "Ab initio calculation of the electronic and optical properties of solid pentacene", Phys. Rev. B **67**, 115212 (2003).

[109]P. Boulanger, D. Jacquemin, I. Duchemin, and X. Blase, "Fast and accurate electronic excitations in cyanines with the many-body bethe-salpeter approach", J. Chem. Theory Comput. **10**, 1212–1218 (2014).

[110]D. Jacquemin, I. Duchemin, and X. Blase, "Benchmarking the Bethe–Salpeter Formalism on a Standard Organic Molecular Set", J. Chem. Theory Comput. **11**, 3290–3304 (2015).

[111]F. Bruneval, S. M. Hamed, and J. B. Neaton, "A systematic benchmark of the ab initio Bethe-Salpeter equation approach for low-lying optical excitations of small organic molecules", J. Chem. Phys. **142**, 244101 (2015).

[112]D. Jacquemin, I. Duchemin, and X. Blase, "0–0 energies using hybrid schemes: Benchmarks of TD-DFT, CIS(D), ADC(2), CC2, and BSE/GW formalisms for 80 real-life compounds", J. Chem. Theory Comput. **11**, 5340–5359 (2015).

[113]D. Hirose, Y. Noguchi, and O. Sugino, "All-electron GW+Bethe-Salpeter calculations on small molecules", Phys. Rev. B **91**, 205111 (2015).

[114]D. Jacquemin, I. Duchemin, and X. Blase, "Is the Bethe–Salpeter formalism accurate for excitation energies? Comparisons with TD-DFT, CASPT2, and EOM-CCSD", J. Phys. Chem. Lett. **8**, 1524–1529 (2017).

[115]D. Jacquemin, I. Duchemin, A. Blondel, and X. Blase, "Benchmark of bethe-salpeter for triplet excited-states", J. Chem. Theory Comput. **13**, 767–783 (2017).

[116]T. Rangel, S. M. Hamed, F. Bruneval, and J. B. Neaton, "An assessment of low-lying excitation energies and triplet instabilities of organic molecules with an *ab initio* Bethe-Salpeter equation approach and the Tamm-Dancoff approximation", J. Chem. Phys. **146**, 194108 (2017).

[117]K. Krause and W. Klopper, "Implementation of the Bethe-Salpeter equation in the TURBOMOLE program", J. Comput. Chem. **38**, 383–388 (2017).

[118]X. Gui, C. Holzer, and W. Klopper, "Accuracy assessment of GW starting points for calculating molecular excitation energies using the Bethe–Salpeter formalism", J. Chem. Theory Comput. **14**, 2127–2136 (2018).

[119]C. Liu, J. Kloppenburg, Y. Yao, X. Ren, H. Appel, Y. Kanai, and V. Blum, "All-electron ab initio Bethe-Salpeter equation approach to neutral excitations in molecules with numeric atom-centered orbitals", J. Chem. Phys. **152**, 044105 (2020).

[120]C. Holzer and W. Klopper, "Communication: A hybrid Bethe–Salpeter/time-dependent density-functional-theory approach for excitation energies", J. Chem. Phys. **149**, 101101 (2018).

[121]C. Holzer, X. Gui, M. E. Harding, G. Kresse, T. Helgaker, and W. Klopper, "Bethe–Salpeter correlation energies of atoms and molecules", J. Chem. Phys. **149**, 144106 (2018).

[122]F. Bruneval, T. Rangel, S. M. Hamed, M. Shao, C. Yang, and J. B. Neaton, "Molgw 1: Many-Body perturbation theory software for atoms, molecules, and clusters", Comput. Phys. Commun. **208**, 149–161 (2016).

[123]N. T. Maitra, R. J. C. F. Zhang, and K. Burke, "Double excitations within time-dependent density functional theory linear response", J. Chem. Phys. **120**, 5932–5937 (2004).

[124]R. J. Cave, F. Zhang, N. T. Maitra, and K. Burke, "A dressed TDDFT treatment of the 21Ag states of butadiene and hexatriene", Chem. Phys. Lett. **389**, 39–42 (2004).

[125]B. Saha, M. Ehara, and H. Nakatsuji, "Singly and doubly excited states of butadiene, acrolein, and glyoxal: Geometries and electronic spectra", J. Chem. Phys. **125**, 014316 (2006).

[126]M. A. Watson and G. K.-L. Chan, "Excited states of butadiene to chemical accuracy: Reconciling theory and experiment", J. Chem. Theory Comput. **8**, 4013–4018 (2012).

[127]Y. Shu and D. G. Truhlar, "Doubly Excited Character or Static Correlation of the Reference State in the Controversial 2 ^{1} A $_g$ State of *trans* -Butadiene?", J. Am. Chem. Soc. **139**, 13770–13778 (2017).

[128]G. M. Barca and P.-F. Loos, "Recurrence Relations for Four-Electron Integrals Over Gaussian Basis Functions", in *Adv. Quantum chem.* Vol. 76 (Elsevier, 2018), pp. 147–165.

[129]G. M. J. Barca, A. T. B. Gilbert, and P. M. W. Gill, "Simple Models for Difficult Electronic Excitations", J. Chem. Theory. Comput. **14**, 1501–1509 (2018).

[130]P.-F. Loos, M. Boggio-Pasqua, A. Scemama, M. Caffarel, and D. Jacquemin, "Reference energies for double excitations", J. Chem. Theory Comput. **15**, 1939–1956 (2019).

[131]M. E. Casida, "Propagator corrections to adiabatic time- dependent density-functional theory linear response theory", J. Chem. Phys. **122**, 054111 (2005).

[132]M. Huix-Rotllant, "Improved correlation kernels for linear-response time-dependent density-functional theory", PhD thesis (Université de Grenoble, 2011).

[133]P.-F. Loos, A. Scemama, M. Boggio-Pasqua, and D. Jacquemin, "Mountaineering strategy to excited states: Highly accurate energies and benchmarks for exotic molecules and radicals", J. Chem. Theory Comput. **16**, 3720–3736 (2020).

[134]B. G. Levine, C. Ko, J. Quenneville, and T. J. Martinez, "Conical intersections and double excitations in time-dependent density functional theory", Mol. Phys. **104**, 1039–1051 (2006).

[135]D. J. Tozer and N. C. Handy, "On the determination of excitation energies using density functional theory", Phys. Chem. Chem. Phys. **2**, 2117–2121 (2000).

[136]P. Elliott, S. Goldson, C. Canahui, and N. T. Maitra, "Perspectives on double-excitations in TDDFT", Chem. Phys. **391**, 110–119 (2011).

[137]N. T. Maitra, "Memory: History , initial-state dependence , and double-excitations", in *Fundamentals of time-dependent density functional theory*, Vol. 837, edited by M. A. Marques, N. T. Maitra, F. M. Nogueira, E. Gross, and A. Rubio (Springer Berlin Heidelberg, Berlin, Heidelberg, 2012), pp. 167–184.

[138]N. T. Maitra, "Fundamental aspects of time-dependent density functional theory", J. Chem. Phys. **144**, 220901 (2016).

[139]R. Martin, L. Reining, and D. Ceperley, *Interacting electrons: Theory and computational approaches* (Cambridge University Press, 2016).

[140]P. Romaniello, D. Sangalli, J. A. Berger, F. Sottile, L. G. Molinari, L. Reining, and G. Onida, "Double excitations in finite systems", J. Chem. Phys. **130**, 044108 (2009).

[141]D. Sangalli, P. Romaniello, G. Onida, and A. Marini, "Double excitations in correlated systems: A many–body approach", J. Chem. Phys. **134**, 034115 (2011).

[142]J. Authier and P.-F. Loos, "Dynamical kernels for optical excitations", J. Chem. Phys. **153**, 184105 (2020).

[143]P. F. Loos, A. Scemama, A. Blondel, Y. Garniron, M. Caffarel, and D. Jacquemin, "A mountaineering strategy to excited states: Highly-accurate reference energies and benchmarks", J. Chem. Theory Comput. **14**, 4360 (2018).

[144]P. F. Loos, F. Lipparini, M. Boggio-Pasqua, A. Scemama, and D. Jacquemin, "A mountaineering strategy to excited states: Highly-accurate energies and benchmarks for medium sized molecules", J. Chem. Theory Comput. **16**, 1711–1741 (2020).

[145]M. Véril, A. Scemama, M. Caffarel, F. Lipparini, M. Boggio-Pasqua, D. Jacquemin, and P.-F. Loos, "QUESTDB: A database of highly accurate excitation energies for the electronic structure community", WIREs Computational Molecular Science **11**, e1517 (2021).

[146]O. Christiansen, H. Koch, and P. Jørgensen, "Response functions in the CC3 iterative triple excitation model", J. Chem. Phys. **103**, 7429–7441 (1995).

[147]H. Koch, O. Christiansen, P. Jorgensen, A. M. Sanchez de Merás, and T. Helgaker, "The CC3 model: An iterative coupled cluster approach including connected triples", J. Chem. Phys. **106**, 1808–1818 (1997).

[148]S. A. Kucharski and R. J. Bartlett, "Recursive intermediate factorization and complete computational linearization of the coupled-cluster single, double, triple, and quadruple excitation equations", Theor. Chim. Acta **80**, 387–405 (1991).

[149]M. Kállay and J. Gauss, "Calculation of excited-state properties using general coupled-cluster and configuration-interaction models", J. Chem. Phys. **121**, 9257–9269 (2004).

[150]S. Hirata, M. Nooijen, and R. J. Bartlett, "High-order determinantal equation-of-motion coupled-cluster calculations for electronic excited states", Chem. Phys. Lett. **326**, 255–262 (2000).

[151]S. Hirata, "Higher-order equation-of-motion coupled-cluster methods", J. Chem. Phys. **121**, 51–59 (2004).

[152]A. I. Krylov, "Size-consistent wave functions for bond-breaking: The equation-of-motion spin-flip model", Chem. Phys. Lett. **338**, 375–384 (2001).

[153]A. I. Krylov, "Spin-flip configuration interaction: An electronic structure model that is both variational and size-consistent", Chem. Phys. Lett. **350**, 522–530 (2001).

[154]A. I. Krylov and C. D. Sherrill, "Perturbative corrections to the equation-of-motion Spin–Flip self-consistent field model: Application to bond-breaking and equilibrium properties of diradicals", J. Chem. Phys. **116**, 3194–3203 (2002).

[155]H. Bethe, "Zur theorie der metalle", Z Phys. **71**, 205–226 (1931).

[156]T.-I. Shibuya and V. McKoy, "Higher Random-Phase Approximation as an Approximation to the Equations of Motion", Phys. Rev. A **2**, 2208–2218 (1970).

[157]A. I. Krylov, "Equation-of-motion coupled-cluster methods for open-shell and electronically excited species: The hitchhiker's guide to fock space", Annu. Rev. Phys. Chem. **59**, 433–462 (2008).

[158]Y. Yang, H. van Aggelen, and W. Yang, "Double, Rydberg and charge transfer excitations from pairing matrix fluctuation and particle-particle random phase approximation", J. Chem. Phys. **139**, 224105 (2013).

[159]Z.-H. Yang, J. R. Trail, A. Pribram-Jones, K. Burke, R. J. Needs, and C. A. Ullrich, "Exact and approximate Kohn-Sham potentials in ensemble density-functional theory", Phys. Rev. A **90**, 042501 (2014).

[160]D. Peng, Y. Yang, P. Zhang, and W. Yang, "Restricted second random phase approximations and Tamm-Dancoff approximations for electronic excitation energy calculations", J. Chem. Phys. **141**, 214102 (2014).

[161]D. Zhang and W. Yang, "Accurate and efficient calculation of excitation energies with the active-space particle-particle random phase approximation", J. Chem. Phys. **145**, 144105 (2016).

[162]C. Sutton, Y. Yang, D. Zhang, and W. Yang, "Single, double electronic excitations and exciton effective conjugation lengths in π-Conjugated systems", J. Phys. Chem. Lett. **9**, 4029–4036 (2018).

[163]A. I. Krylov, "Spin-contamination of coupled-cluster wave functions", J. Chem. Phys. **113**, 6052–6062 (2000).

[164]J. S. Sears, C. D. Sherrill, and A. I. Krylov, "A spin-complete version of the spin-flip approach to bond breaking: What is the impact of obtaining spin eigenfunctions?", J. Chem. Phys. **118**, 9084–9094 (2003).

[165]D. Casanova and M. Head-Gordon, "The spin-flip extended single excitation configuration interaction method", J. Chem. Phys. **129**, 064104 (2008).

[166]M. Huix-Rotllant, B. Natarajan, A. Ipatov, C. Muhavini Wawire, T. Deutsch, and M. E. Casida, "Assessment of noncollinear spin-flip Tamm–Dancoff approximation time-dependent density-functional theory for the photochemical ring-opening of oxirane", Phys. Chem. Chem. Phys. **12**, 12811 (2010).

[167]Z. Li and W. Liu, "Spin-adapted open-shell random phase approximation and time-dependent density functional theory. I. Theory", J. Chem. Phys. **133**, 064106 (2010).

[168]Z. Li, W. Liu, Y. Zhang, and B. Suo, "Spin-adapted open-shell time-dependent density functional theory. II. Theory and pilot application", J. Chem. Phys. **134**, 134101 (2011).

[169]Z. Li and W. Liu, "Spin-adapted open-shell time-dependent density functional theory. III. An even better and simpler formulation", J. Chem. Phys. **135**, 194106 (2011).

[170]X. Zhang and J. M. Herbert, "Analytic derivative couplings in time-dependent density functional theory: Quadratic response theory versus pseudo-wavefunction approach", J. Chem. Phys. **142**, 064109 (2015).

[171]J. Lee and M. Head-Gordon, "Regularized orbital-optimized second-order Møller–Plesset perturbation theory: A reliable fifth-order-scaling electron correlation model with orbital energy dependent regularizers", J. Chem. Theory Comput., ASAP article (2018).

[172]S. V. Levchenko and A. I. Krylov, "Equation-of-motion spin-flip coupled-cluster model with single and double substitutions: Theory and application to cyclobutadiene", J. Chem. Phys. **120**, 175–185 (2004).

[173]P. U. Manohar and A. I. Krylov, "A noniterative perturbative triples correction for the spin-flipping and spin-conserving equation-of-motion coupled-cluster methods with single and double substitutions", J. Chem. Phys. **129**, 194105 (2008).

[174]D. Casanova, L. V. Slipchenko, A. I. Krylov, and M. Head-Gordon, "Double spin-flip approach within equation-of-motion coupled cluster and configuration interaction formalisms: Theory, implementation, and examples", J. Chem. Phys. **130**, 044103 (2009).

[175]A. K. Dutta, S. Pal, and D. Ghosh, "Perturbative approximations to single and double spin flip equation of motion coupled cluster singles doubles methods", J. Chem. Phys. **139**, 124116 (2013).

[176]J. Mato and M. S. Gordon, "A general spin-complete spin-flip configuration interaction method", Phys. Chem. Chem. Phys. **20**, 2615–2626 (2018).

[177]D. Casanova and M. Head-Gordon, "Restricted active space spin-flip configuration interaction approach: theory, implementation and examples", Phys. Chem. Chem. Phys. **11**, 9779–9790 (2009).

[178]Y. Shao, M. Head-Gordon, and A. I. Krylov, "The spin–flip approach within time-dependent density functional theory: Theory and applications to diradicals", J. Chem. Phys. **118**, 4807–4818 (2003).

[179]F. Wang and T. Ziegler, "Time-dependent density functional theory based on a noncollinear formulation of the exchange-correlation potential", J. Chem. Phys. **121**, 12191 (2004).

[180]Y. A. Bernard, Y. Shao, and A. I. Krylov, "General formulation of spin-flip time-dependent density functional theory using non-collinear kernels: Theory, implementation, and benchmarks", J. Chem. Phys. **136**, 204103 (2012).

[181]D. Lefrancois, M. Wormit, and A. Dreuw, "Adapting algebraic diagrammatic construction schemes for the polarization propagator to problems with multi-reference electronic ground states exploiting the spin-flip ansatz", J. Chem. Phys. **143**, 124107 (2015).

[182]D. Lefrancois, D. R. Rehn, and A. Dreuw, "Accurate adiabatic singlet-triplet gaps in atoms and molecules employing the third-order spin-flip algebraic diagrammatic construction scheme for the polarization propagator", J. Chem. Phys. **145**, 084102 (2016).

[183]N. J. Mayhall and M. Head-Gordon, "Increasing spin-flips and decreasing cost: Perturbative corrections for external singles to the complete active space spin flip model for low-lying excited states and strong correlation", J. Chem. Phys. **141**, 044112 (2014).

[184]N. J. Mayhall, M. Goldey, and M. Head-Gordon, "A quasidegenerate second-order perturbation theory approximation to RAS-nSF for excited states and strong correlations", J. Chem. Phys. **10**, 589–599 (2014).

[185]F. Bell, P. M. Zimmerman, D. Casanova, M. Goldey, and M. Head-Gordon, "Restricted active space spin-flip (RAS-SF) with arbitrary number of spin-flips", Phys. Chem. Chem. Phys. **15**, 358–366 (2013).

[186]N. J. Mayhall, P. R. Horn, E. J. Sundstrom, and M. Head-Gordon, "Spin–flip non-orthogonal configuration interaction: a variational and almost black-box method for describing strongly correlated molecules", Phys. Chem. Chem. Phys. **16**, 22694–22705 (2014).

[187] A. A. Golubeva, A. V. Nemukhin, S. J. Klippenstein, L. B. Harding, and A. I. Krylov, "Performance of the spin-flip and multireference methods for bond breaking in hydrocarbons: A benchmark study", J. Phys. Chem. A **111**, 13264–13271 (2007).

[188] L. V. Slipchenko and A. I. Krylov, "Singlet-triplet gaps in diradicals by the spin-flip approach: A benchmark study", J. Chem. Phys. **117**, 4694–4708 (2002).

[189] T. Wang and A. I. Krylov, "The effect of substituents on electronic states' ordering in meta-xylylene diradicals: Qualitative insights from quantitative studies", J. Chem. Phys. **123**, 104304 (2005).

[190] L. V. Slipchenko and A. I. Krylov, "Electronic structure of the trimethylenemethane diradical in its ground and electronically excited states: Bonding, equilibrium geometries, and vibrational frequencies", J. Chem. Phys. **118**, 6874–6883 (2003).

[191] Z. Rinkevicius and H. Ågren, "Spin-flip time dependent density functional theory for singlet–triplet splittings in sigma-sigma-biradicals", Chem. Phys. Lett. **491**, 132–135 (2010).

[192] C. U. Ibeji and D. Ghosh, "Singlet–triplet gaps in polyacenes: a delicate balance between dynamic and static correlations investigated by spin–flip methods", Phys. Chem. Chem. Phys. **17**, 9849–9856 (2015).

[193] E. Hossain, S. M. Deng, S. Gozem, A. I. Krylov, X.-B. Wang, and P. G. Wenthold, "Photoelectron spectroscopy study of quinonimides", J. Am. Chem. Soc. **139**, 11138–11148 (2017).

[194] N. Orms, D. R. Rehn, A. Dreuw, and A. I. Krylov, "Characterizing bonding patterns in diradicals and triradicals by density-based wave function analysis: A uniform approach", J. Chem. Theory Comput. **14**, 638–648 (2018).

[195] A. R. Luxon, N. Orms, R. Kanters, A. I. Krylov, and C. A. Parish, "An ab initio exploration of the bergman cyclization", J. Phys. Chem. A **122**, 420–430 (2018).

[196] D. Casanova, "Avoided crossings, conical intersections, and low-lying excited states with a single reference method: The restricted active space spin-flip configuration interaction approach", J. Chem. Phys. **137**, 084105 (2012).

[197] S. Gozem, F. Melaccio, R. Lindh, A. I. Krylov, A. A. Granovsky, C. Angeli, and M. Olivucci, "Mapping the Excited State Potential Energy Surface of a Retinal Chromophore Model with Multireference and Equation-of-Motion Coupled-Cluster Methods", J. Chem. Theory Comput. **9**, 4495–4506 (2013).

[198] A. Nikiforov, J. A. Gamez, W. Thiel, M. Huix-Rotllant, and M. Filatov, "Assessment of approximate computational methods for conical intersections and branching plane vectors in organic molecules", J. Chem. Phys. **141**, 124122 (2014).

[199] G. Strinati, "Dynamical shift and broadening of core excitons in semiconductors", Phys. Rev. Lett. **49**, 1519 (1982).

[200] M. Rohlfing and S. G. Louie, "Electron-hole excitations and optical spectra from first principles", Phys. Rev. B **62**, 4927–4944 (2000).

[201] Y. Ma, M. Rohlfing, and C. Molteni, "Excited states of biological chromophores studied using many-body perturbation theory: Effects of resonant-antiresonant coupling and dynamical screening", Phys. Rev. B **80**, 241405 (2009).

[202] Y. Ma, M. Rohlfing, and C. Molteni, "Modeling the excited states of biological chromophores within many-body green's function theory", J. Chem. Theory. Comput. **6**, 257–265 (2009).

[203]B. Baumeier, D. Andrienko, Y. Ma, and M. Rohlfing, "Excited states of dicyanovinyl-substituted oligothiophenes from many-body green's functions theory", J. Chem. Theory Comput. **8**, 997–1002 (2012).

[204]T. Lettmann and M. Rohlfing, "Electronic excitations of polythiophene within many-body perturbation theory with and without the tamm-dancoff approximation", J. Chem. Theory Comput. **15**, 4547–4554 (2019).

[205]R. G. Parr and W. Yang, *Density-functional theory of atoms and molecules* (Oxford, Clarendon Press, 1989).

[206]P. M. W. Gill, "Molecular integrals over gaussian basis functions", Adv. Quantum Chem. **25**, 141–205 (1994).

[207]G. Strinati, H. J. Mattausch, and W. Hanke, "Dynamical correlation effects on the quasiparticle bloch states of a covalent crystal", Phys. Rev. Lett. **45**, 290–294 (1980).

[208]M. S. Hybertsen and S. G. Louie, "First-Principles Theory of Quasiparticles: Calculation of Band Gaps in Semiconductors and Insulators", Phys. Rev. Lett. **55**, 1418–1421 (1985).

[209]M. S. Hybertsen and S. G. Louie, "Electron correlation in semiconductors and insulators: Band gaps and quasiparticle energies", Phys. Rev. B **34**, 5390–5413 (1986).

[210]R. W. Godby, M. Schlüter, and L. J. Sham, "Self-energy operators and exchange-correlation potentials in semiconductors", Phys. Rev. B **37**, 10159–10175 (1988).

[211]W. von der Linden and P. Horsch, "Precise quasiparticle energies and hartree-fock bands of semiconductors and insulators", Phys. Rev. B **37**, 8351–8362 (1988).

[212]J. E. Northrup, M. S. Hybertsen, and S. G. Louie, "Many-body calculation of the surface-state energies for Si(111)2××1", Phys. Rev. Lett. **66**, 500–503 (1991).

[213]X. Blase, X. Zhu, and S. G. Louie, "Self-energy effects on the surface-state energies of H-Si(111)1×1", Phys. Rev. B **49**, 4973–4980 (1994).

[214]M. Rohlfing, P. Krüger, and J. Pollmann, "Efficient scheme for GW quasiparticle band-structure calculations with applications to bulk si and to the Si(001)-(2×1) surface", Phys. Rev. B **52**, 1905–1917 (1995).

[215]M. Shishkin and G. Kresse, "Self-consistent GW calculations for semiconductors and insulators", Phys. Rev. B **75**, 235102 (2007).

[216]P. F. Loos, P. Romaniello, and J. A. Berger, "Green functions and self-consistency: Insights from the spherium model", J. Chem. Theory Comput. **14**, 3071–3082 (2018).

[217]X. Blase and C. Attaccalite, "Charge-transfer excitations in molecular donor-acceptor complexes within the many-body bethe-salpeter approach", Appl. Phys. Lett. **99**, 171909 (2011).

[218]C. Faber, C. Attaccalite, V. Olevano, E. Runge, and X. Blase, "First-principles GW calculations for DNA and RNA nucleobases", Phys. Rev. B **83**, 115123 (2011).

[219]T. Rangel, S. M. Hamed, F. Bruneval, and J. B. Neaton, "Evaluating the GW approximation with CCSD(T) for charged excitations across the oligoacenes", J. Chem. Theory Comput. **12**, 2834–2842 (2016).

[220]S. V. Faleev, M. van Schilfgaarde, and T. Kotani, "All-Electron Self-Consistent GW Approximation: Application to Si, MnO, and NiO", Phys. Rev. Lett. **93**, 126406 (2004).

[221]M. van Schilfgaarde, T. Kotani, and S. Faleev, "Quasiparticle Self-Consistent GW Theory", Phys. Rev. Lett. **96**, 226402 (2006).

[222]T. Kotani, M. van Schilfgaarde, and S. V. Faleev, "Quasiparticle self-consistent GW method: A basis for the independent-particle approximation", Phys. Rev. B **76**, 165106 (2007).

[223]S.-H. Ke, "All-electron GW methods implemented in molecular orbital space: Ionization energy and electron affinity of conjugated molecules", Phys. Rev. B **84**, 205415 (2011).

[224]F. Kaplan, M. E. Harding, C. Seiler, F. Weigend, F. Evers, and M. J. van Setten, "Quasi-Particle Self-Consistent *GW* for Molecules", J. Chem. Theory Comput. **12**, 2528–2541 (2016).

[225]W. Hanke and L. J. Sham, "Many-particle effects in the optical spectrum of a semiconductor", Phys. Rev. B **21**, 4656 (1980).

[226]F. Sottile, V. Olevano, and L. Reining, "Parameter-free calculation of response functions in time-dependent density-functional theory", Phys. Rev. Lett. **91**, 056402 (2003).

[227]P. Myöhänen, A. Stan, G. Stefanucci, and R. van Leeuwen, "A many-body approach to quantum transport dynamics: Initial correlations and memory effects", Europhys. Lett. **84**, 67001 (2008).

[228]N. Sakkinen, M. Manninen, and R. van Leeuwen, "The Kadanoff-Baym approach to double excitations in finite systems", New J. Phys. **14**, 013032 (2012).

[229]D. Zhang, S. N. Steinmann, and W. Yang, "Dynamical second-order Bethe-Salpeter equation kernel: A method for electronic excitation beyond the adiabatic approximation", J. Chem. Phys. **139**, 154109 (2013).

[230]E. Rebolini and J. Toulouse, "Range-separated time-dependent density-functional theory with a frequency-dependent second-order Bethe-Salpeter correlation kernel", J. Chem. Phys. **144**, 094107 (2016).

[231]V. Olevano, J. Toulouse, and P. Schuck, "A formally exact one-frequency-only Bethe-Salpeter-like equation. Similarities and differences between GW+BSE and self-consistent RPA", J. Chem. Phys. **150**, 084112 (2019).

[232]M. E. Casida and M. Huix-Rotllant, "Many-Body Perturbation Theory (MBPT) and Time-Dependent Density-Functional Theory (TD-DFT): MBPT Insights About What Is Missing In, and Corrections To, the TD-DFT Adiabatic Approximation", Top. Curr. Chem. **368**, 1–60 (2016).

[233]D. Kánnár and P. G. Szalay, "Benchmarking coupled cluster methods on valence singlet excited states", J. Chem. Theory Comput. **10**, 3757–3765 (2014).

[234]A. Chrayteh, A. Blondel, P. F. Loos, and D. Jacquemin, "A mountaineering strategy to excited states: Highly-accurate oscillator strengths and dipole moments of small molecules", J. Chem. Theory Comput. **17**, 416–438 (2021).

[235]R. Sarkar, M. Boggio-Pasqua, P. F. Loos, and D. Jacquemin, "Benchmark of TD-DFT and wavefunction methods for oscillator strengths and excited-state dipole moments", J. Chem. Theory Comput. **17**, 1117–1132 (2021).

[236]M. Véril, P. Romaniello, J. A. Berger, and P. F. Loos, "Unphysical discontinuities in GW methods", J. Chem. Theory Comput. **14**, 5220 (2018).

[237]J. A. Berger, P.-F. Loos, and P. Romaniello, "Potential energy surfaces without unphysical discontinuities: the Coulomb-hole plus screened exchange approach", J. Chem. Theory Comput. **17**, 191 (2020).

[238]T. Stein, L. Kronik, and R. Baer, "Reliable prediction of charge transfer excitations in molecular complexes using time-dependent density functional theory", J. Am. Chem. Soc. **131**, 2818–2820 (2009).

[239]T. Stein, H. Eisenberg, L. Kronik, and R. Baer, "Fundamental gaps in finite systems from eigenvalues of a generalized kohn-sham method", Phys. Rev. Lett. **105**, 266802 (2010).

[240]S. Refaely-Abramson, S. Sharifzadeh, N. Govind, J. Autschbach, J. B. Neaton, R. Baer, and L. Kronik, "Quasiparticle spectra from a nonempirical optimally tuned range-separated hybrid density functional", Phys. Rev. Lett. **109**, 226405 (2012).

[241]L. Kronik, T. Stein, S. Refaely-Abramson, and R. Baer, "Excitation gaps of finite-sized systems from optimally tuned range-separated hybrid functionals", J. Chem. Theory Comput. **8**, 1515–1531 (2012).

[242]P. F. Loos, *QuAcK: a software for emerging quantum electronic structure methods*, 2019.

[243]Y. Shao, L. Fusti-Molnar, Y. Jung, J. Kussmann, C. Ochsenfeld, S. T. Brown, A. T. B. Gilbert, L. V. Slipchenko, S. V. Levchenko, D. P. O'Neill, R. A. Distasio Jr., R. C. Lochan, T. Wang, G. J. O. Beran, N. A. Besley, J. M. Herbert, C. Y. Lin, T. Van Voorhis, S. H. Chien, A. Sodt, R. P. Steele, V. A. Rassolov, P. E. Maslen, P. P. Korambath, R. D. Adamson, B. Austin, J. Baker, E. F. C. Byrd, H. Dachsel, R. J. Doerksen, A. Dreuw, B. D. Dunietz, A. D. Dutoi, T. R. Furlani, S. R. Gwaltney, A. Heyden, S. Hirata, C.-P. Hsu, G. Kedziora, R. Z. Khalliulin, P. Klunzinger, A. M. Lee, M. S. Lee, W. Liang, I. Lotan, N. Nair, B. Peters, E. I. Proynov, P. A. Pieniazek, Y. M. Rhee, J. Ritchie, E. Rosta, C. D. Sherrill, A. C. Simmonett, J. E. Subotnik, H. L. Woodcock III, W. Zhang, A. T. Bell, A. K. Chakraborty, D. M. Chipman, F. J. Keil, A. Warshel, W. J. Hehre, H. F. Schaefer III, J. Kong, A. I. Krylov, P. M. W. Gill, and M. Head-Gordon, "Advances in methods and algorithms in a modern quantum chemistry program package", PCCP **8**, 3172–3191 (2006).

[244]J. D. Chai and M. Head-Gordon, "Systematic optimization of long-range corrected hybrid density functionals", J. Chem. Phys. **128**, 084106 (2008).

[245]H. Koch, H. J. A. Jensen, P. Jorgensen, and T. Helgaker, "Excitation energies from the coupled cluster singles and doubles linear response function (CCSDLR). Applications to Be, CH^+, CO, and H_2O", J. Chem. Phys. **93**, 3345–3350 (1990).

[246]J. F. Stanton and R. J. Bartlett, "The equation of motion coupled-cluster method. A systematic biorthogonal approach to molecular excitation energies, transition probabilities, and excited state properties", J. Chem. Phys. **98**, 7029–7039 (1993).

[247]H. Koch, R. Kobayashi, A. Sanchez de Merás, and P. Jorgensen, "Calculation of size-intensive transition moments from the coupled cluster singles and doubles linear response function", J. Chem. Phys. **100**, 4393–4400 (1994).

[248]M. J. Frisch, G. W. Trucks, H. B. Schlegel, G. E. Scuseria, M. A. Robb, J. R. Cheeseman, G. Scalmani, V. Barone, B. Mennucci, G. A. Petersson, H. Nakatsuji, M. Caricato, X. Li, H. P. Hratchian, A. F. Izmaylov, J. Bloino, G. Zheng, J. L. Sonnenberg, M. Hada, M. Ehara, K. Toyota, R. Fukuda, J. Hasegawa, M. Ishida, T. Nakajima, Y. Honda, O. Kitao, H. Nakai, T. Vreven, J. A. Montgomery Jr., J. E. Peralta, F. Ogliaro, M. Bearpark, J. J. Heyd, E. Brothers, K. N. Kudin, V. N. Staroverov, R. Kobayashi, J. Normand, K. Raghavachari, A. Rendell, J. C. Burant, S. S. Iyengar, J. Tomasi, M. Cossi, N. Rega, J. M. Millam, M. Klene, J. E. Knox, J. B. Cross, V. Bakken, C. Adamo, J. Jaramillo, R. Gomperts, R. E. Stratmann, O. Yazyev, A. J. Austin, R. Cammi, C. Pomelli, J. W. Ochterski, R. L. Martin, K. Morokuma, V. G. Zakrzewski, G. A. Voth,

P. Salvador, J. J. Dannenberg, S. Dapprich, A. D. Daniels, Ö. Farkas, J. B. Foresman, J. V. Ortiz, J. Cioslowski, and D. J. Fox, *Gaussin 09 Revision E.01*.

[249]F. Caruso, D. R. Rohr, M. Hellgren, X. Ren, P. Rinke, A. Rubio, and M. Scheffler, "Bond Breaking and Bond Formation: How Electron Correlation is Captured in Many-Body Perturbation Theory and Density-Functional Theory", Phys. Rev. Lett. **110**, 146403 (2013).

[250]G. M. J. Barca, A. T. B. Gilbert, and P. M. W. Gill, "Hartree–Fock description of excited states of H2", J. Chem. Phys. **141**, 111104 (2014).

[251]S. Vuckovic and P. Gori-Giorgi, "Simple fully nonlocal density functionals for electronic repulsion energy", J. Phys. Chem. Lett. **8**, 2799–2805 (2017).

[252]J. Li and V. Olevano, "Hydrogen-molecule spectrum by the many-body GW approximation and the Bethe-Salpeter equation", Phys. Rev. A **103**, 012809 (2021).

[253]A. J. Cohen, P. Mori-Sánchez, and W. Yang, "Fractional spins and static correlation error in density functional theory", J. Chem. Phys. **129**, 121104 (2008).

[254]A. J. Cohen, P. Mori-Sánchez, and W. Yang, "Insights into current limitations of density functional theory", Science **321**, 792–794 (2008).

[255]A. J. Cohen, P. Mori-Sánchez, and W. Yang, "Challenges for Density Functional Theory", Chem. Rev. **112**, 289–320 (2012).

[256]C. Coulson and I Fischer, "XXXIV. Notes on the molecular orbital treatment of the hydrogen molecule", Philos. Mag. **40**, 386 (1949).

[257]A. Balková and R. J. Bartlett, "A multireference coupled-cluster study of the ground state and lowest excited states of cyclobutadiene", J. Chem. Phys. **101**, 8972–8987 (1994).

[258]P. B. Karadakov, "Ground- and excited-state aromaticity and antiaromaticity in benzene and cyclobutadiene", J. Phys. Chem. A **112**, 7303–7309 (2008).

[259]X. Li and J. Paldus, "Accounting for the exact degeneracy and quasidegeneracy in the automerization of cyclobutadiene via multireference coupled-cluster methods", J. Chem. Phys. **131**, 114103 (2009).

[260]J. Shen and P. Piecuch, "Combining active-space coupled-cluster methods with moment energy corrections via the CC(P;Q) methodology, with benchmark calculations for biradical transition states", J. Chem. Phys. **136**, 144104 (2012).

[261]E. Vitale, A. Alavi, and D. Kats, "FCIQMC-Tailored distinguishable cluster approach", J. Chem. Theory Comput. **16**, 5621–5634 (2020).

[262]M. Head-Gordon, R. J. Rico, M. Oumi, and T. J. Lee, "A doubles correction to electronic excited states from configuration interaction in the space of single substitutions", Chem. Phys. Lett. **219**, 21–29 (1994).

[263]M. Head-Gordon, D. Maurice, and M. Oumi, "A perturbative correction to restricted open-shell configuration-interaction with single substitutions for excited-states of radicals", Chem. Phys. Lett. **246**, 114–121 (1995).

[264]A. Trofimov and J. Schirmer, "Polarization propagator study of electronic excitation in key heterocyclic molecules II. Furan", Chem. Phys. **224**, 175–190 (1997).

[265]O. Christiansen, H. Koch, and P. Jørgensen, "The second-order approximate coupled cluster singles and doubles model CC2", Chem. Phys. Lett. **243**, 409–418 (1995).

[266] A. B. Trofimov, G. Stelter, and J. Schirmer, "Electron excitation energies using a consistent third-order propagator approach: Comparison with full configuration interaction and coupled cluster results", J. Chem. Phys. **117**, 6402–6410 (2002).

[267] F. Bernardi, S. De, M. Olivucci, and M. A. Robb, "The mechanism of ground-state-forbidden photochemical pericyclic reactions: Evidence for real conical intersections", J. Am. Chem. Soc. **112**, 1737–1744 (1990).

[268] F. Bernardi, M. Olivucci, and M. A. Robb, "Potential energy surface crossings in organic photochemistry", Chem. Soc. Rev. **25**, 321 (1996).

[269] M. Boggio-Pasqua, M. J. Bearpark, and M. A. Robb, "Toward a Mechanistic Understanding of the Photochromism of Dimethyldihydropyrenes", J. Org. Chem. **72**, 4497–4503 (2007).

[270] M. Klessinger and J. Michl, "Excited states and photochemistry of organic molecules", in (VCH, New York, 1995).

[271] M. Olivucci, *Computational photochemistry* (Elsevier Science, Amsterdam; Boston (Mass.); Paris, 2010).

[272] M. A. Robb, M. Garavelli, M. Olivucci, and F. Bernardi, "A Computational Strategy for Organic Photochemistry", in *Reviews in Computational Chemistry*, edited by K. B. Lipkowitz and D. B. Boyd (John Wiley & Sons, Inc., Hoboken, NJ, USA, 2007), pp. 87–146.

[273] W. Th. A. M. Van der Lugt and L. J. Oosterhoff, "Symmetry control and photoinduced reactions", J. Am. Chem. Soc. **91**, 6042–6049 (1969).

[274] R. Kancherla, K. Muralirajan, A. Sagadevan, and M. Rueping, "Visible light-induced excited-state transition-metal catalysis", Trends Chem. **1**, 510–523 (2019).

[275] D. Hait and M. Head-Gordon, "Orbital optimized density functional theory for electronic excited states", J. Phys. Chem. Lett. **12**, 4517–4529 (2021).

[276] J. P. Zobel and L. González, "The quest to simulate excited-state dynamics of transition metal complexes", JACS Au **1**, 1116–1140 (2021).

[277] T. Bally and S. Masamune, "Cyclobutadiene", Tetrahedron **36**, 343–370 (1980).

[278] V. I. Minkin, M. N. Glukhovtsev, and B. Y. Simkin, *Aromaticity and Antiaromaticity: Electronic and Structural Aspects — Wiley* (1994).

[279] A. Baeyer, "Ueber Polyacetylenverbindungen", Berichte Dtsch. Chem. Ges. **18**, 2269–2281 (1885).

[280] P. C. Reeves, J. Henery, and R. Pettit, "Further experiments pertaining to the ground state of cyclobutadiene", J. Am. Chem. Soc. **91**, 5888–5890 (1969).

[281] H. Irngartinger and M. Nixdorf, "Bonding Electron Density Distribution in Tetra-Tert-Butylcyclobutadiene— A Molecule with an Obviously Non-Square Four-Membered ring", Angew. Chem. Int. Ed. Engl. **22**, 403–404 (1983).

[282] O. Ermer and E. Heilbronner, "Three Arguments Supporting a Rectangular Structure for Tetra-tert-butylcyclobutadiene", Angew. Chem. Int. Ed. Engl. **22**, 402–403 (1983).

[283] J. Kreile, N. Münzel, A. Schweig, and H. Specht, "Uv photoelectron spectrum of cyclobutadiene. Free cyclobutadiene stable up to high temperatures", Chem. Phys. Lett. **124**, 140–146 (1986).

[284] D. W. Whitman and B. K. Carpenter, "Limits on the activation parameters for automerization of Cyclobutadiene-1,2-D2", J. Am. Chem. Soc. **104**, 6473–6474 (1982).

[285]M. Eckert-Maksić, M. Vazdar, M. Barbatti, H. Lischka, and Z. B. Maksić, "Automerization reaction of cyclobutadiene and its barrier height: An ab initio benchmark multireference average-quadratic coupled cluster study", J. Chem. Phys. **125**, 064310 (2006).

[286]T. Zhang, C. Li, and F. A. Evangelista, "Improving the Efficiency of the Multireference Driven Similarity Renormalization Group via Sequential Transformation, Density Fitting, and the Noninteracting Virtual Orbital Approximation", J. Chem. Theory Comput. **15**, 4399–4414 (2019).

[287]N. T. Maitra, "Charge transfer in time-dependent density functional theory", J. Phys. Cond. Matt. **29**, 423001 (2017).

[288]S. Hirata and R. J. Bartlett, "High-order coupled-cluster calculations through connected octuple excitations", Chem. Phys. Lett. **321**, 216–224 (2000).

[289]Kerstin. Andersson, P. A. Malmqvist, B. O. Roos, A. J. Sadlej, and Krzysztof. Wolinski, "Second-order perturbation theory with a CASSCF reference function", J. Phys. Chem. **94**, 5483–5488 (1990).

[290]K. Andersson, P.-A. Malmqvist, and B. O. Roos, "Second-order perturbation theory with a complete active space self-consistent field reference function", J. Chem. Phys. **96**, 1218–1226 (1992).

[291]B. O. Roos, M. Fülscher, P.-Å. Malmqvist, M. Merchán, and L. Serrano-Andrés, "Theoretical studies of the electronic spectra of organic molecules", in *Quantum mechanical electronic structure calculations with chemical accuracy* (Springer Netherlands, Dordrecht, 1995), pp. 357–438.

[292]C. Angeli, R. Cimiraglia, and J.-P. Malrieu, "N-electron valence state perturbation theory: A fast implementation of the strongly contracted variant", Chem. Phys. Lett. **350**, 297–305 (2001).

[293]C. Angeli, R. Cimiraglia, S. Evangelisti, T. Leininger, and J.-P. Malrieu, "Introduction of n -Electron valence states for multireference perturbation theory", J. Chem. Phys. **114**, 10252–10264 (2001).

[294]C. Angeli, R. Cimiraglia, and J.-P. Malrieu, "N -Electron valence state perturbation theory: A spinless formulation and an efficient implementation of the strongly contracted and of the partially contracted variants", J. Chem. Phys. **117**, 9138–9153 (2002).

[295]D. J. Rowe, "Equations-of-motion method and the extended shell model", Rev. Mod. Phys. **40**, 153–166 (1968).

[296]M. Kállay, J. Gauss, and P. G. Szalay, "Analytic first derivatives for general coupled-cluster and configuration interaction models", J. Chem. Phys. **119**, 2991–3004 (2003).

[297]B. Jeziorski and H. J. Monkhorst, "Coupled-cluster method for multideterminantal reference states", Phys. Rev. A **24**, 1668–1681 (1981).

[298]U. S. Mahapatra, B. Datta, and D. Mukherjee, "A state-specific multi-reference coupled cluster formalism with molecular applications", Mol. Phys. **94**, 157–171 (1998).

[299]U. S. Mahapatra, B. Datta, and D. Mukherjee, "A size-consistent state-specific multireference coupled cluster theory: Formal developments and molecular applications", J. Chem. Phys. **110**, 6171–6188 (1999).

[300]D. I. Lyakh, M. Musiał, V. F. Lotrich, and R. J. Bartlett, "Multireference Nature of Chemistry: The Coupled-Cluster View", Chem. Rev. **112**, 182–243 (2012).

[301] A. Köhn, M. Hanauer, L. A. Mück, T.-C. Jagau, and J. Gauss, "State-specific multireference coupled-cluster theory", WIREs Comput. Mol. Sci. **3**, 176–197 (2013).

[302] C. F. Bender and E. R. Davidson, "Studies in configuration interaction: The first-row diatomic hydrides", Phys. Rev. **183**, 23–30 (1969).

[303] J. L. Whitten and M. Hackmeyer, "Configuration interaction studies of ground and excited states of polyatomic molecules. I. The CI formulation and studies of formaldehyde", J. Chem. Phys. **51**, 5584–5596 (1969).

[304] B. Huron, J. P. Malrieu, and P. Rancurel, "Iterative perturbation calculations of ground and excited state energies from multiconfigurational zeroth-order wavefunctions", J. Chem. Phys. **58**, 5745–5759 (1973).

[305] E. Giner, A. Scemama, and M. Caffarel, "Using perturbatively selected configuration interaction in quantum Monte Carlo calculations", Can. J. Chem. **91**, 879–885 (2013).

[306] F. A. Evangelista, "Adaptive multiconfigurational wave functions", J. Chem. Phys. **140**, 124114 (2014).

[307] E. Giner, A. Scemama, and M. Caffarel, "Fixed-node diffusion Monte Carlo potential energy curve of the fluorine molecule F2 using selected configuration interaction trial wavefunctions", J. Chem. Phys. **142**, 044115 (2015).

[308] M. Caffarel, T. Applencourt, E. Giner, and A. Scemama, "Using CIPSI nodes in diffusion monte carlo", in *Recent progress in quantum monte carlo* (2016) Chap. 2, pp. 15–46.

[309] A. A. Holmes, H. J. Changlani, and C. J. Umrigar, "Efficient heat-bath sampling in fock space", J. Chem. Theory Comput. **12**, 1561–1571 (2016).

[310] N. M. Tubman, J. Lee, T. Y. Takeshita, M. Head-Gordon, and K. B. Whaley, "A deterministic alternative to the full configuration interaction quantum Monte Carlo method", J. Chem. Phys. **145**, 044112 (2016).

[311] W. Liu and M. R. Hoffmann, "iCI: Iterative CI toward full CI", J. Chem. Theory Comput. **12**, 1169–1178 (2016).

[312] Y. Ohtsuka and J.-y. Hasegawa, "Selected configuration interaction method using sampled first-order corrections to wave functions", J. Chem. Phys. **147**, 034102 (2017).

[313] P. M. Zimmerman, "Incremental full configuration interaction", J. Chem. Phys. **146**, 104102 (2017).

[314] J. P. Coe, "Machine learning configuration interaction", J. Chem. Theory Comput. **14**, 5739–5749 (2018).

[315] Y. Garniron, A. Scemama, E. Giner, M. Caffarel, and P. F. Loos, "Selected configuration interaction dressed by perturbation", J. Chem. Phys. **149**, 064103 (2018).

[316] M. Caffarel, E. Giner, A. Scemama, and A. Ramírez-Solís, "Spin density distribution in open-shell transition metal systems: A comparative Post-Hartree–Fock, density functional theory, and quantum monte carlo study of the $CuCl_2$ molecule", J. Chem. Theory Comput. **10**, 5286–5296 (2014).

[317] M. Caffarel, T. Applencourt, E. Giner, and A. Scemama, "Communication: Toward an improved control of the fixed-node error in quantum Monte Carlo: The case of the water molecule", J. Chem. Phys. **144**, 151103 (2016).

[318] A. Scemama, T. Applencourt, E. Giner, and M. Caffarel, "Quantum Monte Carlo with very large multideterminant wavefunctions", J. Comput. Chem. **37**, 1866–1875 (2016).

[319] A. A. Holmes, C. J. Umrigar, and S. Sharma, "Excited states using semistochastic heat-bath configuration interaction", J. Chem. Phys. **147**, 164111 (2017).

[320] J. Li, M. Otten, A. A. Holmes, S. Sharma, and C. J. Umrigar, "Fast semistochastic heat-bath configuration interaction", J. Chem. Phys. **149**, 214110 (2018).

[321] A. Scemama, Y. Garniron, M. Caffarel, and P. F. Loos, "Deterministic construction of nodal surfaces within quantum monte carlo: The case of FeS", J. Chem. Theory Comput. **14**, 1395 (2018).

[322] A. Scemama, A. Benali, D. Jacquemin, M. Caffarel, and P. F. Loos, "Excitation energies from diffusion monte carlo using selected configuration interaction nodes", J. Chem. Phys. **149**, 034108 (2018).

[323] J. Li, Y. Yao, A. A. Holmes, M. Otten, Q. Sun, S. Sharma, and C. J. Umrigar, "Accurate many-body electronic structure near the basis set limit: Application to the chromium dimer", Phys. Rev. Research **2**, 012015 (2020).

[324] A. D. Chien, A. A. Holmes, M. Otten, C. J. Umrigar, S. Sharma, and P. M. Zimmerman, "Excited States of Methylene, Polyenes, and Ozone from Heat-Bath Configuration Interaction", J. Phys. Chem. A **122**, 2714–2722 (2018).

[325] P.-F. Loos, Y. Damour, and A. Scemama, "The performance of CIPSI on the ground state electronic energy of benzene", J. Chem. Phys. **153**, 176101 (2020).

[326] Y. Garniron, T. Applencourt, K. Gasperich, A. Benali, A. Ferté, J. Paquier, B. Pradines, R. Assaraf, P. Reinhardt, J. Toulouse, P. Barbaresco, N. Renon, G. David, J.-P. Malrieu, M. Véril, M. Caffarel, P.-F. Loos, E. Giner, and A. Scemama, "Quantum package 2.0: An open-source determinant-driven suite of programs", J. Chem. Theory Comput. **15**, 3591–3609 (2019).

[327] J. J. Eriksen, T. A. Anderson, J. E. Deustua, K. Ghanem, D. Hait, M. R. Hoffmann, S. Lee, D. S. Levine, I. Magoulas, J. Shen, N. M. Tubman, K. B. Whaley, E. Xu, Y. Yao, N. Zhang, A. Alavi, G. K.-L. Chan, M. Head-Gordon, W. Liu, P. Piecuch, S. Sharma, S. L. Ten-no, C. J. Umrigar, and J. Gauss, "The ground state electronic energy of benzene", J. Phys. Chem. Lett. **11**, 8922–8929 (2020).

[328] Y. Yao, E. Giner, J. Li, J. Toulouse, and C. J. Umrigar, "Almost exact energies for the Gaussian-2 set with the semistochastic heat-bath configuration interaction method", J. Chem. Phys. **153**, 124117 (2020).

[329] K. T. Williams, Y. Yao, J. Li, L. Chen, H. Shi, M. Motta, C. Niu, U. Ray, S. Guo, R. J. Anderson, et al., "Direct comparison of many-body methods for realistic electronic Hamiltonians", Phys. Rev. X **10**, 011041 (2020).

[330] P.-F. Loos, M. Comin, X. Blase, and D. Jacquemin, "Reference energies for intramolecular charge-transfer excitations", J. Chem. Theory Comput. **17**, 3666–3686 (2021).

[331] Y. Damour, M. Véril, F. Kossoski, M. Caffarel, D. Jacquemin, A. Scemama, and P.-F. Loos, "Accurate full configuration interaction correlation energy estimates for five- and six-membered rings", J. Chem. Phys. **155**, 134104 (2021).

[332] Y. Garniron, A. Scemama, P.-F. Loos, and M. Caffarel, "Hybrid stochastic-deterministic calculation of the second-order perturbative contribution of multireference perturbation theory", J. Chem. Phys. **147**, 034101 (2017).

[333]H.-G. Martin, "Characterizing unpaired electrons from the one-particle density matrix", Chem. Phys. Lett. **372**, 508–511 (2003).

[334]A. Scemama, M. Caffarel, A. Benali, D. Jacquemin, and P. F. Loos., "Influence of pseudopotentials on excitation energies from selected configuration interaction and diffusion Monte Carlo", Res. Chem. **1**, 100002 (2019).

[335]J. J. Eriksen, "The shape of full configuration interaction to come", J. Phys. Chem. Lett. **12**, 418–432 (2021).

[336]J. Čížek, "On the Correlation Problem in Atomic and Molecular Systems. Calculation of Wavefunction Components in Ursell-Type Expansion Using Quantum-Field Theoretical Methods", J. Chem. Phys. **45**, 4256–4266 (1966).

[337]J. Paldus, J. Cizek, and I. Shavitt, "Correlation problems in atomic and molecular systems. IV. Extended coupled-pair many-electron theory and its application to the bH_3 molecule", Phys. Rev. A **5**, 50–67 (1972).

[338]T. D. Crawford and H. F. Schaefer, "An Introduction to Coupled Cluster Theory for Computational Chemists", in *Reviews in Computational Chemistry* (John Wiley & Sons, Ltd, 2000), pp. 33–136.

[339]R. J. Bartlett and M. Musiał, "Coupled-cluster theory in quantum chemistry", Rev. Mod. Phys. **79**, 291–352 (2007).

[340]I. Shavitt and R. J. Bartlett, *Many-Body Methods in Chemistry and Physics: MBPT and Coupled-Cluster Theory*, Cambridge Molecular Science (Cambridge University Press, Cambridge, 2009).

[341]G. D. Purvis and R. J. Bartlett, "A full coupled-cluster singles and doubles model: The inclusion of disconnected triples", J. Chem. Phys. **76**, 1910–1918 (1982).

[342]J. Noga and R. J. Bartlett, "The full CCSDT model for molecular electronic structure", J. Chem. Phys. **86**, 7041–7050 (1987).

[343]G. E. Scuseria and H. F. Schaefer, "A new implementation of the full CCSDT model for molecular electronic structure", Chem. Phys. Lett. **152**, 382–386 (1988).

[344]N. Oliphant and L. Adamowicz, "Coupled-cluster method truncated at quadruples", J. Chem. Phys. **95**, 6645–6651 (1991).

[345]S. A. Kucharski and R. J. Bartlett, "The coupled-cluster single, double, triple, and quadruple excitation method", J. Chem. Phys. **97**, 4282–4288 (1992).

[346]O. Christiansen, J. F. Stanton, and J. Gauss, "A coupled cluster study of the 1 1A1g and 1 1B2u states of benzene", J. Chem. Phys. **108**, 3987–4001 (1998).

[347]S. A. Kucharski, M. Włoch, M. Musiał, and R. J. Bartlett, "Coupled-cluster theory for excited electronic states: The full equation-of-motion coupled-cluster single, double, and triple excitation method", J. Chem. Phys. **115**, 8263–8266 (2001).

[348]K. Kowalski and P. Piecuch, "The active-space equation-of-motion coupled-cluster methods for excited electronic states: Full EOMCCSDt", J. Chem. Phys. **115**, 643–651 (2001).

[349]C. Hättig and F. Weigend, "CC2 excitation energy calculations on large molecules using the resolution of the identity approximation", J. Chem. Phys. **113**, 5154–5161 (2000).

[350]H. Koch, O. Christiansen, P. Jørgensen, and J. Olsen, "Excitation energies of BH, CH2 and Ne in full configuration interaction and the hierarchy CCS, CC2, CCSD and CC3 of coupled cluster models", Chem. Phys. Lett. **244**, 75–82 (1995).

[351]M. Kállay and J. Gauss, "Approximate treatment of higher excitations in coupled-cluster theory", J. Chem. Phys. **123**, 214105 (2005).

[352]D. A. Matthews, L. Cheng, M. E. Harding, F. Lipparini, S. Stopkowicz, T.-C. Jagau, P. G. Szalay, J. Gauss, and J. F. Stanton, "Coupled-cluster techniques for computational chemistry: The CFOUR program package", J. Chem. Phys. **152**, 214108 (2020).

[353]K. Aidas, C. Angeli, K. L. Bak, V. Bakken, R. Bast, L. Boman, O. Christiansen, R. Cimiraglia, S. Coriani, P. Dahle, E. K. Dalskov, U. Ekström, T. Enevoldsen, J. J. Eriksen, P. Ettenhuber, B. Fernández, L. Ferrighi, H. Fliegl, L. Frediani, K. Hald, A. Halkier, C. Hättig, H. Heiberg, T. Helgaker, A. C. Hennum, H. Hettema, E. Hjertenæs, S. Høst, I.-M. Høyvik, M. F. Iozzi, B. Jansík, H. J. A. Jensen, D. Jonsson, P. Jørgensen, J. Kauczor, S. Kirpekar, T. Kjærgaard, W. Klopper, S. Knecht, R. Kobayashi, H. Koch, J. Kongsted, A. Krapp, K. Kristensen, A. Ligabue, O. B. Lutnæs, J. I. Melo, K. V. Mikkelsen, R. H. Myhre, C. Neiss, C. B. Nielsen, P. Norman, J. Olsen, J. M. H. Olsen, A. Osted, M. J. Packer, F. Pawlowski, T. B. Pedersen, P. F. Provasi, S. Reine, Z. Rinkevicius, T. A. Ruden, K. Ruud, V. V. Rybkin, P. Sałek, C. C. M. Samson, A. S. de Merás, T. Saue, S. P. A. Sauer, B. Schimmelpfennig, K. Sneskov, A. H. Steindal, K. O. Sylvester-Hvid, P. R. Taylor, A. M. Teale, E. I. Tellgren, D. P. Tew, A. J. Thorvaldsen, L. Thøgersen, O. Vahtras, M. A. Watson, D. J. D. Wilson, M. Ziolkowski, and H. Ågren, "The Dalton quantum chemistry program system", WIREs Comput. Mol. Sci. **4**, 269–284 (2014).

[354]M. Kállay, Z. Rolik, J. Csontos, P. Nagy, G. Samu, D. Mester, J. Csóka, B. Szabó, I. Ladjánszki, L. Szegedy, B. Ladóczki, K. Petrov, M. Farkas, P. D. Mezei, and B. Hégely., *MRCC, quantum chemical program*, 2017.

[355]H.-J. Werner, P. J. Knowles, F. R. Manby, J. A. Black, K. Doll, A. Heßelmann, D. Kats, A. Köhn, T. Korona, D. A. Kreplin, Q. Ma, T. F. Miller, A. Mitrushchenkov, K. A. Peterson, I. Polyak, G. Rauhut, and M. Sibaev, "The Molpro quantum chemistry package", J. Chem. Phys. **152**, 144107 (2020).

[356]E. R. Davidson, "The spatial extent of the v state of ethylene and its relation to dynamic correlation in the cope rearrangement", J. Phys. Chem **100**, 6161–6166 (1996).

[357]C. Angeli, R. Cimiraglia, and M. Cestarri, "A multireference n-electron Valence State Perturbation Theory study of the electronic spectrum of s-tetrazine", Theor. Chem. Acc. **123**, 287–298 (2009).

[358]N. Ben Amor, C. Noûs, G. Trinquier, and J.-P. Malrieu, "Spin polarization as an electronic cooperative effect", J. Chem. Phys **153**, 044118 (2020).

[359]B. O. Roos and K. Andersson, "Multiconfigurational perturbation theory with level shift — the cr_2 potential revisited", Chem. Phys. Lett. **245**, 215–223 (1995).

[360]G. Ghigo, B. O. Roos, and P.-Å. Malmqvist, "A modified definition of the zeroth-order hamiltonian in multiconfigurational perturbation theory (CASPT2)", Chem. Phys. Lett. **396**, 142–149 (2004).

[361]I. Schapiro, K. Sivalingam, and F. Neese, "Assessment of n-Electron valence state perturbation theory for vertical excitation energies", J. Chem. Theory Comput. **9**, 3567–3580 (2013).

[362]J. P. Zobel, J. J. Nogueira, and L. Gonzalez, "The IPEA dilemma in CASPT2", Chem. Sci. **8**, 1482–1499 (2017).

[363]R. Sarkar, P. F. Loos, M. Boggio-Pasqua, and D. Jacquemin., "Assessing the performances of CASPT2 and NEVPT2 for vertical excitation energies," J. Chem. Theory Comput. **18**, 2418–2436 (2022).

[364]P. J. Knowles and H.-J. Werner, "An efficient method for the evaluation of coupling coefficients in configuration interaction calculations", Chem. Phys. Lett. **145**, 514–522 (1988).

[365]H.-J. Werner and P. J. Knowles, "An efficient internally contracted multiconfiguration–reference configuration interaction method", J. Chem. Phys. **89**, 5803–5814 (1988).

[366]P.-F. Loos and D. Jacquemin, "Is ADC(3) as accurate as CC3 for valence and rydberg transition energies?", J. Phys. Chem. Lett. **11**, 974–980 (2020).

[367]M. Ernzerhof and G. E. Scuseria, "Assessment of the Perdew–Burke–Ernzerhof exchange-correlation functional", J. Chem. Phys. **110**, 5029–5036 (1999).

[368]T. Yanai, D. P. Tew, and N. C. Handy, "A new hybrid Exchange–Correlation functional using the Coulomb-attenuating method (CAM-B3LYP)", Chem. Phys. Lett. **393**, 51–57 (2004).

[369]N. Mardirossian and M. Head-Gordon, "ωB97X-V: A 10-Parameter, range-separated hybrid, generalized gradient approximation density functional with nonlocal correlation, designed by a survival-of-the-fittest strategy", Phys. Chem. Chem. Phys. **16**, 9904–9924 (2014).

[370]Y. Zhao and D. G. Truhlar, "The M06 suite of density functionals for main group thermochemistry, thermochemical kinetics, noncovalent interactions, excited states, and transition elements: Two new functionals and systematic testing of four M06-class functionals and 12 other functionals", Theor Chem Acc. **120**, 215–241 (2008).

[371]R. Peverati and D. G. Truhlar, "Improving the Accuracy of Hybrid Meta-GGA Density Functionals by Range Separation", J. Phys. Chem. Lett. **2**, 2810–2817 (2011).

[372]S. Hirata and M. Head-Gordon, "Time-dependent density functional theory within the Tamm–Dancoff approximation", Chem. Phys. Lett. **314**, 291–299 (1999).

[373]R. S. Mulliken, "Report on notation for the spectra of polyatomic molecules", J. Chem. Phys. **23**, 1997–2011 (1955).

[374]T. H. Dunning, "Gaussian basis sets for use in correlated molecular calculations. I. The atoms boron through neon and hydrogen", J. Chem. Theory Comput. **90**, 1007–1023 (1989).

[375]G. Karthik, D. J. Emiliano, S. Jun, and P. Piotr, "High-level coupled-cluster energetics by merging moment expansions with selected configuration interaction", J. Chem. Phys. **155**, 174114 (2021).

[376]D. J. Emiliano, S. Jun, and P. Piotr, "High-level coupled-cluster energetics by Monte Carlo sampling and moment expansions: Further details and comparisons", J. Chem. Phys. **154**, 124103 (2021).

[377]P. F. Loos, B. Pradines, A. Scemama, J. Toulouse, and E. Giner, "A density-based basis-set correction for wave function theory", J. Phys. Chem. Lett. **10**, 2931–2937 (2019).

[378]M. Wormit, D. R. Rehn, P. H. Harbach, J. Wenzel, C. M. Krauter, E. Epifanovsky, and A. Dreuw, "Investigating excited electronic states using the algebraic diagrammatic construction (ADC) approach of the polarisation propagator", Mol. Phys. **112**, 774–784 (2014).

[379]E. Giner, A. Scemama, J. Toulouse, and P. F. Loos, "Chemically accurate excitation energies with small basis sets", J. Chem. Phys. **151**, 144118 (2019).

[380]F. Aryasetiawan and O. Gunnarsson, "The GW method", Rep. Prog. Phys. **61**, 237–312 (1998).

[381]L. Reining, "The GW approximation: Content, successes and limitations: The GW approximation", Wiley Interdiscip. Rev. Comput. Mol. Sci. **8**, e1344 (2017).

[382]F. Bruneval, "Ionization energy of atoms obtained from *GW* self-energy or from random phase approximation total energies", J. Chem. Phys. **136**, 194107 (2012).

[383]F. Bruneval and M. A. L. Marques, "Benchmarking the Starting Points of the *GW* Approximation for Molecules", J. Chem. Theory Comput. **9**, 324–329 (2013).

[384]X. Blase, P. Boulanger, F. Bruneval, M. Fernandez-Serra, and I. Duchemin, "*GW* and Bethe-Salpeter study of small water clusters", J. Chem. Phys. **144**, 034109 (2016).

[385]F. Bruneval, "Optimized virtual orbital subspace for faster GW calculations in localized basis", J. Chem. Phys. **145**, 234110 (2016).

[386]P. Koval, D. Foerster, and D. Sánchez-Portal, "Fully self-consistent GW and quasiparticle self-consistent GW for molecules", Phys. Rev. B **89**, 155417 (2014).

[387]L. Hung, F. H. da Jornada, J. Souto-Casares, J. R. Chelikowsky, S. G. Louie, and S. Öğüt, "Excitation spectra of aromatic molecules within a real-space GW -BSE formalism: Role of self-consistency and vertex corrections", Phys. Rev. B **94**, 085125 (2016).

[388]J. Li, M. Holzmann, I. Duchemin, X. Blase, and V. Olevano, "Helium Atom Excitations by the GW and Bethe-Salpeter Many-Body Formalism", Phys. Rev. Lett. **118**, 163001 (2017).

[389]L. Hung, F. Bruneval, K. Baishya, and S. Öğüt, "Benchmarking the *GW* Approximation and Bethe–Salpeter Equation for Groups IB and IIB Atoms and Monoxides", J. Chem. Theory Comput. **13**, 2135–2146 (2017).

[390]M. J. van Setten, F. Weigend, and F. Evers, "The *GW* -Method for Quantum Chemistry Applications: Theory and Implementation", J. Chem. Theory Comput. **9**, 232–246 (2013).

[391]M. J. van Setten, F. Caruso, S. Sharifzadeh, X. Ren, M. Scheffler, F. Liu, J. Lischner, L. Lin, J. R. Deslippe, S. G. Louie, C. Yang, F. Weigend, J. B. Neaton, F. Evers, and P. Rinke, "*GW* 100: Benchmarking G_0W_0 for Molecular Systems", J. Chem. Theory Comput. **11**, 5665–5687 (2015).

[392]M. J. van Setten, R. Costa, F. Viñes, and F. Illas, "Assessing *GW* Approaches for Predicting Core Level Binding Energies", J. Chem. Theory Comput. **14**, 877–883 (2018).

[393]E. Maggio, P. Liu, M. J. van Setten, and G. Kresse, "*GW* 100: A Plane Wave Perspective for Small Molecules", J. Chem. Theory Comput. **13**, 635–648 (2017).

[394]R. M. Richard, M. S. Marshall, O. Dolgounitcheva, J. V. Ortiz, J.-L. Brédas, N. Marom, and C. D. Sherrill, "Accurate Ionization Potentials and Electron Affinities of Acceptor Molecules I. Reference Data at the CCSD(T) Complete Basis Set Limit", J. Chem. Theory Comput. **12**, 595–604 (2016).

[395]L. Gallandi, N. Marom, P. Rinke, and T. Körzdörfer, "Accurate Ionization Potentials and Electron Affinities of Acceptor Molecules II: Non-Empirically Tuned Long-Range Corrected Hybrid Functionals", J. Chem. Theory Comput. **12**, 605–614 (2016).

[396]J. W. Knight, X. Wang, L. Gallandi, O. Dolgounitcheva, X. Ren, J. V. Ortiz, P. Rinke, T. Körzdörfer, and N. Marom, "Accurate Ionization Potentials and Electron Affinities of Acceptor Molecules III: A Benchmark of *GW* Methods", J. Chem. Theory Comput. **12**, 615–626 (2016).

[397]O. Dolgounitcheva, M. Díaz-Tinoco, V. G. Zakrzewski, R. M. Richard, N. Marom, C. D. Sherrill, and J. V. Ortiz, "Accurate Ionization Potentials and Electron Affinities of Acceptor Molecules IV: Electron-Propagator Methods", J. Chem. Theory Comput. **12**, 627–637 (2016).

[398]K. Krause, M. E. Harding, and W. Klopper, "Coupled-cluster reference values for the GW27 and GW100 test sets for the assessment of GW methods", Mol. Phys. **113**, 1952 (2015).

[399]M. Govoni and G. Galli, "GW100: Comparison of methods and accuracy of results obtained with the WEST code", J. Chem. Theory Comput. **14**, 1895–1909 (2018).

[400]F. Caruso, M. Dauth, M. J. van Setten, and P. Rinke, "Benchmark of GW approaches for the GW100 test set", J. Chem. Theory Comput. **12**, 5076 (2016).

[401]D. Foerster, P. Koval, and D. Sánchez-Portal, "An O(N3) implementation of hedin's GW approximation for molecules", J. Chem. Phys. **135**, 074105 (2011).

[402]P. Liu, M. Kaltak, J. Kliměsš, and G. Kresse, "Cubic scaling GW: Towards fast quasiparticle calculations", Phys. Rev. B **94**, 165109 (2016).

[403]J. Wilhelm, D. Golze, L. Talirz, J. Hutter, and C. A. Pignedoli, "Toward GW calculations on thousands of atoms", J. Phys. Chem. Lett. **9**, 306–312 (2018).

[404]A. Förster and L. Visscher, "Low-order scaling quasiparticle self-consistent GW for molecules", Front. Chem. **9**, 736591 (2021).

[405]I. Duchemin and X. Blase, "Cubic-scaling all-electron GW calculations with a separable density-fitting Space–Time approach", J. Chem. Theory Comput. **17**, 2383–2393 (2021).

[406]S. Körbel, P. Boulanger, I. Duchemin, X. Blase, M. A. L. Marques, and S. Botti, "Benchmark many-body GW and Bethe–Salpeter calculations for small transition metal molecules", J. Chem. Theory Comput. **10**, 3934–3943 (2014).

[407]F. Bruneval, N. Dattani, and M. J. van Setten, "The GW miracle in many-body perturbation theory for the ionization potential of molecules", Front. Chem. **9**, 749779 (2021).

[408]S. Di Sabatino, P.-F. Loos, and P. Romaniello, "Scrutinizing GW-Based methods using the hubbard dimer", Front. Chem. **9**, 751054 (2021).

[409]M. Seidl, "Adiabatic connection in density-functional theory: Two electrons on the surface of a sphere", Phys. Rev. A **75**, 062506 (2007).

[410]P. F. Loos and P. M. W. Gill, "Two electrons on a hypersphere: A quasiexactly solvable model", Phys. Rev. Lett. **103**, 123008 (2009).

[411]P.-F. Loos and P. M. W. Gill, "Correlation energy of two electrons in the high-density limit", J. Chem. Phys. **131**, 241101 (2009).

[412]I. Duchemin and X. Blase, "Robust analytic-continuation approach to many-body GW calculations", J. Chem. Theory Comput. **16**, 1742–1756 (2020).

[413]P. Pokhilko and D. Zgid, "Interpretation of multiple solutions in fully iterative GF2 and GW schemes using local analysis of two-particle density matrices", J. Chem. Phys. **155**, 024101 (2021).

[414]P. Pokhilko, S. Iskakov, C.-N. Yeh, and D. Zgid, "Evaluation of two-particle properties within finite-temperature self-consistent one-particle Green's function methods: Theory and application to GW and GF2", J. Chem. Phys. **155**, 024119 (2021).

[415]D. Golze, J. Wilhelm, M. J. van Setten, and P. Rinke, "Core-level binding energies from GW: An efficient full-frequency approach within a localized basis", J. Chem. Theory Comput. **14**, 4856–4869 (2018).

[416]D. Golze, L. Keller, and P. Rinke, "Accurate absolute and relative core-level binding energies from GW", J. Phys. Chem. Lett. **11**, 1840–1847 (2020).

[417]P. Pulay, "Convergence acceleration of iterative sequences. the case of scf iteration", Chem. Phys. Lett. **73**, 393–398 (1980).

[418]P. Pokhilko, C.-N. Yeh, and D. Zgid, "Iterative subspace algorithms for finite-temperature solution of Dyson equation", J. Chem. Phys. **156**, 094101 (2022).

[419]P. Romaniello, F. Bechstedt, and L. Reining, "Beyond the GW approximation: Combining correlation channels", Phys. Rev. B **85**, 155131 (2012).

[420]J. Li, Z. Chen, and W. Yang, "Renormalized singles green's function in the T-matrix approximation for accurate quasiparticle energy calculation", J. Phys. Chem. Lett. **12**, 6203–6210 (2021).

[421]M. E. Casida and D. P. Chong, "Physical interpretation and assessment of the Coulomb-Hole and screened-exchange approximation for molecules", Phys. Rev. A **40**, 4837–4848 (1989).

[422]M. E. Casida and D. P. Chong, "Quasi-particle equation from the configuration-interaction (CI) wave-function method", Int. J. Quantum Chem. **40**, 225–242 (1991).

[423]G. Stefanucci and R. van Leeuwen, *Nonequilibrium many-body theory of quantum systems: A modern introduction* (Cambridge University Press, Cambridge, 2013).

[424]J. V. Ortiz, "Electron propagator theory: An approach to prediction and interpretation in quantum chemistry: Electron propagator theory", Wiley Interdiscip. Rev. Comput. Mol. Sci. **3**, 123–142 (2013).

[425]J. J. Phillips and D. Zgid, "Communication: The description of strong correlation within self-consistent Green's function second-order perturbation theory", J. Chem. Phys. **140**, 241101 (2014).

[426]J. J. Phillips, A. A. Kananenka, and D. Zgid, "Fractional charge and spin errors in self-consistent Green's function theory", J. Chem. Phys. **142**, 194108 (2015).

[427]A. A. Rusakov, J. J. Phillips, and D. Zgid, "Local Hamiltonians for quantitative Green's function embedding methods", J. Chem. Phys. **141**, 194105 (2014).

[428]A. A. Rusakov and D. Zgid, "Self-consistent second-order Green's function perturbation theory for periodic systems", J. Chem. Phys. **144**, 054106 (2016).

[429]S. Hirata, M. R. Hermes, J. Simons, and J. V. Ortiz, "General-Order Many-Body Green's Function Method", J. Chem. Theory Comput. **11**, 1595–1606 (2015).

[430]L. Hedin, "On correlation effects in electron spectroscopies and the GW approximation", J. Phys. Condens. Matter **11**, R489–R528 (1999).

[431]F. Bruneval, N. Vast, and L. Reining, "Effect of self-consistency on quasiparticles in solids", Phys. Rev. B **74**, 045102 (2006).

[432]A Stan, N. E Dahlen, and R. van Leeuwen, "Fully self-consistent *GW* calculations for atoms and molecules", Europhys. Lett. EPL **76**, 298–304 (2006).

[433] A. Stan, N. E. Dahlen, and R. van Leeuwen, "Levels of self-consistency in the GW approximation", J. Chem. Phys. **130**, 114105 (2009).

[434] C. Rostgaard, K. W. Jacobsen, and K. S. Thygesen, "Fully self-consistent GW calculations for molecules", Phys. Rev. B **81**, 085103 (2010).

[435] F. Caruso, P. Rinke, X. Ren, M. Scheffler, and A. Rubio, "Unified description of ground and excited states of finite systems: The self-consistent GW approach", Phys. Rev. B **86**, 081102(R) (2012).

[436] F. Caruso, P. Rinke, X. Ren, A. Rubio, and M. Scheffler, "Self-consistent GW : All-Electron implementation with localized basis functions", Phys. Rev. B **88**, 075105 (2013).

[437] F. Caruso, "Self-consistent GW approach for the unified description of ground and excited states of finite systems", PhD thesis (Freie Universität Berlin, 2013).

[438] S. Lee, M. Filatov, S. Lee, and C. H. Choi, "Eliminating spin-contamination of spin-flip time dependent density functional theory within linear response formalism by the use of zeroth-order mixed-reference (MR) reduced density matrix", J. Chem. Phys. **149**, 104101 (2018).

[439] F. A. Evangelista, "A driven similarity renormalization group approach to quantum many-body problems", J. Chem. Phys. **141**, 054109 (2014).

[440] P. C. Martin and J. Schwinger, "Theory of Many-Particle Systems. I", Phys. Rev. **115**, 1342–1373 (1959).

[441] G. Baym and L. P. Kadanoff, "Conservation Laws and Correlation Functions", Phys. Rev. **124**, 287–299 (1961).

[442] G. Baym, "Self-Consistent Approximations in Many-Body Systems", Phys. Rev. **127**, 1391–1401 (1962).

[443] G. Riva, T. Audinet, M. Vladaj, P. Romaniello, and J. A. Berger, "Photoemission spectral functions from the three-body Green's function", SciPost Phys. **12**, 093 (2022).

[444] I. Duchemin and X. Blase, "Separable resolution-of-the-identity with all-electron Gaussian bases: Application to cubic-scaling RPA", J. Chem. Phys. **150**, 174120 (2019).

[445] M. Dvorak and P. Rinke, "Dynamical configuration interaction: Quantum embedding that combines wave functions and Green's functions", Phys. Rev. B **99**, 115134 (2019).

[446] M. Dvorak, D. Golze, and P. Rinke, "Quantum embedding theory in the screened Coulomb interaction: Combining configuration interaction with GW/BSE", Phys. Rev. Mat. **3**, 070801(R) (2019).

[447] N. Forsberg and P.-Å. Malmqvist, "Multiconfiguration perturbation theory with imaginary level shift", Chem. Phys. Lett. **274**, 196–204 (1997).

[448] J. Shee, M. Loipersberger, A. Rettig, J. Lee, and M. Head-Gordon, "Regularized second-order Møller–Plesset theory: A more accurate alternative to conventional MP2 for noncovalent interactions and transition metal thermochemistry for the same computational cost", J. Phys. Chem. Lett. **12**, 12084–12097 (2021).

[449] D. Stück and M. Head-Gordon, "Regularized orbital-optimized second-order perturbation theory", J. Chem. Phys. **139**, 244109 (2013).

[450]R. M. Razban, D. Stück, and M. Head-Gordon, "Addressing first derivative discontinuities in orbital-optimised opposite-spin scaled second-order perturbation theory with regularisation", Mol. Phys. **115**, 2102–2109 (2017).

[451]F. Wegner, "Flow-equations for hamiltonians", Ann. Phys. Leipzig **3**, 77 (1994).

[452]S. D. Glazek and K. G. Wilson, "Perturbative renormalization group for Hamiltonians", Phys. Rev. D **49**, 4214–4218 (1994).

[453]S. R. White, "Numerical canonical transformation approach to quantum many-body problems", J. Chem. Phys. **117**, 7472–7482 (2002).

[454]J. Li, N. D. Drummond, P. Schuck, and V. Olevano, "Comparing many-body approaches against the helium atom exact solution", SciPost Phys. **6**, 040 (2019).

[455]A. Marie, H. G. A. Burton, and P.-F. Loos, "Perturbation theory in the complex plane: exceptional points and where to find them", J. Phys. Condens. Matter **33**, 283001 (2021).

[456]E. Maggio and G. Kresse, "Correlation energy for the homogeneous electron gas: Exact Bethe-Salpeter solution and an approximate evaluation", Phys. Rev. B **93**, 235113 (2016).

[457]G. Csanak, HS Taylor, and R. Yaris, "Green's function technique in atomic and molecular physics", in *Advances in atomic and molecular physics*, Vol. 7 (Elsevier, 1971), pp. 287–361.

[458]G. Das, "Multiconfiguration self-consistent field (MCSCF) theory for excited states", J. Chem. Phys. **58**, 5104–5110 (1973).

[459]E. Dalgaard and P. Jørgensen, "Optimization of orbitals for multiconfigurational reference states", J. Chem. Phys. **69**, 3833–3844 (1978).

[460]B. H. Lengsfield, "General second order MCSCF theory: A density matrix directed algorithm", J. Chem. Phys. **73**, 382–390 (1980).

[461]C. W. Bauschlicher and D. R. Yarkony, "MCSCF wave functions for excited states of polar molecules: Application to BeO", J. Chem. Phys. **72**, 1138–1144 (1980).

[462]C. W. Bauschlicher, D. M. Silver, and D. R. Yarkony, "An SCF and MCSCF description of the low-lying states of MgO", J. Chem. Phys. **73**, 2867–2870 (1980).

[463]H.-J. Werner and W. Meyer, "A quadratically convergent MCSCF method for the simultaneous optimization of several states", J. Chem. Phys. **74**, 5794–5801 (1981).

[464]J. T. Golab, D. L. Yeager, and P. Jørgensen, "Proper characterization of MC SCF stationary points", Chem. Phys. **78**, 175–199 (1983).

[465]T. Ziegler, A. Rauk, and E. Baerends, "On the calculation of multiplet energies by the hartree-fock-slater method", Theor. Chim. Acta **43**, 261–271 (1977).

[466]T. Kowalczyk, S. Yost, and T. Voorhis, "Assessment of the ΔSCF density functional theory approach for electronic excitations in organic dyes", Chem. Phys. **134**, 054128 (2011).

[467]G. Strinati, H. J. Mattausch, and W. Hanke, "Dynamical aspects of correlation corrections in a covalent crystal", Phys. Rev. B **25**, 2867–2888 (1982).

[468]R. W. Godby, M. Schlüter, and L. J. Sham, "Accurate Exchange-Correlation Potential for Silicon and Its Discontinuity on Addition of an Electron", Phys. Rev. Lett. **56**, 2415–2418 (1986).

[469]R. W. Godby, M. Schlüter, and L. J. Sham, "Trends in self-energy operators and their corresponding exchange-correlation potentials", Phys. Rev. B **36**, 6497–6500 (1987).

[470]R. W. Godby, M. Schlüter, and L. J. Sham, "Quasiparticle energies in GaAs and AlAs", Phys. Rev. B **35**, 4170–4171 (1987).

[471]X. Blase, A. Rubio, S. G. Louie, and M. L. Cohen, "Quasiparticle band structure of bulk hexagonal boron nitride and related systems", Phys. Rev. B **51**, 6868–6875 (1995).

[472]D. Rocca, D. Lu, and G. Galli, "Ab initio calculations of optical absorption spectra: Solution of the Bethe–Salpeter equation within density matrix perturbation theory", J. Chem. Phys. **133**, 164109 (2010).

[473]C. Li and F. A. Evangelista, "Multireference theories of electron correlation based on the driven similarity renormalization group", Annu. Rev. Phys. Chem. **70**, 245–273 (2019).

[474]J. Li, I. Duchemin, X. Blase, and V. Olevano, "Ground-state correlation energy of beryllium dimer by the Bethe-Salpeter equation", SciPost Phys. **8**, 20 (2020).

[475]C. A. McKeon, S. M. Hamed, F. Bruneval, and J. B. Neaton, "An optimally tuned range-separated hybrid starting point for ab initio GW plus Bethe–Salpeter equation calculations of molecules", J. Chem. Phys. **157**, 074103 (2022).

[476]Y. Jin, N. Q. Su, and W. Yang, "Renormalized singles green's function for quasiparticle calculations beyond the G_0W_0 approximation", J. Phys. Chem. Lett. **10**, 447–452 (2019).

[477]Y. Jin and W. Yang, "Excitation energies from the single-particle green's function with the GW approximation", J. Phys. Chem. A **123**, 3199–3204 (2019).

[478]J. Li, Y. Jin, P. Rinke, W. Yang, and D. Golze, "Benchmark of GW methods for core-level binding energies", J. Chem. Theory Comput. **18**, 7570–7585 (2022).

[479]J. Li, D. Golze, and W. Yang, "Combining renormalized singles GW methods with the Bethe–Salpeter equation for accurate neutral excitation energies", J. Chem. Theory Comput. **18**, 6637–6645 (2022).

[480]J. Li and W. Yang, "Renormalized singles with correlation in GW green's function theory for accurate quasiparticle energies", J. Phys. Chem. Lett. **13**, 9372–9380 (2022).

[481]A. Förster and L. Visscher, "Quasiparticle self-consistent GW-Bethe–Salpeter equation calculations for large chromophoric systems", J. Chem. Theory Comput. **18**, 6779–6793 (2022).

[482]A. Liebsch, "Ni d-band self-energy beyond the low-density limit", Phys. Rev. B **23**, 5203–5212 (1981).

[483]N. E. Bickers, D. J. Scalapino, and S. R. White, "Conserving approximations for strongly correlated electron systems: Bethe-salpeter equation and dynamics for the two-dimensional hubbard model", Phys. Rev. Lett. **62**, 961–964 (1989).

[484]N. E. Bickers and S. R. White, "Conserving approximations for strongly fluctuating electron systems. II. Numerical results and parquet extension", Phys. Rev. B **43**, 8044–8064 (1991).

[485]M. I. Katsnelson and A. I. Lichtenstein, "LDA approach to the electronic structure of magnets: correlation effects in iron", J. Phys. Condens. Matter **11**, 1037–1048 (1999).

[486]M. Katsnelson and A. Lichtenstein, "Electronic structure and magnetic properties of correlated metals", Eur. Phys. J. B **30**, 9–15 (2002).

[487]V. P. Zhukov, E. V. Chulkov, and P. M. Echenique, "GW + T theory of excited electron lifetimes in metals", Phys. Rev. B **72**, 155109 (2005).

[488]M. Puig von Friesen, C. Verdozzi, and C.-O. Almbladh, "Kadanoff-Baym dynamics of Hubbard clusters: Performance of many-body schemes, correlation-induced damping and multiple steady and quasi-steady states", Phys. Rev. B **82**, 155108 (2010).

[489]J. Gukelberger, L. Huang, and P. Werner, "On the dangers of partial diagrammatic summations: Benchmarks for the two-dimensional Hubbard model in the weak-coupling regime", Phys. Rev. B **91**, 235114 (2015).

[490]M. C. T. D. Müller, S. Blügel, and C. Friedrich, "Electron-magnon scattering in elementary ferromagnets from first principles: Lifetime broadening and band anomalies", Phys. Rev. B **100**, 045130 (2019).

[491]C. Friedrich, "Tetrahedron integration method for strongly varying functions: Application to the GT self-energy", Phys. Rev. B **100**, 075142 (2019).

[492]T. Biswas and A. Singh, "Excitonic effects in absorption spectra of carbon dioxide reduction photocatalysts", npj Comput. Mater. **7**, 189 (2021).

[493]H. A. Bethe and J. Goldstone, "Effect of a repulsive core in the theory of complex nuclei", Proc. Math. Phys. Eng. Sci. **238**, 551–567 (1957).

[494]P Danielewicz, "Quantum theory of nonequilibrium processes II. Application to nuclear collisions", Ann. Phys. **152**, 305–326 (1984).

[495]P Danielewicz, "Quantum theory of nonequilibrium processes, I", Ann. Phys. **152**, 239–304 (1984).

[496]C. De Dominicis and P. C. Martin, "Stationary entropy principle and renormalization in normal and superfluid systems. I. Algebraic formulation", J. Math. Phys. **5**, 14–30 (1964).

[497]C. De Dominicis and P. C. Martin, "Stationary entropy principle and renormalization in normal and superfluid systems. II. Diagrammatic formulation", J. Math. Phys. **5**, 31–59 (1964).

[498]N. Bickers and D. Scalapino, "Conserving approximations for strongly fluctuating electron systems. I. Formalism and calculational approach", Ann. Phys. **193**, 206–251 (1989).

[499]N. E. Bickers, "Self-consistent many-body theory for condensed matter systems", in *Theoretical methods for strongly correlated electrons*, edited by D. Sénéchal, A.-M. Tremblay, and C. Bourbonnais (Springer New York, 2004), pp. 237–296.

[500]E. L. Shirley, "Self-consistent GW and higher-order calculations of electron states in metals", Phys. Rev. B **54**, 7758–7764 (1996).

[501]R. Del Sole, L. Reining, and R. W. Godby, "GWΓ approximation for electron self-energies in semiconductors and insulators", Phys. Rev. B **49**, 8024–8028 (1994).

[502]A. Schindlmayr and R. W. Godby, "Systematic vertex corrections through iterative solution of Hedin's equations beyond the GW approximation", Phys. Rev. Lett. **80**, 1702 (1998).

[503]A. J. Morris, M. Stankovski, K. T. Delaney, P. Rinke, P. García-González, and R. W. Godby, "Vertex corrections in localized and extended systems", Phys. Rev. B **76**, 155106 (2007).

[504]M. Shishkin, M. Marsman, and G. Kresse, "Accurate quasiparticle spectra from self-consistent GW calculations with vertex corrections", Phys. Rev. Lett. **99**, 246403 (2007).

[505]P. Romaniello, S. Guyot, and L. Reining, "The self-energy beyond GW: Local and nonlocal vertex corrections", J. Chem. Phys. **131**, 154111 (2009).

[506]A. Grüneis, G. Kresse, Y. Hinuma, and F. Oba, "Ionization potentials of solids: The importance of vertex corrections", Phys. Rev. Lett. **112**, 096401 (2014).

[507]E. Maggio and G. Kresse, "GW vertex corrected calculations for molecular systems", J. Chem. Theory Comput. **13**, 4765–4778 (2017).

[508]C. Mejuto-Zaera and V. Vĺcček, "Self-consistency in GWΓ formalism leading to quasiparticle-quasiparticle couplings", Phys. Rev. B **106**, 165129 (2022).

[509]X. Ren, N. Marom, F. Caruso, M. Scheffler, and P. Rinke, "Beyond the GW approximation: A second-order screened exchange correction", Phys. Rev. B **92**, 081104 (2015).

[510]Y. Wang, P. Rinke, and X. Ren, "Assessing the G0W0Γ0(1) approach: beyond G0W0 with hedin's full second-order self-energy contribution", J. Chem. Theory Comput. **17**, 5140–5154 (2021).

[511]Y. Wang and X. Ren, "Vertex effects in describing the ionization energies of the first-row transition-metal monoxide molecules", J. Chem. Theory Comput. **157**, 214115 (2022).

[512]A. Förster and L. Visscher, "Exploring the statically screened $g3w2$ correction to the gw self-energy: charged excitations and total energies of finite systems", Phys. Rev. B **105**, 125121 (2022).

[513]V. Vlček, "Stochastic vertex corrections: linear scaling methods for accurate quasiparticle energies", J. Chem. Theory Comput. **15**, 6254–6266 (2019).

[514]Y. Pavlyukh, G. Stefanucci, and R. van Leeuwen, "Dynamically screened vertex correction to *GW*", Phys. Rev. B **102**, 045121 (2020).

[515]A. M. Lewis and T. C. Berkelbach, "Vertex corrections to the polarizability do not improve the gw approximation for the ionization potential of molecules", J. Chem. Theory Comput. **15**, 2925 (2019).

[516]W. Dou, J. Lee, J. Zhu, L. Mejía, D. R. Reichman, R. Baer, and E. Rabani, "Time-dependent second-order green's function theory for neutral excitations", J. Chem. Theory Comput. **18**, 5221–5232 (2022).

[517]C. J. C. Scott, O. J. Backhouse, and G. H. Booth, "A "moment-conserving" reformulation of GW theory", J. Chem. Phys. **158**, 124102 (2023).

[518]A. Marie and P.-F. Loos, "A similarity renormalization group approach to Green's function methods", J. Chem. Theory Comput. **XXXX**, XXX–XXX (2023).

[519]A. L. Ankudinov, A. I. Nesvizhskii, and J. J. Rehr, "Dynamic screening effects in x-ray absorption spectra", Phys. Rev. B **67**, 115120 (2003).

[520]M. S. Kaczmarski, Y. Ma, and M. Rohlfing, "Diabatic states of a photoexcited retinal chromophore from ab initio many-body perturbation theory", Phys. Rev. B **81**, 115433 (2010).

[521]B. Baumeier, D. Andrienko, and M. Rohlfing, "Frenkel and charge-transfer excitations in Donor–Acceptor complexes from many-body green's functions theory", J. Chem. Theory Comput. **8**, 2790–2795 (2012).

[522]M. Rohlfing, "Redshift of excitons in carbon nanotubes caused by the environment polarizability", Phys. Rev. Lett. **108**, 087402 (2012).

[523]D. Bohm and D. Pines, "A collective description of electron interactions. I. Magnetic interactions", Phys. Rev. **82**, 625–634 (1951).

[524]D. Pines and D. Bohm, "A collective description of electron interactions: II. Collective vs individual particle aspects of the interactions", Phys. Rev. **85**, 338–353 (1952).

[525]D. Bohm and D. Pines, "A collective description of electron interactions: III. Coulomb interactions in a degenerate electron gas", Phys. Rev. **92**, 609–625 (1953).

[526]X. Ren, P. Rinke, C. Joas, and M. Scheffler, "Random-phase approximation and its applications in computational chemistry and materials science", J. Mater. Sci. **47**, 7447–7471 (2012).

[527]G. P. Chen, V. K. Voora, M. M. Agee, S. G. Balasubramani, and F. Furche, "Random-phase approximation methods", Ann. Rev. Phys. Chem. **68**, 421–445 (2017).

[528]E. Monino, M. Boggio-Pasqua, A. Scemama, D. Jacquemin, and P.-F. Loos, "Reference energies for cyclobutadiene: Automerization and excited states", J. Phys. Chem. A **126**, 4664–4679 (2022).

[529]M. F. Lange and T. C. Berkelbach, "On the Relation between Equation-of-Motion Coupled-Cluster Theory and the *GW* Approximation", J. Chem. Theory. Comput. **14**, 4224–4236 (2018).

[530]R. Quintero-Monsebaiz, E. Monino, A. Marie, and P.-F. Loos, "Connections between many-body perturbation and coupled-cluster theories", J. Chem. Phys. **157**, 231102 (2022).

[531]J. Tölle and G. Kin-Lic Chan, "Exact relationships between the GW approximation and equation-of-motion coupled-cluster theories through the quasi-boson formalism", J. Chem. Phys. **158**, 124123 (2023).

[532]V. Rishi, A. Perera, and R. J. Bartlett, "A route to improving RPA excitation energies through its connection to equation-of-motion coupled cluster theory", J. Chem. Phys. **153**, 234101 (2020).

[533]R. D. Mattuck, *A guide to Feynman diagrams in the many-body problem*, Second, Dover Books on Physics and Chemistry (Dover Publications, New York, 1992).

[534]L. S. Cederbaum and W. Domcke, "Theoretical aspects of ionization potentials and photoelectron spectroscopy: A greens function approach", in *Adv. Chem. Phys.* (John Wiley & Sons, Inc., Mar. 1977), pp. 205–344.

[535]J. Oddershede, P. Jørgensen, and D. L. Yeager, "Polarization propagator methods in atomic and molecular calculations", Comp. Phys. Comm. **2**, 33–92 (1984).

[536]M. Gell-Mann and K. A. Brueckner, "Correlation energy of an electron gas at high density", Phys. Rev. **106**, 364–368 (1957).

[537]P. Nozières and D. Pines, "Correlation energy of a free electron gas", Phys. Rev. **111**, 442–454 (1958).

[538]B. Cunningham, M. Grüning, P. Azarhoosh, D. Pashov, and M. van Schilfgaarde, "Effect of ladder diagrams on optical absorption spectra in a quasiparticle self-consistent *GW* framework", Phys. Rev. Mater. **2**, 034603 (2018).

[539]N. Dadkhah, W. R. L. Lambrecht, D. Pashov, and M. van Schilfgaarde, "Improved quasiparticle self-consistent electronic band structure and excitons in $LiGaO_2$", Phys. Rev. B **107**, 165201 (2023).

[540]M. Grzeszczyk, S. Acharya, D. Pashov, Z. Chen, K. Vaklinova, M. van Schilfgaarde, K. Watanabe, T. Taniguchi, K. S. Novoselov, M. I. Katsnelson, and M. Koperski, "Strongly correlated exciton-magnetization system for optical spin pumping in $CrBr_3$ and CrI_3.", Adv. Mater. **35**, 2209513 (2023).

[541]W. Chen and A. Pasquarello, "Accurate band gaps of extended systems via efficient vertex corrections in *GW*", Phys. Rev. B **92**, 041115 (2015).

[542]H. van Aggelen, Y. Yang, and W. Yang, "Exchange-correlation energy from pairing matrix fluctuation and the particle-particle random-phase approximation", Phys. Rev. A **88**, 030501 (2013).

[543]Y. Yang, H. van Aggelen, S. N. Steinmann, D. Peng, and W. Yang, "Benchmark tests and spin adaptation for the particle-particle random phase approximation", J. Chem. Phys. **139**, 174110 (2013).

[544]H. van Aggelen, Y. Yang, and W. Yang, "Exchange-correlation energy from pairing matrix fluctuation and the particle-particle random phase approximation", J. Chem. Phys. **140**, 18A511 (2014).

[545]C. Bannwarth, J. K. Yu, E. G. Hohenstein, and T. J. Martínez, "Hole–hole Tamm–Dancoff-approximated density functional theory: A highly efficient electronic structure method incorporating dynamic and static correlation", J. Chem. Phys. **153**, 024110 (2020).

[546]E. Rebolini, "Range-separated density-functional theory for molecular excitation energies", PhD thesis (Université Pierre et Marie Curie — Paris VI, 2014).

[547]J. Schirmer and A. B. Trofimov, "Intermediate state representation approach to physical properties of electronically excited molecules", J. Chem. Phys. **120**, 11449–11464 (2004).

[548]M. Wormit, "Development and application of reliable methods for the calculation of excited states: From light-harvesting complexes to medium-sized molecules", PhD thesis (Frankfurt University, 2009).

[549]A. Marini and R. Del Sole, "Dynamical excitonic effects in metals and semiconductors", Phys. Rev. Lett. **91**, 176402 (2003).

[550]S. Yamada, Y. Noguchi, K. Ishii, D. Hirose, O. Sugino, and K. Ohno, "Development of the Bethe-Salpeter method considering second-order corrections for a GW electron-hole interaction kernel", Phys. Rev. B **106**, 045113 (2022).

[551]M. Schreiber, M. R. Silva-Junior, S. P. A. Sauer, and W. Thiel, "Benchmarks for electronically excited states: CASPT2, CC2, CCSD and CC3", J. Chem. Phys. **128**, 134110 (2008).

[552]M. R. Silva-Junior, M. Schreiber, S. P. A. Sauer, and W. Thiel, "Benchmarks of electronically excited states: Basis set effects on CASPT2 results", J. Chem. Phys. **133**, 174318 (2010).

[553]M. R. Silva-Junior, S. P. A. Sauer, M. Schreiber, and W. Thiel, "Basis set effects on coupled cluster benchmarks of electronically excited states: CC3, CCSDR(3) and CC2", Mol. Phys. **108**, 453–465 (2010).

[554]M. R. Silva-Junior, M. Schreiber, S. P. A. Sauer, and W. Thiel, "Benchmarks of electronically excited states: Basis set effecs on CASPT2 results", J. Chem. Phys. **133**, 174318 (2010).

[555]J. Čížek and J. Paldus, "Stability conditions for the solutions of the Hartree—Fock equations for atomic and molecular systems. Application to the Pi-Electron model of cyclic polyenes", J. Chem. Phys. **47**, 3976–3985 (1967).

[556]A. Endo, M. Ogasawara, A. Takahashi, D. Yokoyama, Y. Kato, and C. Adachi, "Thermally activated delayed fluorescence from sn4-Porphyrin complexes and their application to organic light emitting diodes - A novel mechanism for electroluminescence", Adv. Mater. **21**, 4802–4806 (2009).

[557]H. Uoyama, K. Goushi, K. Shizu, H. Nomura, and C. Adachi, "Highly efficient organic light-emitting diodes from delayed fluorescence", Nature **492**, 234–238 (2012).

[558]M. A. Baldo, D. F. OBrien, Y. You, A. Shoustikov, S. Sibley, M. E. Thompson, and S. R. Forrest, "Highly efficient phosphorescent emission from organic electroluminescent devices", Nature **395**, 151–154 (1998).

[559]C. Adachi, M. A. Baldo, M. E. Thompson, and S. R. Forrest, "Nearly 100% internal phosphorescence efficiency in an organic light-emitting device", J. Appl. Phys. **90**, 5048–5051 (2001).

[560]P. de Silva, "Inverted Singlet–Triplet gaps and their relevance to thermally activated delayed fluorescence", J. Phys. Chem. Lett. **10**, 5674–5679 (2019).

[561]J. Sanz-Rodrigo, G. Ricci, Y. Olivier, and J. C. Sancho-García, "Negative Singlet–Triplet excitation energy gap in triangle-shaped molecular emitters for efficient triplet harvesting", J. Phys. Chem. A **125**, 513–522 (2021).

[562]G. Ricci, E. San-Fabián, Y. Olivier, and J. C. Sancho-García, "Singlet-triplet excited-state inversion in heptazine and related molecules: Assessment of TD-DFT and ab initio methods", ChemPhysChem **22**, 553–560 (2021).

[563]Y. Olivier, B. Yurash, L. Muccioli, G. D'Avino, O. Mikhnenko, J. C. Sancho-García, C. Adachi, T.-Q. Nguyen, and D. Beljonne, "Nature of the singlet and triplet excitations mediating thermally activated delayed fluorescence", Phys. Rev. Mater. **1**, 075602 (2017).

[564]Y. Olivier, J.-C. Sancho-Garcia, L. Muccioli, G. D'Avino, and D. Beljonne, "Computational design of thermally activated delayed fluorescence materials: The challenges ahead", J. Chem. Theory Comput. **9**, 6149–6163 (2018).

[565]J. C. Sancho-García, E. Brémond, G. Ricci, A. J. Pérez-Jiménez, Y. Olivier, and C. Adamo, "Violation of Hund's rule in molecules: Predicting the excited-state energy inversion by TD-DFT with double-hybrid methods", J. Chem. Phys. **156**, 034105 (2022).

[566]K. Curtis, O. Adeyiga, O. Suleiman, and S. O. Odoh, "Building on the strengths of a double-hybrid density functional for excitation energies and inverted singlet-triplet energy gaps", J. Chem. Phys. **158**, 024116 (2023).

[567]F. Jensen, *Introduction to computational chemistry*, 3rd (Wiley, New York, 2017).

[568]T. Helgaker, P. Jørgensen, and J. Olsen, *Molecular electronic-structure theory* (John Wiley & Sons, Inc., 2013).

[569]M. N. Tahir and X. Ren, "Comparing particle-particle and particle-hole channels of the random phase approximation", Phys. Rev. B **99**, 195149 (2019).

[570]M. Degroote, "Faddeev random phase approximation applied to molecules", Eur. Phys. J. Spec. Top. **218**, 1–70 (2013).

[571]D Nabok, S. Blügel, and C Friedrich, "Electron–plasmon and electron–magnon scattering in ferromagnets from first principles by combining gw and gt self-energies", npj Comput Mater **7**, 178 (2021).

[572]R. A. Smith, "Planar version of baym-kadanoff theory", Phys. Rev. A **46**, 4586–4597 (1992).

[573]L. D. Faddeev, "Scattering theory for a three-particle system", Soviet Physics JETP **12**, 1459–1467 (1961).

[574]R. Quintero-Monsebaiz and P.-F. Loos, *Equation generator for equation-of-motion coupled cluster assisted by computer algebra system*, 2023.

[575]G. Sahil, F. K. Eirik, F. S. John, K. Henrik, and A. I. Krylov, "Equation-of-motion coupled-cluster method with double electron-attaching operators: Theory, implementation, and benchmarks", J. Chem. Phys. **154**, 114115 (2021).

[576]O. A. Adeayo, S. Jun, and P. Piotr, "Economical doubly electron-attached equation-of-motion coupled- cluster methods with an active-space treatment of three-particle–one-hole and Four-Particle–Two-Hole excitations", J. Phys. Chem. A **121**, 3469–3485 (2017).